The University Of Sheffield.

New Developments in InAs/InGaAs Quantum Dot-in-a-well Infrared Photodetectors

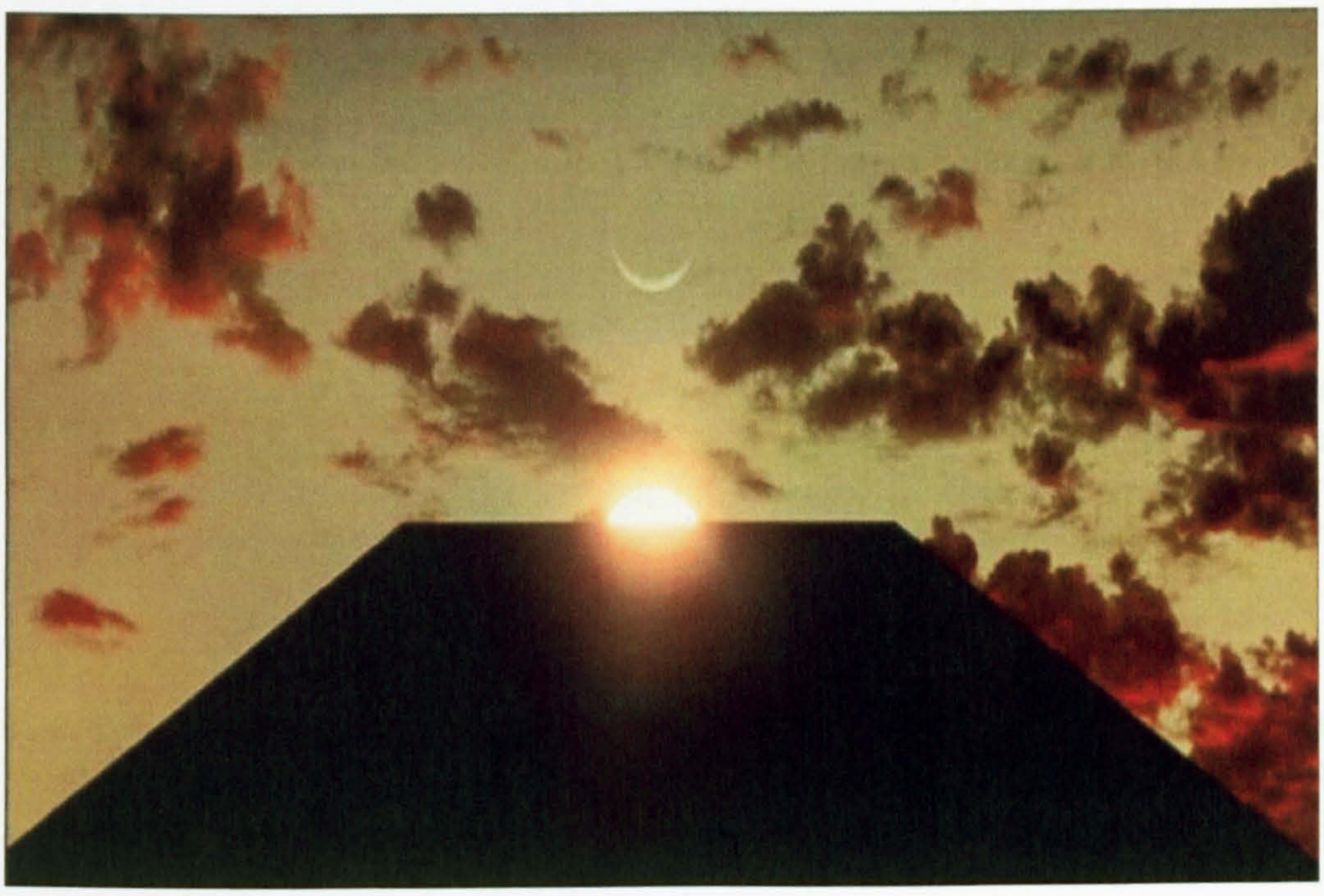

Thesis submitted for the Degree of Doctor of Philosophy

by Pantelis Aivaliotis
Department of Physics and Astronomy
University of Sheffield

October 2007

Picture of one black body behind another, from '2001 A Space Odyssey' by Stanley Kubrick.© Metro-Goldwyn-Mayer (MGM), Polaris, Stanley Kubrick Productions

Abstract

This thesis presents experimental studies of InAs/InGaAs/GaAs quantum dot-in-a-well infrared photodetectors (DWELL QDIPs) grown by molecular beam epitaxy (MBE). Detailed studies were carried out to investigate the effects of design parameters on the performance of DWELL photodetectors, along with fundamental studies to determine the intraband optical and electronic properties of such structures. Using the results of these studies, an optimised structure was designed. In addition, the observation of a strong bias dependent spectral photoresponse demonstrated the capability of post growth spectral tunability within the long wavelength IR (LWIR) atmospheric window.

Various approaches were investigated for enhancing the performance of quantum dot (QD) based devices. The main shortcoming of QDIPs versus quantum well infrared photodetectors (QWIPs) has been addressed i.e. the low dot density, which prohibits the high doping of these structures. The use of an antimonide surfactant to enhance the dot density in DWELL QDIPs is presented here for the first time. Also a method for decreasing the dark current in QDIPs was investigated, via the use of wide band gap AlGaAs barriers. Another technique using GaP strain balancing layers to reduce the strain in multilayer structures and allow the growth of >20 layer QD devices was illustrated.

The effects of intermixing via thermal annealing are also reported in for DWELL QDIPs. As part of this study, the possibility of using such a technique to shift the spectral photoresponse across the 8-12μm LWIR window is demonstrated, and it is shown that the performance still remains in a competitive range within the LWIR range.

Non-linear two photon absorption in QDIPs was demonstrated and studied. As a result of this study, the capability of QDIPs to operate as quadratic detectors in the far-infrared was established, which could prove very significant, since detector availability is reduced in that range.

Finally, a novel approach to photovoltaic QDIPs was investigated experimentally, using a purpose built design in order to provide an internal electric field, which preferentially drives carriers in one direction.

Acknowledgements

I would first of all like to express my gratitude to my supervisor Dr. Luke Wilson, for all his invaluable guidance and feedback as well as his patience throughout these 3 years. I would also like to thank Dr. Evgeny Zibik, who I had the chance of working with extensively, and without whose guidance and assistance in my experiments, I would have never accomplished what I have in my PhD.

Other members of Sheffield academic staff during my PhD that I am grateful to include Dr. Dmitry Revin, Prof. John Cockburn, and Dr. Sabine Laurent for their help with several aspects of the work. Also Ben Carpenter for happily providing endless IT assistance. In addition, all the people who contributed or where associated with the work, Prof. John David, Dr. Chris Groves, Prof. Mark Hopkinson, Dr. R. J. Airey, Dr. H.Y. Liu, Dr. M. J. Steer, Dr. Chee-Hing Tan, Stefan Menzel and S.C. Liew-Tat-Mun, and everybody in the National Centre for III-V growth in Sheffield, for their help and services and for providing all the devices for this thesis.

I would also like to thank all the collaborators in this project including: Prof. H.C. Liu and Dr. Aslan Bulent from NRC Canada, for their help in the initial stages of the project, all the people at the EMRS DTC, Dr. Olek Kowalski from Intense Photonics, Dr. Britta Redlich, Dr. N.Q. Vinh, Mr. Rene van Buuren and Dr. Lex van der Meer from the FELIX facility in FOM Institute of Plasma Physics, for their contribution to the measurements I performed there, as well as their personal help, and their efforts to facilitate my stay there. Also, I would like to thank our collaborators in the Institute of Microwave and Photonics, Leeds University, Prof. Paul. Harrisson, Dr. Dragan Indjin, and particularly Dr. Nenad Vukmirovic, who provided all the theoretical work that was used to support some of the experimental observations in this thesis.

I would also like to thank Chris Vickers and Paul Kemp-Russell for their truly valuable technical help, and for their efficacy in dealing with equipment, when for very mysterious reasons they stopped working or where damaged.

I would not of course in any case forget to acknowledge the support of my family. I would especially like to thank my parents Aristotelis and Anna and my sister Maria for calling me so often and asking me if I was going to finish soon (from year one), and what it was exactly I was doing.

Finally I would like to thank all my friends in Sheffield, without whose company and pleasant nights out and in, I would have definitely gone mad. Namely, Kevin Jobson, Dr. Wing H Ng, Tom Badcock, Elham Nabavi, to whom I also owe thanks for help with physics-related subjects, Tim and Claire Phillips, Sam Bunn, Sam Marsh, Lucy Davies, Daniel Leary, Tom Bates, George Lovett, Helen Campion-Smith, Sarah Hollingsworth, Claudia Amico, Matt Bell, Saioa San Miguel, (Sir)Panos Papastergeiou, Dr. Calliopi Chourmouziadou, Kwstas Sakantamis, Lucy Johnston, John Rothwell, Josie Gill, Kate Walsh, Leandros Andrikopoulos, Kyriakos Eleutheriades, Dr. Vassilis Avdikos, Dr. Nikos Stavropoulos, Dr. Giwrgos Chliveros, Giwrgos Zaxarioudakis, and Mal Lorrimer. Also my friends in Greece and elsewhere who at times provided me with a great few day escape plan when I most needed it, or with an electronic or telephonic conversation, Agelis Tsotras, Isidoros Moulas, Maria Giannakopoulou, Electra Pasti, and many more who I could probably fill another page with.

To anyone who I might have forgotten, sorry and…Thanks!

Pantelis Aivaliotis

January 2007

List of Publications

Chapter 3

- *'Energy level structure and electron relaxation times in InAs/InxGa1-xAs quantum dot-in-a-well structures'*
  P. Aivaliotis, S. Menzel, E. A. Zibik, J. W. Cockburn, L. R. Wilson, M. Hopkinson, Applied Physics Letters, **91** (25) 253502(2007)
- *'Stark shift of the spectral response in quantum dots-in-a-well infrared photodetectors'*
  P. Aivaliotis, N. Vukmirovic, E. A. Zibik, J. W. Cockburn, D. Indjin, P. Harrison, C. Groves, J. P. R. David, M. Hopkinson and L. R. Wilson, Journal of Physics D **40** 5537-5540 (2007)
- *'Optimisation of quantum dot infrared photodetectors (QDIPs) for imaging applications'*
  P. Aivaliotis, E. Zibik, L. R. Wilson, J. P. R. David, M. Hopkinson, C. Groves, SPIE Conference proceedings, Proc. SPIE Vol. 6395(2006)

Chapter 4

- *'Enhancing the dot density in quantum dot infrared photodetectors via the incorporation of antimony'*
  P. Aivaliotis, L. R. Wilson, E. A. Zibik, J. W. Cockburn, M. J. Steer, H. Y. Liu, Applied Physics Letters **91** (1) 013503 (2007)

Chapter 5

- *'Tuning the photoresponse of quantum dot infrared photodetectors across the 8-12μm atmospheric window via rapid thermal annealing'*
  P. Aivaliotis, E. A. Zibik, L. R. Wilson, J. W. Cockburn, M. Hopkinson and R.. J. Airey, Applied Physics Letters **91** (14) 143502 (2007)
- *'Two photon absorption in quantum dot-in-a-well infrared photodetectors'*
  P. Aivaliotis, E. A. Zibik, L. R. Wilson, J. W. Cockburn, M. Hopkinson, N. Q. Vinh, Applied Physics Letters **92** (2) 023501 (2008)

Conferences attended

- *'Increasing the dot density in quantum dot infrared photodetectors via antimony mediated dot formation'*

  P. Aivaliotis, E.A. Zibik, M.J. Steer, H.Y.Liu, G. Hill, C. Calder, J.W. Cockburn, L.R. Wilson, poster presentation, The Ninth International Conference on Intersubband Transitions in Quantum Wells, ITQW2007, (2007)

- *'Experimental and theoretical investigation of the spectral Stark shift in quantum dots-in-a-well infrared photodetector'*

  P. Aivaliotis, N. Vukmirović, E. A. Zibik, D. Indjin, J. W. Cockburn, P. Harrison, C. Groves, J. P. R. David, M. Hopkinson, and L. R. Wilson, poster presentation at The Ninth International Conference on Intersubband Transitions in Quantum Wells, ITQW07 (2007)

- *'Design strategies in InAs/InGaAs quantum dots-in-a-well infrared photodetectors'*

  P. Aivaliotis, E.A. Zibik, L.R.Wilson, S. Menzel, J. W. Cockburn, J.P.R. David, M. Hopkinson, C. Groves, S.L. Liew, poster presentation, 28th International Conference on the Physics of Semiconductors (ICPS) Vienna, Austria, 24-28/07 (2006)

- *'On the performance of Quantum dot infrared photodetectors based on a dots-in-a-well structure'*

  P. Aivaliotis, E.A. Zibik, L.R. Wilson, J.W. Cockburn, oral presentation, Electro-Magnetic Remote Sensing (EMRS) Defence Technology Centre, 3d Annual Technical Conference 13-14th July, Edinburgh (2006)

- *'InAs/InGaAs quantum dots-in-a-well infrared photodetectors'*

  P. Aivaliotis, E.A. Zibik, L.R. Wilson, J.P.R. David, J.W. Cockburn, M. Hopkinson, C. Groves, C. H. Tan and S.C. Liew Tat Mun, oral presentation at UK Compound Semiconductors, Sheffield, UK, 4-5th of July, (2006)

- *'Enhancing the performance of InAs/InGaAs quantum dots-in-a-well infrared photodetectors'*

  P. Aivaliotis, E.A. Zibik, L.R. Wilson, S. Menzel, J.W. Cockburn, J.P.R. David, M. Hopkinson, C. Groves, S.L. Liew, C.H. Tan, S.C. Liew-Tat-Mun, oral presentation, International Workshop on Quantum Well Infrared Photodetectors, QWIP 2006, 18-24/06/2006, Kandy, Sri Lanka (2006)

- *'High performance quantum dots-in-a-well infrared photodetectors'*

  P. Aivaliotis, E.A. Zibik, L.R. Wilson, J.W. Cockburn, J.P.R. David, M. Hopkinson, C. Groves, oral presentation, Condensed Matter and Materials Physics organized by the Institute of Physics in Exeter, UK 19-21/04/2006 (2006)

- *'Optimisation of quantum dot infrared photodetectors (QDIPs) for imaging applications'*

  P. Aivaliotis, E. Zibik, L. R. Wilson, J. P. R. David, M. Hopkinson, and C. Groves, oral presentation, SPIE Europe Remote Sensing, 11 - 14 September 2006, Stockholm, Sweden, Proceedings of SPIE -- Volume 6395 Electro-Optical and Infrared Systems: Technology and Applications III (published online Oct. 5) (2006)

- *'Intraband stark shift in two-colour quantum dot infrared photodetectors'*

  P. Aivaliotis, E.A. Zibik, L.R.Wilson, J.P.R David, M. Hopkinson, C. Groves, J.W. Cockburn, oral presentation, MIOMD-VII, Mid-infrared Optoelectronics: Materials and Devices, 12th -14th September 2005, Lancaster UK (2005)

- *'Quantum dot infrared photodetectors'*

  P. Aivaliotis, E. A. Zibik, L. R. Wilson, J. P. R. David, C. Groves, J. W. Cockburn, M. Hopkinson, oral presentation, Electro-Magnetic Remote Sensing(EMRS) Defence Technology Centre, 2nd Annual Technical Conference, 16th-17th June, Edinburgh (2005)

Contents

1. Introduction

1.1. Infrared Radiation

The detection of infrared radiation (IR) has been a subject of interest for almost 200 years, since the discovery of IR in 1800 by William Herschel [1]. However it was after the end of World War II that IR technology became widespread in military as well as civilian applications. Today, IR emitters and detectors can be found in several research and commercial applications such as in meteorology, defence, medical imaging, solid state spectrometry, chemical analysis, communications etc.

Infrared radiation covers the region in the electromagnetic spectrum with wavelengths ranging from 1μm-1000μm. The wavelength regions which are of common interest for IR detection are the 1-3μm, 3-5μm and 8-14μm regions of the electromagnetic spectrum, since atmospheric transmission is the highest in these bands, which are also denoted as the near-IR (NIR), middle wavelength-IR (MWIR), and long-wavelength IR (LWIR) 'atmospheric windows' respectively. In particular the 3-5μm and 8-14μm windows are useful for thermal imaging applications, and detectors operating in these windows will be the main emphasis of this thesis. Detectors reaching into the far-infrared (>25μm) (or terahertz region) will also be discussed, since they are attracting increasing attention in a variety of applications such as spectroscopy, detection of explosives, and medical imaging.

1.1.1. Thermal and Photon Detectors

IR detectors commonly operate by converting infrared radiation into an electrical signal. IR detectors can be either thermal or photonic devices. Thermal detectors absorb the incident radiation and a change in a temperature dependent physical property of the material of the active region - such as electrical conductivity, is used to generate an electrical output [2,3]. Since these detectors rely on heat exchange they are generally wavelength non-specific and are characterised by modest sensitivity and slow response. However, they are cost-effective as they do not require cooling, and this makes them suitable for low cost applications where high performance and speed are of less importance. They are generally more suitable for far-infrared detection, and they are often used in spectrometers. Common types include thermopiles, pyroelectric detectors and bolometers [3,4].

In photon detectors the radiation is absorbed within the material by interaction with electrons which are either bound to lattice atoms or to impurity atoms or with free electrons. The absorption of photons and hence quantum transitions between different energy states causes a change in the electronic energy distribution, which results in an electrical signal [3]. In photon detectors the electrical signal is dependent on the number of photons absorbed rather than their energy and they have beneficial properties such as being wavelength dependent, having good signal to noise ratios and fast response making them suitable for various imaging applications. However they require cryogenic cooling, which makes them bulky and expensive. The main objectives of IR photon detector research are to produce

detectors that work at higher temperatures, whilst being suitable for integration onto large and cost-effective focal plane arrays (FPA).

Infrared photodetectors commonly have active regions made from semiconductor heterostructures consisting of parts where a narrow band gap material is surrounded by a wide band-gap material. The absorption of photons in such materials is typically associated with electronic transitions between valence and conduction bands (interband transitions), or between discrete bound states within the conduction (or valence) band (intersublevel transitions) or bound subbands (intersubband transitions) within the conduction (or valence) bands.

Both intersublevel and intersubband transitions are distinct from interband transitions in that they involve one type of carrier i.e. an electron (or a hole) within either the conduction or valence band respectively. For reasons of clarity the term *intraband* transitions (and *intraband* IR detectors) will be used to describe both intersublevel and intersubband transitions, unless specified.

1.1.2. Planck's Law – black body radiation

Before further details are provided regarding the physics of intraband transitions and the operation of the relevant detectors, a discussion of the general principle of how the emission of infrared radiation by an object is influenced by its temperature, and how the detection of this radiation allows the temperature sensing of this object is presented.

The concept of temperature is equivalent to certain energy distributions [5]. For electromagnetic radiation in an isothermal cavity (i.e. the radiation temperature being constant at each position in the cavity) at thermal equilibrium at a temperature T, the energy distribution of the radiation density (or photon states) in the cavity is described by *Planck's radiation law* [5, 6].

According to this, the total power per unit surface area or *Irradiance* I_ν is given by:

$$dI_\nu = \frac{2\pi h}{c^2} \frac{\nu^3 d\nu}{e^{h\nu/k_B T} - 1} \tag{1.1}$$

Where c: speed of light $=3\text{x}10^8 \text{ms}^{-1}$, h: Planck's constant $= 6.626\times10^{-34}\text{m}^2\text{kgs}^{-1}$ k: Boltzmann constant $= 1.38\times10^{-23}\text{m}^2\text{kgs}^{-2}\text{K}^{-1}$ and ν is the photon frequency.

For thermal equilibrium to exist in the walls of the cavity, the total absorbed radiation must equal the total emitted power at the entire surface. This is usually expressed in terms of the emissivity ε, which at thermal equilibrium equals the absorptivity of an object [5].

However, even in the absence of thermal equilibrium between a body of temperature T and the radiation field, the surface of the body will still emit radiation. Considering this, equation (1.1), for a given emissivity $\varepsilon(\nu, \Omega)$ changes to give the *radiance* $H((\nu, \Omega))$ of the object:

$$dH_{\nu,\Omega} = \varepsilon(\nu,\Omega)\frac{2h}{c^2}\frac{\nu^3 d\nu \cos\theta d\Omega}{e^{h\nu/k_BT}-1} \tag{1.2}$$

where $d\Omega = \sin\theta d\theta d\phi$, θ is the polar angle and ϕ is the azimuthal angle. When ε is equal to unity, the body is referred to as a 'black body' (BB) [5].

Integrating equation 1.2 over θ and for a uniform isotropic radiation field, gives the power density emitted per frequency, which is equivalent to the I_ν in (1.1) multiplied by ε. Substituting E=$h\nu$, gives equation (1.3):

$$dP_E = A\varepsilon\frac{2\pi h}{h^3c^2}\frac{E^3 dE}{e^{E/k_BT}-1} \tag{1.3}$$

which can be integrated over E to give the Stefan-Boltzmann equation [5,6]:

$$P_{TOT} = A\varepsilon\sigma T^4 \tag{1.4}$$

The Stefan Boltzmann constant $\sigma = 5.67\text{x}10^{-8}\text{W/m}^2\text{K}^4$

Thus the emitted radiation of an object with temperature T has a maximum which can be derived by Wien's displacement law [6]:

$$\lambda_{peak}(\mu\text{m}) = \frac{2893}{T(K)} \tag{1.5}$$

For a small detector of area A, additional parameters are introduced in the above expressions, since an optical objective or aperture will be typically used in front of the sensor. In that case the *f*-number, which a ratio of the focal length of the objective divided by the lens (or aperture) diameter, must be included in order to derive the power incident on the detector. If an objective lens is not used, then the field of view is determined by the aperture of the cryogenic enclosure of the sensing area and the viewing angle θ. The relationship between all optical factors and the incident power on a detector are discussed further in the following section on the responsivity of a detector (see section 1.2.3).

Two general characteristics that arise from Planck's law are [3]:

(a) The higher the temperature of an object the more energy it will emit. This is a non-linear dependence whereby small changes in temperature result in large changes in emitted power.

(b) From equation (1.5), the higher the temperature of an object the shorter the wavelength at which the peak of the emitted radiation spectral distribution occurs. If we consider the temperature of the human body (~36°C) to be 309K, from equation (1.5) the wavelength at which the maximum energy is emitted is at ~9μm.

1.2. Basics of intraband infrared detection

1.2.1. Dark Current and BLIP condition

In n-type photoconductive quantum well (QW) and quantum dot (QD) detectors, which are the most common class of intraband detectors, the device is a unipolar photoconductor with n-doped contacts similar to a n-*i*-n diode. In photoconductors, dark current is one of the most crucial parameters in device operation, as it influences the noise of the detector and determines the operating temperature, and in some cases the dynamic range of the device in terms of the maximum external applied field. In this section, the dark current process is discussed in detail as it also aids the understanding of carrier dynamics in QDIPs.

Several general models have been used to describe the principles of carrier transport under dark conditions in quantum well infrared photodetectors (QWIPs), which are also relevant to quantum dot infrared photodetectors (QDIPs), or any intraband photoconductor. Furthermore recent theoretical models have been proposed to explain some of the more complex characteristics of the dark current which have been observed in experimentally investigated QDIPs and QWIPs, and these will presented herein. In this section, the principal models will be described and some of the more specific approaches and calculations regarding QDIPs and dot-in-a-well (DWELL) QDIPs will be presented.

The dark current in a single QW device will be considered. Assuming there is only one bound level in the QW, and the barriers are much thicker than the well

(suppressing carrier tunnelling), and that the electron density is constant throughout the well, the remaining determining processes are outlined in Fig.1.2.1 [5].

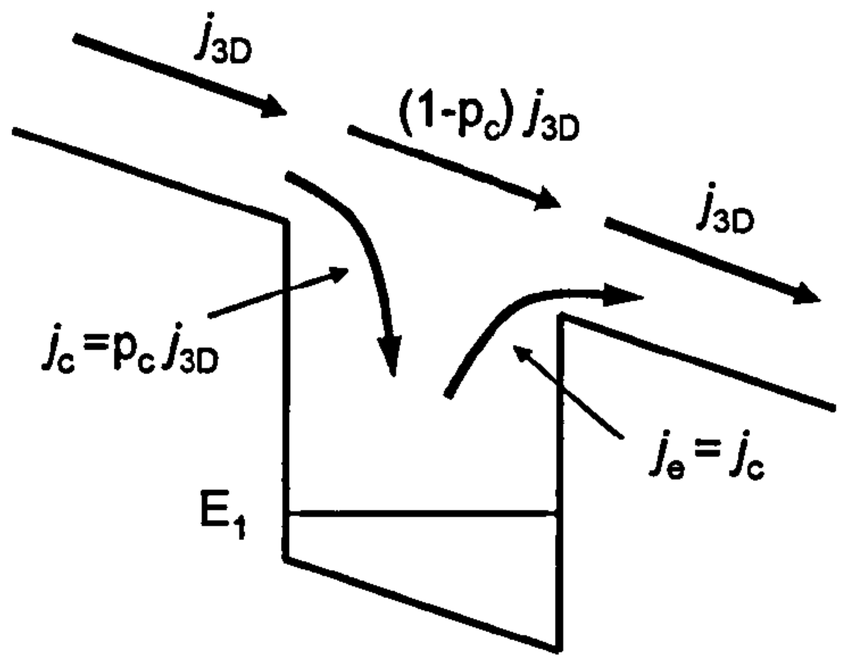

Fig.1.2.1.Single QW and the processes associated with the dark current.

As shown above, the dark current J_d, which will flow in a three-dimensional (3D) manner in the barrier regions, will equal the 3D current density j_{3D}. The dark current will be the same throughout the whole structure. However, at the vicinity of the well electrons will be emitted from the well (j_e) and will contribute to the dark current. Therefore, under steady state (electron density remaining constant in the well) this has to be balanced by the equivalent capture of electrons in the well (j_c). Additionally, j_c will be equal to $p_c * j_{3D}$ where, p_c is the capture probability of an electron traversing a well with energy higher than the barrier height. From the above, the dark current can be derived either by directly calculating the total j_{3D} or by calculating j_e (or j_c).

3D Carrier Drift Model

In order to calculate j_{3D} (=J_d) for a QW with barriers which are much thicker than the wells, a 3D electron density N_{3D} can be assumed on top of the barriers with

diffusion and superlattice band structure effects being neglected [5]. If an electric field F is applied to the structure (see Fig.1.2.1), the dark current density is given by:

$$J_d = eN_{3D}\upsilon(F) \tag{1.6}$$

where $\upsilon(F)$ is the drift velocity as a function of the electric field.

Considering the 2D doping density in a degenerately doped QW in correlation with the above assumptions, N_{3D} can be calculated in terms of the barrier effective mass, thermal activation energy E_{act} (difference between top of barrier and top of Fermi sea in the QW), and temperature [5]. Furthermore assuming a constant mobility the drift velocity in (1.6) can also be calculated, thus allowing the expression above to be expressed in known parameters for a specific structure (i.e. of known mobility, barrier effective mass, etc.) and more details can be found in references [5, 7].

This model is generally accurate, as long as it used to calculate the dark current at low applied fields and for structures with only one bound level. The reason for the first condition is that the calculation of N_{3D} assumes the Fermi level is determined by the well doping at zero bias. As the field increases this assumption is less accurate, as the Fermi levels for the 3D barrier electrons will have a stronger influence [5]. Several models have been proposed to extend the accuracy of this model to higher applied fields [8,9], and it has also been shown that the model accuracy can also be improved by taking into account the barrier lowering due to applied bias [5,10]. Using the model for QWs with more than one bound levels, also shows a good level of agreement with experimental observations [10] but is still limited at higher electric fields.

Emission-Capture

A more accurate model is described by the authors of Ref [5, 10], which describes the scattering assisted escape from QWs, which is the dominant process in typical QWIPs. Although, some assumptions in this model are not valid in the case of QDs (e.g. regarding uniform 2D electron density, and subbands instead of discrete levels), this approach aids the understanding of the general emission-capture model for electrons in a bound state as well as further detector parameters which will be discussed later.

The model assumes 2D confined electrons in the QW that scatter out and become 3D mobile carriers in the barrier. The escape current density from Fig.1.2.1 can be written as:

$$j_e = eN_{2D} / \tau_{scatt} \tag{1.7}$$

where N_{2D} is the electron density in the upper part of the ground state subband (with an energy above the barrier height), and τ_{scatt} is the time for the electrons to scatter from the confined subband to the non-confined continuum of states on top of the barrier. Also, the capture probability will be related to the capture time τ_c and transit time τ_{trans} by:

$$p_c = \frac{\tau_{trans}}{\tau_c + \tau_{trans}} \tag{1.8}$$

where, τ_c is the time it takes for an excited electron to be captured back to the well and τ_{trans} is associated with the time it takes for an excited electron to travel along one QW region and the adjacent barrier (one period of a multi-QW structure).

When an electric field is applied, the capture probability decreases, as the transit process becomes faster ($\tau_{trans} << \tau_c$).

As shown previously and from Fig.1.2.1, $J_d = j_{3D} = j_e/p_c$ and therefore:

$$J_d = e\frac{N_{2D}}{p_c\tau_{scatt}} = e\frac{N_{2D}\tau_c}{\tau_{trans}\tau_{scatt}} = e\frac{\upsilon N_{2D}\tau_c}{L_p\tau_{scatt}} \tag{1.9}$$

where, the drift velocity $\upsilon = L_p/\tau_{trans}$.

Because of the balance between capture and scattering time in steady state as discussed previously:

$$\frac{N_{2D}}{\tau_{scatt}} = \frac{N_{3D}L_p}{\tau_c} \tag{1.10}$$

The first part of (1.10) represents the thermal generation of electrons from the QW.

Substituting (1.10) in (1.9):

$$J_d = e\frac{N_{3D}L_p}{\tau_{trans}} = eN_{3D}\upsilon \tag{1.11}$$

The calculation of N_{2D} and N_{3D} is described in Ref [5], which by including the scattering escape process and the WKB (Wentzel-Kramers-Brillouin) approximation as well as considering electric field effects such as barrier lowering, leads to an accurate model for dark current in QWIPs.

Other models include the approach of Ershov et al [11], where the Poisson equation is solved along with rate equations for electrons in the well and continuity equations for electrons in the barrier. This accounts for experimentally observed capacitance behaviour and non-linear photoconductivity [12]. These effects are strongly dependent on the number of periods in the active region, and hence the model is very useful for realistic devices. Further calculations using the Poisson equation [13], and other numerical methods such as Monte Carlo simulations [14], have been

proposed for QWIPs and have been able to explain several experimentally observed aspects of their dark current behaviour [5].

In QDIPs, several models have been proposed which contain additional complexity compared with those proposed for QWIPs. A general relationship for the dark current in QDIPs, which is equivalent to QWIPs can be expressed as:

$$J_d \simeq e\frac{G_{th}}{p_c}, \tag{1.12}$$

where, G_{th} is the thermal emission (generation) rate.

Early calculations showed how QDIPs should, in principle, have a reduced dark current. Ryzhii [15], in one of the earliest theoretical studies of QDs, used an analytical model to derive the dark current density for a QDIP structure and found that $J_{d(QD)}$ was lower than $J_{d(QW)}$ for 3 different sheet electron densities even for higher temperatures. However, in this model, the QDs are assumed to have no excited bound states, and therefore the estimate for capture probability will not correspond to that in a realistic QD device with several excited states as will be seen later. Furthermore the early model was for an ideal quantum box assumption and not a realistic distribution of QDs, where the dots are typically pyramid or lens shaped (lateral size> vertical size).

Ryzhii et al [16], have more recently used rate equations in a model which assumed an increased complexity in determining the sheet electron density for ensembles of small and large QDs, and compared the characteristics of the simulated QDIPs with calculations for QWIPs. From this study it was proposed that high density

ensembles of small QD, (where the electrons are truly bound) could potentially have improved dark current compared to QWIPs.

Mashade et al [17], used an algorithm in an attempt to accurately model the dark current, considering the thermal excitation of electrons from QD bound states to the continuum, and the capture of mobile electrons as above for QWIPs, as well as the transport of mobile electrons across the potential undulations formed by the QDs, the space charge of electrons in the QDs and contact effects. Another study including the field-assisted tunnelling effects on the dark current of QDIPs has been presented by Stiff-Roberts et al [18].

Also a microscopic model was more recently proposed by Vukmirovic et al [19], where strong coupling of longitudinal-optical phonons with electrons was considered, and longitudinal acoustical phonon interaction with electromagnetic radiation was treated perturbatively within the framework of Fermi's golden rule, to derive the rate equations for the dark current in InAs/GaAs QDIPs with multiple bound excited states. In this study the dependence of the occupancies of the bound levels at different applied fields and temperatures are obtained, thus providing a picture of the carrier distribution at different stages of the thermal activation process.

Of more interest to the present analysis is how the dark current is related to the performance of a detector. The dark current is one of the parameters that affect the noise of a detector. The other main components are $1/f$ noise, Johnson noise, and

photon noise and are described in table 1.1. Generally, noise in a photoconductor can be expressed by:

$$i_{n,gr} = \sqrt{4eg_{photo}I\Delta f} \tag{1.13}$$

This is generally referred to as *generation-recombination* (*g-r*) noise and arises from the fluctuation in the rate of generation and recombination of carriers [5]. In realistic photoconductors other noise contributions due to impurity levels, traps, or impact ionisation can also be present.

The *photoconductive gain* (g_{photo}) is defined as the ratio between the average number of electrons collected in the external circuit and the average number of detected photons $g_{photo} = n_x/n_{det}$. Furthermore in an ideal photoconductor the photoinduced and thermally induced carriers will have the same gain and $g_{photo} = g_{noise} = g$, and this assumption will be adopted for the current discussion.

Table 1.1. Noise sources in detector devices

Noise Source	**Description**
Johnson Noise	Thermal agitation of electrons (independent of bias)
1/*f* noise	Inversely dependent on frequency (not well understood)
Photon noise	Associated with the current induced by incident photons
Shot noise	Lowest noise level obtainable-corresponding to statistics of incident photons
G-R Noise	Fluctuations in the generation and recombination of carriers

The total noise current in a photoconductor (I_T), will not only be due to the dark current I_D, but also due to the noise originating from background photons I_B, and due to the noise induced by the signal itself I_S. This can be expressed by:

$$I_T = I_S + I_B + I_D \tag{1.14}$$

Depending on the relative contribution of each noise current to the total current, three regimes are defined: *signal-noise-limited* (SL), *background limited* (BL), and *dark-current-limited* (DL) [5]. Usually the contribution of either component is dependent on temperature. For example, the detector is said to be background limited when the thermal generation rate exceeds the optical generation rate. The limit at which the two become equal is the *BLIP condition* at a temperature T_{BLIP}. Once this is exceeded, the detector is in the DL regime.

A common assumption in realistic QDIPs is that the Johnson and 1/f noise mentioned above can be neglected [5]. Therefore only the photon and dark current noise currents are significant. The latter can be expressed by:

$$I_{D_{noise}} = \sqrt{4eg_{noise}I_D\Delta f} \tag{1.15}$$

where $g_{noise} \equiv 1/Np_c$, and N is the number of periods in the active region.

The photon noise can be formulated via the same expression as 1.15, by using the photocurrent instead of the dark current g_{photo} in the place of g_{noise}.

1.2.2. Photocurrent and photoconductive gain

As defined in the previous section the photoconductive gain is the number of electrons collected at the external circuit for each absorbed photon, and is the main gain mechanism associated with photocurrent in a photoconductor. Other mechanisms such as avalanche gain due to impact ionisation have been proposed [20], and could affect the photocurrent of a device, but in this section the emphasis will be on photoconductive gain in QWIPs and QDIPs.

The principle of gain is the same in both QWIPs and QDIPs. If the structure discussed in the previous section (see, Fig.1.2.1), is considered, but under IR illumination, the dark current process will be unaffected, but there will be an additional photoinduced process. Upon illumination, electrons bound in the ground state will be directly photo-emitted out of the QW (or QD) onto the barrier. For a system in equilibrium, the electrons in the bound state and the donor atoms maintain charge neutrality in the active region. After photoemission of the electrons, in order for this neutrality to be preserved, electrons are injected from the contact to balance the electron loss, resulting in photoconductive gain. The electrons will either be captured by the successive QWs (or QDs), or travel directly to the other contact. If the latter occurs, then another electron will be injected from the opposite contact, and this will continue until the electron is captured in the wells (or dots).

For calculation of the photoconductive gain, a simple well model is assumed as previously for the dark current (Fig.1.2.1). The model generally describes the

relation between the gain and photocurrent and the relative lifetimes of the transitions involved in an intraband photoconductor with bound states. The emission as consequence of the excitation of electrons in the continuum upon illumination is given by:

$$i_e = e\Phi\eta\frac{p_e}{N} \tag{1.17}$$

where, Φ is the photon number per unit time (or photon flux), η is the total absorption quantum efficiency $\eta=N\eta_1$ [5]. The escape probability p_e is given by:

$$p_e \equiv \frac{\tau_{relax}}{\tau_{relax}+\tau_{esc}} \tag{1.18}$$

where τ_{relax} is the intraband relaxation time and τ_{esc} is the escape time. Note that these times will depend largely on whether the process involves bound-to-bound transitions or bound-to-continuum transitions.

In real QD detector structures the processes involved are more complicated since additional channels (direct tunnelling, thermally assisted processes, and lateral transport) contribute to the total photocurrent. However, this is a good approximation of the probability of the escape process relating to the emission current. The observed photocurrent (I_{photo}) will be equal to the current injected from the contact which refills the bound state (or subband) via electron capture:

$$I_{photo} = \frac{i_e}{p_c} = \frac{e\Phi\eta p_e}{Np_c} \tag{1.19}$$

where p_c is the capture probability from (1.8).

Using (1.8), (1.18) and (1.19), we derive an expression for the photoconductive gain:

$$g_{photo} = \frac{p_e}{Np_c} \approx \frac{1}{N}\left(\frac{\tau_{relax}}{\tau_{relax}+\tau_{esc}}\frac{\tau_{trans}+\tau_c}{\tau_{trans}}\right) \tag{1.20}$$

This expression is very useful when designing a photoconductor, as it shows how the photoconductive gain and hence the photocurrent depends on the carrier lifetimes of the relevant transitions. The lifetimes τ_{relax}, τ_{esc} and τ_c will depend strongly on the position of the excited bound state in a bound-to-bound transition, or in the bound-to-quasi-bound case, which are the transitions used in many modern QWIPs and QDIPs. τ_{trans} on the other hand will depend more on the size of the barrier, which usually lies in a narrow range for one type of device.

The determination of these time constants is a non-trivial task, as it requires sophisticated time resolved ultrafast techniques, since the expected lowest range for times are in the order of hundreds of fs in QWs, and few ps in QDs. Also in both QWs and QDs the relaxation, escape and capture processes are further complicated by the effects of electron-phonon or electron-electron interactions. Further details on the determination of these times will be discussed in chapter 3.1.

1.2.3. Responsivity

The responsivity of a detector is defined as the ratio between $I_{photo} = e\eta g_{photo}\Phi$, and the power signal P with photon energy $h\nu$ which is incident on the detector and is equivalent to $P = h\nu\Phi$. Hence:

$$R = \frac{e\eta g_{photo}}{h\nu} \tag{1.21}$$

From this expression and (1.20), it is obvious that the responsivity of a detector is directly related to the relaxation and capture times involved in the photocurrent process. Therefore and as shown in chapter 3.1 it is of vital importance to design the energy band of the detector with the optimisation of these times in mind.

Interestingly, from (1.20) and (1.21), it arises that the photocurrent and responsivity are independent of the number of periods N, since $\eta \propto N$, and $g_{photo} \propto 1/N$. However this is true under the assumption that the absorption is the same in all layers [5], and a realistic model would be more complex. Nonetheless, although the responsivity cannot be improved by adding more layers, the noise characteristics can improve and hence the overall performance can follow. More details on the number of layers will be discussed on chapter 4.3.

For a realistic QDIP, the peak responsivity is generally of interest which involves the same ratio as (1.21), but with the photocurrent integrated over the spectral distribution of the signal, and the value at the maximum of the spectrum interpolated. The peak photocurrent I_p, when the device is irradiated by a calibrated blackbody (BB) source [21] is given by:

$$I_p = \int_{\lambda_1}^{\lambda_2} R(\lambda)P(\lambda)d\lambda \tag{1.22}$$

where λ_1 and λ_2 are the integration limits of the spectral range of interest, $R(\lambda)$ is the

spectral responsivity and $P(\lambda)$ is the blackbody power per unit wavelength incident on the detector [21]:

$$P(\lambda) = W(\lambda)\sin^2(\frac{\theta}{2})AF\cos\varphi \tag{1.23}$$

Where A is the area of the detector, φ is the angle of incidence, θ is the optical field of view angle determined by the radius ρ of the BB opening and the distance D between BB and detector , so that $\tan(\theta/2) = (\rho/D)$.

F represents coupling factors; $F=T_f(1-r)C$, where T_f is the transmission of windows and filters, r is the reflectivity of the QDIP surface (~0.3 for GaAs), C is the optical beam chopper factor (0,5 ideal chopper), and $W(\lambda)$ is the BB spectral density i.e. the power irradiated per unit wavelength λ per unit area from a BB at temperature T_B. This relates to the *Irradiance* in equation (1.1) and can also be written as:

$$W(\lambda) = \frac{(2\pi c^2 h)}{\lambda^5(e^{hc/\lambda kT_B} - 1)} \tag{1.24}$$

In order to calculate the peak responsivity R_p we use $R(\lambda) = \check{R}(\lambda)R_p$, where $\check{R}(\lambda)$ is the normalised experimentally measured spectral responsivity, along with equations 1.22 and 1.23, to obtain:

$$I_P = R_P G\int_{\lambda_1}^{\lambda_2}\tilde{R}(\lambda)W(\lambda)d\lambda\text{, and hence,}\qquad R_P = \frac{I_P}{G\int_{\lambda_1}^{\lambda_2}\tilde{R}(\lambda)W(\lambda)d\lambda} \tag{1.25}$$

Where G represents all the coupling factors and is given by: $G = \sin^2(\frac{\theta}{2})AF\cos\varphi$.

More details on the measurement of R_p will be discussed in the relevant experimental chapter (see, chapter 2.3).

1.2.4. Detectivity

The *detectivity* (D^*) of a detector is defined as the signal (-per incident power) to noise ratio, normalised by the detector area and bandwidth of the electrical measurements [5]. D^* can be expressed as:

$$D^* = \frac{R\sqrt{A\Delta f}}{i_n} \tag{1.26}$$

In many cases that will be presented in this study, the detectors were measured in the DL regime; in other words above T_{BLIP}. T_{BLIP}, which as discussed above (see, section 1.2.1), is the temperature at which the background noise becomes dominant, and the device is said to be *background limited.* Therefore, the *dark current-limited detectivity* D^*_{DL}, calculated following the assumption that $I_D >> I_B + I_S$ in (1.14), is given by:

$$D^*_{DL} = \frac{R_p}{\sqrt{S_D / A}} \tag{1.27}$$

where the spectral dark current density S_D is given by:

$$S_D = 4egI_D \tag{1.28}$$

(1.27) and (1.28) give:

$$D^*_{DL} = \frac{R_p}{\sqrt{4egJ_D}} \tag{1.29}$$

where J_D is the dark current density of the detector = I_D/A.

The assumption is valid at high temperatures where the dark current is increased. At lower temperatures, it is more accurate to calculate the detectivity by measuring the signal noise of the detector. However, this is a non-trivial task and discrepancies can occur as a result of the experimental configurations used (e.g. variable bandwidths between measurements).

1.3. III-V low dimensional semiconductor physics

1.3.1. Growth and fabrication of low dimensional semiconductor structures and devices

The progress of the semiconductor industry has benefited in recent decades from very sophisticated techniques that are used to grow and fabricate semiconductor materials and devices. In this section, the basics of semiconductor growth will be summarised, and the growth technique which was used to produce the studied samples, will be discussed briefly. Bulk semiconductors are commonly grown by the Czochralski method, which involves melting materials in a crucible [22]. However of more interest here are the techniques that can be used to deposit consecutive thin films on a substrate (epitaxial growth), in order to produce multilayer semiconductor heterostructures with different energy bandgaps, which are useful for a vast number of applications.

Techniques such as Metal-Organic Chemical Vapour Deposition (MOCVD) and Molecular Beam Epitaxy (MBE) have been developed and used to produce perfect crystalline thin films via the deposition of atoms of the desired thin film material on a substrate. The atoms organise on the surface to form a monolayer that can be as thin as only a few nm thick, and the layer is said to have been grown *epitaxially*.

MOCVD is commonly used in industry as it is more cost effective. However for high quality structures MBE can be used, where the reactant atoms are introduced in

an Ultra High Vacuum (UHV) chamber as molecular beams. This technique has been established as a method for reducing contaminants entering the reacting chamber which is a common MOCVD issue. Another advantage of MBE, arising from the use of UHV environment is that the growth can be monitored in-situ by electron beams or ion beams, and monitoring techniques such as Low Energy-Electron Diffraction (LEED) or X-Ray and Ultraviolet Photoemission Spectroscopy (XPS and UPS), or Reflection High-Energy Electron Diffraction (RHEED), are commonly used.

When a semiconductor material of certain chemical composition is grown on a substrate or a layer of a different chemical composition the deposition is called *hetero-epitaxy*. As crystalline materials can differ in lattice constant (i.e. are *lattice mismatched*), strain can be introduced at the interface between the materials. Depending on the magnitude of the difference in lattice constant as well as the thickness and lateral size of the layers different effects can occur. For example, if the mismatch is not very significant then the atomic distances of the material being grown on another can stretch so the atoms 'line up' with the atoms underlying material and the growth is known as *pseudomorphic*.

Another possibility is for the material being grown to retain its lattice constant and for the atomic layers to go out of registry with the underlying crystal, thus creating a lattice defect or *dislocation*. The existence of dislocations in the crystal is usually undesirable, as they can propagate and cause larger dislocations leading to detrimental effects (e.g. producing current leakage paths). The competition between pseudomorphic growth and dislocation formation is often determined by a critical

thickness, after which it is more energetically favourable for the strain to relax into dislocations [22].

Interestingly, it has been shown that the control of the growth conditions of a layer beyond its critical thickness can lead to 3D island formation, in what is called *Stranski-Krastanow* growth. This leads to the coherent formation or self-assembly of quantum dots (QDs) as shown below in Fig.1.3.1. The growth of such structures has enabled various technologies such as QD lasers, detectors, and more recently has been attracting considerable attention for enabling the possibility of quantum computing [23].

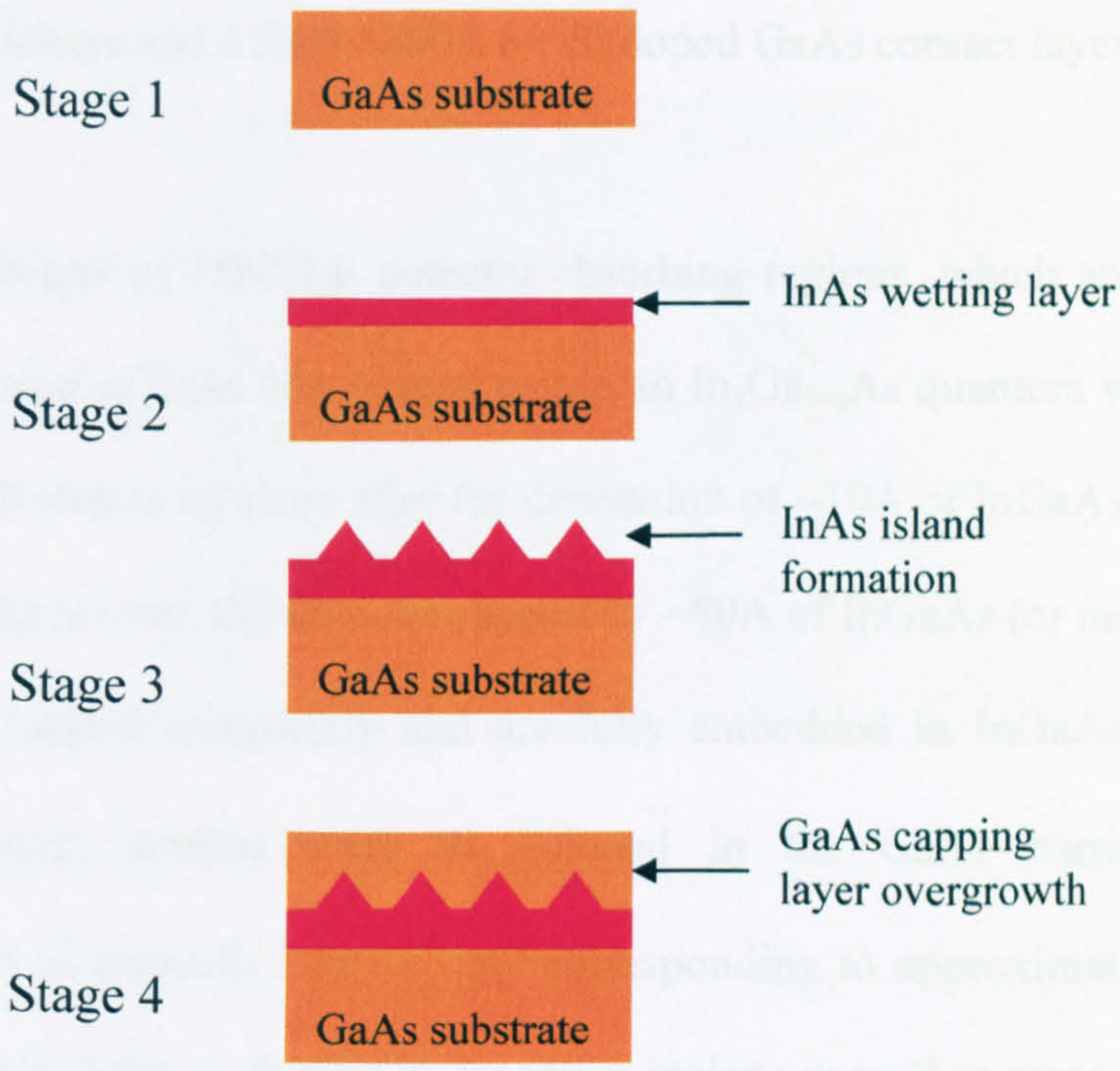

Fig.1.3.1. Schematic representation of the steps in Stranski-Krastanow growth

After the growth of the QDs they are usually capped with another material, quite commonly the same as the underlying one. Devices are typically made from such structures by lithographic patterning techniques such as photolithography, electron beam (e-beam) lithography or focused ion beam (FIB) amongst others.

Growth and Fabrication of the DWELL structures and detectors

All the samples which will be discussed in this thesis were grown by molecular beam epitaxy (MBE) upon semi-insulating GaAs substrates. GaAs barrier layers were typically grown at a temperature of 580°C at a rate of 0.7ML/s, whereas the $In_xGa_{1-x}As$ quantum wells and InAs quantum dots were grown at 510°C at a rate of 0.1ML/s deposited via the Stranski-Krastanow technique. The detector structures, following the growth direction, typically incorporate a layer of 4000Å *n*+ Si doped GaAs, a number of periods of DWELL absorbing region, separated by undoped GaAs barrier layers and a final 4000Å *n*+ Si doped GaAs contact layer.

The initial designs of DWELL detector absorbing regions, which are discussed in chapter 3, consist of InAs dots placed within an $In_xGa_{1-x}As$ quantum well. Typically the dot growth step is initiated after the deposition of ~10A of InGaAs, and after the dot growth step is over, the dots are capped by ~80A of InGaAs (or more), to ensure the dots are capped completely and are fully embedded in InGaAs. The active regions of most devices were Si δ-doped in the GaAs barrier layers, to concentrations of typically ~$6x10^{10}cm^{-2}$ corresponding to approximately 1 electron per dot. Samples with no doping in the active regions as well as more heavily doped structures where grown in order to study the effect of the QD states filling with electrons on the QDIP's performance. Typical InAs/InGaAs QDs have base diameters of 20-40nm and are 6-8nm in height.

Devices were fabricated into mesas using standard photolithography and wet chemical etching. Ni-Ge-Au annular top contacts and grid back contacts were

deposited by evaporation. The devices were subsequently annealed and packaged onto TO-5 headers. Dry plasma-etching was also attempted but did not result in detectors with improved dark current, and therefore was not employed. Hence, wet etching was used for all devices discussed in this thesis.

As shown below in Fig.1.3.2 the top contacts are designed to allow optical access to the top of the semiconductor structure, while accommodating a metallic region which is used to bond the device to allow electrical access. Typically, 400μm and 200μm devices were used, limited by the capability of the bonding equipment.

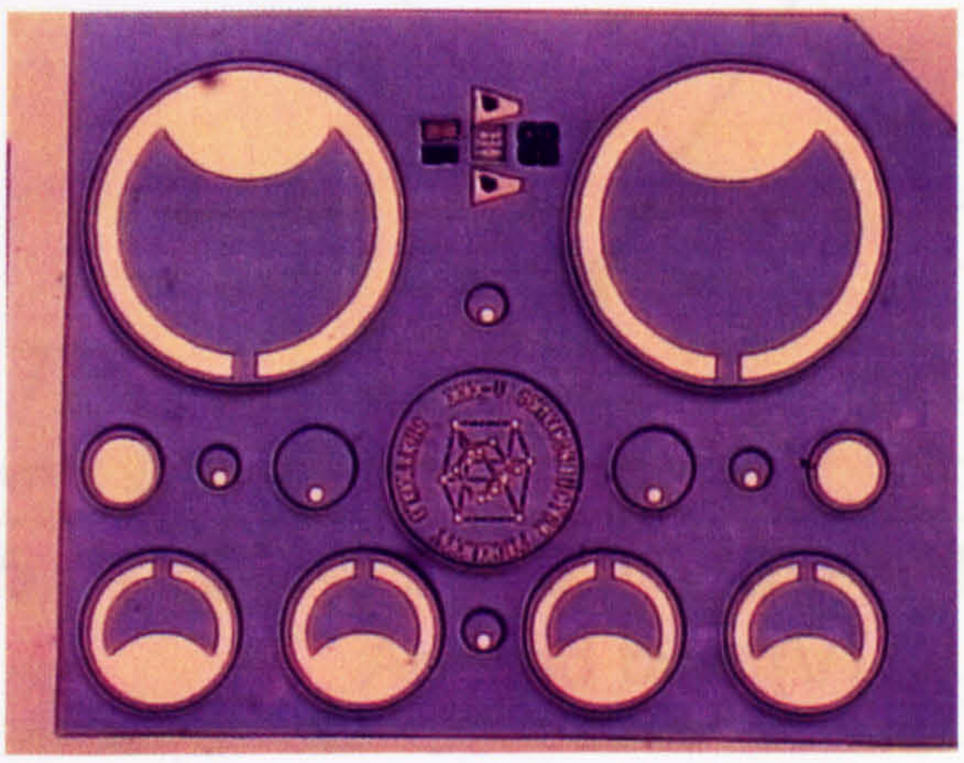

Fig.1.3.2. A mesa etched sample containing various sizes of mesas. The largest mesas have a diameter of 400μm followed by 200μm, 100μm (with full metal coverage and full optical access), and 50μm (full optical access)

Once a device is fabricated and bonded a primary electrical characterisation is performed in dark conditions. This can give information on whether the growth is uniform across the processed area and whether the contacts were successfully bonded. Fig.1.3.3 illustrates that the dark current density is highly uniform for 11 different mesas of two different diameters (400μm and 200μm). The approximately

identical IV characteristics of all devices indicate the good uniformity of a sample. This is demonstrated for most DWELL samples grown in Sheffield. It also provides evidence that the dark current is a bulk related mechanism rather than due to leakage from the edges of the devices, since the current density is the same for both 200 and 400μm devices.

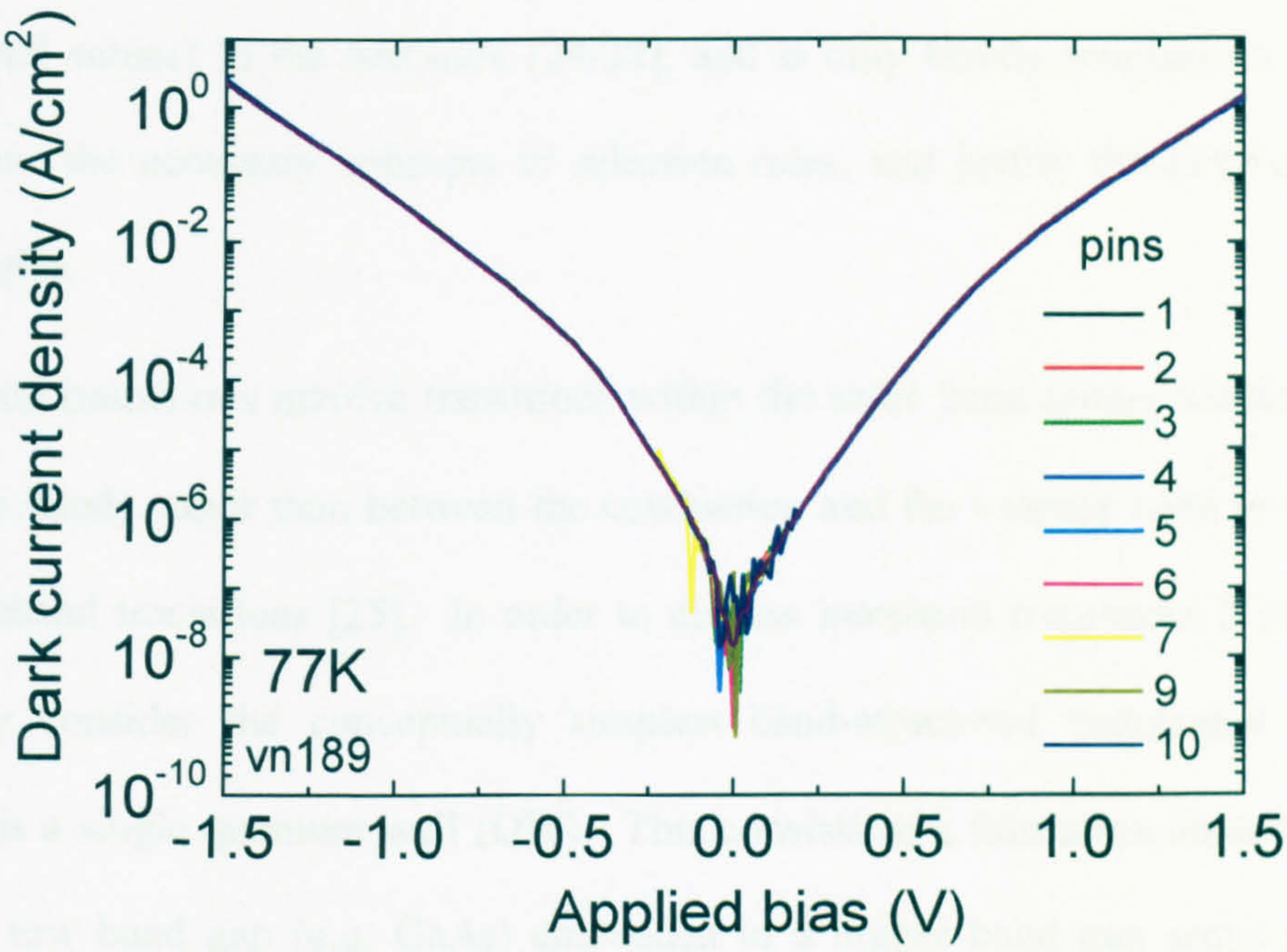

Fig.1.3.3. Dark current density for 200μm and 400μm diameter mesas for the 2.9ML 1e per dot sample, exhibiting excellent uniformity across a range of mesa across the wafer, thus illustrating the good quality of growth and the origin of the dark current from the bulk rather than due to edge effects.

1.3.2. Optical transitions in low dimensional semiconductor systems

A very important concept when discussing low dimensional semiconductor structures, such as QWs and QDs, is how the allowed optical transitions change with the reduction of dimensionality of each system. This section will concentrate on the intraband selection rules for optical transitions in QWs and QDs. This is a widely discussed subject in the literature [24-27], and is only briefly touched on here, to introduce the necessary concepts of selection rules, and justify the motivation for using QDs.

Intraband transitions involve transitions within the same band (either conduction or valence band) rather than between the conduction and the valence band in the case of interband transitions [25]. In order to discuss intraband transitions it is best to initially consider the conceptually simplest band-structured engineered system, which is a single quantum well (QW). This consists of a thin semiconductor layer with a low band gap (e.g. GaAs) embedded in a higher band gap semiconductor material (e.g. AlGaAs) [24, 25]. An intraband transition in a QW can be seen below in Fig.1.3.4.

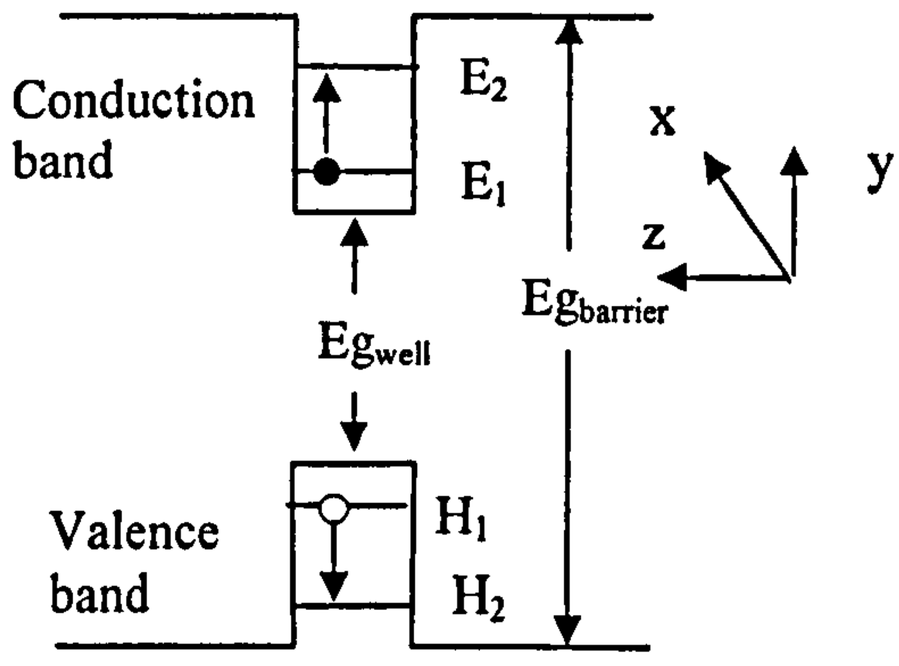

Fig.1.3.4 Schematic of the band structure of a simple quantum well, showing transitions between electron levels E_1 and E_2 or hole levels H_1 and H_2

In a semiconductor material the total wavefunction $\psi_i(\mathrm{r})$ of a state i can be expressed in terms of the lattice-periodic Bloch function of a band v ($u_v(\mathrm{r})$) and the envelope function $F_i(\mathrm{r})$ [27]:

$$\psi_i(\mathrm{r}) = F_i(\mathrm{r})u_v(\mathrm{r}) \tag{1.30}$$

The transition rate from state i to a final state f, can be expressed using Fermi's golden rule [24]:

$$W_{if} = \frac{2\pi}{\hbar}\left|\left\langle \psi_i \left| H' \right| \psi_f \right\rangle\right|^2 \delta\left(E_f - E_i - \hbar\omega\right) \tag{1.31}$$

with the transition induced by an external electromagnetic field in the form of a linearly polarised plane electromagnetic wave, described by:

$$E = E_0 \mathbf{e}\cos(\mathbf{q}\cdot\mathbf{r} - \omega t) \tag{1.32}$$

where $\mathbf{q}$ is the propagation vector, $\mathbf{e}$ is the polarisation vector, and E is the electric field.

In (1.31), H is the interaction Hamiltonian, simplified using the effective mass approximation [24] to give:

$$H' = (e/m^*)\mathrm{A}\cdot\mathbf{p} \tag{1.33}$$

where m^* is the effective mass, and $\mathbf{p}$ is the momentum operator ($\mathbf{p} = i\hbar\nabla$), and A is the vector potential corresponding to the electric field in (1.32):

$$\mathrm{A} = \frac{iE_0 e}{2\omega}\exp(i(\mathbf{q}\cdot\mathrm{r} - \omega t)) + \text{constant} \tag{1.34}$$

The dipole approximation is fulfilled for a QW system, since the radiation wavelength is much larger than the lattice period in the case of interband transitions

and the QW thickness for intraband transitions. From the above, (1.31) can be written as:

$$W_{if} = \frac{2\pi}{\hbar}\frac{e^2 E_0^2}{4m^{*2}\omega^2}\left|\langle i|\mathrm{e}\bullet\mathrm{p}|f\rangle\right|^2 \delta\left(E_f - E_i - \hbar\omega\right) \tag{1.35}$$

By using (1.30) and (1.35), the complete matrix element is split into two terms:

$$\langle i|\mathrm{e}\bullet\mathrm{p}|f\rangle = \mathrm{e}\bullet\langle u_v|\mathrm{p}|u_{v'}\rangle\langle f_n|f_{n'}\rangle + \mathrm{e}\bullet\langle u_v|u_{v'}\rangle\langle f_n|\mathrm{p}|f_{n'}\rangle \tag{1.36}$$

where n and n' are subband or sublevel indices and v and v' are band indices.

From (1.36), if there is change of band index (interband transition from conduction to valence band), then $v \neq v$', and therefore the overlap integral of the Bloch functions in the second term becomes zero, and the second term vanishes. The envelope function overlap integral then determines the transitions allowed (n=n', or in other words, the electron and hole states have to be of the same parity). In the intraband case $v = v$', and the first term disappears. In this case, the term $\langle f_n|\mathrm{p}|f_{n'}\rangle$, called the dipole matrix element, determines that the two electron (or hole states) should have opposite parity for a finite transition probability.

Since in a QW the carriers are confined in the growth direction z, the Schroedinger equation reduces to a one dimensional form [24]. Consequently, this means that only the matrix element of the envelope function proportional to the polarisation vector e_z along the growth direction will result in a finite dipole. Therefore in QWs, the electric field of the incident radiation must have a component along the growth direction to couple to the intraband transition. This selection rule is very significant for devices such as QWIPs, since it determines the geometry of the devices needed, to ensure that the incident radiation is coupled to the active regions. Typically in

FPAs based on QWIPs, diffraction gratings are used to couple the light into the structure, which adds to the complexity of the design of FPAs [26].

Because of the 3-dimensional confinement of the electron wavefunction in a quantum dot, the optical transition is sensitive at normal and angle incidence to the dot plane. Hence, normal incident light having an electric field component parallel to that plane can induce an intraband transition from the *s*-like dot ground state to a *p*-like excited state within the dot (*s-p* transition) as in the case for atomic orbitals. This makes QD structures such as InAs/GaAs, suitable for infrared detectors as the need for diffraction gratings to couple the light (typically used in QWIPs) is eliminated. However the behaviour of dots with respect to this property is not simple, and depends on the size, shape and composition of the dots. There are various complicated effects on the polarisation dependence of the transitions in dot structures, since the relative strength of either polarisation can depend on a number of QD parameters [28].

In addition, in structures such as DWELLs, which are largely the emphasis of this thesis, the optical selection rules become further complicated, since the transitions occur from a QD bound state confined in 3 dimensions to QW states confined in one dimension. In such a system optical transitions between states are expected to require an electric field component along the growth direction, since the wavefunctions of the ground state of the dot and the state in quantum well, will be displaced in that direction. This is experimentally observed in the present studies and chapter 3 discusses these effects in more detail.

1.4. Intraband infrared detectors

1.4.1. Quantum well infrared photodetectors (QWIPs)

The first QWIP was demonstrated in Bell labs by B.F. Levine et al in 1987 [29]. Since then there has been considerable efforts towards the optimisation of such detectors, mainly concentrating on material systems based on GaAs/AlGaAs multi-QWs, with several reports of high performance QWIPs [29-31]. QWIPs are very close to becoming a common option especially for the LWIR window and dual band MWIR and LWIR applications [32-33]. What was once a purely research area is now a commercially available technology. QWIPs benefit from mature material growth, good uniformity over large area and easy wavelength control, making them suitable for integration into large scale FPAs, and allowing multicolour detection. The most attractive attribute, particularly at longer wavelengths is the wafer uniformity (percentage of working pixels on an FPA), which is significantly better than commonly used mercury cadmium telluride (MCT) detectors in that range. The AlGaAs/GaAs QW system is commonly preferred due to the reduced strain, compared to QWIPs based on strained InGaAs/GaAs QWs.

QWIPs in general do have some disadvantages, such as not being able to detect at normal incidence, necessitating the use of diffraction gratings for integration into FPAs. Although this does introduce a component of extra control in the performance of the FPA, (the gratings can be used for example, to change the linewidth of detection), there are applications where having no gratings would be

very beneficial, enabling more cost effective, lighter and simpler FPAs. Asymmetric QWs [34] have been proposed in the past, to achieve normal incidence QWIPs. Another approach is to use p-type QWIPs (typically with Be-, Zn- or Si-doping), which are sensitive to normal incidence due to the band mixing between the off-zone centre heavy hole (HH) and light hole (LH) states [35]. p-type QWIPs however have the disadvantage of lower absorption coefficients (due to the large effective mass and low mobility of holes). Several approaches have been proposed to improve p-type QWIPs such as the use of strained p-type InGaAs/AlGaAs structures [36], or p-type GaAs/AlGaAs grown on (111)A substrates [37]. However, n-type QWIPs are still more commonly used for FPAs, containing gratings in most applications.

QWIPs typically have quite fast relaxation times (~1ps), and this could change from an advantage to a disadvantage depending on the application. For example this can be used beneficially when QWIPs are used for the characterisation of ultrashort laser pulses [5]. However, for a staring detector (such as in night vision cameras), a longer lifetime would be advantageous.

Most QWIPs require cryogenic cooling, since their performance at temperatures over 77K (liquid nitrogen temperature) is limited by the high dark current, which subsequently affects the signal to noise. Nonetheless there have been reports of higher temperatures of operation, in QWIPs with 90% absorption [30], operating up to room temperature, but with a significant degradation in the performance. Still, for commercial QWIPs, typically 75K cooling is used.

The maturity of QW technology has resulted in more research towards the improvement of integration into FPAs, where research is focused on optimisation of

fabrication, hybridisation, passivation and other processes at the FPA manufacturing process or on the architecture of the arrays [38,39]. Other more fundamental studies are also attracting interest with various QWIP detectors designed for uses such as heterodyne detection or quadratic autocorrelation of ultrashort pulses [30,40,41].

1.4.2. Quantum dot infrared photodetectors (QDIPs) and quantum dot-in-a-well infrared photodetectors (DWELL QDIPs)

QDIPs are an evolution of QWIPs which has been initiated since the demonstration of the detection of normal incidence infrared radiation in 1996 by D. Pan et al, using a structure containing 20 periods of InGaAs dots in a GaAs matrix [42]. Since then significant research has been carried out, resulting in many examples of how such devices have potential advantages over QWIPs. As it will be discussed below, state of the art QDIPs are beginning to reach the performance levels of QWIPs.

It had been theoretically predicted that QDIPs should benefit from much lower dark currents [15,16,43], potentially resulting in higher signal to noise ratios and higher temperature operation. It has also been predicted that as a result of the discrete density of states in QDs, there is a largely suppressed longitudinal-optical (LO) phonon assisted relaxation and also a negligible longitudinal acoustic (LA) phonon assisted relaxation with decreasing dot size [44] resulting in longer excited state lifetimes of the final states contributing to the photocurrent (phonon-bottleneck

effect) [45,46], which could result in higher responsivity. However, more recent reports, have demonstrated the significance of multiphonon and polaron relaxation in QDs [44,47,48,49], which results in much shorter lifetimes than those predicted by the theoretical models assuming a 'phonon bottleneck'. Other reports of experimental observation of short times have been reported, with typical times in the order of a few ps for high energy transitions (>100meV) [50,51], and of the order of tens of ps (20-70ps) [47,48], depending on dot parameters, for the low energy *s-p* transitions.

There have also been theoretical reports and experimental observations of high photoconductive gain in QDIPs [52,53], which could result in higher responsivity. High gain could be beneficial in most cases, but as it is also associated with the noise in a photoconductor can be detrimental in others. Other studies have shown how gain can be enhanced by avalanche gain caused by impact ionization [20]. The determination of gain is QDIPs is a non-trivial task, and the gain mechanisms and effects on device performance is still a subject of debate.

There seem to be a few general issues when designing QDIPs, including the growth control of the QDs, the doping of the active region and the device structure. In a recent review of QDIPs [5], Schneider and Liu, have stressed some issues concerning QDIP performance. First, a strongly normal incident detector can only be achieved if the QDs are small in the in-plane direction so the in-plane confinement leads only to one or two states. Therefore a good aspect ratio (base diameter to dot height) of 2:1 would provide efficient normal incidence QDIPs.

However, the base in typical InAs dots is much larger than the height (~4:1) [54]. Secondly a high dot density is required to enhance the absorption of the active region, especially as strain effects do not allow the growth of many layer active regions as in QWIPs. This also relates to the doping of the structure, since if one electron is to occupy each dot; one needs a high density to enable the high doping of the structure. Recent attempts to increase the dot density have been carried out [55], and are also discussed in chapter 4.1. Additionally, in QDIPs it is not possible to have the doping in the same layer as the dots, as it can affect QD formation. Therefore the doping is usually inserted in the barrier, which has some disadvantages such as the introduction of current leakage paths.

The active region of a typical QDIP design consists of periods of InAs (or InGaAs) QDs in a GaAs matrix, just as the equivalent multi InGaAs wells in a GaAs matrix (or GaAs/AlGaAs). The choice of InAs on GaAs has to do with the large lattice mismatch between the two (7%), providing adequate compressive strain to enable growth formation at a small critical thickness (~1.2 monolayers of InAs deposited during growth (ML), depending on growth conditions). In addition to this, the resulting conduction band offset is appropriate for engineering transitions in the MWIR and LWIR with the capacity to extend operation into the FIR.

Several design variations have been suggested to improve the performance of InAs/GaAs QDIPs. A usual approach is the incorporation of AlGaAs or AlAs barrier layers into the InAs/GaAs system to act as blocking layers for the dark current [56-59]. The aim of this is to suppress dark current in order to achieve higher temperature operation. Detectivities of the order of 10^9-10^{10} cmHz$^{-1/2}$/W at 78K for ~3-14μm have been reported from the above references, as well as a

detectivity of $2.4x10^8$ near room temperature (250K) for 4μm [60], competing with detectivities of QWIPs at these temperatures and atmospheric windows. Near room temperature operation designs without AlGaAs barriers have also been reported [61].

Although QDs are usually n-type doped by Si-delta doping, there have been reports on high performance QDIPs with undoped active regions, which aim at reducing the dark current, while relying on the doping from the contact layers or background doping for the generation of carriers. Detectivities in the LWIR as high as 10^{10} - 10^{11} $cmHz^{-1/2}/W$ at 77 and 100K have been reported [59,62,63], using InAs/AlGaAs and InAs /InGaAs/GaAs with undoped active regions. High detectivities of ~$3.6x10^{11}cmHz^{-1/2}/W$ (λ~5μm) have also been achieved from MOCVD growth on InP substrates, with InGaAs/InGaP and InAs/InGaAs/InAlAs/InP systems [57], which are comparable to state of the art QWIPs in the same range, and FPAs using these materials have been fabricated [57].

There has also been a lot of interest in using what is known as a dot-in-a-well design (DWELL) (commonly InAs/InGaAs/GaAs) in QDIPs. This is a principle that was developed initially for QD lasers [64,65] for ~1.3μm emission. Early DWELL QDIPs showed high performance in the LWIR ($D^* = 10^9$ $cmHz^{-1/2}/W$ @78K) while exhibiting interesting properties such as two and three colour behaviour and bias dependent detection wavelength [66-69].

In a DWELL QDIP the dots are embedded within a quantum well, which lowers the ground state of the dot with respect to the bulk barrier band edge when compared to a InAs/GaAs structure [67], which in turn leads to a reduction in thermionic emission and a concurrent increase in operating temperature. The InGaAs QW also has an effect on the nucleation of the InAs dots, resulting in higher dot densities of ~$6x10^{10}cm^{-2}$ [70, 71], compared to standard InAs/GaAs QDs. The DWELL is also useful as it gives a well defined transition from the dot ground state to a state in the well, in contrast to having just InAs dots in GaAs, where the same transition relies on states in the wetting layer. Most QD based photodetectors are now based on DWELL structures and recent reports of FPAs constructed from such devices show the applicability of DWELLs for next generation infrared imaging [72].

1.4.3. Alternative materials and detectors – Current mid-IR technology

The $Hg_{1-x}Cd_xTe$ (MCT) pseudo-binary narrow-gap alloy system is the most commonly used material for infrared detection in both near-infrared (NIR) and mid-infrared atmospheric windows. The devices rely on interband transitions, where carriers are photoexcited across the bandgap E_g i.e. to the transition of an electron from the valence band to the conduction band [4]. The wavelength of the transition can be adjusted by changing the composition x of the alloy. The band gap energy can be tailored between 0 and 1.6eV. However for the detection of long wavelengths (10μm) a very narrow bandgap is required (0.1eV). This makes fabrication very difficult and expensive as the MCT alloy suffers from surface non-uniformity over large areas, and surface instability [3,4]. Thus, even if MCT is still

more efficient for single and small element high performance detectors in the MWIR and LWIR, the operability of MCT FPAs in the LWIR is far from ideal (typically <99.8%).

Recent approaches include trying to grow HgCdTe on Si rather than bulk CdZnTe substrates which would make them much cheaper and potentially easier to fabricate, and also benefit from available larger wafer sizes and Si processing technology [73]. Growing MCT on Si, is a non-trivial task due to the large lattice mismatch (19.3%) [74] but nonetheless, the advantages of such an approach have rejuvenated MCT research. Also there has been interest in MCT on GaAs which has a smaller lattice mismatch (14.6%) with MCT, which would make the fabrication easier, and the performance of the detectors potentially better [74].

Other standard detectors in the 1-3μm and 3-5μm regions include alloys of bulk semiconductors such as InSb, PbSnTe, Ge:Hg, InAs or InGaAs photodiodes. Recent developments in such structures include work on InAsSb alloys [75] grown by liquid phase epitaxy (LPE), which is inexpensive whilst yielding high quality materials. Detectors produced from such structures have been shown to operate without cooling in the 3-5μm region with high detectivities in the order of 10^{9}-10^{10}cmHz$^{1/2}$W^{-1} at room temperature [75,76]

Additionally, a novel type of detector, recently proposed for the 3-5μm atmospheric window is the *nBn* detector [77] which may involve different semiconductor materials depending on the required spectral range. This proposed structure contains a large band gap barrier layer *B* in the active region surrounded by an n-type semiconductor (e.g. InAs, InAsSb). The choice of materials for the

heterostructure is made on the principle that when biased there is a zero valence band offset, whereas there is a high barrier in the conduction band (e.g. InAs/AlGaSb/InAs). This way the majority carrier contribution to the current is suppressed and the device only operates with minority carriers. This can help significantly decrease the dark current and the noise, and hence allow uncooled operation whilst maintaining high performance in the 3-5μm spectral range [77].

Interband Type-II QW systems like InGaAs/InAlAs, InSb/InAsSb or InGaAs/InP amongst others have also been demonstrated [4,25,29] and more recently, Type II InAs/GaInSb strained layer superlattices (SLS), which have a number of advantages including being sensitive to normal incidence, have been studied as a promising alternative for LWIR and very long wavelength (VLWIR) detectors [78,79].

All the above detectors work very efficiently in the MWIR window. However, very few detectors are efficient in the LWIR and VLWIR windows. It is for this reason that the majority of QWIP and QDIP research is concentrated on making detectors for this region, as it is where QWIPs and QDIPs can provide an efficient competitive technology, as well as the capability of dual or multi-band detection.

References

1 W. Herschel, Phil.Tran.R.Soc **90** (1800) 284, 477

2 V. Ryzhii, '*Intersubband infrared photodetectors*' Selected Topics in Electronics and Systems, Vol.27. World Scientific Publishing Co. Pte.Ltd, 2003,

3 J. D. Vincent, '*Fundamental of infrared detection and testing*', Wiley Series on Pure and Applied Optics, Wiley Interscience, 1990.

4 See, for example, A. Rogalski, Progress in Quantum Electronics **27** (2003)59-210; A. Rogalski, '*Quantum Well Infrared Photoconductors in Infrared Detectors technology*' from, 'Intersubband infrared photodetectors' Selected Topics in Electronics and Systems, Vol.27. World Scientific Publishing Co. Pte.Ltd (2003) 1-66

5 H. Schneider and H. C. Liu, *Quantum Well Infrared Photodetectors: Physics and Applications*, Springer Series in Optical Sciences, Springer, Berlin, Heidelberg, 2006, Vol. 126, p. 5-7, 68-69, 142

6 W. Koencher, 'Solid-State Laser Engineering', Springer Series in Optical Sciences, 1999, Vol.1, p.2,

7 V. D. Jovanovic, P. Harrison Z. Ikonic, D. Indjin, J. Phys. D: Appl. Phys. **39** (2006) 1773–1780

8 P. Man and D. S. Pan, Appl.Phys.Lett. **66** (1995)192

9 C. H. Chu, C.I. Hung, Y. H. Wang, M. P. Houng, IEEE Photonics Technol. Lett. **9** (1987) 1262

10 H. C. Liu, 'Quantum Well Infrared Photodetector Physics', Semiconductors and semimetals. **62,** 'Intersubband Transitions in Quantum Wells: Physics and Device Applications I', ch.2. *Academic Press* 2000

11 M. Ershov, V. Ryzhii, C. Hamaguchi, Appl.Phys.Lett. **67** (1995) 3147

12 M. Ershov, H. C. Liu, M. Buchanan, Z. R. Wasilewski, V. Ryzhii, Appl.Phys.Lett. **70** (1997) 414

13 V. Ryzhii, J.Appl.Phys. **81** (1997) 6442

14 M. Ryzhii, V. Ryzhii, M. Willander, J.Appl.Phys **84** (1998) 3403

15 V. Ryzhii, Semicond. Sci.Technol.**11** (1996) 759-765

16 V. Ryzhii, I. Khmyrova, M. Ryzhii, V. Mittin, Semicond. Sci.Technol.**19** (2004) 8-16

17 M. B. El Mashade, M. Ashry, A. Nasr, Semicond. Sci.Technol.**18** (2003) 891

18 A. D. Stiff-Roberts, H. Su, S. Chakrabarti, P. Bhattacharya, IEEE Photonics Technol. Lett. 16 (2004) 867

19 N. Vukmirovic, Z. Ikonic, Ivana Savic, D. Indjin, P. Harrison, J.Appl.Phys.**100**, 074502 (2006)

20 B. Kochman, A.D. Stiff-Roberts, S. Chakrabarti, J. D. Phillips, S. Krishna, J. Singh, P. Bhattacharya, IEEE J.Quantum.Lett. 39 (2003) 459

21 S. D. Gunapala and S. V. Bandara, '*Quantum Well Infrared Photodetector Focal Plane Arrays*', Semiconductors and semimetals. **62,** 'Intersubband Transitions in Quantum Wells: Physics and Device Applications I', ch.4. Academic Press 2000

22 P. Y. Yu, M. Cardona, '*Fundamentals of Semiconductors: Physics and material properties*', Springer-Verlag Berlin Heidelberg 2005

23 A. I. Tartakovskii, T. Wright, A. Russell, V. I. Fal'ko, A. B. Van'kov, J. Skiba-Szymanska, I. Drouzas, R. S. Kolodka, M. S. Skolnick, P.W. Fry, A. Tahraoui, H.-Y. Liu, and M. Hopkinson, Phys. Rev. Lett. **98**, 026806 (2007)

24 M. Helm, Semiconductors and semimetals. **62,** 'Intersubband Transitions in Quantum Wells: Physics and Device Applications I', ch.4. Academic Press 2000

25 B. F. Levine, J. App. Phys **74** (8) R1, (1993)

26 M. Fox, 'Optical properties of solids', *Oxford University Press, 2001*

27 H. Haug and S.W. Koch, 'Quantum Theory of the Optical and Electronic Properties of Semiconductors', *World Scientific,2004*

28 P. Boucaud, S. Sauvage, C. R. Physique **4** (2003) 1133-1154

29 B. F. Levine, K. K. Choi, C. G. Bethea, J. Walker, and R. J. Malik, Appl.Phys.Lett. **50** (1987) 1092

30 H. C. Liu , R. Dudek , A. Shen , E. Dupont , C.Y. Song , Z.R. Wasilewski , M. Buchanan, Appl.Phys.Lett. **79** (2001) 4237-4239

31 B. F. Levine, C. G. Bethea, K. G. Glogovsky, J. W. Stayt, R. E. Leibenguth, Semicond. Sci.Technol. **6** (1991) C114-119

32 E. Costard, Ph. Bois, Infrared. Phys. Technol. **50** (2007) 260-269

33 A. Nedelcu, X. Marcadet, O. Huet, P. Bois, App. Phys. Lett. **88** 191113 (2006)

34 See, for example, D.H. Zhang , W. Shi , N. Li , J.H. Chu, J.Appl.Phys. **92** (2002) 6287-6290; Z. Y. Yuan , Z. H. Chen , D. F. Cui , J. W. Ma , Q. A. Hu , J. M. Zhou , Y. L. Zhou, Appl.Phys.Lett. **67** (1995) 930-931

35 D. H. Zhang, W. Shi, N. Li, J. Chu, J.Appl.Phys. 92 (2002) 6287

36 B. F. Levine, S. D. Gunapala, J. M. Kuo, S. S. Pei, S. Hui, Appl. Phys. Lett. **59** (1991) 1864

37 T. Mei, H. Li, G. Karunasiri, W. J. Fan, D. H. Zhang, S. F. Yoon, K. H. Yuan, Infrared Phys. Technol.50 (2007) 119

38 A. Nedelcu, E. M. Costard, P. Bois, X. Marcadet, Infrared. Phys. Technol. **50** (2007) 227

39 E. M. Costard, P. F. Bois, X. Mercadet, E. Herniou, Infrared. Phys. Technol. 42 (2001). 291

40 H. Schneider, O. Drachenko, S. Winnerl, M. Helm, Appl.Phys.Lett. **89** 133508 (2006)

41 H. Schneider, T. Maier, H. C. Liu, M. Walther, P. Koidl, Optics Letters, **30** 287 (2005)

42 D. Pan, Y. P. Zeng, M. Y. Kong, J. Wu, Y. Q. Zhu, H. Zhang, and J. M. Li, Electron. Lett. **32,** 1726 (1996)

43 V. Ryzhii, V Pipa, I Khmyrova, V Mitin, M Willander, Jpn. J.Appl.Phys. **39** (2000) L1283

44 T. Inoshita, H. Sakaki, Phys. Rev. B, 46 (1992) 7260

45 U. Bockelmann and G. Bastard, Phys.Rev.B **42** (1990) 8947 - 8951

46 Xin-Qi Li, H. Nakayama, Y. Arakawa, Phys.Rev.B **59** (1999) 5069 - 5073

47 S. Sauvage and P. Boucaud, Phys.Rev.Lett. **88** (17) (2002)

48 E. A. Zibik, L. R. Wilson, R. P. Green, G. Bastard, R. Ferreira, P. J. Phillips, D. A. Carder, J. P. R. Wells, J. W. Cockburn, M. S. Skolnick, M. J. Steer, M. Hopkinson, Phys. Rev. B **70**, 161305(R) (2004)

49 E. A. Zibik, L. R. Wilson, R. P. Green, G. Bastard, R. Ferreira, P. J. Phillips, D. A. Carder, J. P. R. Wells, M. S. Skolnick, J. W. Cockburn, M. J. Steer, M. Hopkinson, Physica E 26 (2005) 408-412

50 S. Sauvage, P. Boucaud, F. Glotin, R. Prazeres, J.-M. Ortega, A. Lemaitre, J.-M. Gérard and V. Thierry-Flieg, Appl. Phys. Lett. **73**, 3818 (1998)

51 P. Aivaliotis, S. Menzel, E. A. Zibik, L. R. Wilson, J. W Cockburn, M. Hopkinson, Appl.Phys.Lett (under review)

52 H. Lim, B. Movaghar, S. Tsao, M. Taguchi, W. Zhang, A. A. Quivy, and M. Razeghi, Phys. Rev. B **74** (2006) 205321

53 V. V. Mitin, V. I. Pipa, A. V. Sergeev, M. Dutta, M. Stroscio, Infrared.Phys.Technol. **42** (2001) 467

54 M. Gutiérrez, M. Hopkinson, H.Y. Liu, J.S. Ng, M. Herrera, D. González, R. Garcia, R. Beanland, Physica E**26** (2005) 245

55 P. Aivaliotis, L. R. Wilson, E. A. Zibik, J. W. Cockburn, M. J Steer, H. Y. Liu, Appl.Phys.Lett. **91** (2007) 013503

56 Z. H. Chen , O. Baklenov , E. T. Kim , I. Mukhametzhanov, J. Tie, A. Madhukar , Z. Ye, J. C. Campbell, J. Appl. Phys. **89**, 4558 (2001)

57 See, for example J. Jiang, S. Tsao, T. O'Sullivan, W. Zhang, H. Lim, T. Sills, K. Mi, and M. Razeghi, G. J. Brown, M. Z. Tidrow, Appl.Phys.Lett.**84** (2004) 2166 ; S. Tsao, H. Lim, W. Zhang, M. Razeghi, Appl.Phys.Lett. **90** (2007)201109

58 S. Y. Wang, S. D. Lin, H. W. Wu, C. P. Lee, Infrared.Phys.Technol. **42** (2001) 473-477

59 Z. H. Chen, O. Baklenov, E-T. Kim, I. Mukhametzhanov, J. Tie, A. Madhukar, Z. Ye, J. C. Campbell, Infrared. Phys. Technol. **42** (2001) 479-484

60 S-F. Tang, S-Y. Lin, and S-C. Lee, Appl.Phys.Lett.**78** (17) 2001, pp.2428

61 L. Jiang, S. S. Li. N-T Yeh, J-I Chyi, C. E. Ross, K. S. Jones, Appl.Phys.Lett.**82** (12) 2003, pp.1986

62 Z. Ye, J. C. Campbell, Z. H. Chen, E-T Kim, A. Madhukar, IEEE J. Quantum Electron., **38** (2002) 1234

63 E. T Kim, A. Madhukar, Z. Ye, J. C. Campbell, Appl.Phys.Lett. **84** (2004) 3277

64 V. M. Ustinov, N. A. Maleev, A. E. Zhukov, A. R. Kovsh, A. Yu. Egorov, A. V. Lunev, B. V. Volovik, I. L. Krestnikov, Yu. G. Musikhin, N. A. Bert, P. S. Kop'ev, Zh. I. Alferov, N. N. Ledentsov and D. Bimberg, Appl.Phys.Lett. **74** (1999) 2815

65 G. T. Liu, A. Stintz, H. Li, K. J. Malloy, L. F. Lester, Electron. Lett. **35** (1999) 1163

66 S. Raghavan, P. Rotella, A. Stintz, B. Fuchs, S. Krishna, C. Morath, D. A. Cardimona, S. W. Kennerly, Appl.Phys.Lett. **81** (2002) 1369

67 S. Krishna, S. Raghavan, G. von Winckel, A. Stintz, G. Ariyawansa, S. G. Matsik, A. G. U. Perera, Appl.Phys.Lett. **83** (2003) 2745

68 S. Krishna, S. Raghavan, G. von Winckel, P. Rotella, A. Stintz, C. P. Morath, D. Le, S. W. Kennerly, Appl.Phys.Lett. **82** (2003) 2574

69 S. Raghavan, D. Forman, P. Hill, N. R. Weisse-Bernstein, G. von Winckel, P. Rotella, S. Krishna, S. W. Kennerly, J. W. Little, J. App. Phys **96** (2004) 1036

70 H. Y. Liu, I. R. Sellers, M. Gutiérrez, K. M. Groom, R. Beanland, W. M. Soong, M. Hopkinson, J. P. R. David, T. J. Badcock, D. J. Mowbray, M. S. Skolnick, Materials Science and Engineering C 25, 779 (2005)

71 M. Gutierrez, M. Hopkinson, H. Y. Liu, M. Herrera, D. Gonzalez, R. Garcia, J. Crystal Growth, 278 151–155 (2005)

72 S. Krishna, S. D. Gunapala, S. V. Bandara, C. hill, D. Z. Ting, Proceedings of the IEEE **95** (No.9) (2007)

73 R. Bornfreund, J. P. Rosbeck, Y. N. Thai, E. P. Smith, D. D. Lofgreen, M. F. Vilela, A. A. Buell, M. D. Newton, K. Kosai, S. M. Johnson, T. J. Delyon, J. E. Jensen, M. Z. Tidrow, J. Electron. Mater. **36** (2007) 1085

74 L. He, L. Chen, Y. Wu, X.L. Fu, Y.Z. Wang, J. Wu, M.F. Yu, J.R. Yang, R.J. Ding, X.N. Hu, Y.J. Li and Q.Y. Zhang, J. Cryst. Growth. **301** (2007) 268

75 H. H. Gao, A. Krier, V. V. Sherstnev, Appl. Phys. Lett. **77** (2000) 872

76 A. Krier, W. Suleiman, Appl.Phys.Lett. **89** (2006) 083512

77 S. Maimon, G. W. Wicks, Appl. Phys. Lett. **89** (2006) 151109

78 A. Rogalski, Infrared. Phys. Technol. **50** (2007) 240-252

79 A. Rogalski, P. Martyniuk, Infrared. Phys. Technol. 48 (2006) 39-52

2. Experimental Techniques

In this chapter the various techniques employed to characterise and investigate the performance of DWELL QDIPs are presented. Each method described is related in one or more ways with the previously mentioned figures of merit and detector physics. The structural, optical, and electrical characterisation of the devices that were grown and fabricated is discussed in this chapter, along with a detailed presentation of the instrumentation and experimental configurations used.

First, Fourier transform IR spectroscopy will be presented to illustrate how different measurement configurations using this technique can provide information about the related intraband transitions in the DWELL structure and the detector performance. Also, the instrumentation used to measure the electrical characteristics of the detectors is described. In contrast to the above techniques, which are relatively standard and readily available for detector characterisation, the responsivity measurement instrumentation is somewhat more complex, and was constructed for the purpose of QDIP characterisation and is discussed in detail in this chapter.

Also included is the description of photoluminescence (PL) and PL excitation measurements to study interband optical processes in DWELLs. Finally the basic

concepts of ultrafast spectroscopic methods that were used and free electron laser physics are mentioned as they are related to results in chapters 3.1 and 5.2.

2.1. Fourier transform infrared spectroscopy (FTIR)

The main optical component inside an FTIR spectrometer is based on a Michelson interferometer. The components of a Michelson interferometer can be seen in Fig.2.1.1. The IR light emitted by the broadband glowbar source (S) is collimated at the output. The beam is then divided through a beamsplitter (BMS), with half of the light transmitted to a static mirror (M_1), while the other half is reflected to a moveable mirror (M_2). During a scan the path length of the infrared beam from the BMS to M_2 changes relatively to the path length between BMS and M_1. The optical path difference (OPD or optical retardation δ) is determined as this path traversal difference for the two beams in the two arms of the interferometer. The two beams are reflected by the mirrors and recombined on the other side of the BMS, and the resultant light beam becomes incident upon the detector (D) [1].

The detector sees an image of the composite beam as an interference pattern subject to constructive or destructive interference dependent upon the position of M_2. The resultant interferogram is a plot of this intensity variation as a function of OPD. The maximum constructive interference normally occurs when the two paths are equidistant at the zero path difference (ZPD).

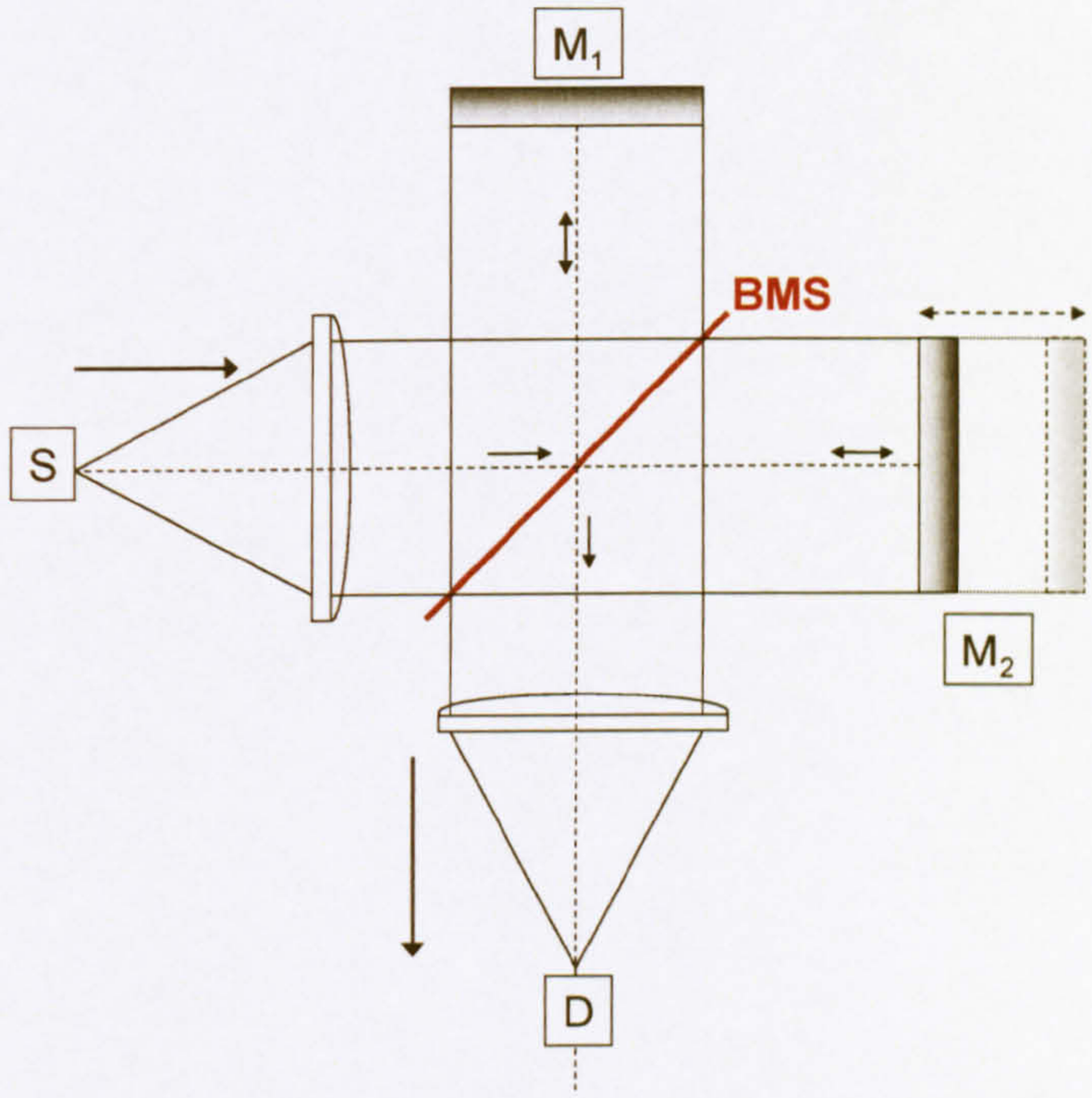

Fig.2.1.1 Schematic of the Michelson interferometer, the source (S), detector (D), static (M_1) and moving (M_2) mirrors, and the beamsplitter (BMS).

In an FTIR measurement the resultant photocurrent signal as a function of wavelength is of interest, rather than the interferogram detected i.e. the light intensity as a function of mirror position in cm. Therefore a Fourier transform (FT) has to be applied that converts the interferogram information ($I(\delta)$) to an $I(\bar{\nu})$ plot of intensity versus wavenumber (frequency) (in cm^{-1}) thus obtaining a single beam spectrum [1,2].

This is expressed by the following equation:

$$I(\bar{\nu}) = \int_{-\infty}^{+\infty} I(\delta)\cos(2\pi\bar{\nu}\delta)d\delta \qquad (.2.1)$$

where δ is the optical path difference.

Using this function we can derive the background spectra from the background interferogram, as shown below in Fig.2.1.2. The following sections discuss how we can use this method to characterise the photocurrent or absorption spectra of a sample.

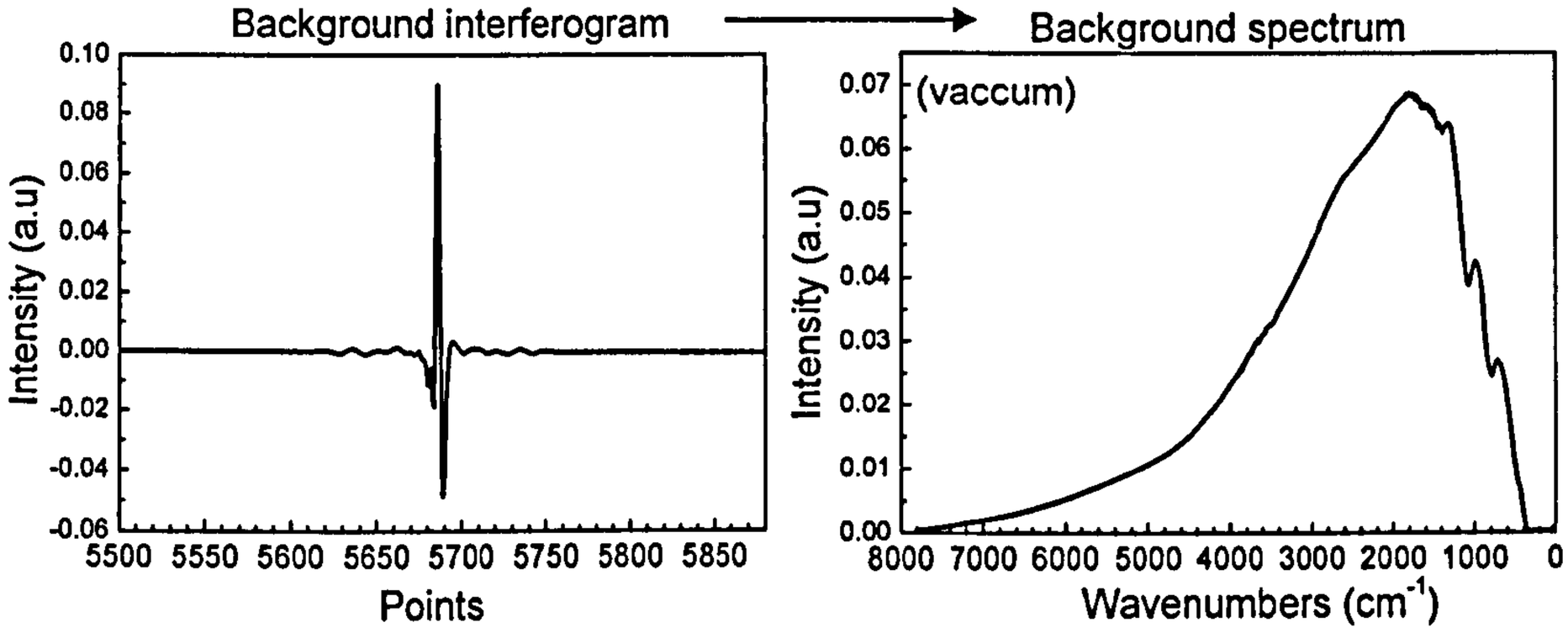

Fig.2.1.2. Background interferogram and its FT spectrum

Photocurrent measurements

FTIR measurements were used to characterise spectral response of QDIPs by using them to detect the infrared beam. In the experimental set-up in question, the glowbar, beamsplitter and mirrors are internal to an evacuated Bruker IFS 66v/s FTIR spectrometer and the QDIP device is placed in a liquid He cryostat (Fig.2.1.3). A Keithley 428 current preamplifier provides a bias voltage for the detector and pre-amplification of photocurrent. The interpretation of the resultant interferogram signal is carried out on a PC using OPUS software which is designed for Bruker spectrometers.

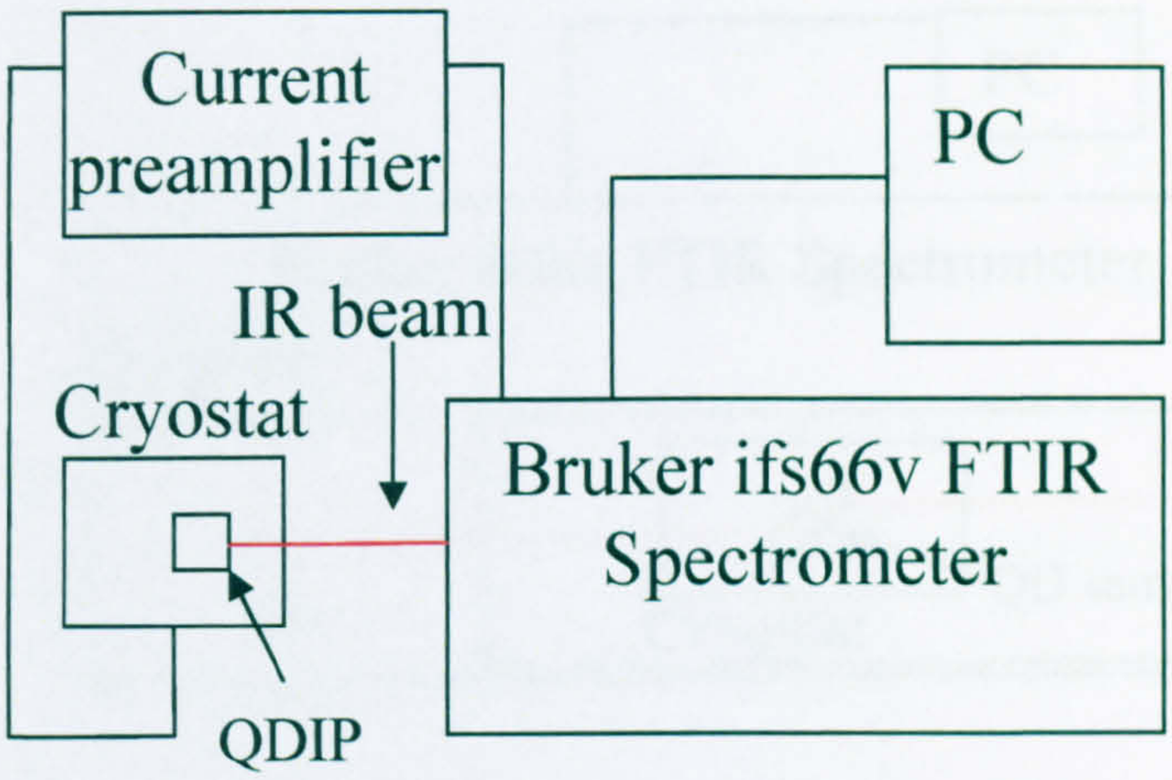

Fig.2.1.3. FTIR configuration for photocurrent measurements

The choice of beamsplitter and windows, is determined by the wavelengths of the transitions under investigation. Typically for the QDIPs, a Ge KBr beamsplitter with a range from ~1μm to ~25μm with ZnSe cryostat windows (0.6-21μm) are used to measure the detector response in the mid- and long-wavelength IR atmospheric windows (MWIR and LWIR respectively). Also for transitions in the very long wavelength IR (VLWIR) and far-IR (FIR), a Mylar beamsplitter with a range from ~14μm to ~300μm with KRS5 (0.6-40μm) or polythene cryostat windows are used.

Transmission measurements

In another arrangement of the FTIR spectrometer, transmission measurements can be carried out. The orientation of the sample with respect to the beam depends on the polarisation selectivity of the transitions under investigation according to the intraband selection rules as discussed in chapter 1. These transmission measurements are helpful to measure the absorption spectra for unprocessed QD structures.

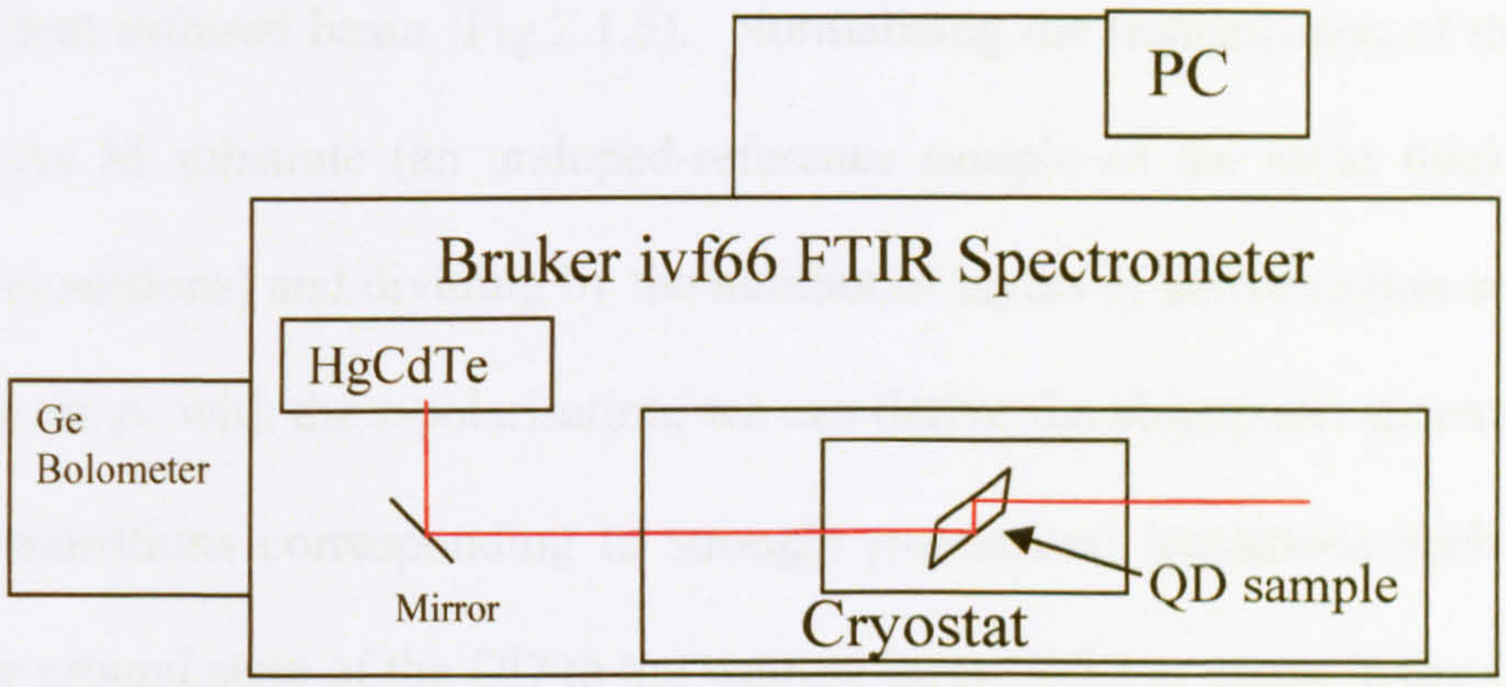

Fig.2.1.4. Transmission set up for p-polarised 45 multipass geometry measurements using an MCT cooled at 77K

For high energy transitions in QDs, the facets of the sample were polished at 45° to provide a multipass waveguide geometry and the signal is collected by a HgCdTe detector (spectral range: 2-14μm, peak at 11μm) cooled to 77K to collect the incident beam after a QD sample has been placed in the beam path (Fig 2.1.4) . Typically the samples are polished down to a size to enable ~8-10 passes depending on sample thickness, to ensure a measurable value of absorption.

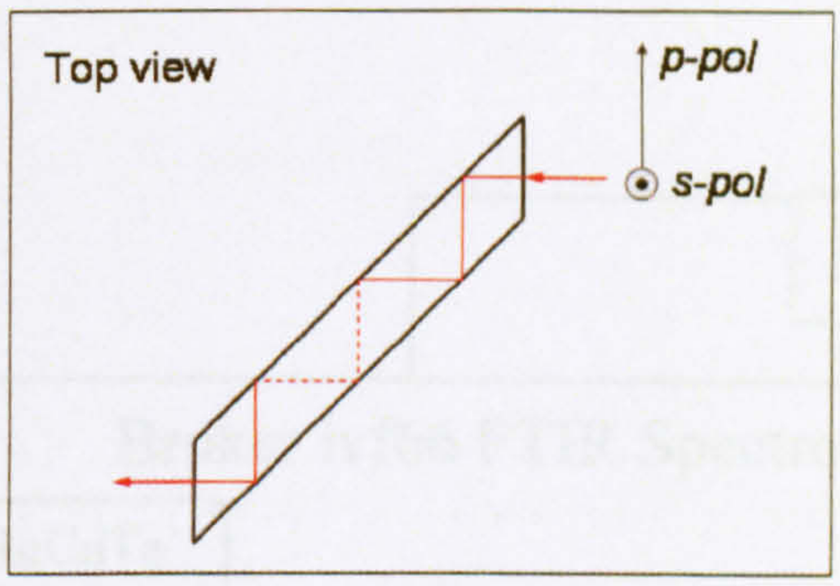

Fig.2.1.5. 45° polished waveguide geometry

Spectra are measured with *s*-polarisation (parallel to the dot layer plane) and *p*-polarisation (50% of the component of the electric field along the growth axis) of

the incident infrared beam (Fig.2.1.5). Normalising the transmission of the sample to a GaAs SI substrate (an undoped-reference sample of the same thickness and growth conditions) and dividing by the number of layers of active region and further dividing the *p*- with the *s*-polarisation, we can derive the absorption spectra for high energy transitions corresponding to strongly *p*-polarised transitions such as those from the ground state of the QD to the wetting layer (WL) or states in the QW if the structure is a DWELL as well as bound *d*-like *f*-like and continuum states.

On the other hand the FIR transmission spectra are measured by placing the sample surface plane in a normal orientation to the beam, and therefore exciting transitions from the ground state to first excited states using radiation linearly polarised in the [011] and [0-11] directions. The transmitted signal is measured using a QMC Instruments 4.2K composite Ge bolometer.

Since the sample is placed at normal incidence to the incident beam as shown in Fig.2.1.6, the electric field component of the incident light will be parallel to the QD plane therefore resolving the absorption of strongly *s*-polarised transitions.

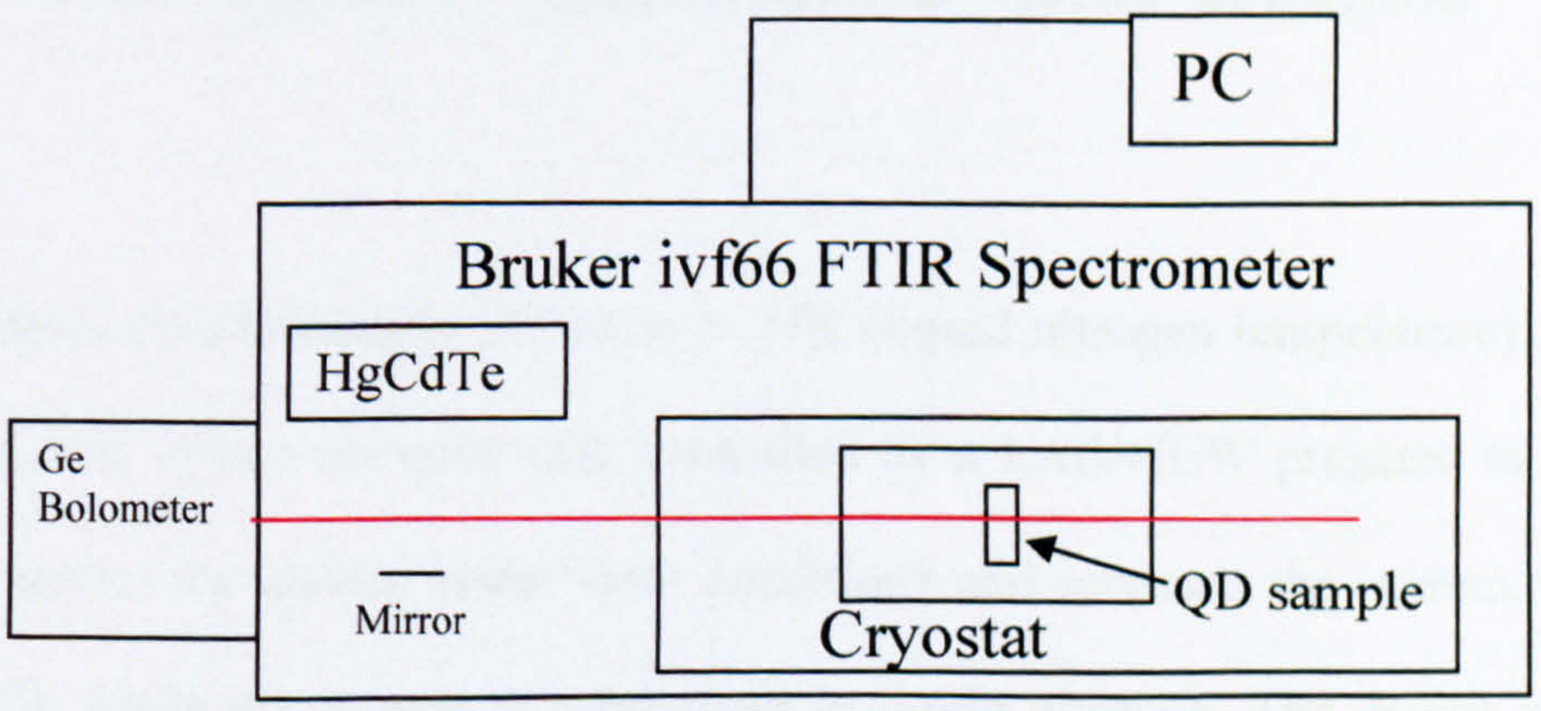

Fig.2.1.6 Transmission set up for *s*-polarised normal incidence geometry measurements using a Ge composite bolometer cooled at 4.2K

Typical normal incidence transmission spectra for InAs/GaAs QDs are shown below in Fig.2.1.7.

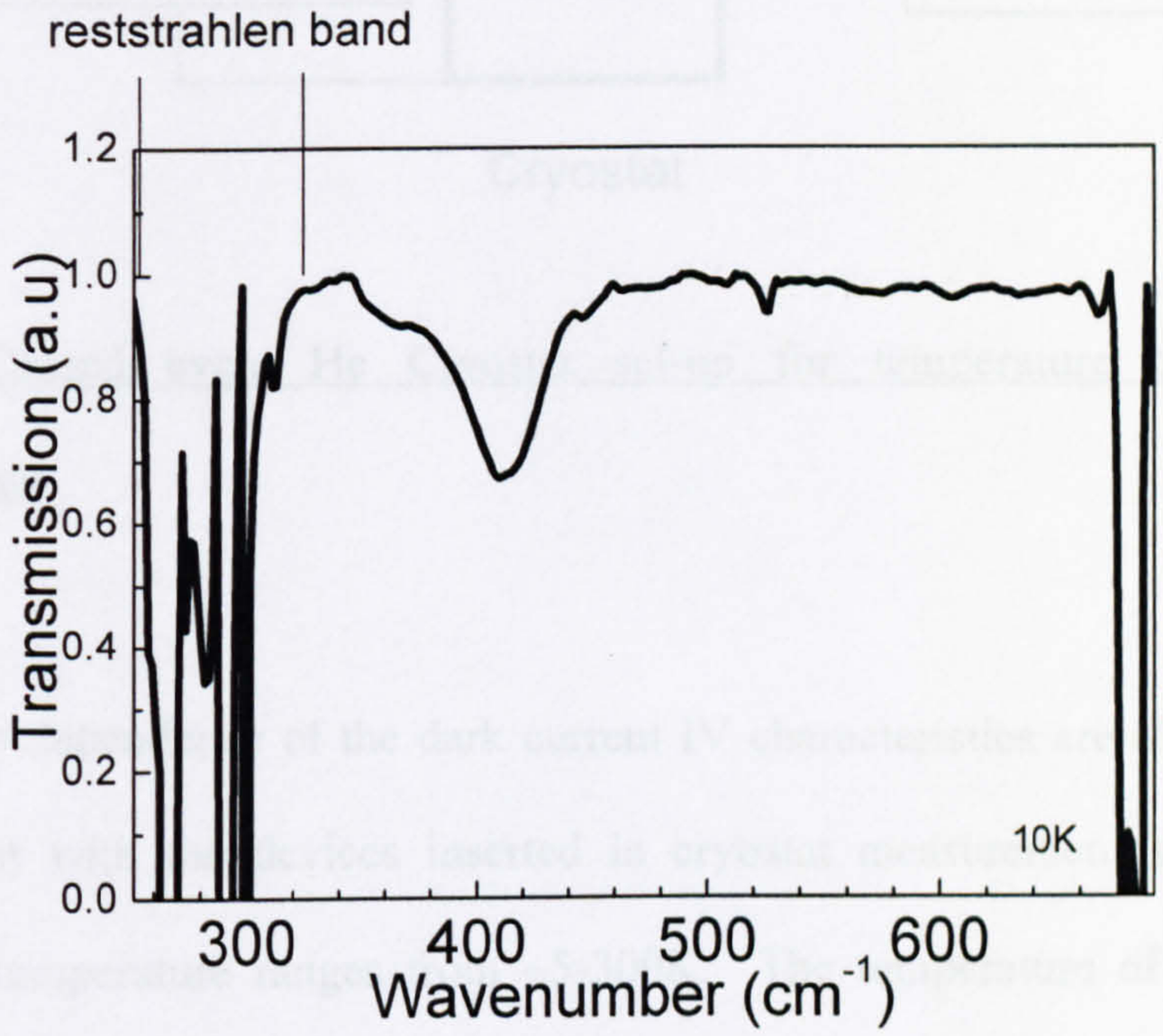

Fig.2.1.7. Transmission spectra of a typical InAs/GaAs QD sample at 10K.

2.2. Dark current IV measurements - BLIP condition

Dark current measurements are taken at 77K (liquid nitrogen temperature), using a Keithley2400 source measure unit, controlled by a LABVIEW program to apply a voltage across the device under dark conditions and measure the current flowing through it, while the sample is submerged in liquid nitrogen. The device seal is a metal lid which ensures dark current conditions and retains the same temperature as the device, thus screening RT background radiation.

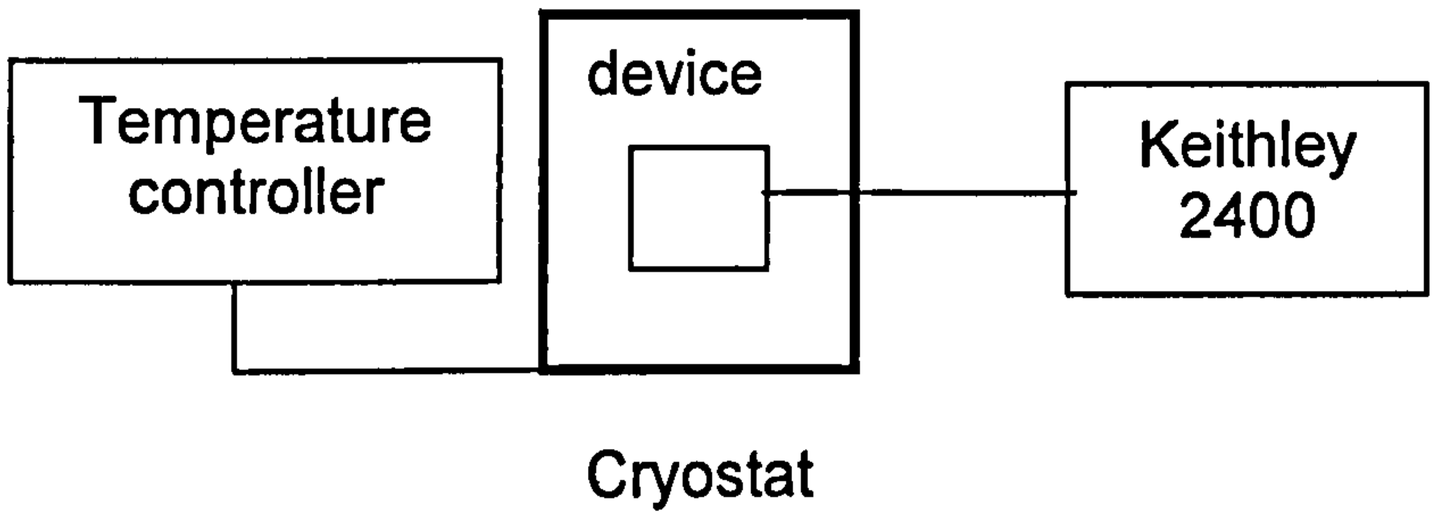

Fig.2.2.1. Closed cycle He Cryostat set-up for temperature dependent IV measurements

Temperature dependence of the dark current IV characteristics are also carried out similarly but with the devices inserted in cryostat measurement system that is capable of temperature ranges from ~5-300K. The temperature of the device is monitored by a thermocouple. The current-voltage characteristics for temperatures ranging from 5K to room temperature (300K) have been measured, in cases where information regarding the thermal behaviour of the dark current for a range of temperatures was required. However, in most cases the dark current was measured at ~77K, by submerging the sealed devices in liquid nitrogen.

The same set up can be used to determine the BLIP condition of the detector (see chapter 1.4.5). In order to find the BLIP temperature of the detector a temperature dependence of the IV characteristics is carried out, initially with the cold shield on, which gives the dark current temperature dependence as discussed above. The same is then carried out without the cold shield, and therefore with the detector under 300K background illumination from the room. Once both temperature dependencies are measured, the dark current IV is subtracted from the illuminated IV and the

temperature at which the resulting subtracted IV curve is equal to the dark IV is the BLIP temperature.

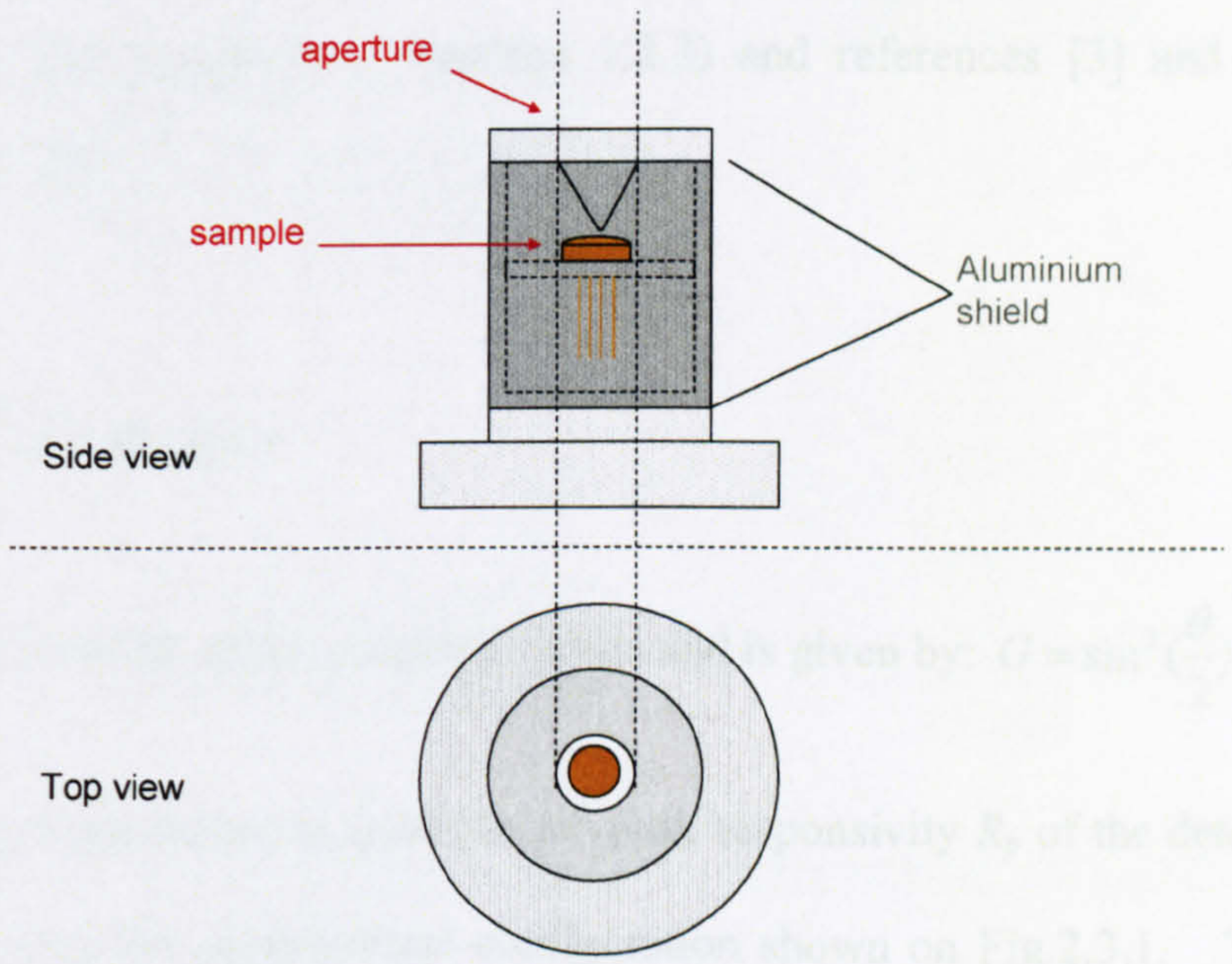

Fig.2.2.2 BLIP condition measurement configuration of TO5 header on cryostat sample holder

To ensure that scattered light from the room is not detected the whole cryostat is covered with a black cloth, and hence there is no light from the room adding to the illuminated current. Also an aperture is placed on top of the detector to define the field of view of detection, as well as the cryostat sample holder being surrounded by an aluminium shield, to ensure that the ambient radiation inside the cryostat (which is at lower temperatures than RT) is not detected. Thus it can be ensured that the photocurrent detected is the 300K background photocurrent. The described configuration can be seen in Fig.2.2.2

2.3. Responsivity Measurements

The responsivity of a detector and its association with the intraband photocurrent were discussed in chapter 1 (section 1.2.3) and references [3] and [4]. From equation (1.25):

$$I_P = R_P G \int_{\lambda_1}^{\lambda_2} \tilde{R}(\lambda) W(\lambda) d\lambda$$

Where G represents all the coupling factors and is given by: $G = \sin^2(\frac{\theta}{2}) AF \cos\varphi$.

The intraband photocurrent I_p and hence peak responsivity R_p of the detector can be measured using the experimental configuration shown on Fig.2.3.1. The lock–in amplifier (EG7265) is connected to a PC interface and all the calculations and measurements are carried out automatically by an in-house Labview program. The Kiethley2400 is the same as for the IV measurements.

When a measurement starts, the Labview program takes an I-V measurement with only the Keithley connected to the device while under illumination from the BB. After the IV is taken the lock-in amplifier is then connected through the load resistor R_L as shown in Fig.2.3.1. The program then uses the IV data to interpolate the differential resistance of the sample R_{diff} vs. applied bias. Then by taking R_{diff} and R_L into account it extrapolates the voltage range that the Keithley needs to apply to the combined R_L and QDIP circuit, in order to obtain the same voltage on the QDIP as that applied for the initial IV measurement.

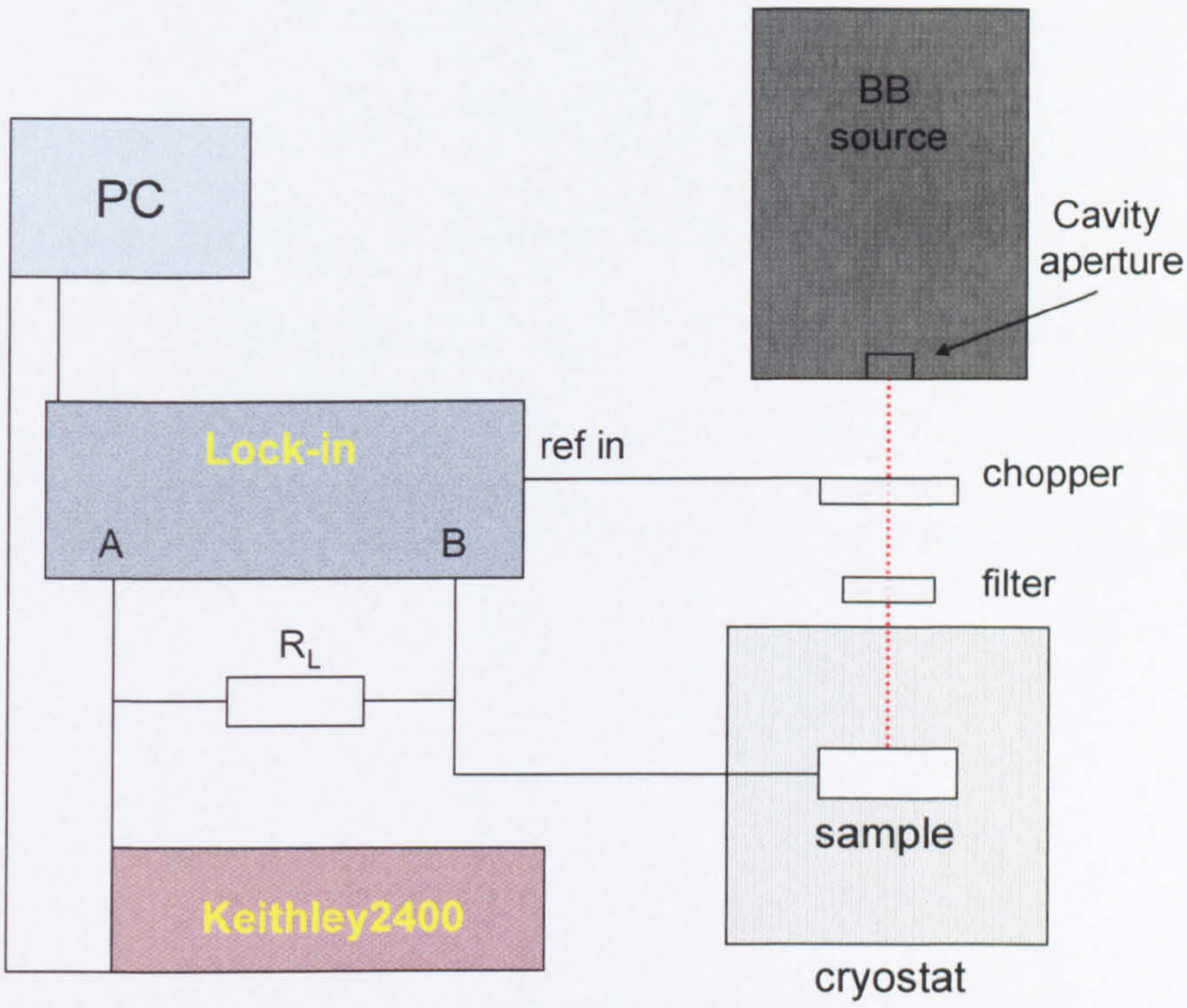

Fig.2.3.1 Experimental set-up for responsivity measurements equivalent circuit

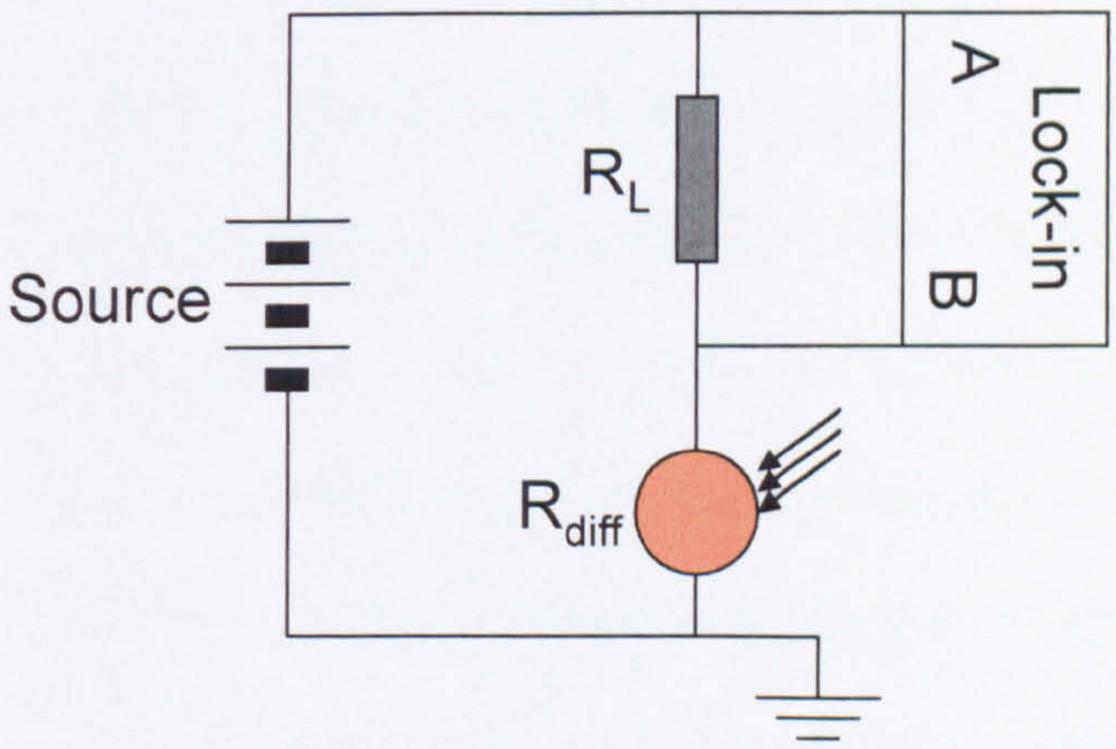

Fig.2.3.2 Equivalent circuit of experimental responsivity measurements set-up

The corresponding circuit is shown on Fig.2.3.2. The lock-in amplifier measures the photoinduced voltage changes (ΔV_{LI}) across R_L with applied bias. The photocurrent is calculated by a MATLAB interface within the program, which uses the total

resistance of R_L& R_{diff} and ΔV_{LI} for the relative applied bias range to calculate the photoinduced current flowing through the device. The photocurrent values (I_p) and the experimental parameters and coupling factors (G) are entered in eq.1.25, as is Ř(λ) which is the normalised FTIR spectral data obtained as discussed in section 2.1. The result is a calculation of peak responsivity in real time i.e. the final output of the program after one measurement finishes is the actual peak responsivity R_p.

2.4. Optical Studies - Photoluminescence (PL) and PL excitation (PLE)

A standard technique for measuring the emission characteristics of a semiconductor material is photoluminescence (PL) spectroscopy. The PL process involves carriers being excited by an excitation source (typically a laser), above the bandgap of the semiconductor, thereby creating electrons in the conduction band and holes in the valence band. The electrons and holes then relax back to the ground state followed by radiative recombination and thereby emission of the PL signal.

The sample is mounted in a cryostat with windows allowing optical access on at least two adjacent sides as shown in Fig.2.4.1, to allow the illumination of the sample as well as the emission of the PL from the side.

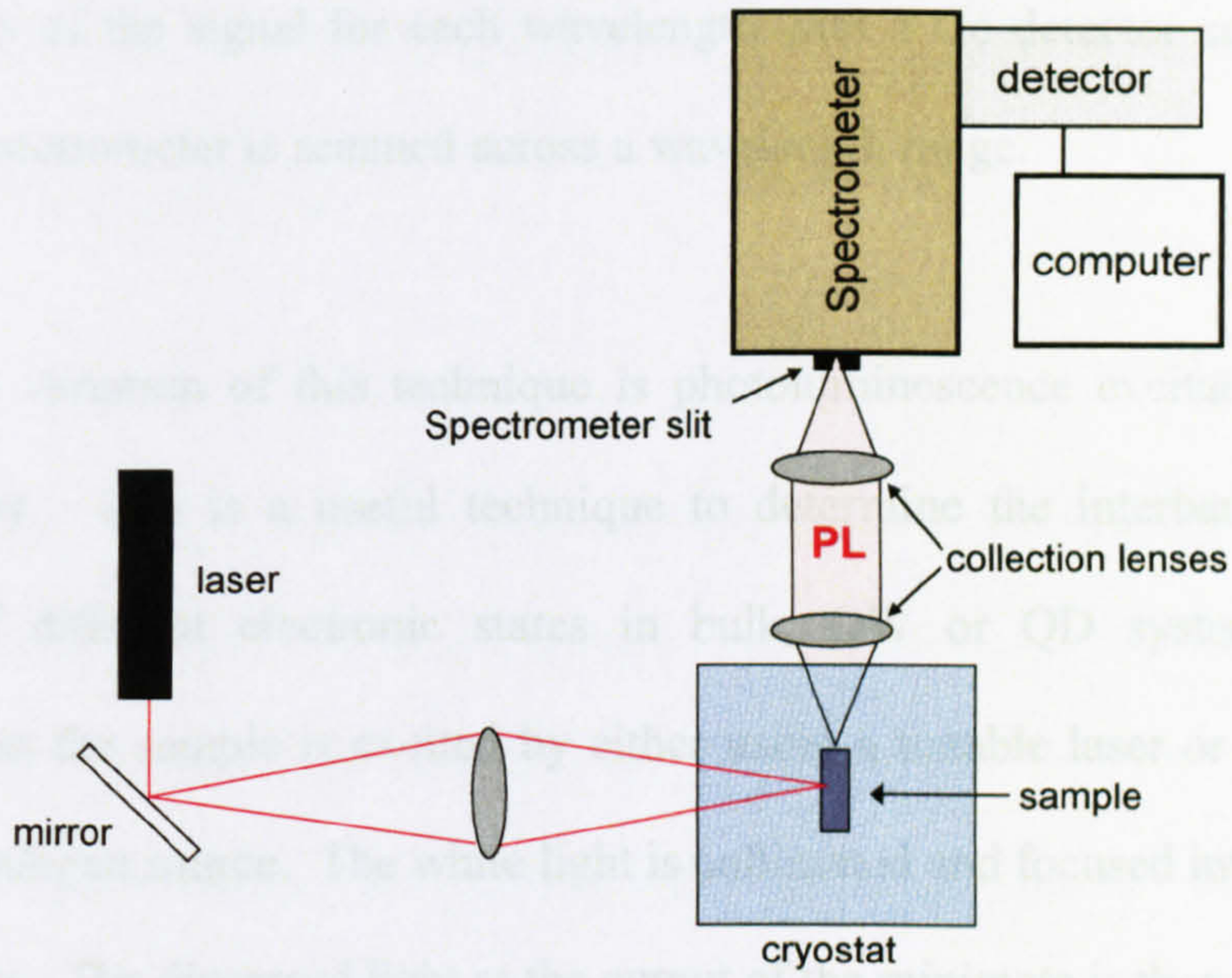

Fig.2.4.1. Experimental arrangement for Photoluminescence measurements

The PL is emitted at longer wavelengths (lower frequencies) and in all directions. A low power (~3mW) laser diode (λ=632nm) is used as an excitation source, such that the emission occurs primarily from the QD ground state. The linewidth of the emission at low temperatures provides information concerning the homogeneity of the QD ensemble.

In this arrangement the PL is collected normally to the angle of incidence to avoid interference from surface reflections of the sample. Typically, the sample is tilted slightly, to produce a smaller angle of incidence ($45°<\theta<90°$), to enhance the signal while avoiding reflections. Part of the emission is collected with two lenses and focused onto the entrance slit of a computer controlled grating spectrometer (SPEX1702/04, focal length: 750mm; 1200lines/mm grating, 1nm/mm dispersion with a maximum resolution of 0.01nm). The PL spectrum is obtained by detecting

the intensity of the signal for each wavelength with a Ge detector cooled to 77K, while the spectrometer is scanned across a wavelength range.

A different variation of this technique is photoluminescence excitation or (PLE) spectroscopy. This is a useful technique to determine the interband absorption strength of different electronic states in bulk, QW or QD systems. In this configuration the sample is excited by either using a tunable laser or a white light Tungsten-halogen source. The white light is collimated and focused into a minimate spectrometer. The dispersed light at the output of the minimate is then re-collimated and focused onto the sample held within the cryostat. The SPEX spectrometer then measures the photoluminescence at the peak of the emission while the excitation wavelength is varied by the minimate [5,6]. The minimate spectrometer slit width is a trade-off between a narrow excitation linewidth and a reasonable incident power. Typically for the studies presented herein slit width ranged from 1mm-2mm [6].

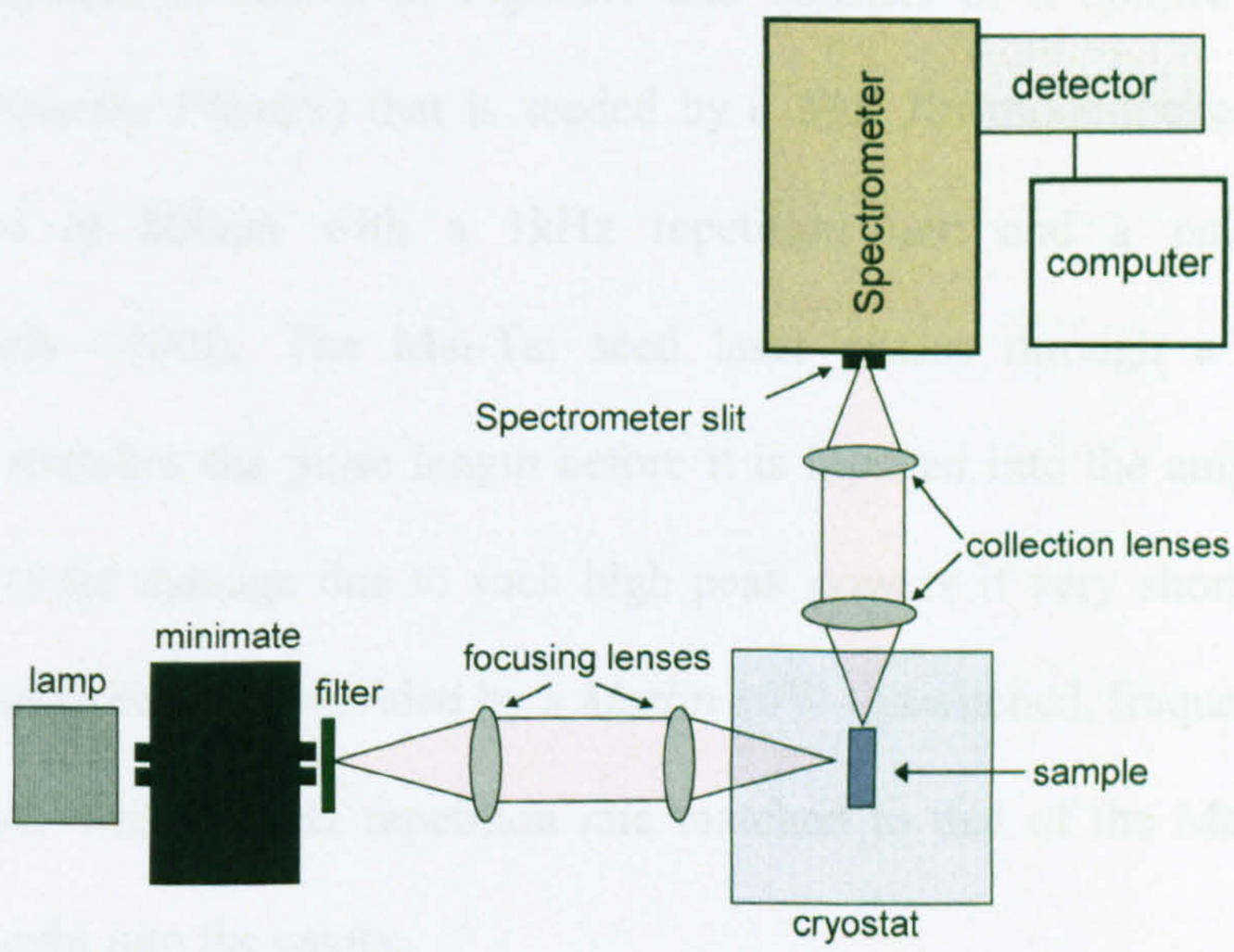

Fig.2.4.2. Photoluminescence excitation spectroscopy configuration

2.5. Ultrafast pump-probe and FEL experimental configuration

The detectors were also characterised via time-resolved ultrafast measurements to determine the carrier dynamics, and examine non-linearilites in DWELL structures. Two different experimental configurations were used. The first that will be discussed is a pump-probe experiment using an optical parametric amplifier (OPA) based set-up, and the relevant results can be found in chapters 3.1, and the second makes use of a free electron laser (FEL) to perform second order autocorrelation measurements, and the relevant results can be found in chapter 5.2.

Pump-probe

The laser system is shown in Fig.2.5.1 and consists of a *Spitfire* regenerative amplifier (*Spectra Physics*) that is seeded by a *Mai Tai* mode-locked Ti:sapphire laser, tuned at 800nm with a 1kHz repetition rate and a pulse width of approximately ~100fs. The Mai-Tai seed laser passes through a stage which temporally stretches the pulse length before it is injected into the amplifier cavity. This helps avoid damage due to such high peak powers if very short pulses were used. The pump beam is provided by a *Merlin* 10W Q-switched, frequency-doubled, Nd:YLF laser with a 1kHz repetition rate matched to that of the Mai Tai, and is injected straight into the cavity.

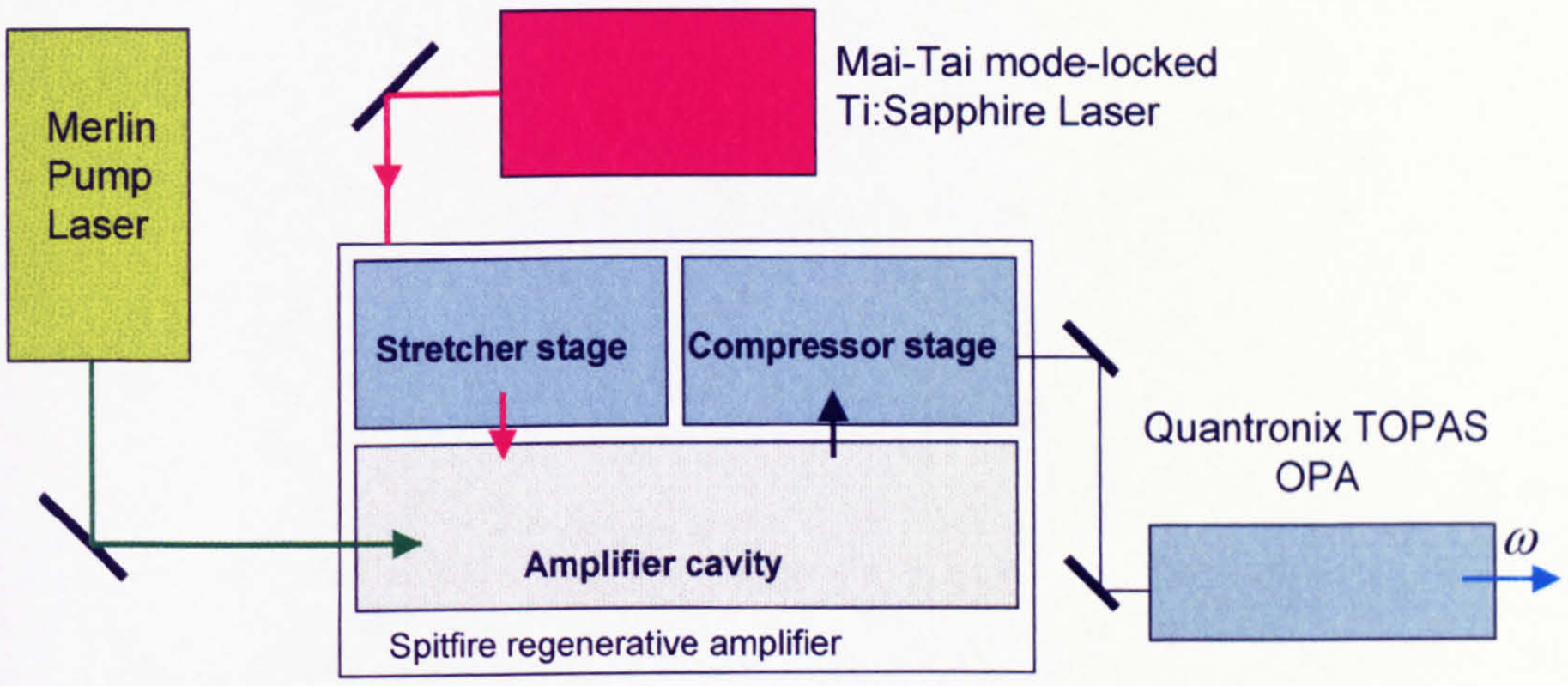

Fig.2.5.1. OPA system used for mid-IR pump-probe measurements

The overlap of the stretched Mai-Tai pulses and the pump beam, within the amplifier cavity provides the amplification. Inside the cavity there are Pockels cells that control the number of round trips of the amplified pulse before exciting the cavity through the output coupler (OC). The final stage is a temporal compressor stage that returns the pulse length to ~100fs. The maximum output power of the Spitfire is approximately 1W after the beam has passed through the compressor section. The output from the *Spitfire* is then sent to a Quantronix *TOPAS* OPA allowing the wavelength selection from 240 nm to 20μm depending on the crystal being used. In this case a crystal allowing a wavelength range of 2.7-11μm is used. The tuning range is further limited by the filters and beamsplitter used, and in the present study wavelengths from 7-11μm were used. Nonetheless as the linewidth of the devices under investigation is narrow and around 8μm this range is sufficient.

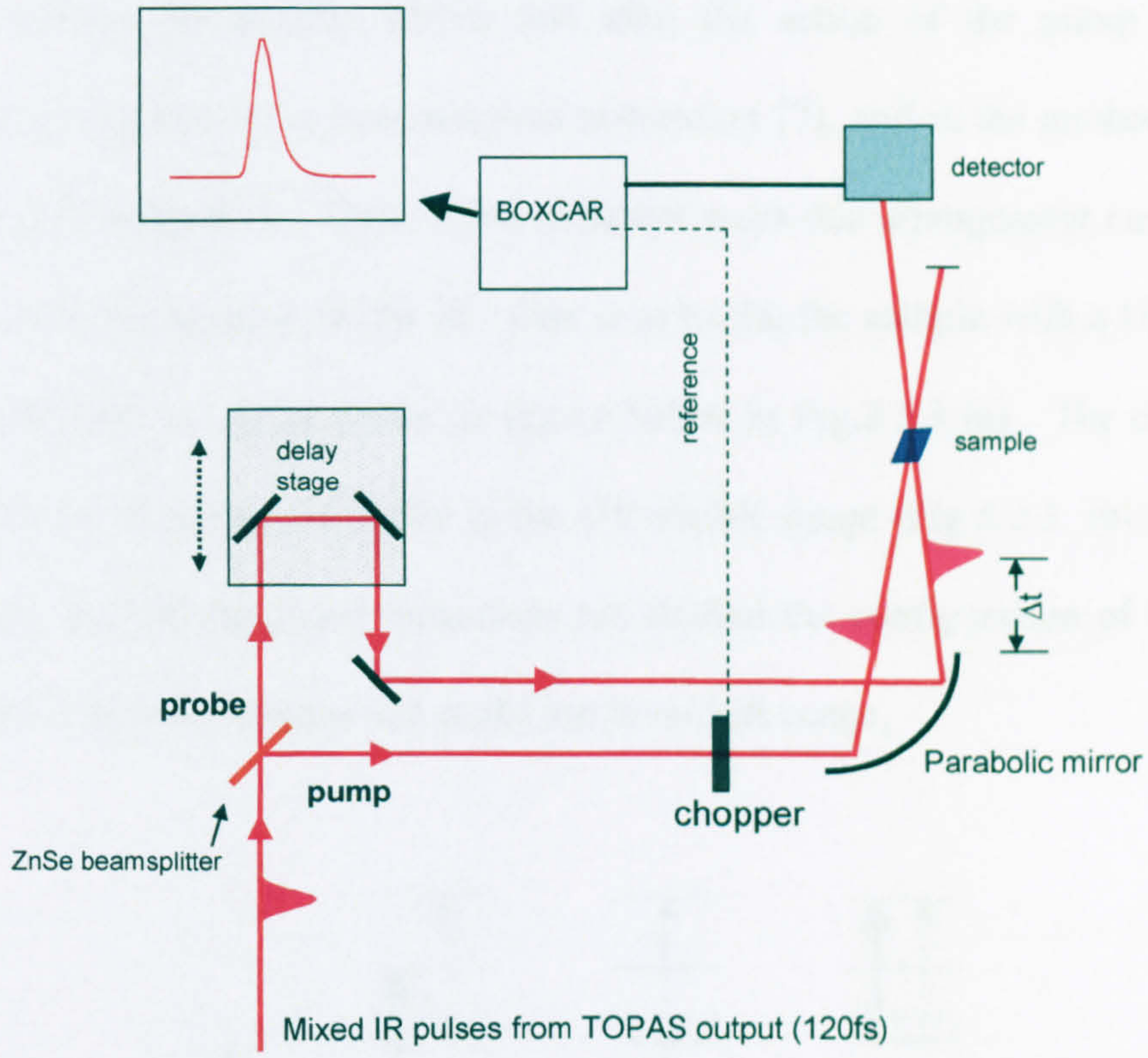

Fig.2.5.2. Mid-IR Pump-Probe set-up for ultrafast transmission spectroscopy

The output of the TOPAS then passes through the pump-probe configuration shown in Fig.2.5.2. The beam is split by a ZnSe beamsplitter into an intense pump pulse and a weaker probe pulse. The probe pulse goes through a motorised delay stage with a retroflector, where it undergoes an adjustable temporal delay Δt with respect to the pump pulse. Both beams are focused using an off-axis parabolic gold mirror on a sample in the 45° waveguide configuration described in section2.1. The focused beam diameter is ~200μm. The probe pulses were attenuated to be about 200 times weaker than the pump pulses (~5 MW/cm^2) using neutral density filters.

At zero time the pump pulse arrives at the sample and after Δt the probe pulse hits the sample. If comparing the characteristics of the probe beam (intensity, phase)

once it crosses the sample, before and after the action of the pump then the technique is referred to as time-resolved absorption [7], and is the method used in the present investigation. There a few different ways this arrangement can be used to study carrier relaxation in the IR. One is to excite the sample with a UV-visible pump pulse and use an IR probe as shown below in Fig.2.5.3 (a). The other is to pump with an IR pulse and probe in the UV-visible range (Fig.5.2.3. (b)). In our case where mid-IR intraband transitions are studied the configuration of Fig.5.2.3. (c) is used, where both pump and probe are in mid IR range.

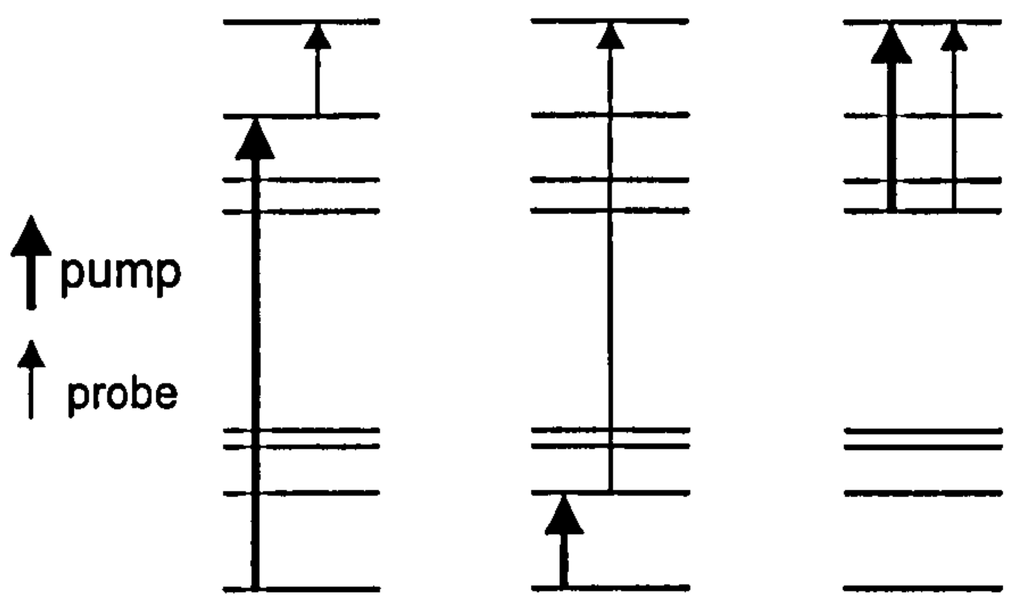

Fig.2.5.3. possible methods using IR pump probe (a) interband pump-intraband probe, (b) intraband pump-interband probe, and (c) intraband pump-probe

This technique can help determine the electron relaxation times in DWELL structures, after a transition has been excited by tuning the excitation source at the wavelength where the absorption is maximal for this transition, as well as slightly off centre from the absorption peak. After electrons populate an excited state, they relax back to the ground state, and the temporal decay is measured by using a boxcar (or a lock-in amplifier). Since the samples are QD based and the absorption is quite low, an average of several scans is required to resolve the time constants of this decay. More details can be found in references [7,8,9].

FEL basics and set-up

The Dutch free electron laser (FEL) known as FELIX, in Nieuwegein, was used to perform autocorrelation measurements in two-photon QDIPs (see chapter 5.2), and hence some FEL basics are included here. The intricate physics and detailed description of the operation of FELs is beyond the scope of this thesis and more information can be found in reference [10] as well as the FOM institute website [12].

FELs make use of a relativistic electron beam, which is forced into a wiggling motion [10, 11]. The electron beam is produced by an accelerator, and is injected into a resonator, consisting of two high-reflectivity mirrors, around the undulator. The magnetic field of the undulator is perpendicular to the direction of the electron beam (Fig.2.5.3) and can periodically change polarity many times along its length. This polarity change results in a periodic deflection of the electrons while traversing the undulator. Thus the electrons will interact with the transverse field of the wave which is to be amplified via the transverse component of their velocity [10]. While in the resonator the wave will interact with 'fresh' electrons. Initially spontaneous emission will occur, peaked at the same frequency as the transverse oscillation with a Doppler shift resulting from the high longitudinal velocity of the relativistic electrons. The weak intensity of the spontaneous emission is due to electrons being spread out over an interval much larger than the radiation wavelength, suppressing coherent emission. Once the wave has a sufficient number of roundtrips in the resonator, the beam amplifies itself through the interaction with fresh electrons until

saturation occurs at a power level which is typically 10^7 to 10^8 times that of the spontaneous emission [10, 12].

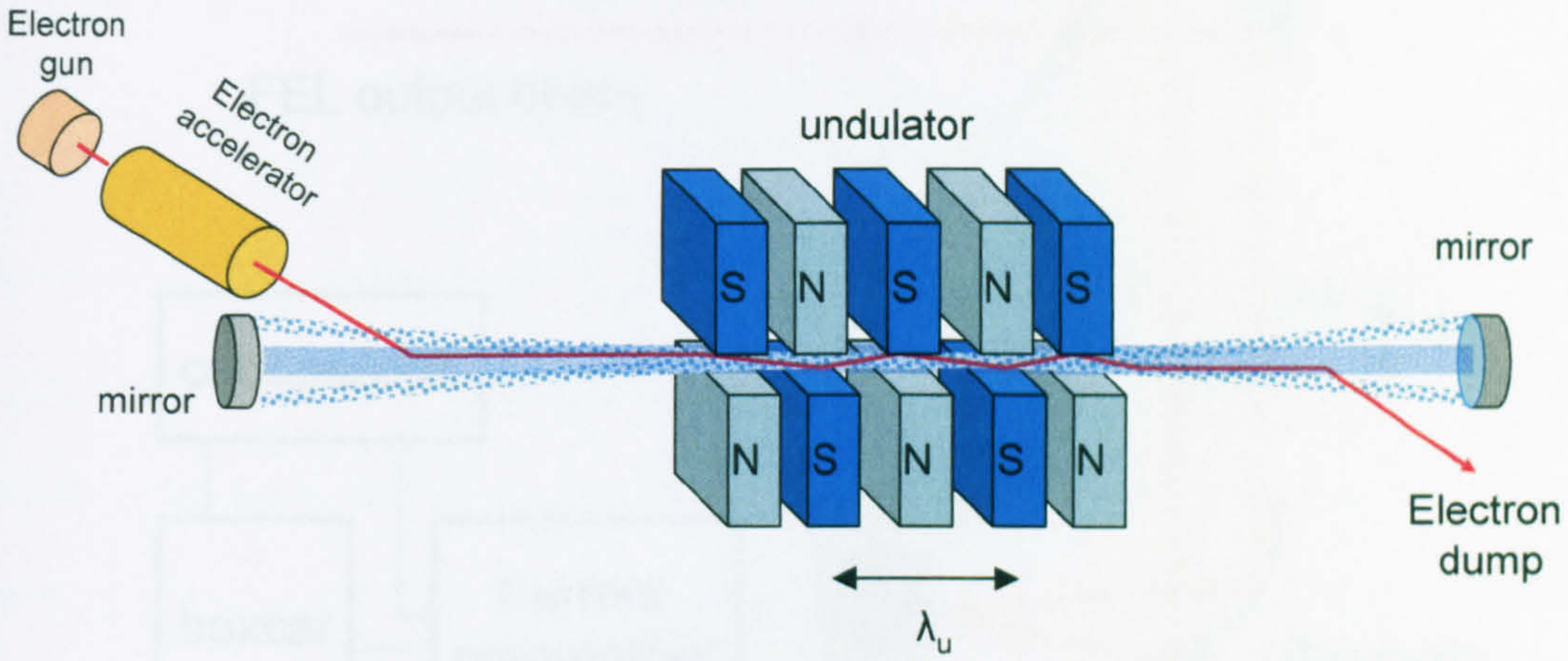

Fig.2.5.3. Schematic representation of an FEL laser.

The aspects of FEL that are particularly useful in this study are the wide spectral tunability, providing laser emission in the far-IR, where high power sources are rare. FELs also provide high power and variable short pulse width, enabling non-linear studies of transitions occurring at >25μm and providing ~ps pulse width, which enables the resolution of carrier dynamical processes with ps lifetimes.

The study of two-photon processes in QDIPs using of the Dutch free electron laser FELIX in Nieuwegein will be presented in chapter 5.2, where second-order autocorrelation measurements were performed to detect ultrashort far-infrared pulses, using a detector with a quadratic photocurrent dependence on power. The autocorrelation set-up that was used to investigate this is shown below in Fig.2.5.4.

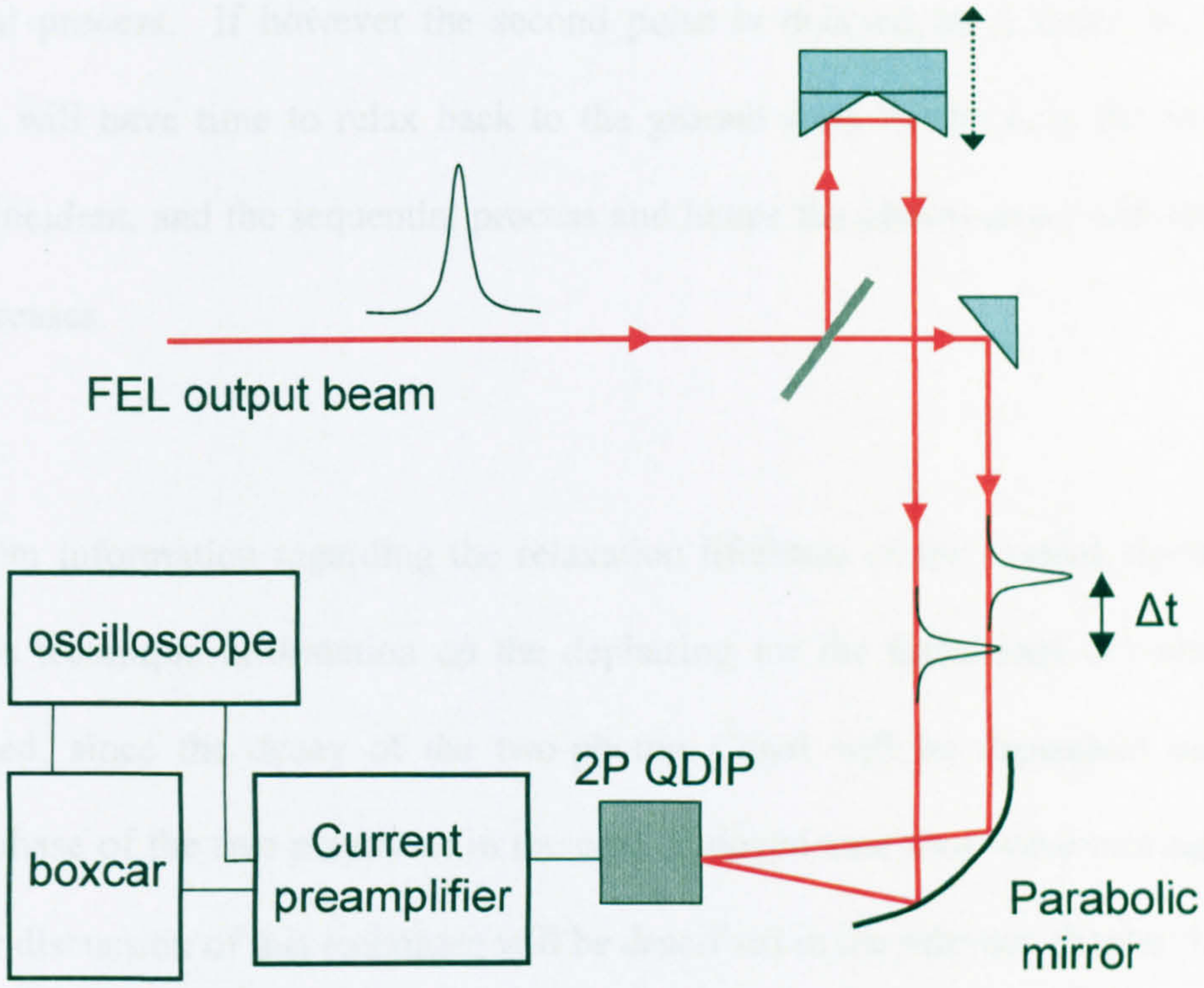

Fig.2.5.4. Autocorrelation measurement configuration for Two-Photon measurements

The experiment resembles the pump-probe technique, although in this case the beam is split into two pulses with approximately equal powers [12]. Again, one beam is focused on the detector directly via the parabolic mirror whereas the other passes through a delay stage and the time difference between the two pulses is Δt.

When the first pulse reaches the QDIP detector, a transition is excited from the ground state to an excited state. Since the second pulse has the same energy as the first one, if it hits the sample at $\Delta t = 0$, then electrons in the excited state will be excited to a second excited state, energetically equidistant to the ground state-to-first excited state energy separation. This will induce a two-photon photocurrent via this

sequential process. If however the second pulse is delayed by a finite Δt, then electrons will have time to relax back to the ground state by the time the second pulse is incident, and the sequential process and hence the photocurrent will reduce as Δt increases.

Apart from information regarding the relaxation lifetimes of the excited electrons, using this technique information on the dephasing for the transitions can also be determined, since the decay of the two-photon signal will be dependent on the relative phase of the two pulses, as in the case of degenerate four wave mixing [6]. A further discussion of this technique will be described in the relevant chapter 5.2.

References

1. T.J. Johnson, G. Zachman, '*Introduction to Step-Scan FTIR*' (Bruker Optik manual)
2. J.F. James, '*A student's guide to Fourier transforms*', Cambridge University press, 1995, Cambridge, UK
3. S.D. Gunapala, S.V. Bandara, 'Intersubband transitions in Quantum Wells: Physics and device applications', Semiconductors and semimetals. Vol.62, ch.4. p.225, Academic Press 2000
4. H. Schneider and H. C. Liu, *Quantum Well Infrared Photodetectors: Physics and Applications*, Springer Series in Optical Sciences, Springer, Berlin, Heidelberg, 2006, Vol. 126, chapter 4, p. 45-69

5. M. Fox, '*Optical properties of solids*', Oxford Master Series in Condensed Matter Physics, Oxford University press, 2001

6. Ian Sellers, '*Optimisation and study of In(Ga)As Quantum dot lasers*', Thesis submitted for PhD, 2004, Department of Physics and Astronomy, University of Sheffield.

7. C. Rulliere, T. Amand and X. Marie, Spectroscopic methods for Analysis of Sample Dynamics, Femtosecond laser pulses, Principles and Experiments, chapter 8, p.225, Springer Science and Business Media, USA, 2005

8. D. Kundys, '*Nonlinear Spectroscopy of Semiconductor Nanostructures*', Thesis submitted for PhD, 2006, Department of Physics and Astronomy, University of Sheffield.

9. J. Shah, '*Ultrafast Spectroscopy of Semiconductors and Semiconductor Nanostructures*', Springer Series in Solid-State Sciences, Vol.115, 1999

10. C.A.J. van der Geer, FELIX Design and Instrumentation, PhD Thesis, Technische Universiteit Eindhoven, CIP Data Library, 1999

11. D. Stehr, '*Infrared studies of impurity states and ultrafast carrier dynamics in semiconductor quantum* structures', PhD thesis, Fakultat Mathematik und Naturwissenschaften der Technischen Universitat Dresden, 2007

12. FOM Rijnhuizen website:

http://www.rijnhuizen.nl/research/guthz/felix_felice/ir_sources/

3. Spectral Studies and performance considerations in InAs/InGaAs DWELL QDIPs

In this chapter the principal issues in the design of DWELL QD structures are presented. Firstly, intraband transitions in DWELLs are discussed, with the aid of intraband absorption and interband photoluminescence experimental studies. Narrow, high energy absorption features were observed in the LWIR atmospheric window associated with transitions between the quantum dot ground state to states within the QW. Ultrafast spectroscopy was also employed to determine the carrier dynamics in DWELLs, where the lifetimes associated with the photocurrent were experimentally measured.

In order to appreciate how individual parameters of the DWELL design affect the performance of DWELL detectors, a number of samples were grown in which various parameters were varied, including: (i) The number of InAs monolayers (ML) deposited during QD growth, (ii) The QW width and composition, in which the dots are embedded, (iii) The thickness of the active region (number of periods), (iv) Doping concentrations.

This chapter documents the characterisation of all these devices and how the attempted design alterations affected the performance. Furthermore, the bias dependent Stark effect in DWELL QDIPs was investigated and the results were interpreted by theoretical modelling using an 8band k•p model. Finally an optimised InAs/$In_xGa_{1-x}As$/GaAs DWELL QDIP is proposed and its high performance is demonstrated.

3.1. Intraband absorption and carrier relaxation dynamics in DWELL structures

3.1.1. Introduction

In order to optimise the performance of DWELL QDIP devices, it is essential to understand the nature of the optical transitions, particularly in the conduction band (CB) in the case of n-type QDIPs. In this section, results of near-infrared (interband) and far-IR and mid-IR (intraband) optical spectroscopy of InAs/$In_{0.1}Ga_{0.9}As$ DWELL structures are presented to investigate the intraband transitions in DWELLs. An accurate knowledge of these energies is important as they determine the operating range of DWELL QDIPs and also have a strong influence on the temperature dependence of general DWELL devices [1]. Strong

intraband absorption and narrow linewidth, high energy transitions are observed compared to InAs/GaAs QD structures. Electron and hole confinement energies can be determined from these studies.

It is also important to determine carrier relaxation dynamics in QD structures and DWELLs. Attempts to estimate the carrier lifetimes in QDs typically used time resolved photoluminescence or non-degenerate pump-probe experiments [2]. Most observation are of picosecond-scale (ps) carrier lifetimes, contradicting the early theoretical predictions of a quantum dot "phonon bottleneck" [3, 4] in the CB, as mentioned in chapter 1.4. The interpretation of results from all these experiments is often difficult as in these techniques electron-hole scattering (Auger-type) processes become possible, influencing the electron intraband relaxation [2].

Intraband studies of carrier relaxation in n-doped QDs have been carried out for the lowest energy conduction band (CB) transitions in QDs [5] and for the carrier lifetimes in wetting layer states in InAs/GaAs QDs [6]. The lifetime of electrons in the QW state in DWELL infrared photodetector structures, which is directly related to the responsivity of such devices had not been studied up until now. In this section, electron relaxation times of ~5ps from high energy states to the QD ground state in DWELLs were measured using a degenerate mid-infrared (intraband) pump-probe technique.

3.1.2. Absorption studies

The structure investigated was grown by molecular beam epitaxy (MBE) upon a semi-insulating GaAs substrate, as discussed in the introduction and in reference [7]. The structure contained 30 layers DWELL absorbing regions, separated by 500Å of undoped GaAs. The DWELL absorbing region consists of 2.55ML of InAs dots grown within an 80Å $In_{0.1}Ga_{0.9}As$ quantum well, with 10Å of the well below the dots and 70Å above. A schematic of the CB profile of a typical DWELL structure is illustrated in Fig.3.1.1.

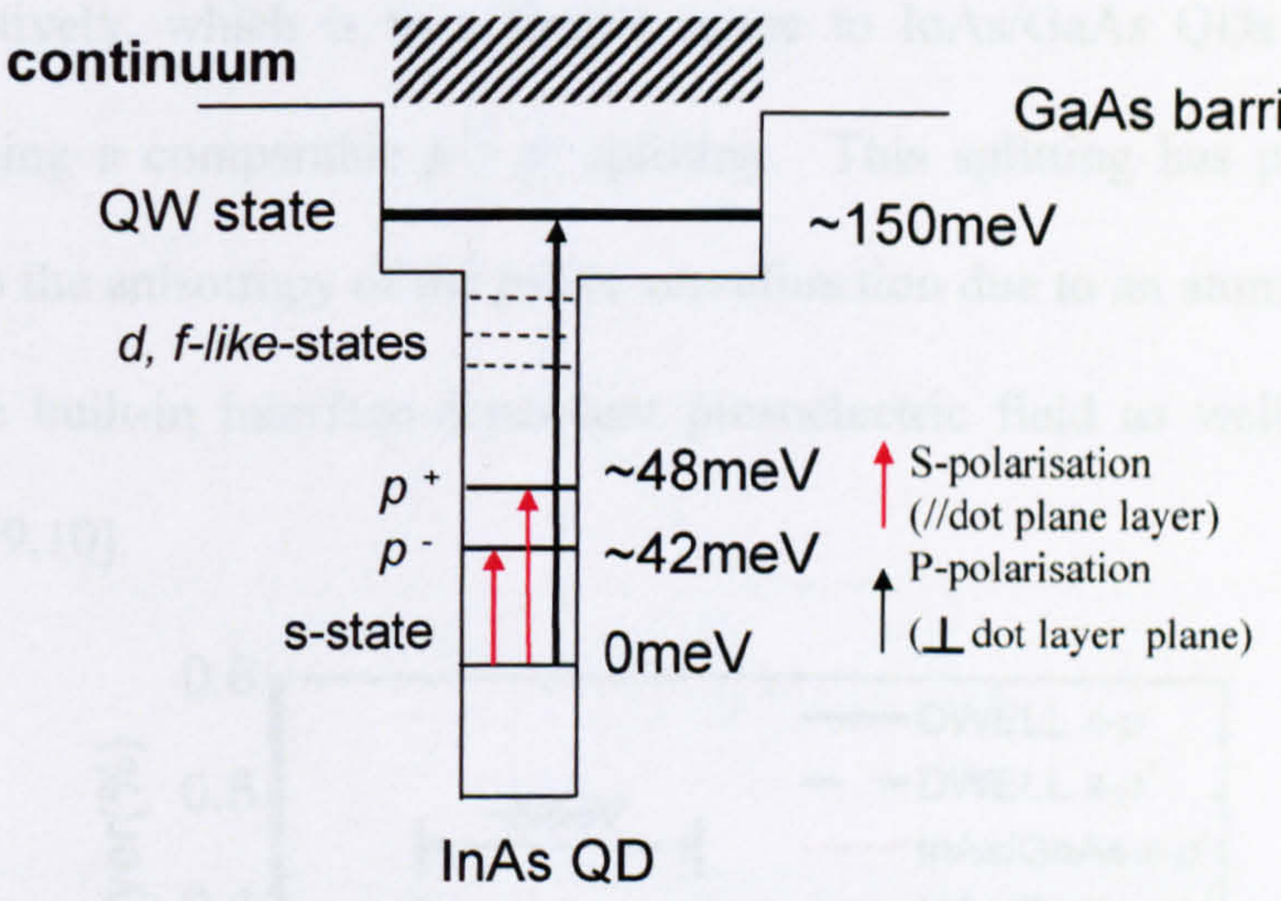

Fig.3.1.1. DWELL conduction band schematic, showing possible transitions from the ground state to high energy states. The optical polarisation required to excite the transitions is also indicated.

The active region is Si δ-doped in the GaAs barrier layers, to a concentration of $6x10^{10}cm^{-2}$ corresponding to approximately 1 electron per dot (e^-/dot). Due to the degeneracy of the QD ground state [8], there can only be a maximum of two

electrons in that state, so the structure can be doped to a level twice that of the dot density, before any excited states start being occupied. A further sample was grown with the same design, but doped to a concentration of $1.2x10^{11}cm^{-2}$ ($2e^-$/dot) to study this effect, and is discussed at the end of this section.

Far-IR transmission spectra were measured at normal incidence to the dot layer plane along the [011] and [0-11] directions (see chapter 2.1). As shown in Fig.3.1.2 the normal incidence absorption per layer is stronger (0.4% per layer - thick line) compared with previously reported [9] InAs/GaAs QDs, (typically 0.2-0.3% per layer - thin line). The transitions occur at energies of 42.2 and 48.5meV for s-p^- and s-p^+ respectively, which is in a similar range to InAs/GaAs QDs (~48-51meV), while showing a comparable p^+- p^- splitting. This splitting has previously been attributed to the anisotropy of the p-like wavefunction due to an atomistic symmetry C_{2v} and the built-in interface-dependent piezoelectric field as well as QD shape anisotropy [9,10].

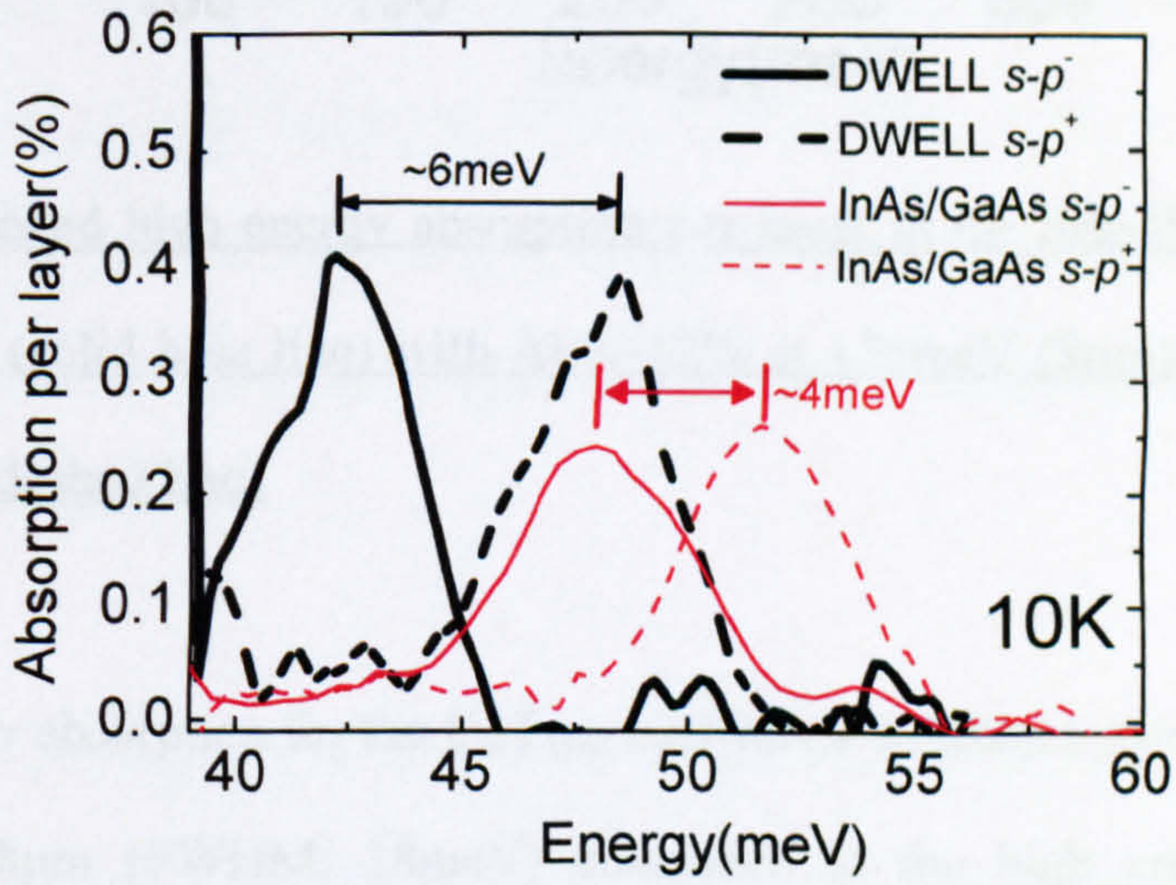

Fig.3.1.2. Far-IR intraband absorption spectra for DWELL sample at 10K (black) and for typical InAs/GaAs QDs (red). s-p^- [011] and s-p^+ [0-11] transitions are shown in solid and dashed lines respectively.

Although the energies are indeed lower and with an increased splitting for the DWELL sample, it is hard to attribute such effects to an increase in the dot size or any other parameter, since the magnitude of the difference is comparable to the observed variation of *s-p* energies in QDs grown in slightly different conditions. The stronger absorption for DWELLs could arise from the higher dot density reported for DWELLs compared with InAs/GaAs QDs [7,11].

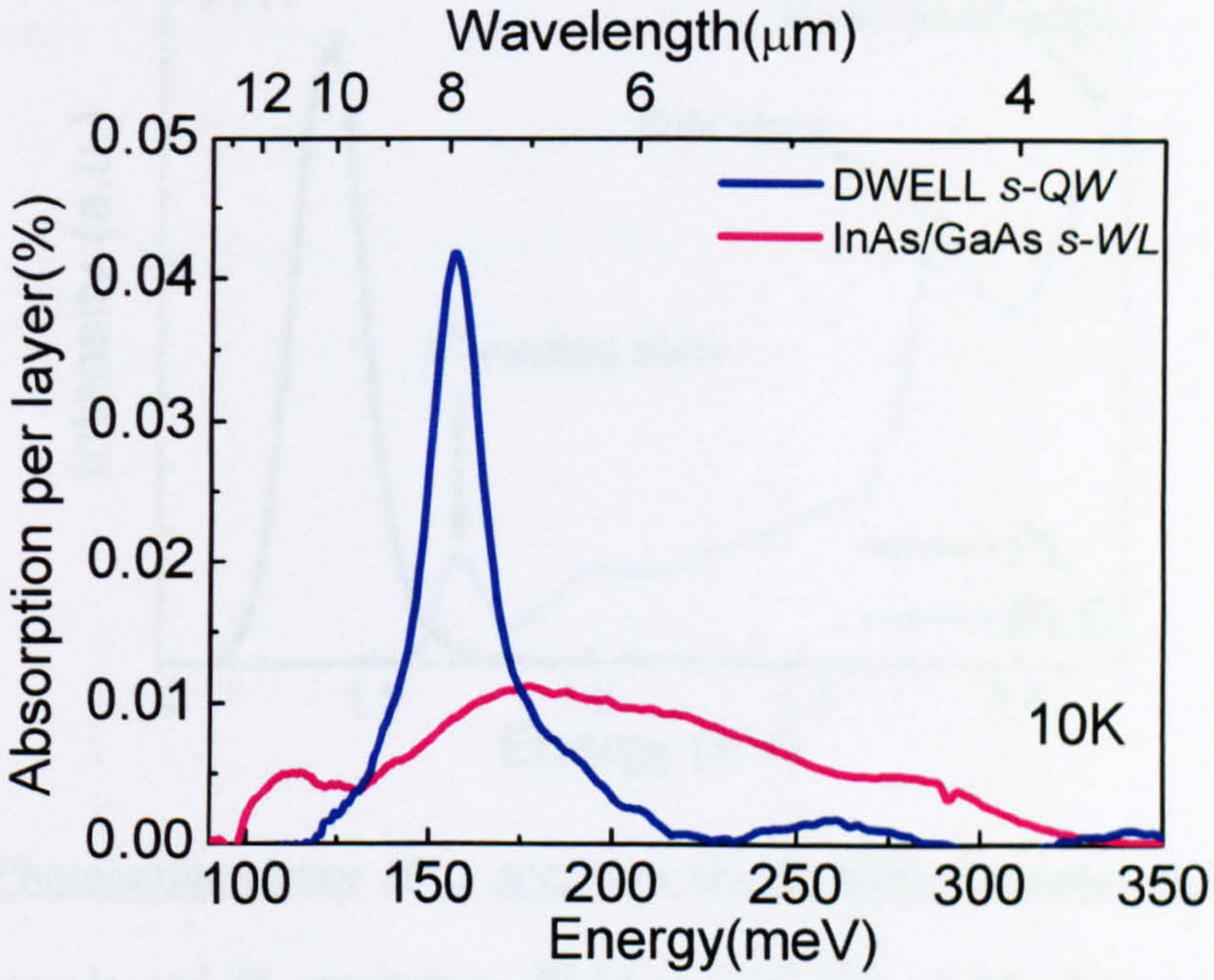

Fig.3.1.3. Intraband high energy absorption per layer in the mid-IR for a DWELL sample at 10K (solid blue line) with $\Delta\lambda/\lambda$~12% at 155meV (8μm) and InAs/GaAs QDs (magenta dashed line)

The high energy absorption for the E_1-E_{QW} transitions exhibits a narrow linewidth of $\Delta\lambda/\lambda$~12% at 8μm (FWHM: 18meV) compared to the high energy absorption spectra for typical InAs/GaAs QDs (Fig 3.1.3, blue and magenta lines respectively), where absorption occurs between the ground state and wetting layer states as well as possibly *d*-like and *f*-like states. This is evidence of the well defined QW state in

DWELLs compared to the broad distribution of levels in (or close to) the wetting layer in the case of InAs/GaAs QDs [8]. More results showing evidence of this can be found in references [12,13,14]. Although the integrated absorption is approximately equal for both samples, the peak absorption for DWELL structure is ~4 times larger compared with a standard InAs/GaAs QD structure.

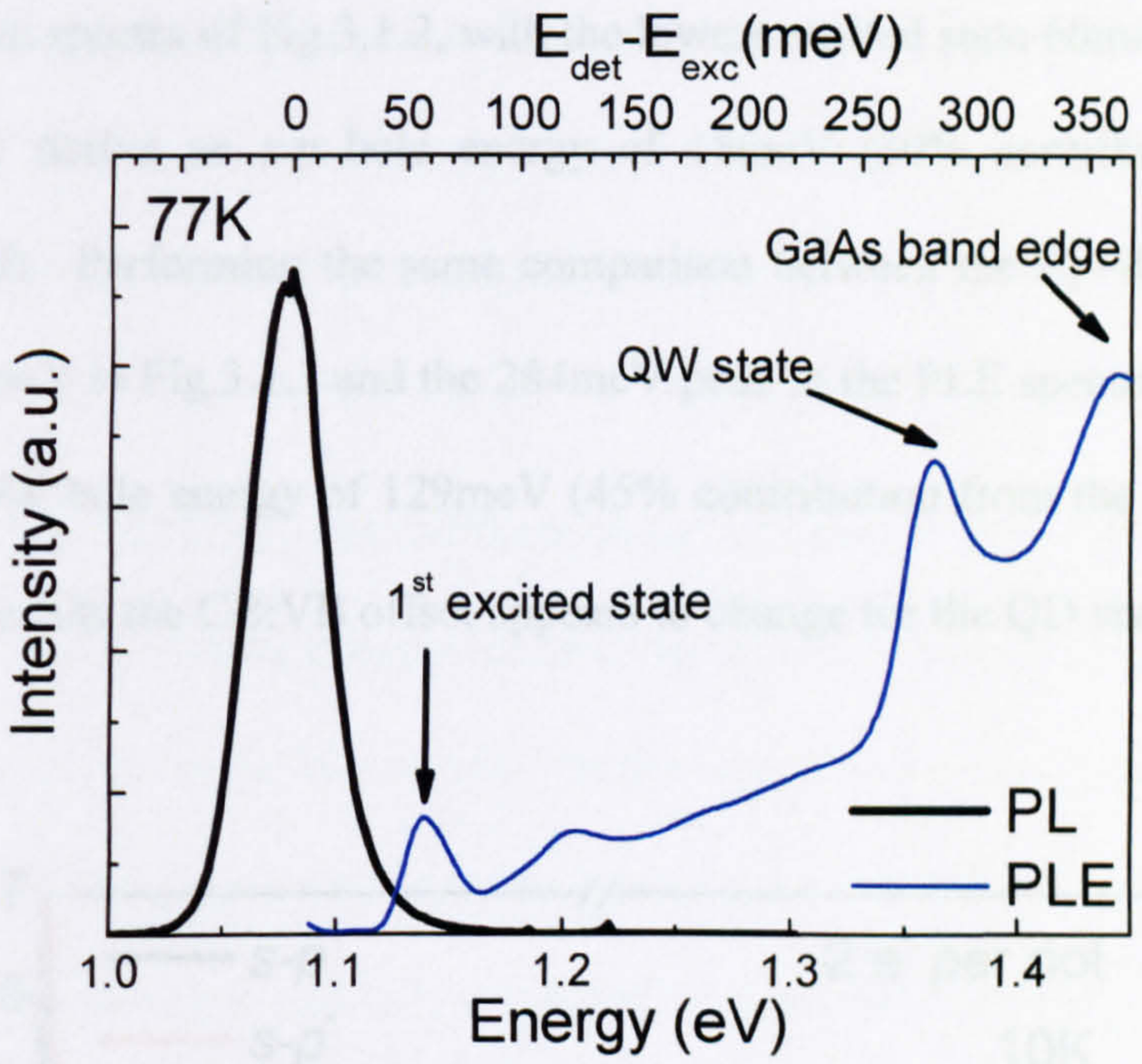

Fig.3.1.4 Photoluminescence (PL) spectrum (black line) measured at 77K for a DWELL sample and PL excitation (PLE) at 77K (blue line), First excited state followed by a peak attributed to the QW state at 60meV and 284meV respectively are indicated. The excitation energy subtracted from the PL peak detection energy is shown on the top axis.

Using the set-up described in chapter 2.4, the QD photoluminescence (PL) was measured at 77K and, as shown in Fig.3.1.4, the spectra exhibited a narrow $\Delta\lambda/\lambda$~3.2% (FWHM = 34meV) peak at 1.08eV. The PL excitation (PLE) spectra exhibited strong features at 60meV and 285meV, which were attributed to the

interband transition between the lowest excited electron and hole states and the transition between electron and hole states confined in the QW, respectively.

These features are attributed to the QD first excited state and QW states respectively. From a comparison of the *s*-p^- intraband absorption peak at 42meV in the absorption spectra of Fig.3.1.2, with the lowest excited state 60meV PLE peak in Fig.3.1.4 we derive an *s*-*p* hole energy of 18meV (30% contribution from the valence band). Performing the same comparison between the $E_1 \rightarrow E_{QW}$ absorption peak at 155meV in Fig.3.1.3 and the 284meV peak in the PLE spectrum in Fig.3.1.4 gives an s-QW hole energy of 129meV (45% contribution from the valence band). From these results the CB:VB offset appears to change for the QD and QW.

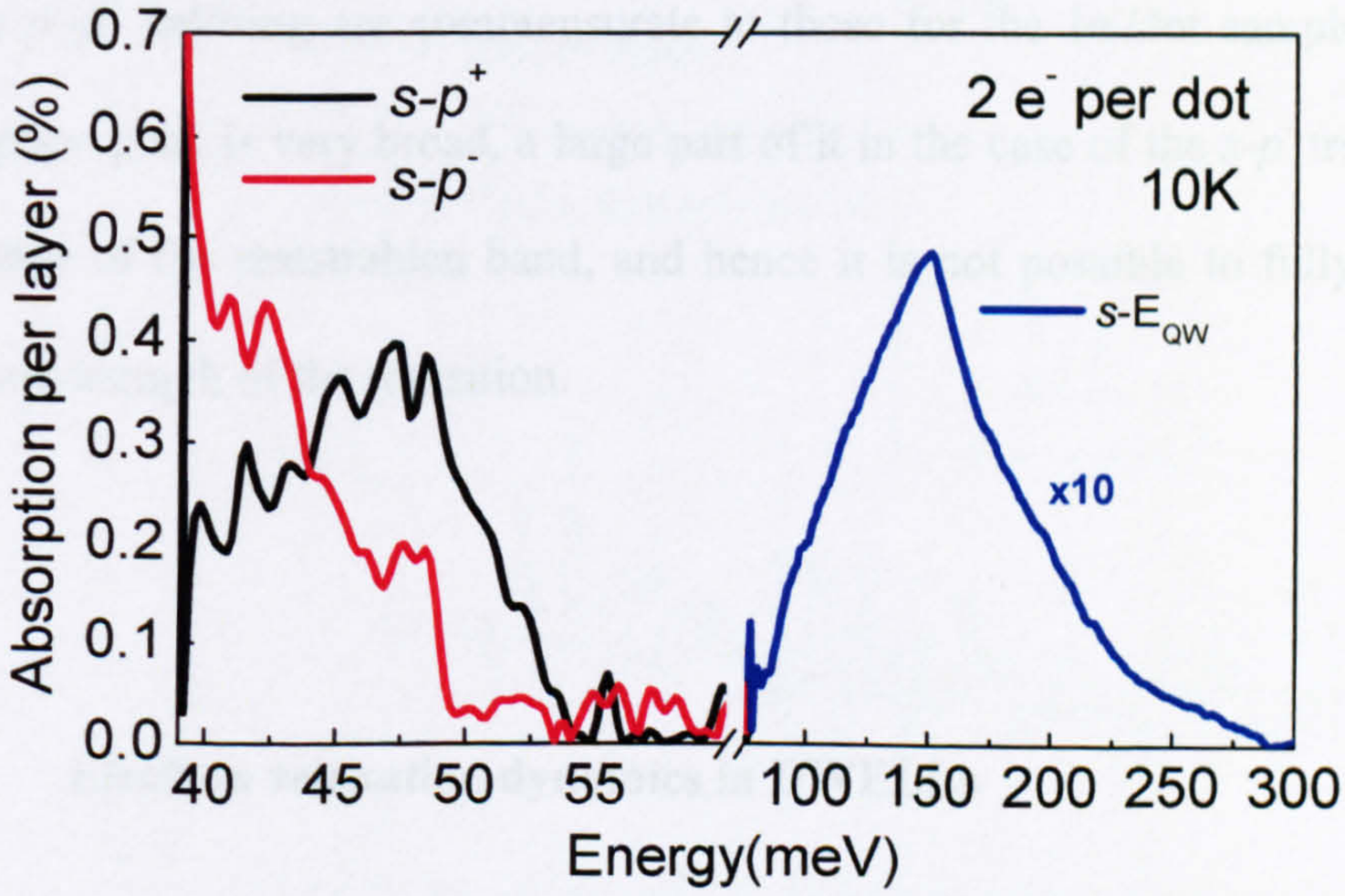

Fig.3.1.5. Intraband absorption spectra for the DWELL sample with 2 e^- per dot. Far-IR, *s*-p^- [011] and *s*-p^+ [0-11] transitions are shown in red and black respectively. The mid-IR absorption per layer for ~10 passes is shown in blue, with $\Delta\lambda/\lambda$~55% at 150meV (8.3μm).

The same measurements were carried out for the sample doped with $2e^-$/dot, and the intraband absorption characteristics were determined. The effect of doping on the absorption characteristics in standard InAs/GaAs QDs with varying doping concentrations has been previously reported [8]. A spectral broadening of the intraband absorption with increasing doping concentrations due to increased inhomogeneous broadening had been observed up to a doping level of $2e^-$/dot, and once this level was exceeded, excited states in the QD became occupied, blocking the *s-p* transition and reducing the photocurrent.

As illustrated in Fig.3.1.5, spectral broadening is observed for both *s-p* and E_1-E_{QW} transitions. As the spectra became broader the integral absorption increased but the peak was similar to the $1e^-$/dot sample. In the case of the *s-p* transition the energies of the p^--p^+ splitting are commensurate to those for the $1e^-$/dot sample, but as the absorption peak is very broad, a large part of it in the case of the *s-p*$^-$ transition is in the range of the reststrahlen band, and hence it is not possible to fully resolve the peak wavelength of the transition.

3.1.3. Electron relaxation dynamics in DWELLs

For the following studies, a degenerate pump-probe technique was employed, using the OPA set-up discussed in chapter 2.5. The transmission change corresponding to the transitions from E_1 to E_{QW} as a function of time delay between the pump and probe pulses is plotted in Fig.3.1.6 (black circles), and the data are fitted by a 2nd

order exponential decay (red dashed line), yielding relaxation times of a short decay of 5±1ps followed by a longer ~150ps decay. The initial short decay time τ_{relax} is attributed to the electron relaxation from the E_{QW} state to the QD ground state (see Fig.3.1.1) whereas the longer decay τ_{cap} indicates a slow thermal re-emission/tunnelling followed by electron capture to adjacent trap states.

It is not possible to determine the nature of the trap states from the present measurements; however they may be adjacent dots or defects. In either of these cases electrons would be able to escape and be captured to these states (E_{trap}) before relaxing back to the ground state, causing a long decay.

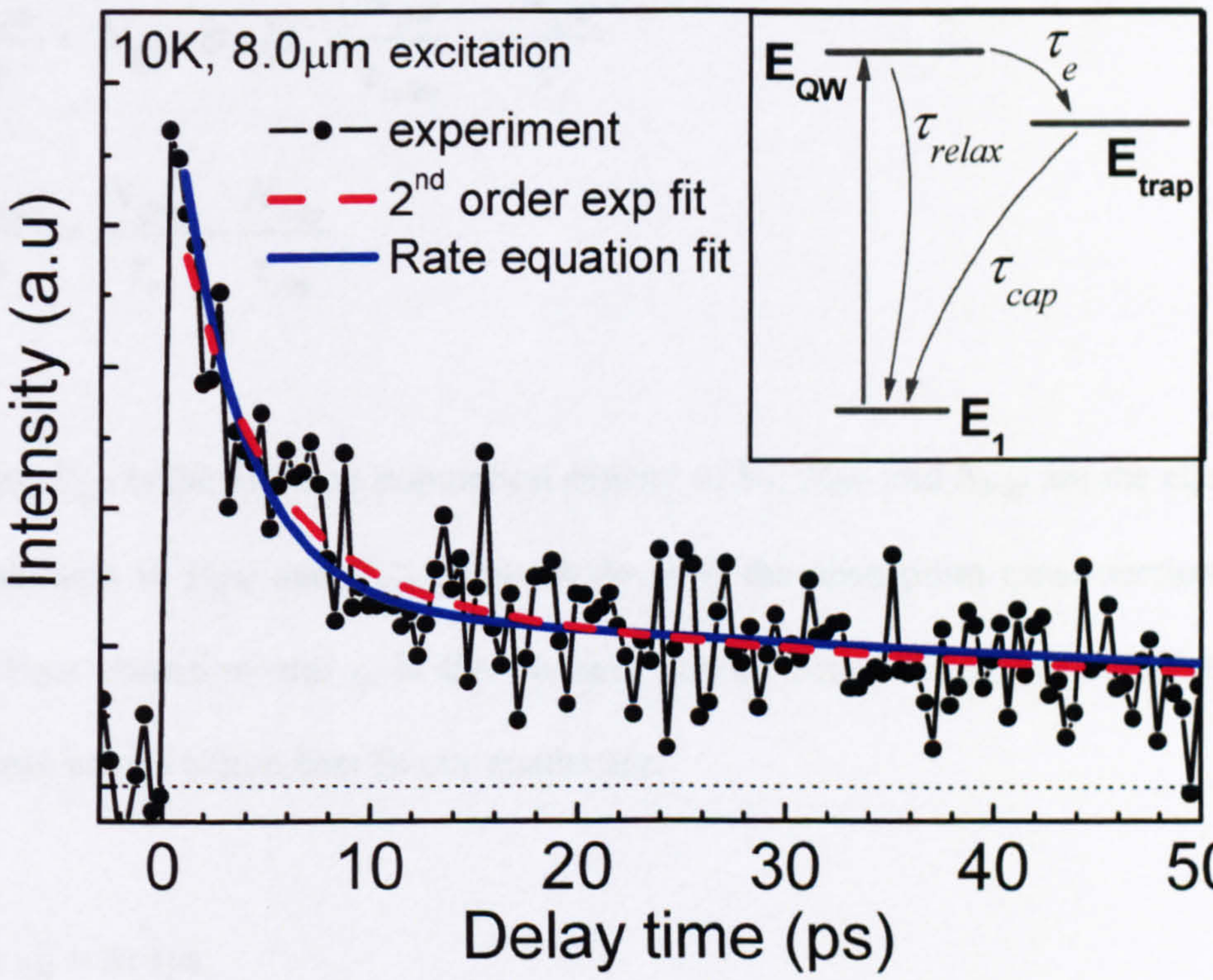

Fig.3.1.6. Intraband electron relaxation at 10K after excitation at 8μm against delay time (black circles). 2nd order exponential fit (red dashed line). The solution to the rate equations gives a good fit (blue solid line), based on a 3-level system (Inset).

Assuming a three level system (Fig.3.1.6, inset), where, the first level is the QD ground state E_1, the second is the QW final state E_{QW} and the intermediate is E_{trap}, rate equations for the transitions between these levels can be used to fit the transmission change as shown in Fig.3.1.6 (blue solid line). This model assumes that electrons are initially excited to the QW state and then either relax back to the ground state (τ_{relax}) or escape from the well (τ_e), and become recaptured by the adjacent trap states (τ_{cap}).

The rate equations which describe the dynamics of these processes are:

$$\frac{dN_{QD}}{dt} = -N_{QD} \cdot \sigma \cdot Ip + \frac{N_{QW}}{\tau_{relax}} + \frac{N_{trap}}{\tau_{cap}} \tag{3.1}$$

$$\frac{dN_{QW}}{dt} = N_{QD} \cdot \sigma \cdot Ip - \frac{N_{QW}}{\tau_{relax}} - \frac{N_{QW}}{\tau_e} \tag{3.2}$$

$$\frac{dN_{trap}}{dt} = \frac{N_{QW}}{\tau_e} - \frac{N_{trap}}{\tau_{cap}} \tag{3.3}$$

Where N_{QD} is the electron population density of E_1, N_{QW} and N_{trap} are the equivalent populations in E_{QW} and E_{trap} respectively, σ is the absorption cross-section of the $E_1 \rightarrow E_{QW}$ transition and I_p is the incident power. From the above calculation the lifetime values which best fit our results are:

(a) $\tau_{relax} = 5 \pm 1$ps

(b) $\tau_e = 9 \pm 2$ps, and

(c) $\tau_{cap} \sim 150$ps and higher

In terms of DWELL detector performance, τ_{relax} and τ_e lifetimes are most relevant as they are closely related to the peak responsivity R_p (for the $E_1 \rightarrow E_{QW}$ transition) as discussed in chapter 1.2. R_p is determined by the lifetimes by:

$$R_p = e \cdot \eta \cdot g_{photo}/h \cdot v, \quad and \quad g_{photo} \propto \tau_{relax}/(\tau_{relax} + \tau_{esc})$$

It should be noted, that τ_{esc} in the above expression is the escape time of carriers contributing to the photocurrent assuming vertical transport in the growth direction (see chapter 1.2, and reference [15]). In equations (3.2) and (3.3) however, τ_e relates to a more complicated process, as lateral transport to adjacent QDs/traps is also involved. In order to accurately determine τ_{esc} in the growth direction, pump-probe measurements under different applied bias could be carried out, which will be the subject of future studies (see chapter 6).

Although τ_{relax} ~5ps is shorter than the early theoretical predictions, it is still longer than the equivalent ~1ps lifetimes in QWIPs (see, chapter 1.2). For efficient QWIP operation, τ_{esc} has to be <<1ps, which makes it necessary to design the final state contributing to the photocurrent very close to the top of the QW, compromising confinement. The 5x longer lifetime measured in QDIPs, indicates the potential of high responsivity devices upon optimisation of the level position in the conduction band.

3.1.4. Summary

This section dealt with the intraband absorption characteristics of InAs/InGaAs DWELL structures for mid-IR and far-IR transitions. DWELL structures have been found to have relatively strong high energy peak absorption compared to InAs/GaAs QDs, while exhibiting very narrow linewidth. Also, complimentary interband and intraband spectroscopic techniques demonstrated the capability of estimating hole quantisation energies in DWELLs or other QD structures. The electron relaxation dynamics in DWELLs were investigated using ultrafast spectroscopy and relaxation times of ~5ps were obtained. All the above studies have enabled the probing of the CB and VB of DWELLs, resulting in an experimental demonstration of the optical transitions involved in the operation of DWELL based devices.

3.2. Design approaches and their effect on the performance of DWELL QDIPs

3.2.1. Introduction

In this section the polarisation dependence of DWELL QDIPs is initially discussed, in order to demonstrate that, although DWELL QDIPs are sensitive to normal incidence, a stronger response was observed for radiation polarised in the growth direction. The following parts of this section concentrate on the effects of different design alterations of the DWELL configuration on the performance. It had been previously reported that the photoresponse can be tailored by changing the quantum well thickness [16]. Also, there have been studies on the effects of doping on QD structures and detectors [8,17]. The latter is very important in order to optimise the performance of a detector structure, whereas the former provides a useful tool for specifying the wavelength range prior to growth. In addition, the effects of the number of InAs monolayers deposited during growth (N_{ML}), on detector performance are demonstrated. Furthermore, the effects of doping on the spectral response and dark current are illustrated.

3.2.2. Photocurrent in DWELL QDIPs and polarisation dependence

The spectral dependence of a DWELL QDIP on applied bias is shown in Fig 3.2.1. This behaviour is observed for all the structures discussed in this chapter. Two photocurrent peaks centred at ~130 meV (λ~9μm) and ~230 meV (λ~5μm) are observed (exact peak wavelength varying from sample to sample), arising from electron transitions from the InAs QD ground state E_1 to states in the $In_xGa_{1-x}As$ QW state, denoted as E_{QW}, and GaAs continuum states denoted as E_{cont} respectively. The $E_1 \rightarrow E_{QW}$ photoresponse correlates well with the narrow high energy absorption of Fig.3.1.3 in the previous section.

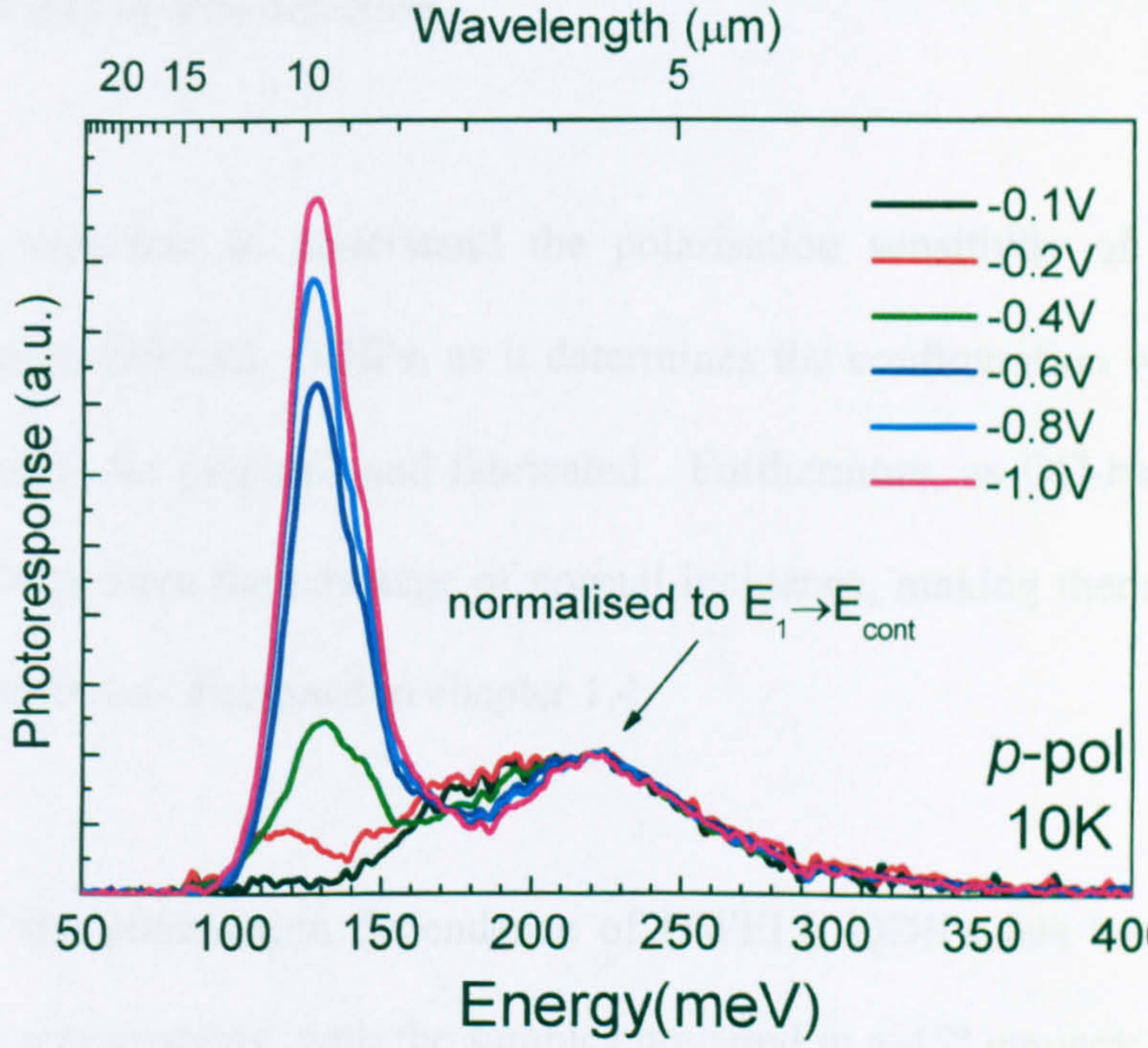

Fig.3.2.1. Bias dependence of the intensity of the $E_1 \rightarrow E_{QW}$ transition for a DWELL QDIP sample. The $E_1 \rightarrow E_{QW}$ photocurrent is suppressed at low biases, and increases faster with bias relative to the $E_1 \rightarrow E_{cont}$ (normalised)

The magnitude of the $E_1 \rightarrow E_{QW}$ and $E_1 \rightarrow E_{cont}$ peaks increases with applied bias. However, the $E_1 \rightarrow E_{QW}$ photocurrent increases more rapidly and becomes dominant for biases $\geq \pm 0.6$V. Fig.3.2.1. shows the spectral dependence of the 2.2ML sample on applied bias, in the negative range. The data are normalised to the $E_1 \rightarrow E_{cont}$ transition. Near zero bias only transitions to states in the continuum are evident due to the low probability of electrons escaping from the QW. As the applied electric field is increased, the escape probability increases, and the $E_1 \rightarrow E_{QW}$ transition becomes stronger until it dominates the spectra at higher biases. This chapter concentrates on the characteristics of mainly the $E_1 \rightarrow E_{QW}$ photocurrent, as it is the main spectral feature which determines the operation of the photodetector. However the $E_1 \rightarrow E_{cont}$ photocurrent could be useful in application requiring dual-band LWIR and MWIR detection.

It is very important to understand the polarisation sensitivity of the $E_1 \rightarrow E_{QW}$ photocurrent in DWELL QDIPs, as it determines the configuration with which the devices need to be prepared and fabricated. Furthermore, as QD-based detectors, they potentially have the advatage of normal incidence, making them attractive for FPA applications as discussed in chapter 1.4.

A study of the polarisation dependence of DWELL QDIPs has been carried out using FTIR spectroscopy, with the samples prepared in a 45° geometry with respect to the plane of the dots, as can be seen in Fig.3.2.2, and discussed previously in chapter 2.1.

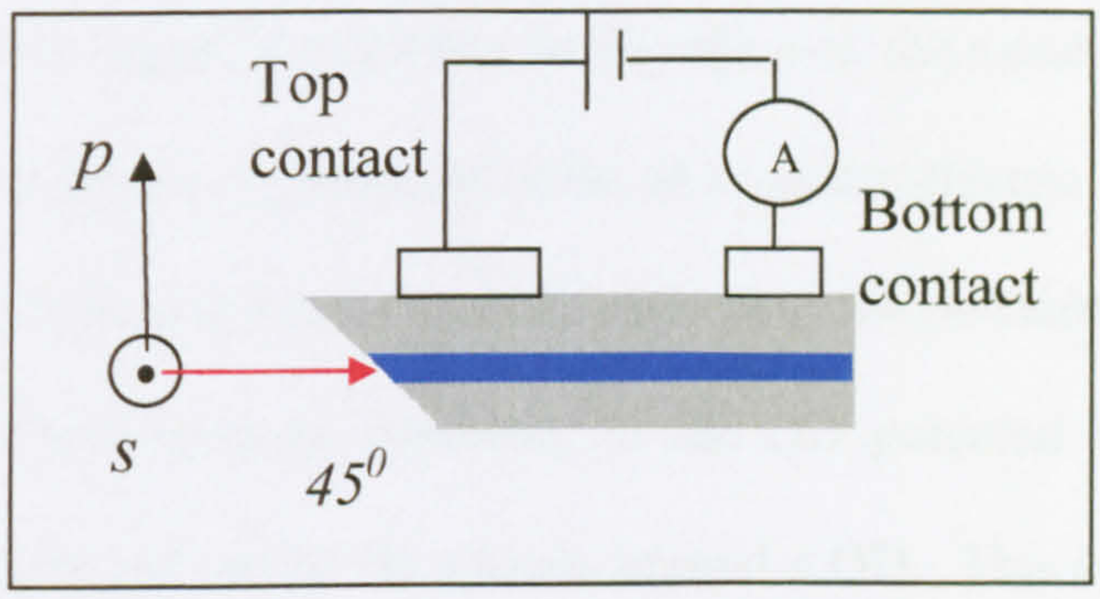

Fig 3.2.2. 45° polished sample for polarisation dependence measurements

As described in the previous section on absorption studies, the transitions which occur at higher energies are not bound to bound transitions within the dot, but are attributed to transitions from the QD ground state to quasi-bound states in the QW, and in the continuum. These transitions have been found to be strongly *p*-polarised (Fig.3.2.3) as the incident light has an electrical field component parallel the growth direction.

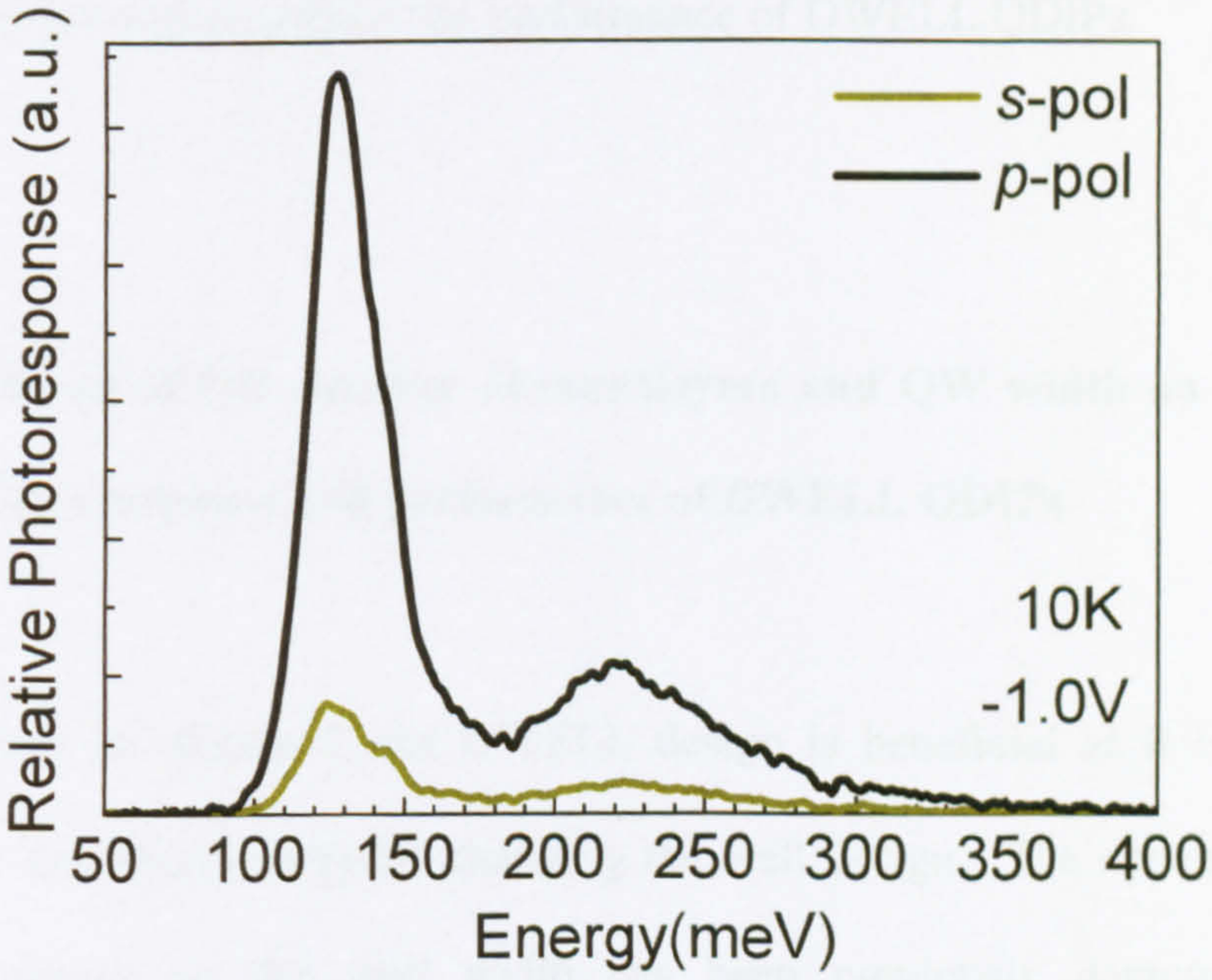

Fig.3.2.3. polarisation dependence of DWELL showing a stronger *p*-polarisation compared to *s*-polarised incidence

However, a weaker signal is observed for $E_1 \rightarrow E_{QW}$ at the same wavelength, even when the incident light is *s*-polarised (with an in-plane electric field component). This indicates a more complicated picture regarding the polarisation sensitivity of the QW state, which could be attributed to the QD potential affecting the QW wavefunction in QW regions in the vicinity around a QD. This could hybridise the polarisation of the QW state making it sensitive to multi-angle incidence. This suggests that although the *p*-polarised photocurrent is ~5xhigher, DWELL detectors are still capable of normal incidence detection.

The configuration required for NI detection is much simpler to fabricate, and even though the photoresponse would be higher if the devices were polished at 45° waveguide geometry, in many occasions in the following chapters devices have been fabricated for normal incidence as the photoresponse and general performance is adequate to make comparisons and draw conclusions regarding various effects of DWELL design and growth on the performance of DWELL QDIPs.

3.2.3. Effects of QD number of monolayers and QW width on the spectral photoresponse and performance of DWELL QDIPs

As mentioned in chapter 1, the DWELL design is beneficial as it is possible to control the transition energy by changing the well design. The dependence of the transition energy on the well width has been previously demonstrated [16]. However, changing the QW width has some drawbacks. In particular, an increase of

the QW width leads to deeper confinement of the final photocurrent state, hence less probable electron escape and a consequent decrease of the responsivity. Furthermore, a device containing wider InGaAs QWs may suffer from strain induced dislocation formation due to the increased amount of indium in the structure, while a decrease in the composition could increase the transition energies out of the desired atmospheric window, as well as affecting the linewidth and strength of the photoresponse. Finally it has been shown that variations in the well width can not be purely responsible for the shifts reported in the literature as they are followed by unintentional changes in the dot dimensions [18]. In this section the ability to control the operating wavelength by varying the numbers of monolayers deposited during the growth of the QDs (N_{ML}) as well as varying the QW width are discussed.

In table 3.1 below, a summary of the samples that are discussed in this section is illustrated along with the parameters that were altered.

Table.3.1. Summary of DWELL QDIP sample designs investigated

Sample no	N_{ML}	Doping (e/dot)	QW width (Å)	QW indium concentration (x)	Number of periods
vn189	2.9	1	80	0.15	5
vn190	2.55	1	80	0.15	5
vn191	2.2	1	80	0.15	5
vn192	2.2	2	80	0.15	5
vn193	2.55	2	80	0.15	5
vn194	2.9	2	80	0.15	5
vn195*	2.55	1	80	0.15	5
vn356	2.55	1	80	0.15	5
vn357	2.55	1	100	0.15	5
vn358	2.55	1	130	0.1	5
vn406	2.55	0	80	0.15	5
*Si-delta doping place on top of dots					

The first set of samples were grown with different N_{ML} of InAs (N_{ML}=2.2, 2.55 or 2.9) for two different doping concentrations. The device structures incorporate a bottom contact layer of 4000Å *n*+ Si doped GaAs, 5 periods of DWELL absorbing region, separated by 500Å of undoped GaAs and a final 4000Å *n*+ Si doped GaAs contact layer.

The DWELL absorbing region for the first set of samples (vn189-vn195) consists of InAs dots placed within an 80Å $In_{0.15}Ga_{0.85}As$ quantum well, with 10Å of the well below the dots and 70Å above. The active regions are doped to approximately 1 electron per dot (e^-/dot) for samples vn189-vn191 and 2e^-/dot for samples vn192-vn194. Also, for sample vn195 the position of the Si-delta doping is again in the GaAs barrier but at the bottom of the barrier just above each DWELL layer. The CB diagram of a typical DWELL structure was previously shown in Fig 3.1.1 in the first section of this chapter.

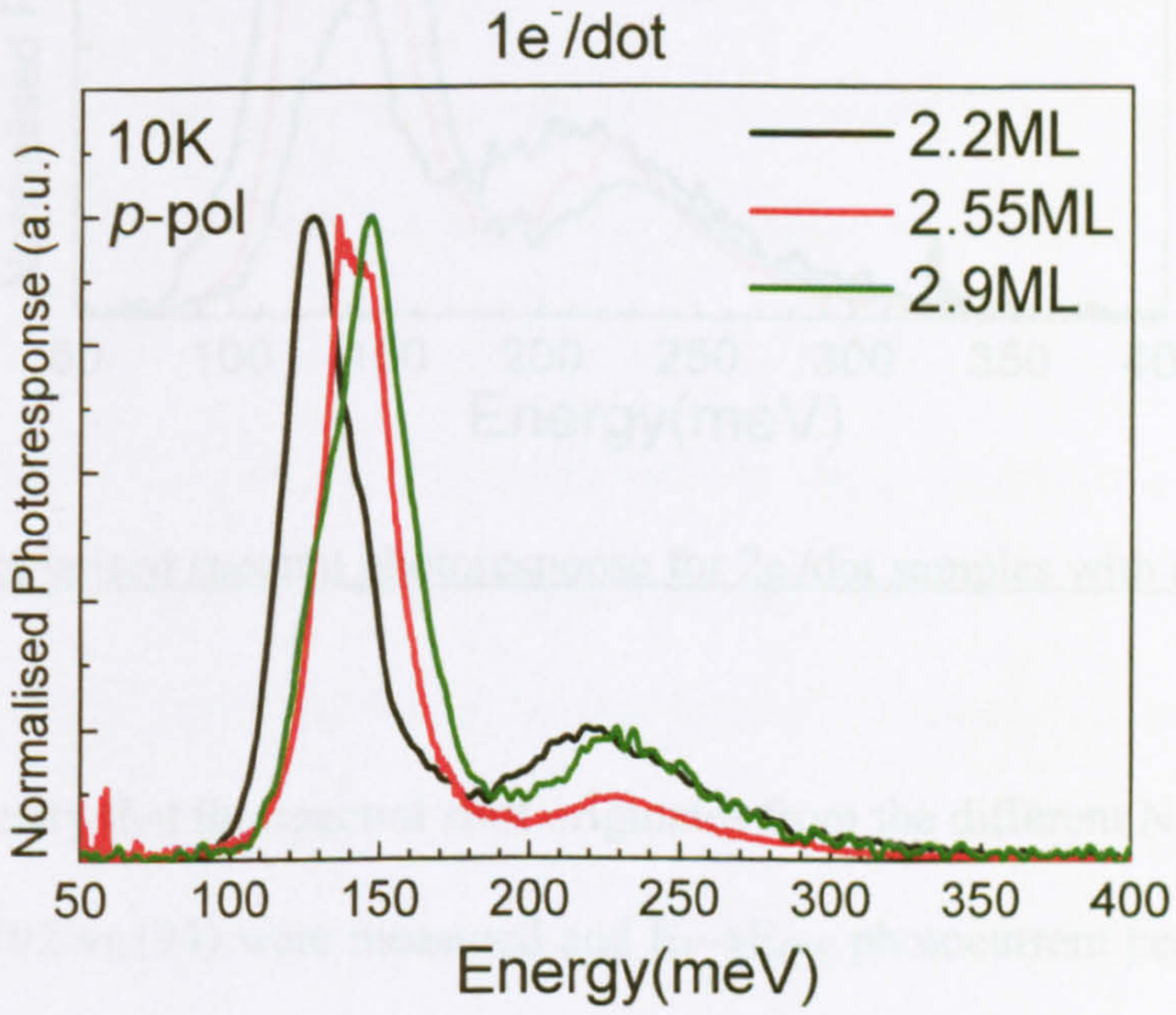

Fig.3.2.4. *p*-polarised spectral photoresponse for 1e^-/dot samples with different N_{ML}

The 10K *p*-polarised spectral photoresponse for the DWELL QDIP samples with $1e^-$ /dot and different number of N_{ML} is shown in Fig 3.2.4 for the same applied bias (-1V). By varying N_{ML} from 2.2 to 2.9, a significant blue-shift (~15%) of the $E_1 \rightarrow E_{QW}$ peak (Fig.3.2.3) from 126meV (N_{ML}=2.2) to 146meV (N_{ML}=2.9) is observed, due to the increased localization of the QD ground state with increasing QD size. The 2.55ML sample has a very similar peak energy position to the 2.9ML indicating a non-linear dependence of the size on number of ML. Nevertheless, such behaviour could provide additional freedom during the design stage of the DWELL QDIP.

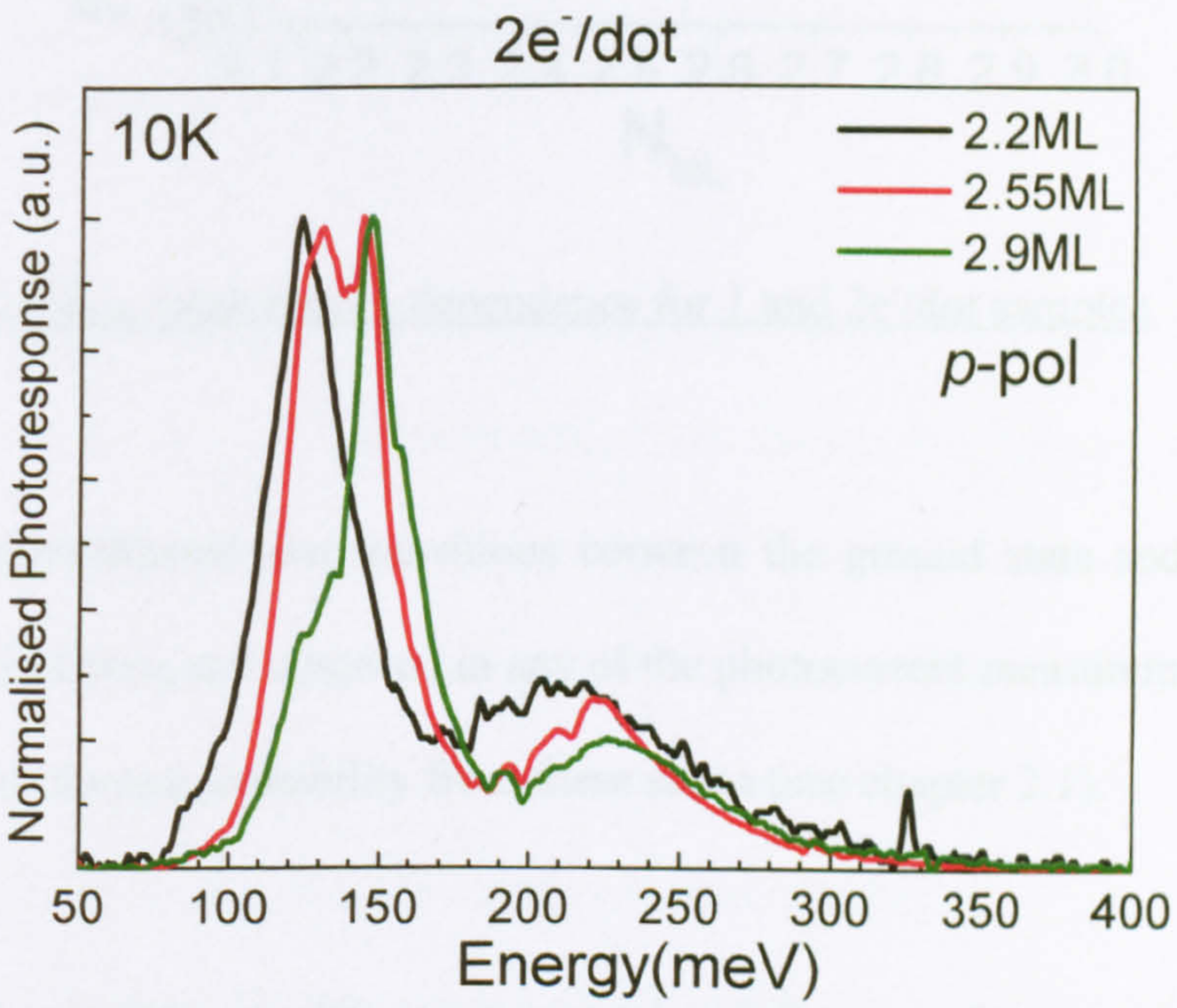

Fig.3.2.5. *p*-polarised spectral photoresponse for $2e^-$/dot samples with different N_{ML}

In order to verify that the spectral shift originates from the different N_{ML}, the $2e^-$/dot samples (vn192-vn194) were measured and $E_1 \rightarrow E_{QW}$ photocurrent peak energies of 125meV and 147meV for N_{ML}=2.2 and 2.9 were observed, respectively, as shown in

Fig.3.2.5. The trend seems to be similar for both sets of samples (see Fig.3.2.6), which confirms the interpretation of the effect of N_{ML} on the spectral tuning of the photocurrent, ruling out error due to small variations in the growth.

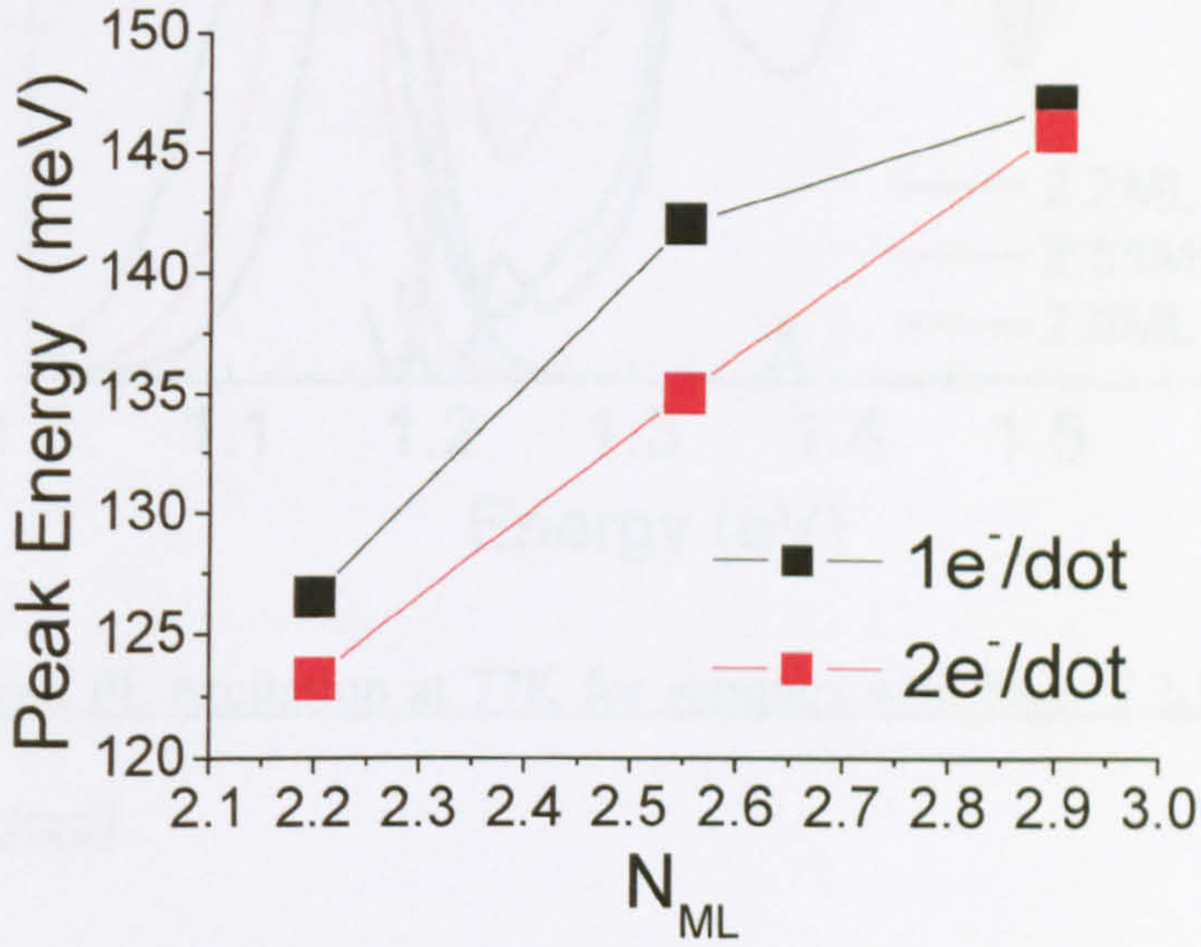

Fig.3.2.6. $E_1 \rightarrow E_{QW}$ peak energy dependence for 1 and $2e^-$/dot samples

It should be mentioned that transitions between the ground state and *d*- or *f*-like states in the dot were not observed in any of the photocurrent measurements. This is due to the low escape probability from these states (see chapter 2.1).

The PL of the $1e^-$/dot samples was measured and the ground state shifted to lower energy with increasing N_{ML}, shown in Fig.3.2.7. PLE measurements we also carried out and the peaks corresponding to the first excited state and E_{QW} are indicated in Fig.3.2.7.

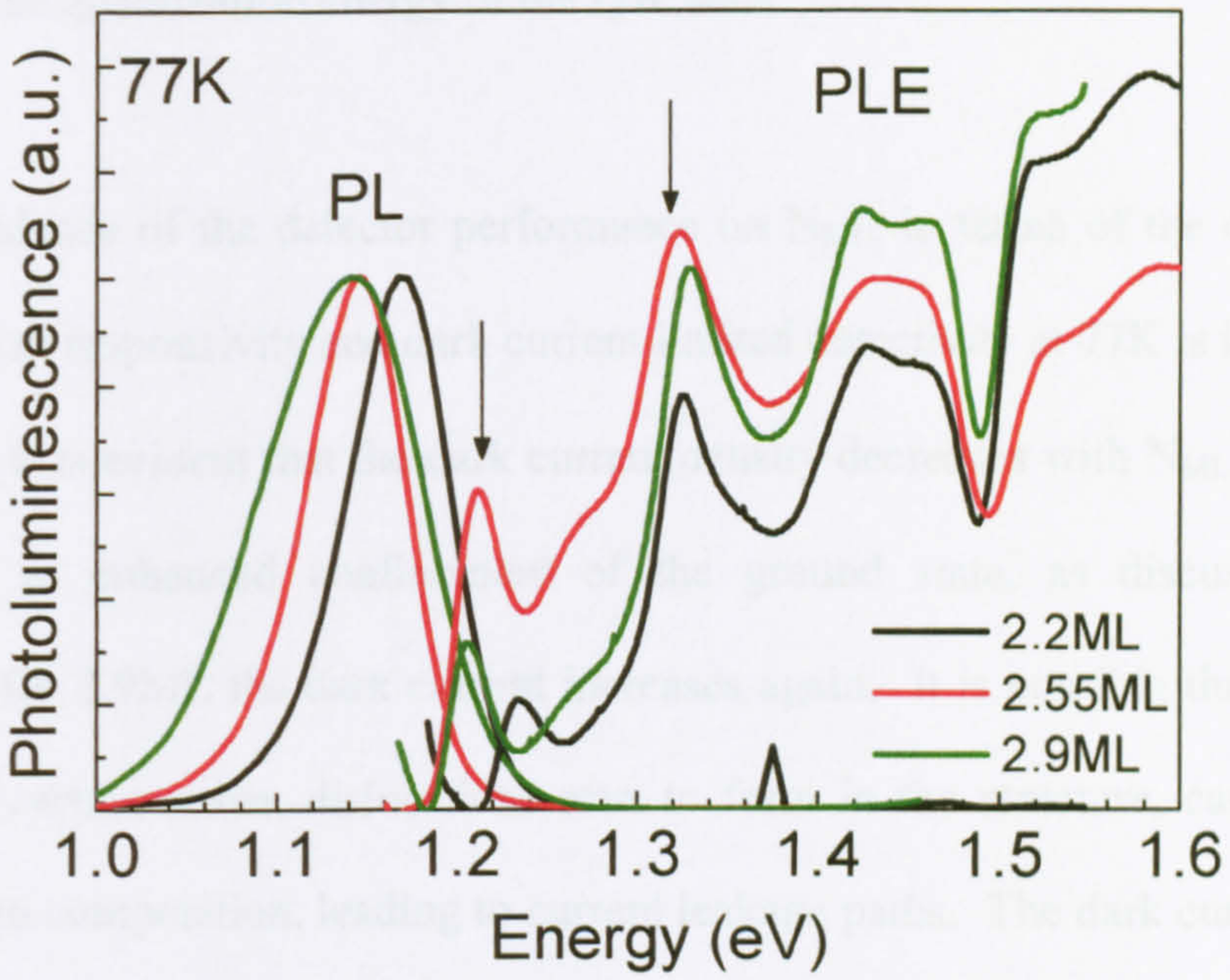

Fig.3.2.7. PL and PL excitation at 77K for samples with N_{ML}=2.2(black), 2.55ML (red) and 2.9(green)

It is evident from these results that the energy separation between ground state and E_{QW} increases with N_{ML}, in good agreement with the intraband photocurrent spectra. Of note is also that the PL peaks of the 2.55ML and 2.9ML samples are same in energy, while the latter shows a broader PL spectrum. The similar peak position correlates with intraband photocurrent results shown above, while the enhanced FWHM could be due to enhanced inhomogeneous broadening, caused by changes in the size distribution of the dots, when a certain value of N_{ML} is exceeded.

What is also interesting from Fig.3.2.7 is that the increasing N_{ML} has a more pronounced effect on the QD ground and first excited state peaks but does not seem to affect significantly the higher energy peaks attributed to the QW. This indicates that changes in N_{ML} mainly affect the QD dimensions and do not significantly

influence the quantization energy of the QW state.

The dependence of the detector performance on N_{ML}, in terms of the dark current density, peak responsivity and dark current limited detectivity at 77K is illustrated in Fig.3.2.8. It is evident that the dark current density decreases with N_{ML} from 2.2 to 2.55, due to enhanced confinement of the ground state, as discussed above. However, for 2.9ML the dark current increases again. It is possible that once N_{ML} exceeds a certain value, dislocations start to form in the structure, caused by the increased In composition, leading to current leakage paths. The dark current as well as the responsivity was measured for 11 devices for each sample, to ensure this was consistent across each wafer and the curves presented below are averaged over 11 mesas.

In the case of the peak responsivity, it seems the trend is the same as for the dark current. Although for N_{ML}=2.2, R_p is the highest for a lower operating voltage range, the highest detectivity, is calculated for N_{ML}=2.55, since the dark current for the former is higher. The above results yielded that for the InAs/InGaAs system and our current growth conditions, N_{ML}=2.55 was optimum with a detectivity of $D^*= 2x10^9 cmHz^{1/2}W^{-1}$ at 77K and -1.0V, in a wavelength range of 8-10μm.

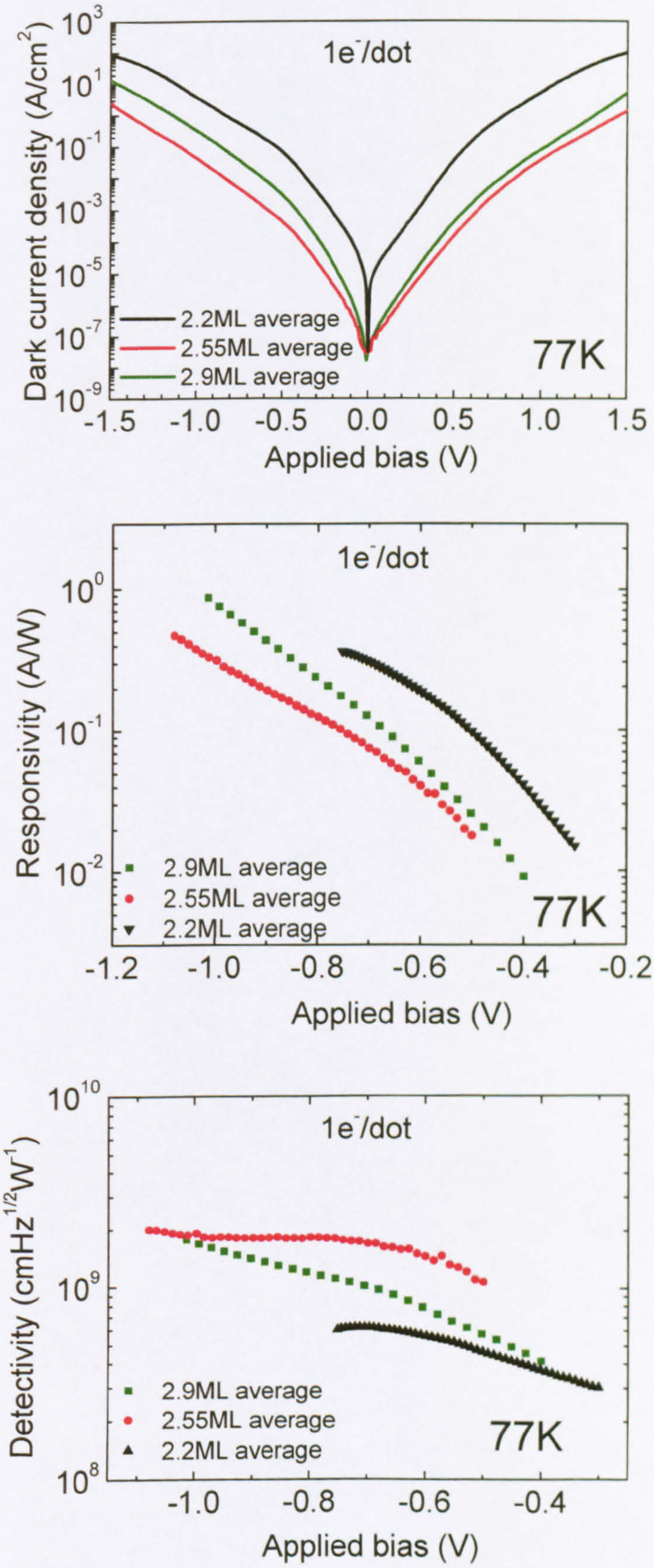

Fig.3.2.8. Detector Performance for samples with different number of ML for 1e per dot (left) and 2 e per dot (right)

- *Well Width Variation*

Three samples (vn356, vn357 and vn358 on table. 3.1) were grown with different well widths by increasing the InGaAs thickness grown on top of the dots which lies above the dot layer in the growth direction, whilst keeping all other parameters the same within this set, with the exception of the 10-120Å sample (vn358), where the In composition of the well was reduced to 10% to compensate for the strain introduced when growing such a thick layer of InGaAs. The reduction in transition energy as the well width increases from 70 to 90Å is small but evident (Fig.3.2.9).

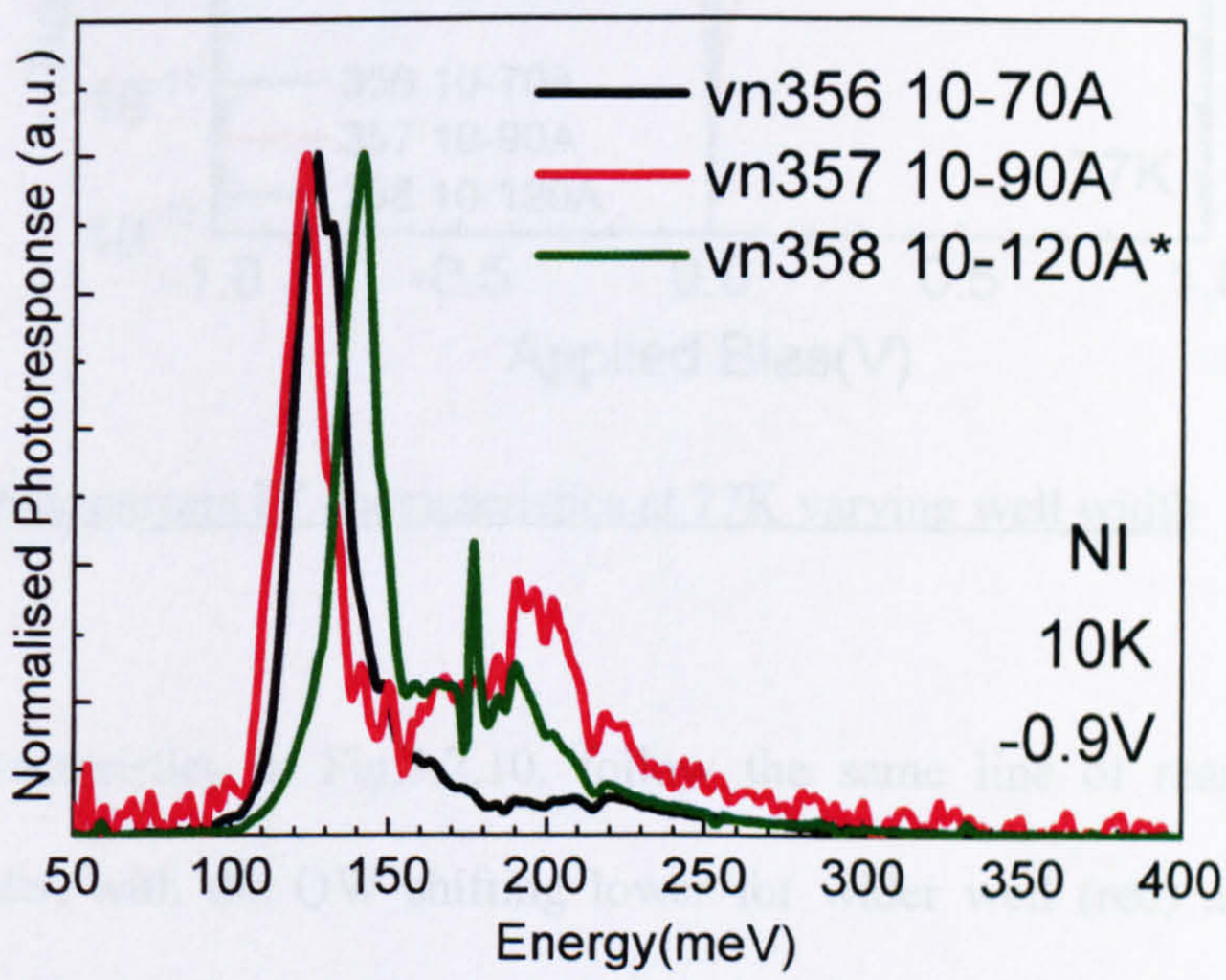

Fig.3.2.9. Well width spectral dependence of DWELL QDIP. *10% Indium

Fig.3.2.9. illustrates the spectral dependence of samples with different dimensions of the QW embedding the dots. Although with increasing well width the energy of the $E_1 \rightarrow E_{QW}$ transition would in principle decrease, the opposite is observed for the sample with the 130Å QW (vn358). The reduced In composition causes a shallower

confinement potential of the QW states, and hence the QW states shift to higher energy. It is therefore possible to assume that the reduction of In composition has a stronger effect on the energy of $E_1 \rightarrow E_{QW}$ compared to the well thickness. However the effects could be more complicated as it has been reported that the In content in the QW affects the nucleation of the InAs dots in DWELLs [11].

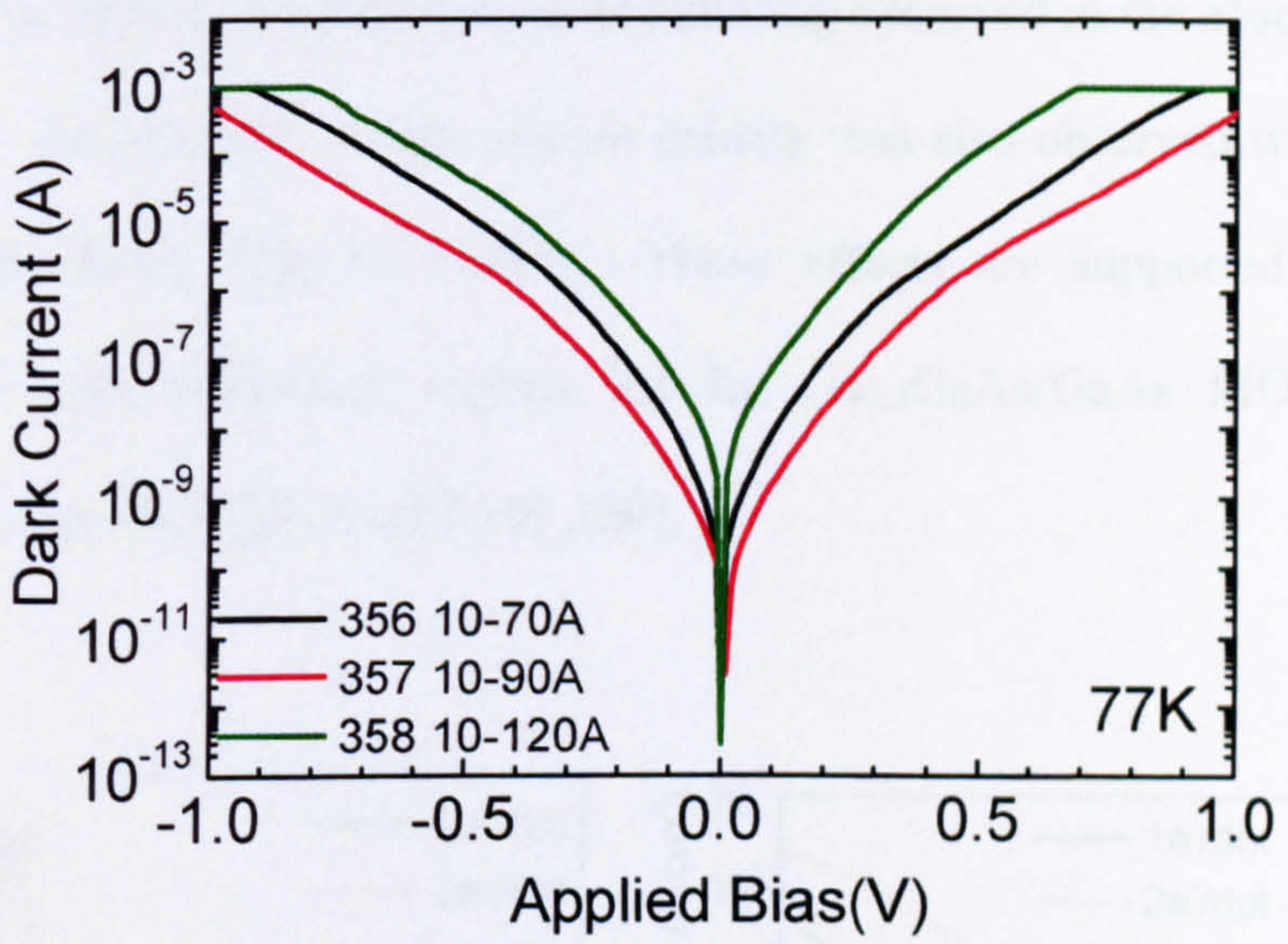

Fig.3.2.10. Dark current IV characteristics at 77K varying well width

The IV characteristics in Fig.3.2.10. follow the same line of reasoning as the spectral results, with the QW shifting lower for wider well (red) and higher for smaller % of In (green) with respect to the top of the well, decreasing or increasing thermionic emission respectively. These samples were grown in a different growth run and were found to have an inferior dark current performance due to the lack of temperature control during growth. This lack of control occurred as the new structures (vn356, vn357, and vn358) were grown on a double polished substrate which at the time, had not been optimised for this type of structures.

3.2.4. Effect of doping

As mentioned above, samples with 2 electrons per dot were grown, in all other aspects identical to the $1e^-$/dot samples. The effect of doubling the doping concentration was evident in a broadening of the spectral photoresponse for samples with otherwise similar growth parameters, as shown in Fig.3.2.11.(a), which corresponds to similar inhomogeneous broadening observed in the absorption results in Fig.3.1.5. An increase in dark current density was also observed with increasing doping concentration (Fig.3.2.11.(b)). These effects are supported by previous experimental and theoretical reports for $In_{0.5}Ga_{0.5}GaAs/GaAs$ MOCVD grown QDIPs [19], and other QDIPs [17,19] ,[20].

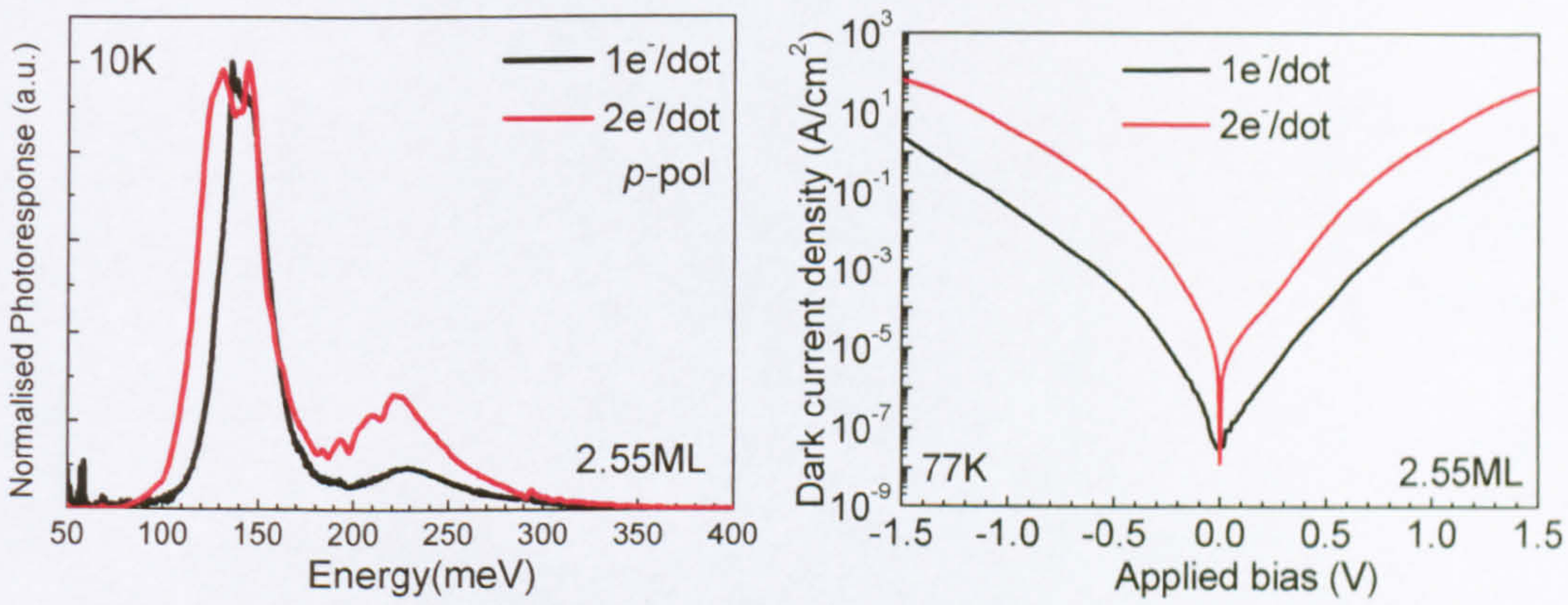

Fig.3.2.11. (a) Spectra at 10K for 1 and 2 electron per dot for 2.55ML and (b) comparison of IV dark current density at 77K for 1 and 2 electrons per dot

A sample with the doping introduced above the dot layer was grown (vn195) to investigate possible effects of doping position on dot nucleation. However there did not seem to be a very strong dependence of the doping position, since the values were comparable with the previous 2.55ML sample (vn190), albeit with slightly

higher dark current. Therefore it was considered adequate to insert the doping below the dots as before.

An undoped sample was also grown (vn406), with an otherwise identical design to vn190 (1e^-/dot, 2.55ML etc). QDIPs with undoped active regions have been demonstrated with low dark currents and good performance, whereby the carriers are introduced from the doped contacts and background doping [21]. Although this sample showed a lower dark current, as would be expected, it was grown using slightly different conditions and therefore was difficult to make a direct comparison with the 1e^-/dot sample (vn190). It was demonstrated however that good performance could be achieved from DWELL QDIPs with undoped active region, with responsivity of ~1A/W, and D^* in the order of 10^9cmHz$^{1/2}$W^{-1} at~8μm.

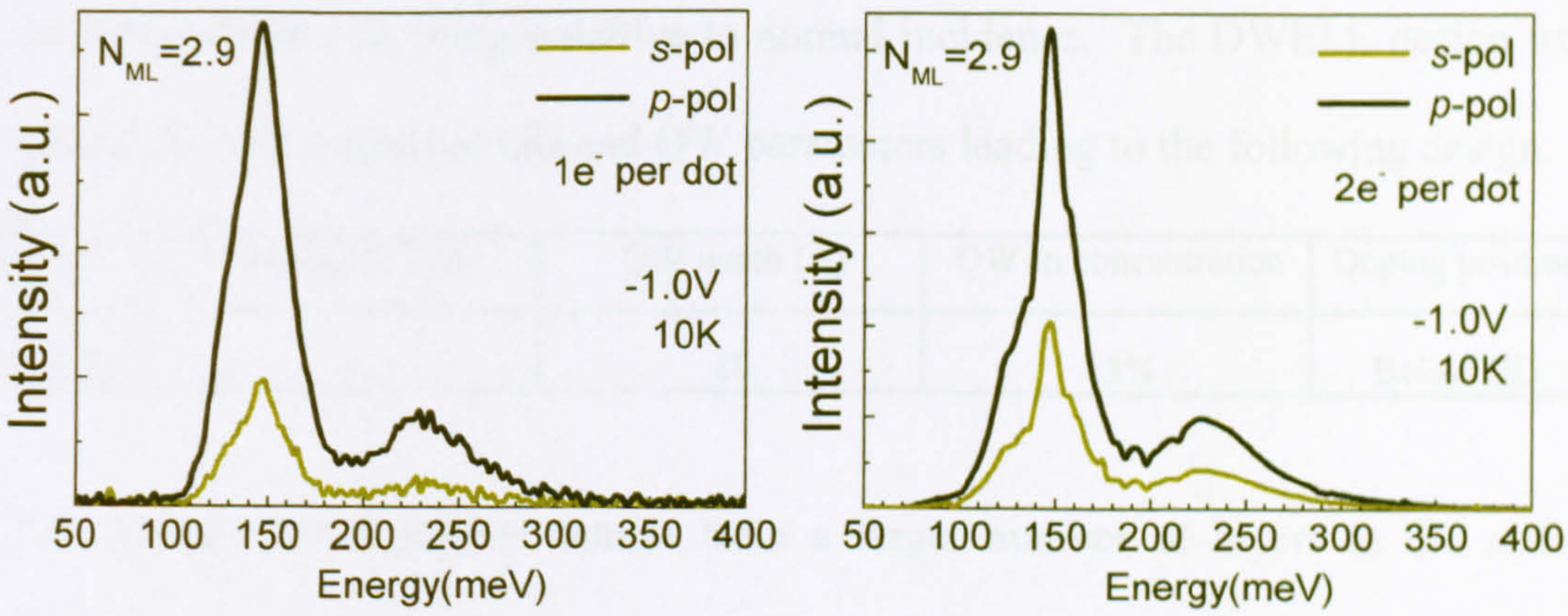

Fig.3.2.12. Polarisation dependence of two different samples with different doping concentrations (1 and 2e^-/dot) at-1.0V and 10K

The *s*- and *p*-polarised responses for the samples with N_{ML}=2.9, with 1 and 2 electrons per dot were compared as shown in Fig.3.2.12, and the results indicate that

the detector normal incidence sensitivity increases with respect to the 45° waveguide incidence, with increasing doping concentration. However, as mentioned previously, increasing the doping can be detrimental to other aspects of detector performance such as the dark current. Previous reports [22] have also shown a polarisation sensitivity of QDIP photoresponse on doping concentration. This behaviour was attributed to the dependence of the scattering processes strongly contributing to the photocurrent, on the doping concentration.

3.2.5. Summary

The performance of DWELL QDIPs has been experimentally investigated, and it was found that these devices have a stronger *p*-polarised photoresponse in the LWIR window, whilst still being sensitive to normal incidence. The DWELL design was optimised with respect to QD and QW parameters leading to the following design.

N_{ML}	Doping (e/dot)	QW width (Å)	QW In concentration	Doping position
2.55	1	80	15%	Below QD

This design would further benefit from a larger number of layers in the active region, and as will be seen in section 3.4, a detector with the above parameters and a 10 layer active region was grown, and exhibited very high performance. The above analysis would become more comprehensive if structural methods such as cross sectional transmission electron microscopy (X-TEM), or cross sectional scanning tunnelling microscopy (X-STM) were employed to observe the effects of the N_{ML} deposited during growth.

3.3. Stark shift of the spectral photoresponse in DWELL QDIPs

3.3.1. Introduction

The development of QDIPs with a detection wavelength which can be Stark-shifted with an external bias would offer further benefits such as the ability to tune the peak wavelength of the photoresponse within one infrared (IR) atmospheric window or between two IR atmospheric windows, as previously demonstrated for QWIP devices [23, 24, 25]. Stark shifts of ~10meV for *interband* transitions in QDs have previously been reported [26], however relatively large fields of ~300kV/cm were necessary to observe these effects. For typical QDIP structures one order of magnitude smaller electric fields are typically used which makes it difficult to observe and utilize the *intraband* Stark shift.

As discussed in the previous sections, mid-infrared intraband absorption transitions involving higher energy states are strongest for radiation polarised in the growth direction (z) due to the much larger QD dimensions in the lateral direction than in the growth direction. A significant Stark effect for these transitions is possible if there is a large z-component of the dipole moment, i.e. if there is a difference of the z-coordinate of the centroids of the two states. As QD heights are small (a few nanometres), this difference becomes small as well. DWELL structures are more suitable for observing the Stark shift than conventional quantum dot structures, since the difference between the centroids of the two electron states, is increased by

the displacement of the excited state by embedding the dot in the well. In order for this effect to be efficient the excited state should be above the quantum well confinement potential.

3.3.2. Experimental results

In Fig.3.3.1 below, the bias dependent *p*-polarised photoresponse of the sample with 2.2ML and $1e^-$/dot is illustrated. The same bias dependence is observed for the equivalent sample with $2e^-$/dot. As shown in Fig.3.3.1 the $E_1 \rightarrow E_{QW}$ peak was found to be tunable with applied bias. The observed photocurrent spectrum at +1V was red-shifted with respect to that at -1V, thus indicating an asymmetric dependence with applied bias due to the off-centre position of the QD layer in the well.

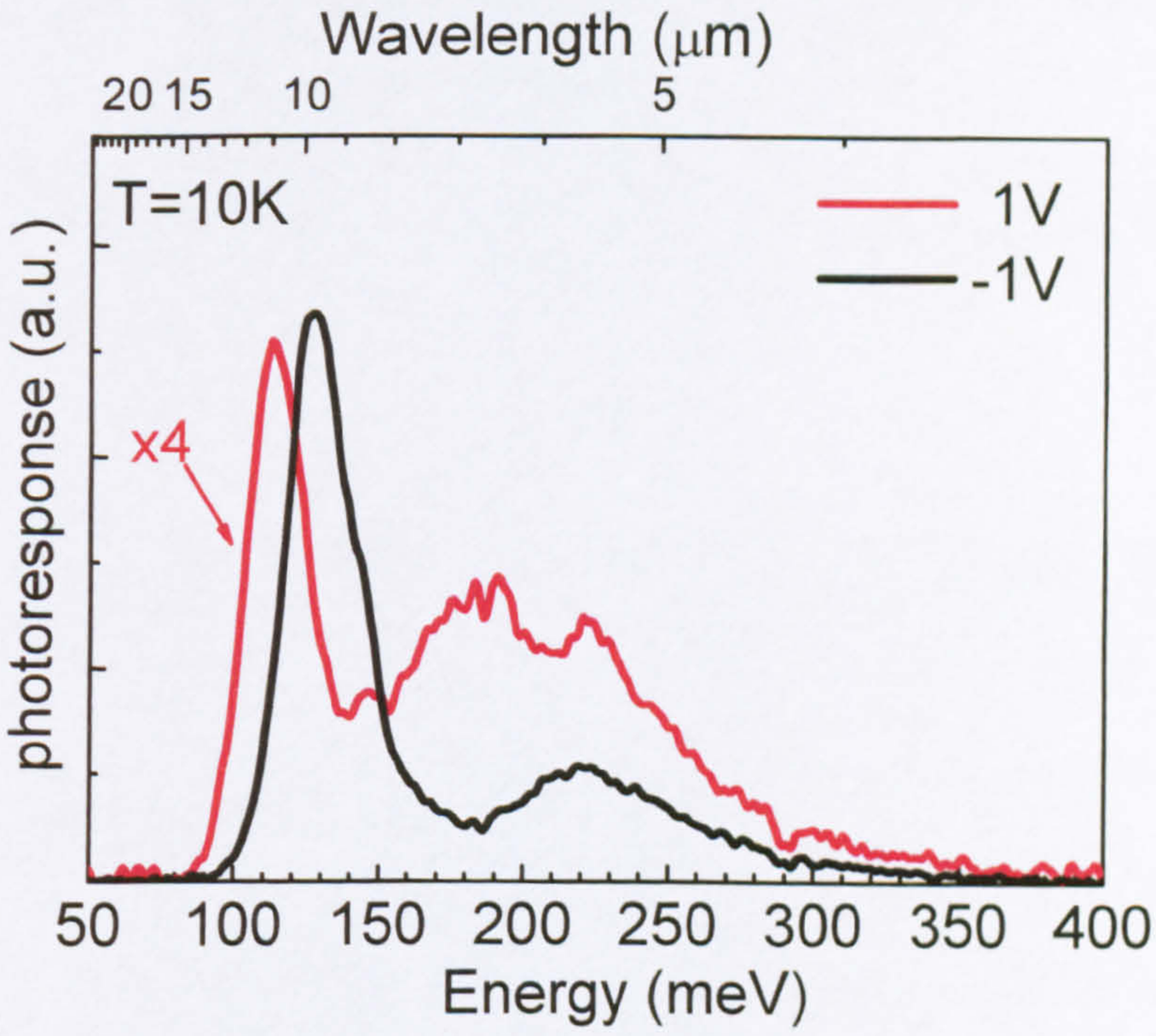

Fig 3.3.1. *p*-polarised photoresponse for QDIP at 10K at +1V (black line), –1V (red line) and 0V (blue line), for 2.2ML(left)

The sample with 2.9ML showed a larger shift between -1.0V and 1.0V, as shown in Fig.3.3.2. The same shift was also observed for the $2e^-$/dot samples following the same increasing trend with N_{ML}.

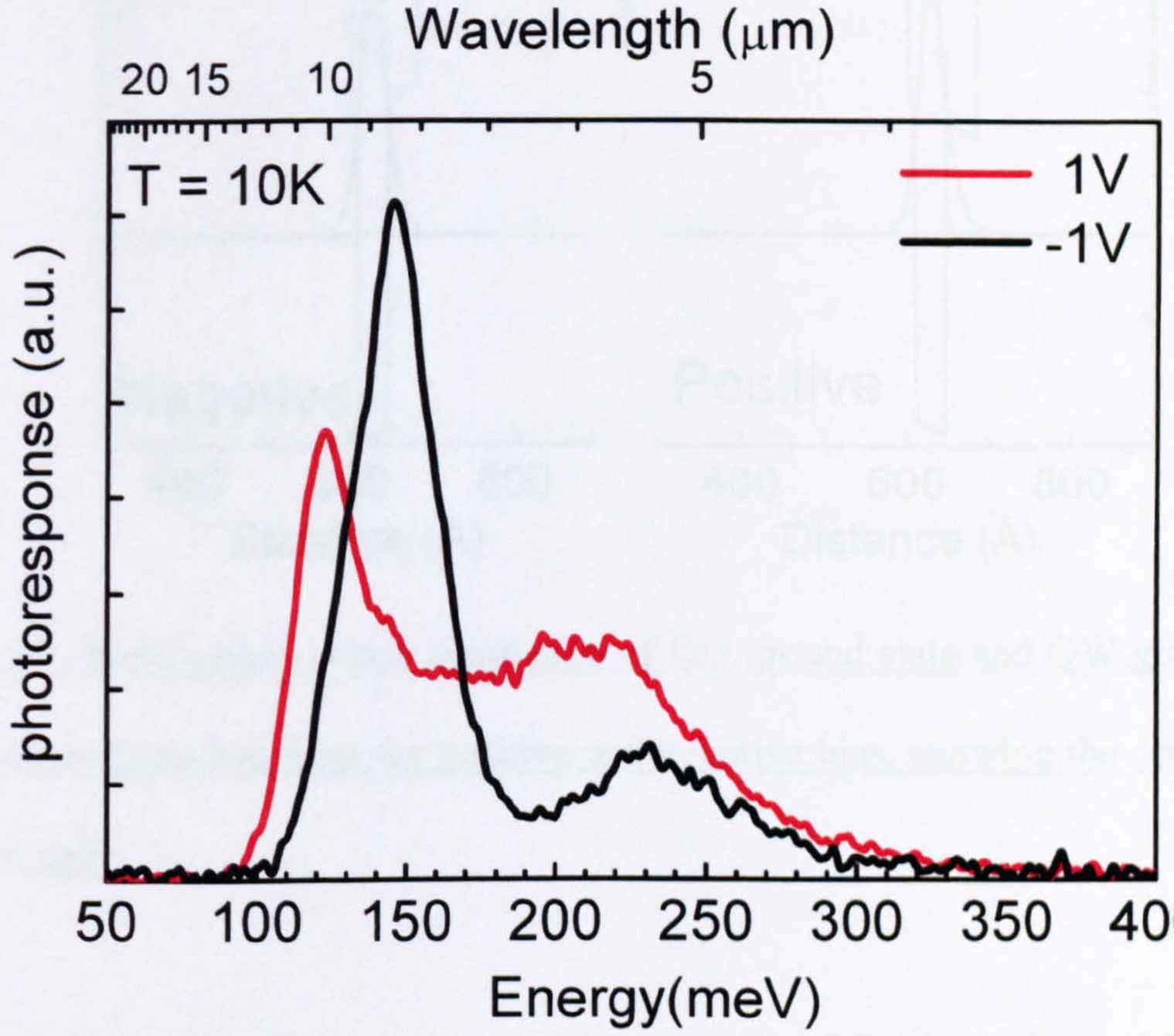

Fig.3.3.2. *p*-polarised photoresponse for QDIP at 10K at +1V (black line), –1V (red line) for 2.9ML

In order to study the shift of the QD wavefunction and interpret the above experimental observations a well-within-a-well model was initially used. In this model the QD layer was approximated using a narrow InGaAs QW (Fig. 3.3.2). This model is a satisfactory assumption to simulate the basic principle of the bias dependence of a transition between two confined levels in an asymmetric structure. Since the applied electric field is in the growth direction, hence the ground state energy will be affected by changing the confinement potential in this direction.

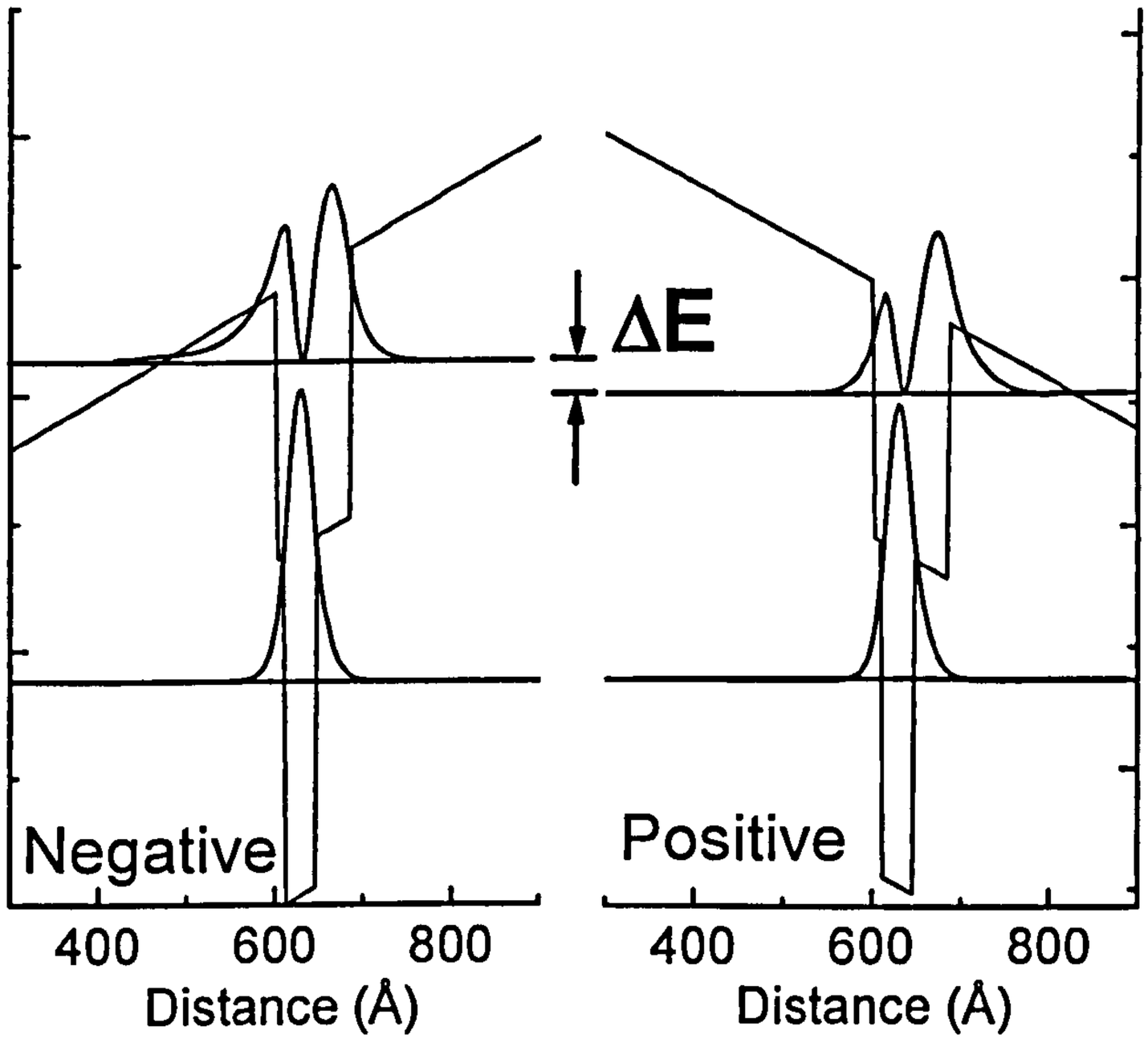

Fig. 3.3.3. Well-within-a-well simulation of QD ground state and QW ground state squared envelope functions for positive and negative bias, showing the origin of the spectral shift.

Fig.3.3.3 shows the two squared wavefunctions for either state (E_I and E_{QW}) with different parity. The effect of the asymmetry on the E_{QW} bias dependence is evident. This model demonstrates the principle of the observed dependence. Also by increasing the asymmetry of the structure an increased ΔE shift is observed. However in order to quantify the Stark shift in DWELL QDIPs a more accurate model is required.

Therefore, in collaboration with the Institute of Microwaves and Photonics (IMP) in the University of Leeds, led by Prof. P. Harrison, a theoretical 8-band k•p model was provided by N. Vukmirovic, and a detailed analysis of the model can be found in N. Vukmirovic thesis*. This collaboration resulted in the publication of reference [13].

*N. Vukmirovic, '*Physics of Intraband Optoelectronic devices*' PhD Thesis, Institute of Microwaves and Photonics (IMP), Leeds University, 2007

3.3.3. Theoretical calculations of the Stark shift in DWELL QDIPs

The theoretical model used to calculate the electronic structure in the CB and consequently the intraband absorption spectrum, is based on the 8 band k•p method, with the effects of strain and electric field taken into account. More details of the theoretical method were published and can be found in references [18] and [27]. Fig.3.3.4 below shows the conduction band of the 2.9ML DWELL QDIP calculated using the above method with no external applied field. All the states to which absorption from the ground state is allowed by selection rules are shown, with the one mostly contributing to the absorption marked by longer line.

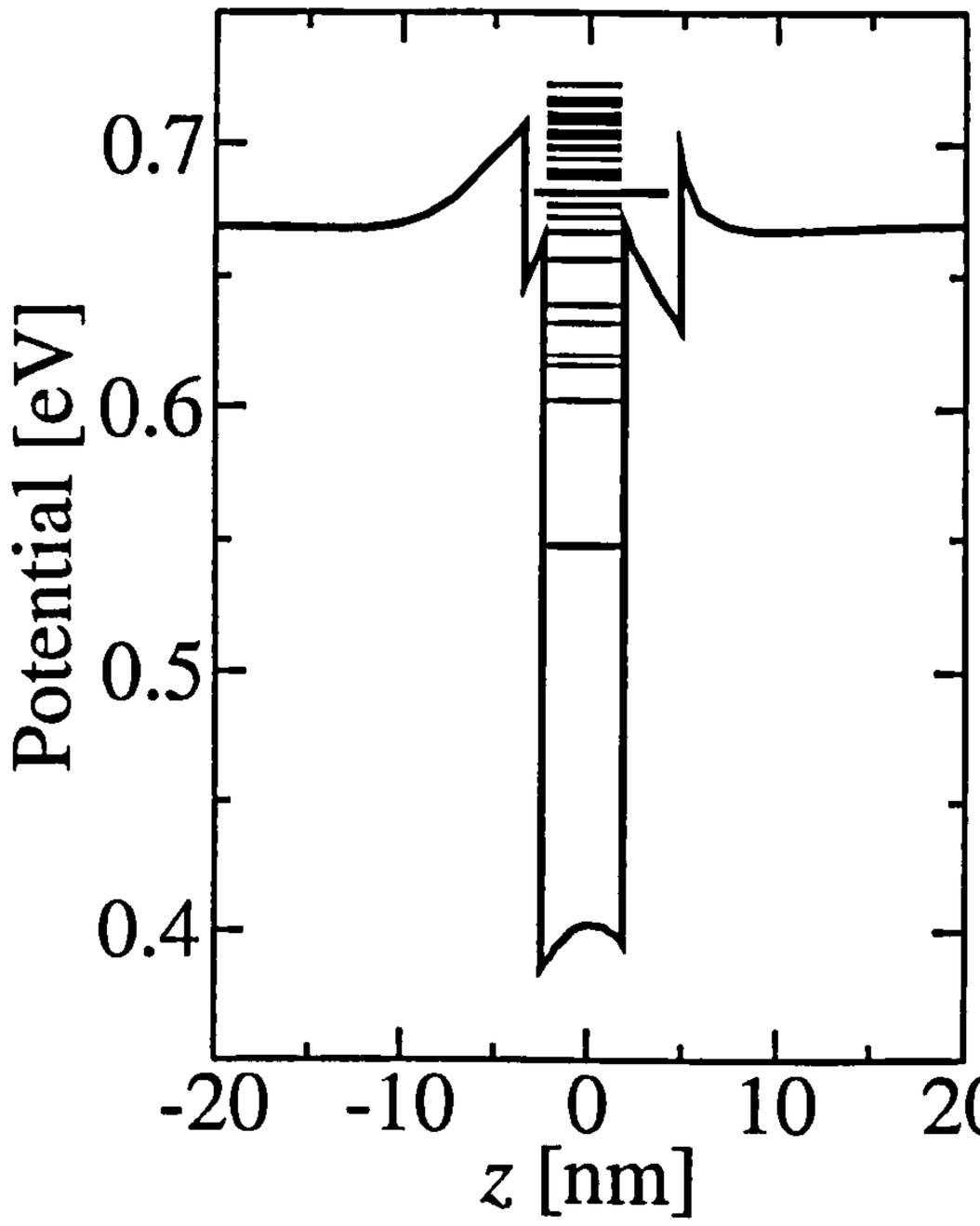

Fig.3.3.4. Calculated conduction band profile of one period of an InAs/InGaAs DWELL using the 8-band k•p method

In the bottom part of Fig.3.3.5 the wavefunctions of the ground and the excited state to which the absorption is maximal are shown, for biases of -0.6V and +0.6V, as well as the on-axis potential profile with the energies of the states that mostly contribute to the absorption for the sample with N_{ML}=2.9. The quasi-continuum density of states is represented by a discrete set of states which is a consequence of embedding the dot in a cylinder of finite size. It has been checked that the embedding cylinder is large enough so that the calculated absorption spectrum and the position of its maximum have converged.

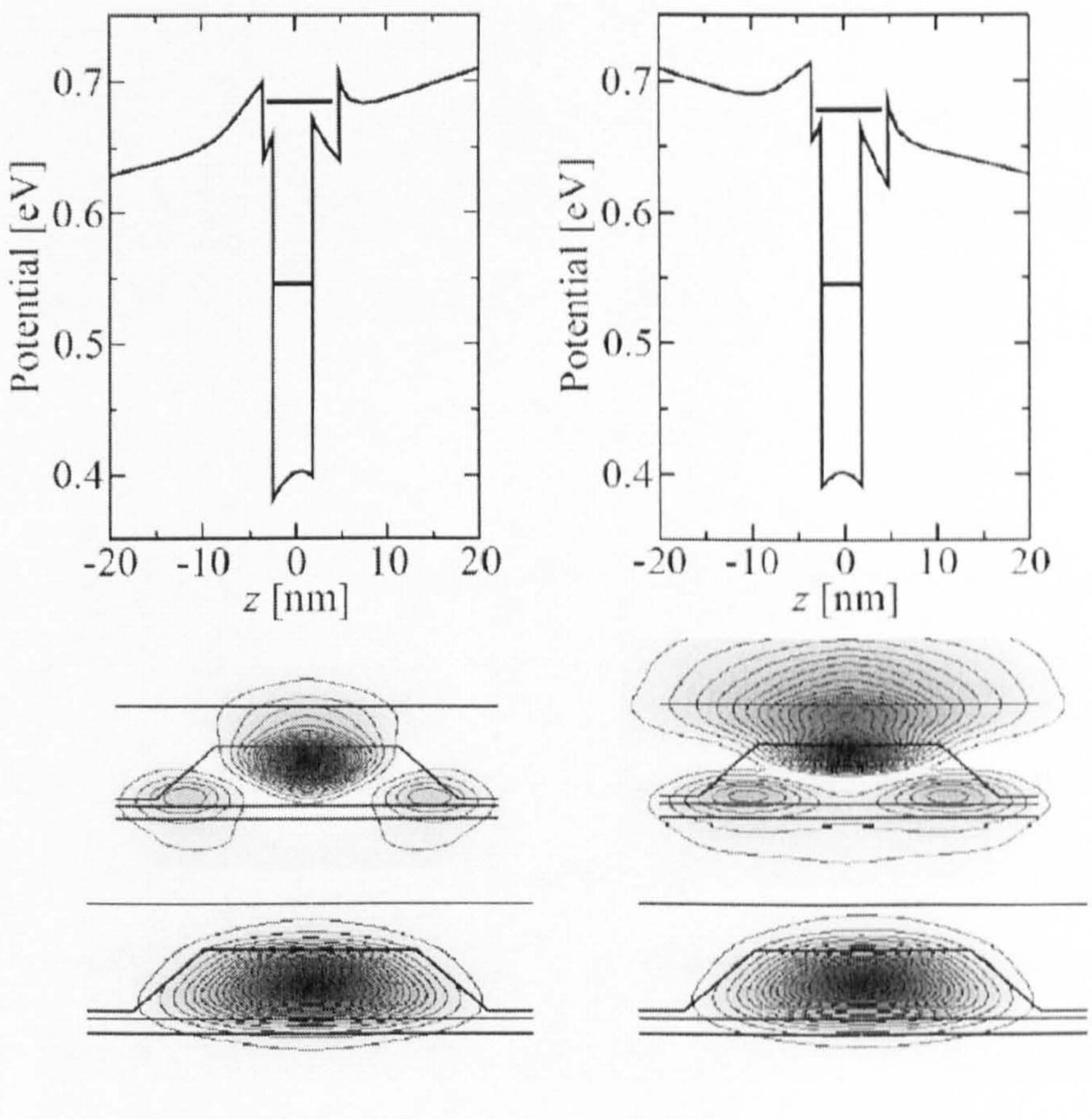

Fig.3.3.5. Calculated potential profile along the z-axis (top) and contour plots of wave function moduli of the ground state (bottom) and the state to which absorption is maximal (middle) in the case of dot dimensions that best fit the 2.9ML sample for -0.6V (left) and +0.6V (right).

It is evident from the wave functions shown in Fig.3.3.5, that the ground state wavefunction is weakly influenced by the electric field, while the influence of the electric field on the wavefunction of higher energy quasi-bound states which mostly contribute to the absorption is much stronger. Negative bias shifts the wavefunction towards the region of low potential and decreases the distance between the centroids and the dipole moment of the transition.

The calculation was performed assuming dots of truncated shape with base diameter *D*, height if the dot were not truncated *H*, actual height *h*, and indium content in the dot *x*. In these simulations, these parameters were varied in the range where the calculated absorption spectrum exhibits a maximum in the same spectral region as the experimental spectrum: *h* was varied in the interval 4-7 nm; *x* from 0.6 to 0.75, *D* in the range 15-22 nm, and *H* was set to 10nm.

3.3.4. Discussion – comparison of experimental and theoretical results

In Fig.3.3.6, the experimental (open squares) bias dependence of the $E_1 \rightarrow E_{QW}$ transition for N_{ML}=2.9 is plotted over the range of biases for which the photocurrent peak is observable. The best fit for the dependence of the transition energy on bias was obtained when *h*=4nm, x=0.7, *D*=17nm, as shown in Fig.3.3.6 (dashed line). Calculated absorption spectra showing the bias dependent shift can be seen in the inset of Fig.3.3.6.

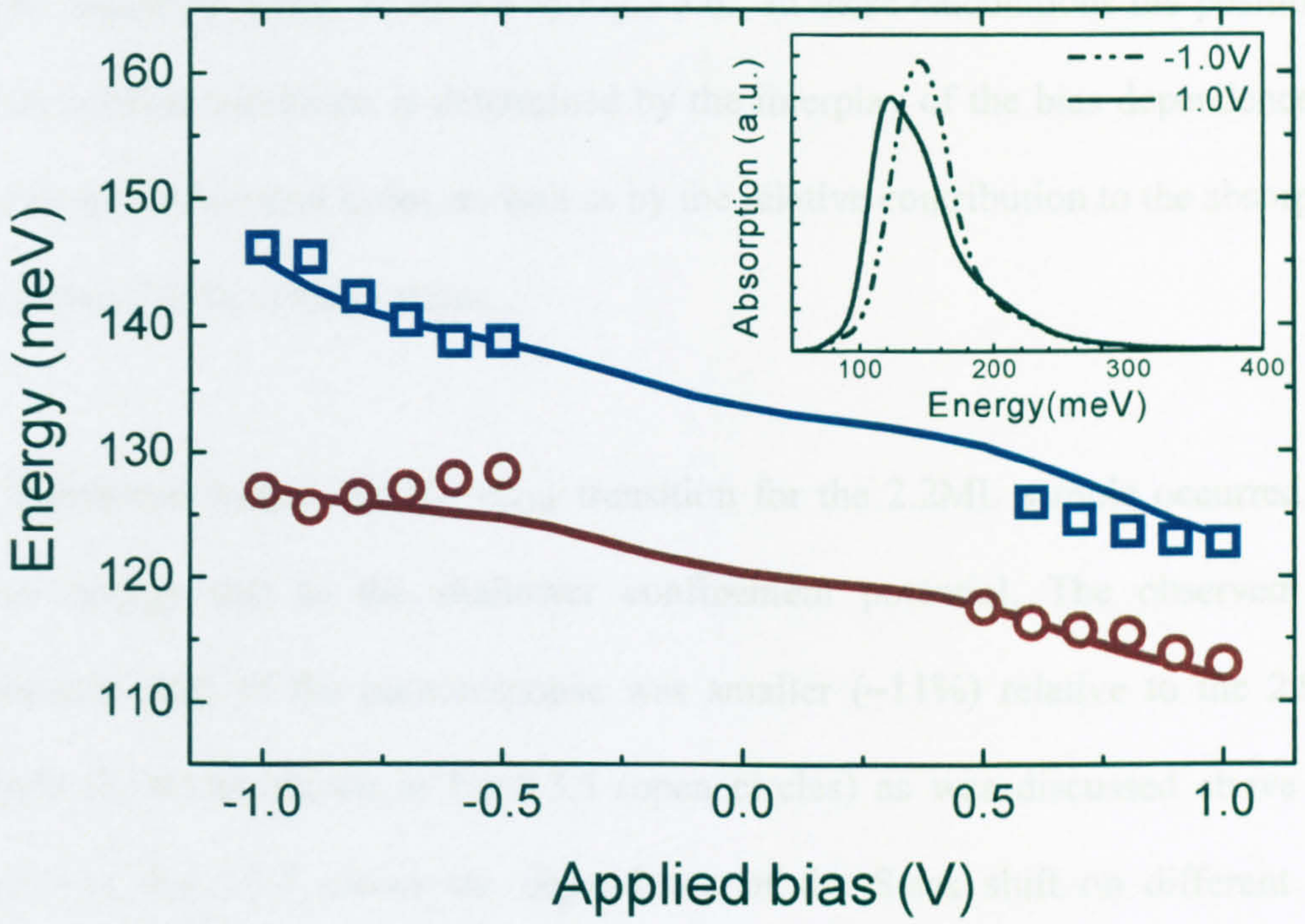

Fig.3.3.6 Bound-to-bound transition energy dependence on applied bias: for 2.9ML sample experimental (open squares) and calculated (dashed line), and for 2.2ML sample experimental (open circles) and calculated (solid line). Inset: Calculated absorption spectra for 2.9ML at -1.0V and 1.0V.

It is known that for the transition between two truly discrete states the following dependence of the transition energy on the electric field is obtained (including the terms up to second order of perturbation theory) $E=E_0+pF+\beta F^2$, where E_0 is the energy at F = 0, the second term arises from the nonzero dipole moment p at F=0, and the third term arises from polarisation of the dots in the applied field (the quantum confined Stark effect).

However, in this case the transition takes place between a truly discrete bound state and a quasi-continuum density of states. The maximum of the absorption spectrum is then determined by complex changes in the density of states and does not follow a

simple quadratic trend, as shown in Fig.3.3.6. In these calculations the position of the absorption maximum is determined by the interplay of the bias dependences of the energies of several states, as well as by the relative contribution to the absorption spectrum of each of these states.

As mentioned before, the $E_1 \rightarrow E_{QW}$ transition for the 2.2ML sample occurred at a lower energy due to the shallower confinement potential. The observed bias dependent shift of the photoresponse was smaller (~11%) relative to the 2.9ML sample (15%) as shown in Fig.3.3.5 (open circles) as was discussed above (see Fig.3.3.1). Fig.3.3.7 shows the dependence of the Stark shift on different N_{ML} including the 2.55ML sample.

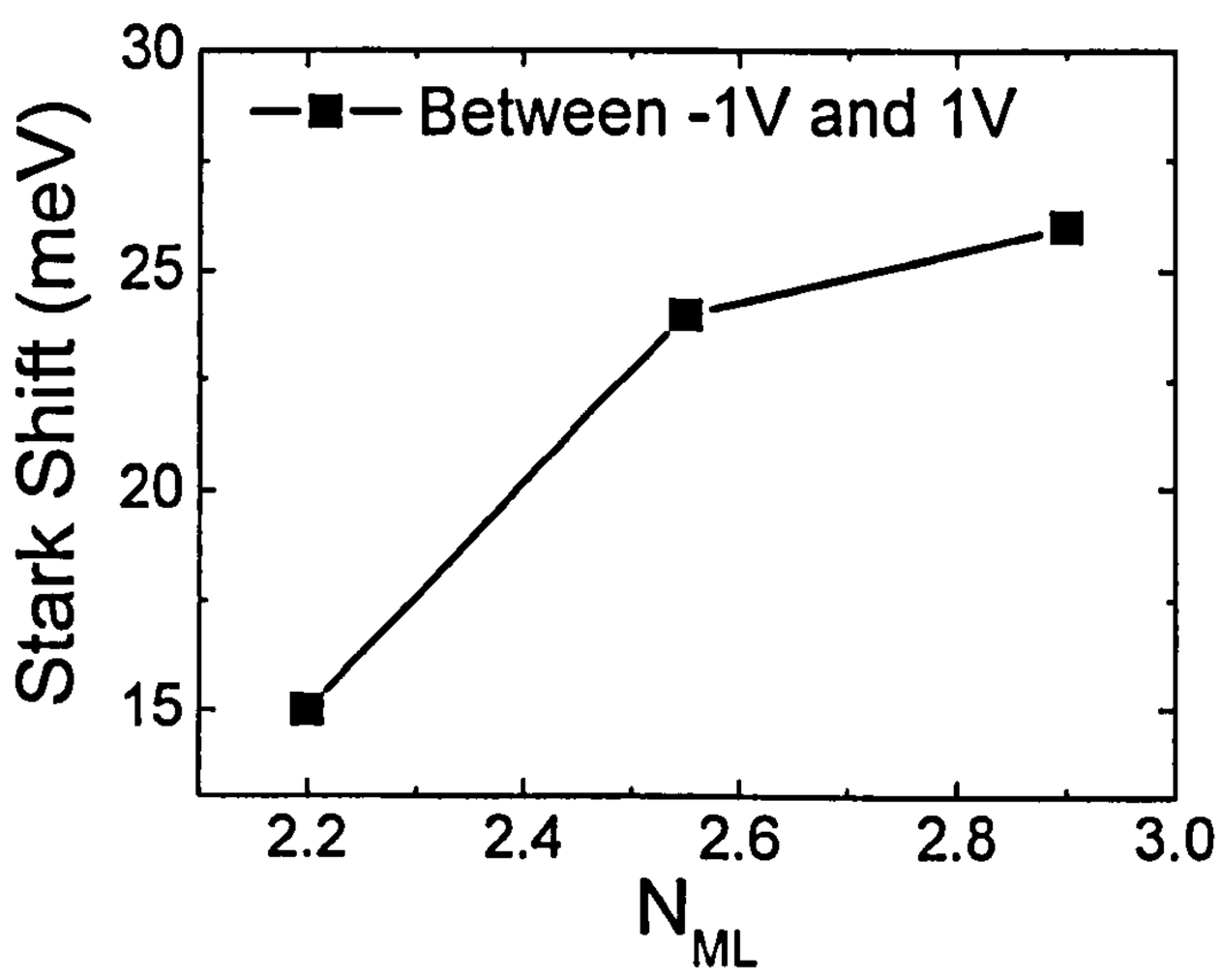

Fig.3.3.7. Stark shift dependence on N_{ML}.

This indicates that the 2.2ML sample has a smaller separation between the centroids of the QD ground state and QW wavefunctions (i.e. is *more* symmetric). Because of the non-uniformity of the indium composition in QDs [28, 29], one possible

explanation of these results is that the indium composition at the base of the 2.9ML sample is larger than for 2.2ML. This means the electron wavefunction for 2.2ML is more localised towards the apex of the QD, thus reducing the separation between the QD and QW wavefunction centroids.

Detailed information about the QDs structure would be necessary to introduce a non-uniform indium profile in the simulation, however satisfactory agreement is still obtained with the experimental results using a significantly larger QD height (h=6nm) for the 2.2ML sample. The dots are then placed in the middle part of the well and the asymmetry of the system is smaller. The best fit to the experimental results (Fig.3.3.7, solid line) is obtained when h=6nm, x=0.66, D=17nm. Therefore the most probable explanation for the observed differences in the photoresponse of the two samples is an increased In content in the dot for 2.9ML, leading to a higher transition energy and either a change in the indium compositional profile or a decrease of the dot height leading to an increased Stark shift.

Additional structural investigations would be necessary to unambiguously identify the origin of the increased Stark shift, by using cross sectional scanning tunnelling microscopy (X-STM), or transmission electron microscopy (TEM). However, the results clearly show that the bias dependent spectral shift of the photoresponse is sensitive to QD growth parameters and may be controlled by varying the asymmetry of the DWELL system. The understanding of the bias dependence in DWELL detectors could provide the ability to maximise the Stark effect for applications where a considerable tunability over the IR spectrum is required.

3.3.5. Summary

In conclusion, the observation of the intraband Stark shift in DWELL structures was discussed and a good agreement was found with a theoretical model based on the 8-band k•p method. A non-quadratic behaviour of the Stark shift indicates that the transition takes place between a truly discrete dot bound state and a quasi-continuum density of states whereby complex changes in the density of states determine the maximum of the absorption spectrum. An increase of the transition energy and the amount of Stark shift with increasing N_{ML} was also observed.

3.4. Performance characteristics of an optimised InAs/InGaAs DWELL QDIP

3.4.1. Introduction

In this section, the high performance of a narrow band InAs/$In_{0.15}Ga_{0.85}As$ dot-in-a-well (DWELL) detector doped with 1 electron per dot is presented. The studies that were carried out in section 3.1, and 3.2, enabled the optimisation of QD and QW parameters, whereby it was possible to design a detector, which would be expected to have high performance. The detector was characterised and exhibited a very high responsivity for a sample doped at $1e^-$/dot, while exhibiting narrow spectral features as well as a narrow photoluminescence linewidth, indicating the high quality and homogeneity of the structure. The device also showed a low dark current and high detectivity.

The optimised DWELL structure contained 2.55ML of InAs QDs in an 80Å $In_{0.15}Ga_{0.85}As$ well, with a bottom contact layer of 4000Å *n*+ Si doped GaAs, 10 periods of DWELL active region, separated by a 500Å undoped GaAs spacer and a final 4000Å *n*+ Si doped GaAs top contact layer. The active region was Si δ-doped in the top of the GaAs barrier prior to the deposition of the QDs, to a concentration of $6x10^{10}cm^{-2}$ corresponding to approximately 1 e^-/dot.

3.4.2. Detector characterisation

Fig.3.4.1 shows the temperature dependence of the normal incidence photoresponse spectra of the sample at -2.5V. As mentioned in previous sections the response would be ~5x higher for *p*-polarisation. However a strong signal is observed for normal incidence for this sample. The spectra exhibit a narrow $E_1 \rightarrow E_{QW}$ photocurrent peak centred at λ~7.5μm (~165 meV) and a broad shoulder from 5 to ~6.5μm (200-250meV) at an applied bias of -2.5V the latter being more clearly resolved for biases near zero applied field where tunnelling from E_{QW} is less probable. The detector also showed a bias dependence of the photocurrent peak position as mentioned in the previous section. The positive 2.5V photoresponse at 77K showed a peak at 8μm as shown in Fig.3.4.1 (dashed line).

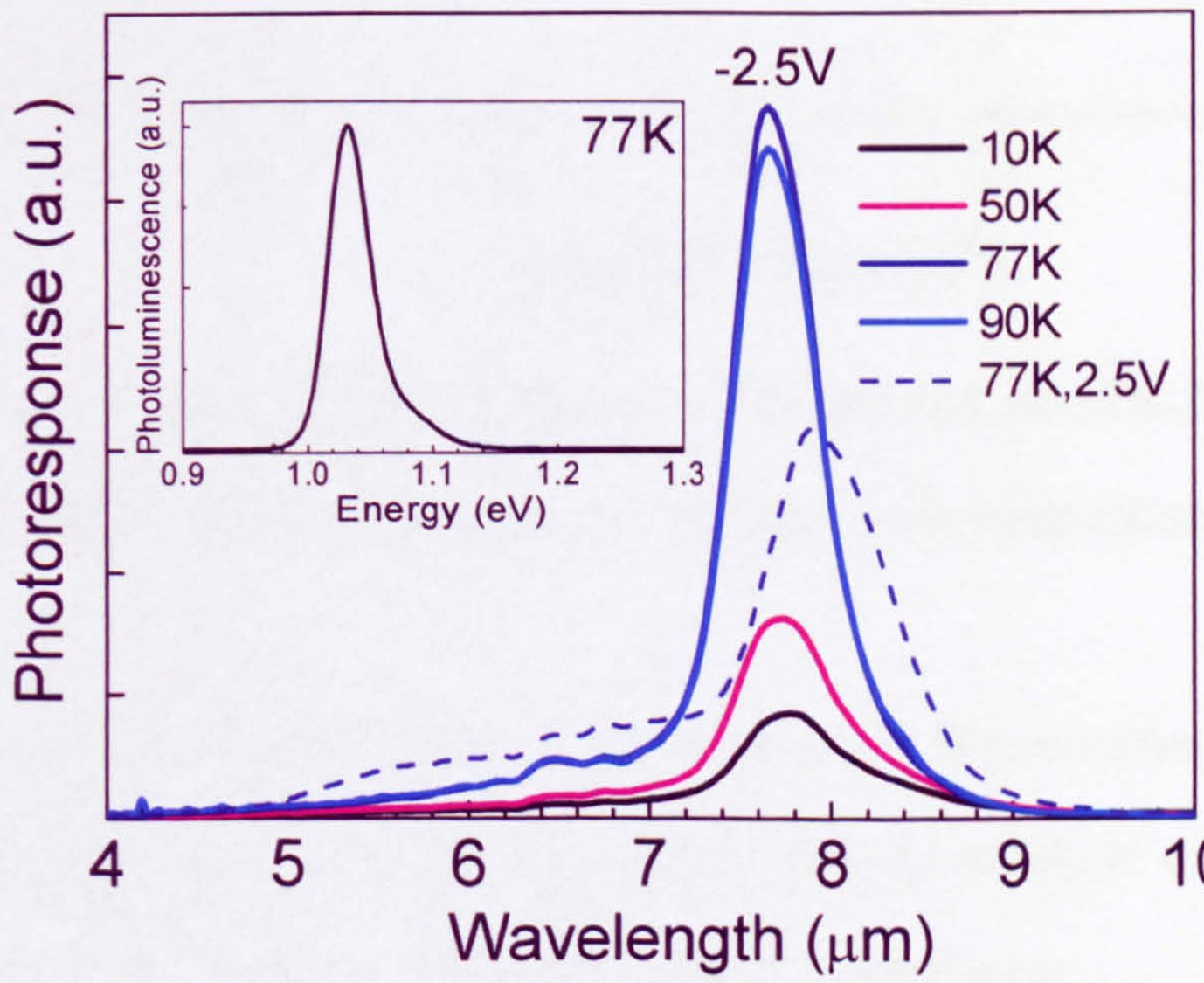

Fig.3.4.1: Normal incidence photoresponse of DWELL QDIP at different temperatures. Response at positive bias at 77K shown in dashed line. Inset: Photoluminescence at 77K at1.03eV, with FWHM = 40meV.

The dark current density characteristics for 400μm mesa etched devices for each of the structures are presented in Fig.3.4.2. The device exhibits very low dark current density of 0.1mA/cm^2 at 77K and 1mA/cm^2 at 90K and -2.0V. A high homogeneity of the dark current response was observed over a large number of mesa devices (>10).

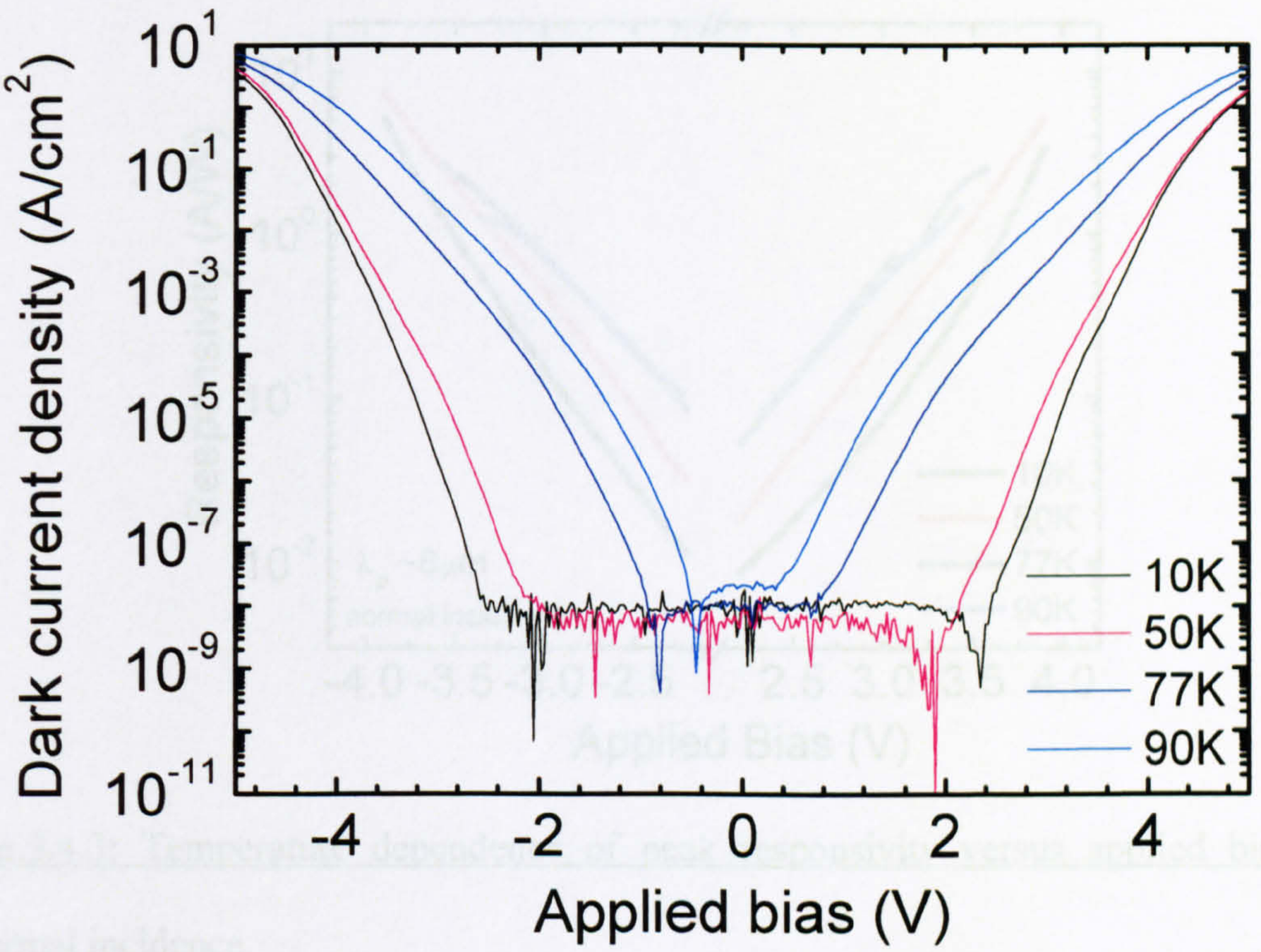

Fig.3.4.2: Dark current density dependence on temperature, at 10K, 50K, 77K.and 90K. the plateau region is defined by the noise floor of the measurement unit.

The dark current density homogeneity across the wafer demonstrates the ability to grow high quality structures, with reproducible results, which in turn proves the suitability of this technology for large FPA array manufacturing.

Peak responsivity (R_P) measurements were carried out using a calibrated black body source with a temperature of 1005K and a modulation frequency of 160Hz, as

described in section 3 of chapter 2. Fig.3.4.3 shows the peak responsivities for different temperatures versus applied bias. A peak responsivity of 8A/W at -3.8V at 50K and $\lambda \approx 7.6\mu m$ is observed, reducing to about 3A/W at-3.5V at 77K. These values are very high and comparable to previously reported high responsivity QDIPs [30] at the same wavelength range.

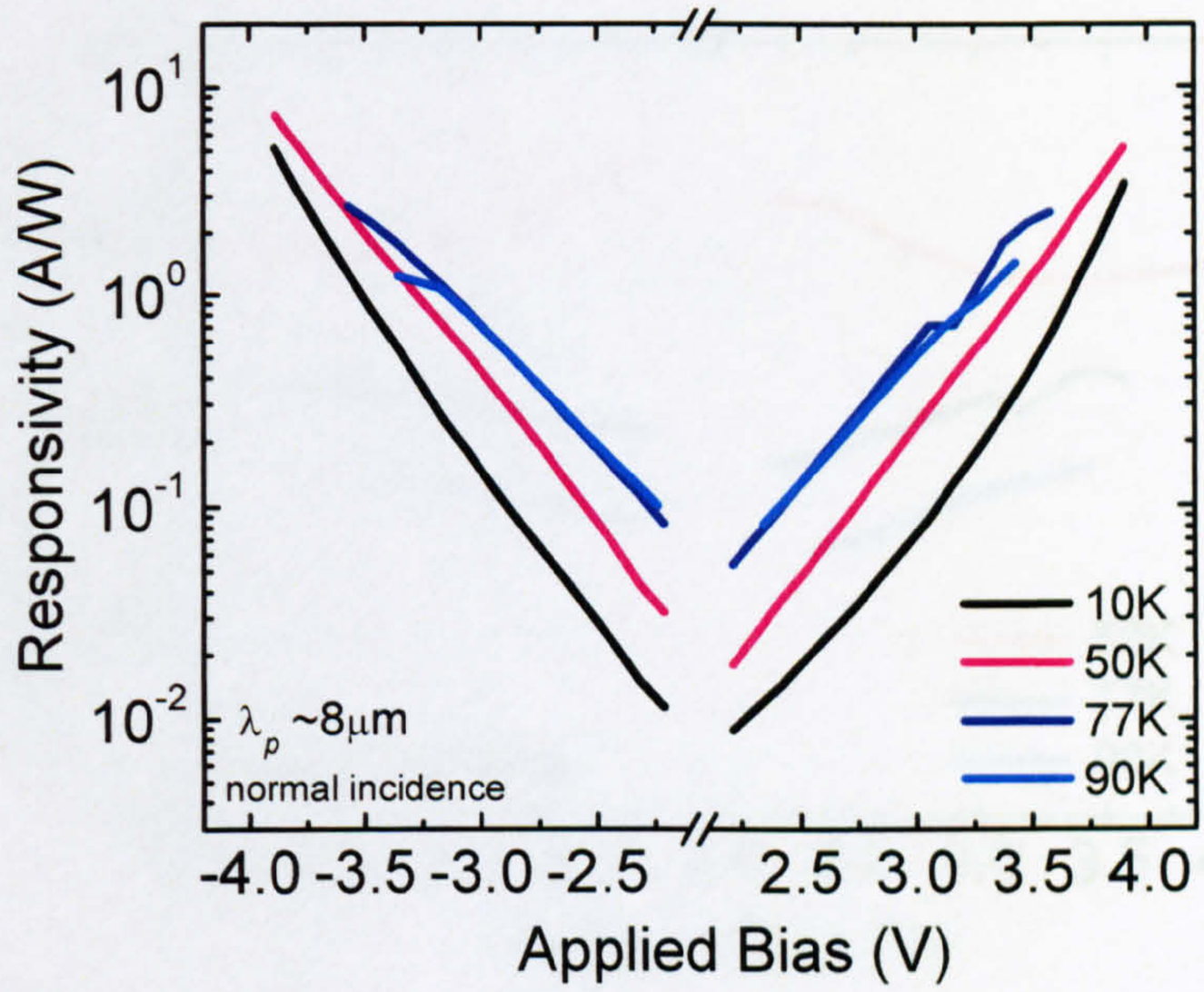

Fig.3.4.3: Temperature dependence of peak responsivity versus applied bias at normal incidence.

Of note is the increasing trend of the responsivity with temperature up to 77K. Such an increasing trend has been previously attributed to thermally-assisted tunnelling in QWIPs and QDIPs [15]. In addition, the responsivity at 90K is the same as that at 77K for most of the bias range. However the rate at which R_p increases with temperature is not the same across the whole bias range. As the temperature increases, the detector operating range is limited at higher biases since the dark current becomes too high.

Fig.3.4.4 shows the dark current limited detectivity, which has been calculated by taking into account the dark current density and the peak responsivity (see chapter 1.2). The maximum detectivity was $1.5x10^{10}cmHz^{1/2}W^{-1}$ at -3V and 77K. D^* is reduced at 90K to the order of $\sim5x10^{9}.cmHz^{1/2}W^{-1}$ at -3V, which is an expected reduction as the thermally activated dark current is increased.

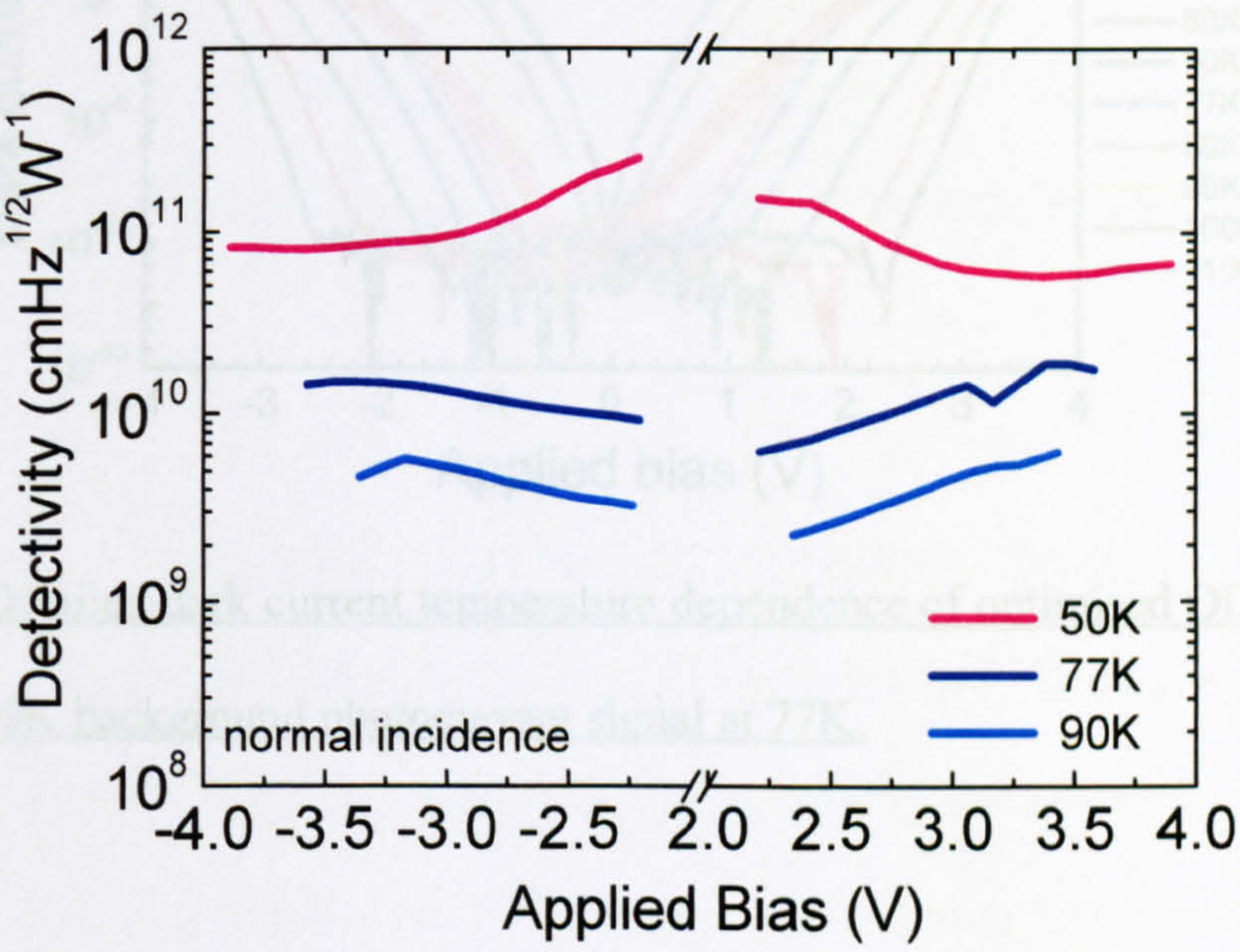

Fig.3.4.4. Dark current limited detectivity at 50K, 77K and 90K for optimised DWELL QDIP

Although the dark current limited detectivity is of a very high value of $\sim2x10^{11}cmHz^{1/2}W^{-1}$ at 50K and ~-2.0V, it is not such an accurate estimate, since for low temperatures other noise sources also become significant compared to the dark current as it was discussed in chapter 1.2. The detector was background limited at 77K and ±2.0V at a field of view of 33° (f/3), as illustrated in Fig.3.4.5. Therefore the D^* values are accurate for temperatures above 77K and above ±2.0V. The operation of an LWIR detector at these temperatures is of great technological

significance since they would require less sophisticated cooling, making QDIPs a more competitive technology for cooled infrared detectors.

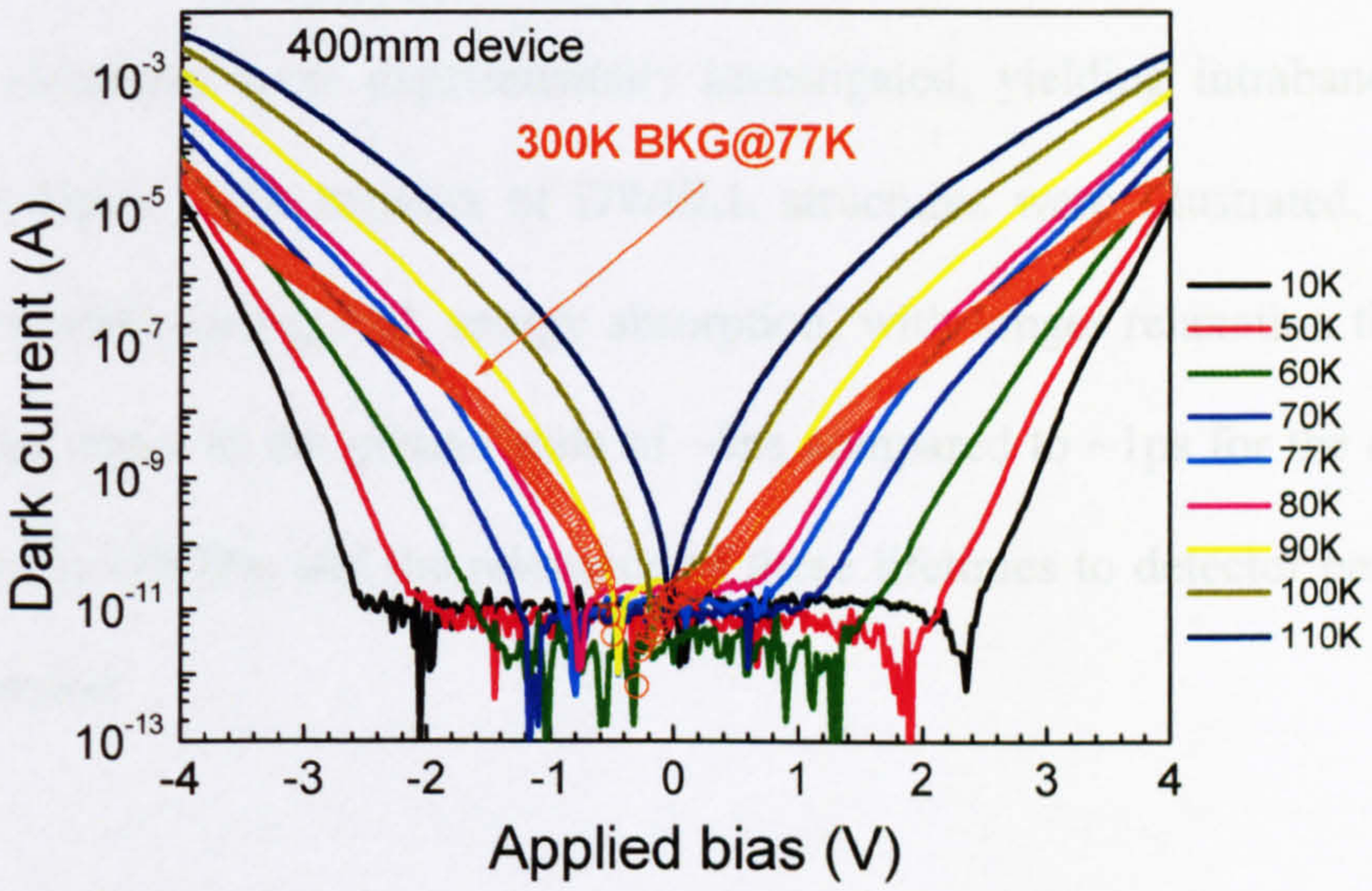

Fig.3.4.5. Detailed dark current temperature dependence of optimised QDIP, plotted with the 300K background photocurrent signal at 77K.

3.4.3. Summary

In conclusion, this section presented results from a high performance DWELL photodetector, which was result of the optimisation of DWELL design parameters (N_{ML}, doping concentration, well width etc.). The detector exhibited strong, narrow linewidth features in the LWIR (~8μm) with responsivity values of ~3A/W at 77K, and $D^* = 1.5\text{x}10^{10}\text{cmHz}^{1/2}\text{W}^{-1}$ at 77K, reducing to $5\text{x}10^{9}\text{cmHz}^{1/2}\text{W}^{-1}$ at 90K for the same bias while being background limited at 77K.

3.5. Discussion

In this chapter, the intraband absorption characteristics and carrier dynamics in DWELL structures were experimentally investigated, yielding intraband electron relaxation times. The benefits of DWELL structures were illustrated, including narrow linewidth strong high energy absorption, with longer relaxation times from high energy states to the ground state of ~5ps compared to ~1ps for the equivalent relaxations in QWIPs, and the relevance of these lifetimes to detector performance were discussed.

Furthermore the performance characteristics of DWELL QDIPs and the design parameters that determine these were systematically studied. It was shown how by changing the number of ML deposited during growth the photoresponse can be tailored to a desired wavelength. It was also demonstrated how the same can be done by changing the well width, within which the dots are embedded. Other aspects such as the effects of doping and the dependence of the performance on polarisation of incident radiation were experimentally investigated.

A comprehensive study of the Stark shift in QDIPs was presented, where the bias dependence of the photoresponse and its subsequent dependence on ML was experimentally determined and simulated using an 8 band k•p method. The Stark shift was related to transitions taking place between a truly discrete dot bound state and a quasi-continuum density of states whereby complex changes in the density of states determined the maximum of the absorption spectrum.

Finally an optimised design considering all the findings from the first sections of the chapter was suggested for the InAs/InGaAs/GaAs system, which was fully characterised, and high performance levels were achieved, with responsivities of 3A/W at 77K and 8μm, and D^*~10^{10}cmHz$^{1/2}$W^{-1}.

References

1 I. R. Sellers, D. J. Mowbray, T. J. Badcock, J. P. R. Wells, P. J. Phillips, D. A. Carder, H. Y. Liu, K. M. Groom, M. Hopkinson, Appl.Phys.Lett. **88**, 081108, (2006)

2 See, for example, J. Siegert, S. Marcinkevičius, Q. X. Zhao, Phys. Rev. B **72**, 085316 (2005); S. Trumm, M. Wesseli, H. J. Krenner, D. Schuh, M. Bichler, J. J. Finley and M. Betz, Appl. Phys. Lett. **87**, 153113 (2005); T. Müller, F. F. Schrey, G. Strasser and K. Unterrainer, *ibis* **83**, 3572 (2003); A. V. Uskov, F. Adler, H. Schweizer and M. H. Pilkuhn, J. Appl. Phys. **81**, 7895 (1997)

3 See, for example, U. Bockelmann and G. Bastard, Phys.Rev.B 42 8947 (1990); X.Q. Li, H. Nakayama, Y. Arakawa, Phys. Rev. B 59 5069 (1999)

4 J. Urayama, T. B. Norris, J. Singh, P. Bhattacharya, Phys. Rev. Lett. **86** (2001) 4930

5 See, for example, S. Sauvage, P. Boucaud, R. P. S. M. Lobo, F. Bras, G. Fishman, R. Prazeres, F. Glotin, J-M. Ortega, J.-M. Gérard, Phys.Rev.Lett. **88**, 177402-1 (2002); E. A. Zibik, L. R. Wilson, R. P. Green, G. Bastard, R.

Ferreira, P. J. Phillips, D. A. Carder, J-P. R. Wells, J. W. Cockburn, M. S. Skolnick, M. J. Steer and M. Hopkinson, Phys. Rev. B **70**, 161305 (2004).

6 S. Sauvage, P. Boucaud, F. Glotin, R. Prazeres, J.-M. Ortega, A. Lemaitre, J.-M. Gérard and V. Thierry-Flieg, Appl. Phys. Lett. **73**, 3818 (1998)

7 H. Y. Liu, I. R. Sellers, M. Gutiérrez, K. M. Groom, R. Beanland, W. M. Soong, M. Hopkinson, J. P. R. David, T. J. Badcock, D. J. Mowbray, M. S. Skolnick, Materials Science and Engineering C 25, 779 (2005)

8 E. A. Zibik, A. D. Andreev, L. R. Wilson, M. J. Steer, R. P. Green, W. H. Ng, J. W. Cockburn, M. S. Skolnick, M. Hopkinson, Physica E **26** 105-109 (2005)

9 E. A. Zibik, W. H. Ng, L. R. Wilson, M. S. Skolnick, J. W. Cockburn, M. Gutierrez, M. J. Steer, M. Hopkinson, Appl.Phys.Lett. **90**, 163107 (2007)

10 See, for example, G. Bester and A. Zunger, Phys. Rev. B **71**, 045318 (2005); M. A. Migliorato, D. Powell, S. L. Liew, A. G. Cullis, P. Navaretti, M. J. Steer, M. Hopkinson, M. Fearn, and J. H. Jefferson, J. Appl. Phys. **96**, 5169 (2004)

11 M. Gutierrez, M. Hopkinson, H. Y. Liu, M. Herrera, D. Gonzalez, R. Garcia, J. Crystal Growth, 278 151–155 (2005); L. Seravalli, M. Minelli, P. Frigeri, P. Allegri, V. Avanzini, and S. Franchi, Appl.Phys.Lett. **82**, 2341 (2003)

12 P. Aivaliotis, E. A. Zibik, L. R. Wilson, J. W. Cockburn, M. Hopkinson, R. J. Airey, Appl.Phys.Lett. **91** 143502 (2007)

13 P. Aivaliotis, N. Vukmirovic, E. A. Zibik, J. W. Cockburn, D. Indjin, P. Harrison, C. Groves, J. P. R. David, M. Hopkinson and L. R Wilson, J. Phys. D: Appl. Phys. **40** 5537-5540, (2007)

14 S. Krishna, S. Raghavan, G. von Winckel, A. Stintz, G. Ariyawansa, S.G. Matsik, A.G.U. Perera, App. Phys. Lett. 83, 2745 (2003)

15 H. Schneider, H. C. Liu, 'Quantum Well Infrared Photodetectors, Physics and Applications', Springer Series in Optical Sciences, vol.126, p.57-65 (Springer, Berlin, Heidelberg) 2007

16 S. Raghavan, D. Forman, P. Hill, N.R. Weisse-Bernstein, G. von Winckel, P. Rotella, S. Krishna, S.W. Kennerly, J.W. Little, J. App. Phys. **96**, 1036 (2004)

17 R. S. Attaluri, S. Annamalai, K. T. Posani, A. Stintz, and S. Krishna, J. Appl. Phys. **99** (2006) 083105

18 N. Vukmirović, D. Indjin, Z. Ikonić, and P. Harrison, Appl. Phys. Lett. 88, 251107 (2006)

19 K. Drozdowicz-Tomsia, E. M. Goldys, L. Fu, C. Jagadish, Appl.Phys.Lett. **89** (2006) 113

20 V. Ryzhii, V. Pipa, I. Khmyrova, V. Mitin, M. Willander, Jpn. J. Appl. Phys. **39**, 1283 (2000)

21 E.T Kim, A. Madhukar, Z. Ye, J. C. Campbell, Appl.Phys.Lett. **84** (2004) 3277

22 S. -T. Chou, M. -C. Wu, S. -Y. Lin, J. -Y. Chi, Appl. Phys. Lett. **88** (2006) 173511

23 J. Li, K.K. Choi, D.C. Tsui, Appl. Phys. Lett. **86** 211114 (2005)

24 S.R. Parihar, S.A. Lyon, M. Santos, M. Shayegan, Appl. Phys. Lett. **55** 2417 (1989)

25 E. Martinet, E. Rosencher, F. Luc, Ph. Bois, E. Costard, and S. Delaitre, Appl. Phys. Lett. **61** 246 (1992)

26 P. W. Fry, I. E. Itskevich, D. J. Mowbray, M. S. Skolnick, J. J. Finley, J. A. Barker, E. P. O'Reilly, L. R. Wilson, I. A. Larkin, P. A. M. Hopkinson, M. Al-

Khafaji, J. P. R. David, A. G. Cullis, G. Hill, and J. C. Clark, Phys. Rev. Lett. **84**, 733 (2000)

27 N. Vukmirović, Ž. Gačević, Z. Ikonić, D. Indjin, P. Harrison, and V. Milanović, Semicond. Sci. Technol. 21, 1098 (2006)

28 P. B. Joyce, T. J. Krzyzewski, G. R. Bell, B. A. Joyce, and T. S. Jones, Phys. Rev. B **58**, R15981 (1998)

29 T. Walther, A. G. Cullis, D.J. Norris and M. Hopkinson, Phys. Rev. Lett. **86**, 2381 (2001)

30 S Chakrabarti, A D Stiff-Roberts, X H Su, P Bhattacharya, G Ariyawansa and A G U Perera, J. Phys. D: Appl. Phys. **38** (2005) 2135-2141

4. Methods of enhancement of DWELL QDIP performance

In this chapter, three different approaches are presented towards the improvement of DWELL QDIP performance. As mentioned in the introduction, one of the key factors limiting the performance levels of QDIPs or DWELLs relative to quantum well infrared photodetectors (QWIPs) is the typically ~10x lower intraband absorption strength for a single layer of QDs compared to a single QW.

The first approach in tackling this issue is to increase the dot density in each active absorbing QD layer. This has been shown to be possible in non-detector InAs/GaAs structures via the use of surfactants [1]. The incorporation of antimony surfactant was used to increase the dot density in InAs/GaAs QD structures and DWELL QDIPs, resulting in 2x higher dot densities, which in turn resulted in higher intraband absorption, and improved detector performance.

Another major factor in the performance of QDIPs is the reduction of dark current. Several designs had been previously shown to reduce dark currents in QDIPs with the use of AlGaAs and AlAs layers [2]. The 2nd section of this chapter presents

designs variations of structures incorporating AlGaAs current blocking layers and barrier layers to optimise the suppression of thermionic emission.

Another approach to address the absorption issue is to increase the number of periods in the absorbing region. However, particularly in the InAs/InGaAs DWELL system, the strain build-up for multilayer structures with >20 layers lead to defects, which are detrimental to the performance. A technique using GaP strain balancing layers had been previously demonstrated for MOCVD grown QDs [3]. This technique was applied in MBE grown InAs/InGaAs DWELL QDIPs and the results are discussed in section 3.

4.1. Enhancing the dot density in QD structures via the incorporation of antimony

4.1.1. Introduction

The main reason for the lower absorption is that the in-plane QD density limits the number of absorbing electrons to a few $10^{10}cm^{-2}$ in a QDIP, compared with a few $10^{11}cm^{-2}$ in a typical QWIP. Therefore higher dot densities are required in QDIPs in order to reach the performance levels of QWIPs. Recent reports have shown how the QD density can be increased by decreasing In surface diffusion of adatoms, via the use of a low-growth temperature and/or a high-growth rate [4]. However, the increase of density in this case can lead to the formation of coalesced plastically relaxed giant islands, which deteriorate the QD optical properties. Other methods of increasing the dot density such as those involving QD growth on InP substrates, also often lead to coalesced dots or dashes where the oscillator strength is exhausted by the lower energy transitions [5]. It has been reported [4,6-9] that QD formation can be influenced by using surfactants, such as antimony. The exact mechanism of surfactant-mediated growth is still under debate, but the most generally reported effect of antimony surfactant species is to lower the surface energy and to drive the growth in a diffusion-limited regime, as well as to segregate to the growth front [4]. Enhanced dot densities have been reported in growth related publications for InAs dots either grown by MOCVD [4,8,9] or MBE [1], as well as for other material systems such as Ge/Sb:Si QDs [7,10].

In this section an enhanced dot density resulting from QD formation on an antimony-rich surface is presented. Interband and intraband studies revealed that the electron energy structure is similar to standard InAs QDs; however, the intraband absorption strength is increased by about a factor of 2, scaling linearly with increased QD density. In addition the results for a DWELL QDIP where this technique of QD density enhancement is employed are presented. The DWELL QDIP demonstrates very good performance with a 77 K responsivity of ~1 A/W, a very low dark current compared to the previously lowest DWELL QDIP, and dark current limited detectivity of ~5×10^{10}cmHz$^{1/2}$W^{-1} at 7.5μm, showing high potential of this technique for QDIP development.

4.1.2. Structural Characterisation

The investigated QD structures were grown by molecular beam epitaxy (MBE). An initial sample was grown for intraband absorption studies. The active region contained 50 layers of InAs quantum dots separated by 1000Å of undoped GaAs, with 1 monolayer (ML) of GaSb deposited prior to QD growth. The method of growing GaSb has been previously demonstrated and more details can be found in reference [1]. The InAs quantum dots were grown after the deposition of GaSb. 3.25ML of InAs were deposited during QD growth. The active region is Si δ-doped to approximately 1 electron per dot.

After the wafers were grown a PL mapping was carried out to check the quality of the growth. As shown below in Fig.4.1.1, measurements of the wafers provided

very non-uniform emission wavelengths, intensities and FWHM. The reason for this was a problem with the way the substrate was placed within the MBE reactor, causing a slight tilt of the surface from the horizontal plane, which affected the uniform temperature distribution across the wafer during growth. Even though this was quite unfortunate, the red areas near the major flat of the wafers exhibited very high PL intensity compared to typical QD structures. Therefore all samples discussed in this section were processed from that area as indicated in the bottom left of Fig.4.1.1.

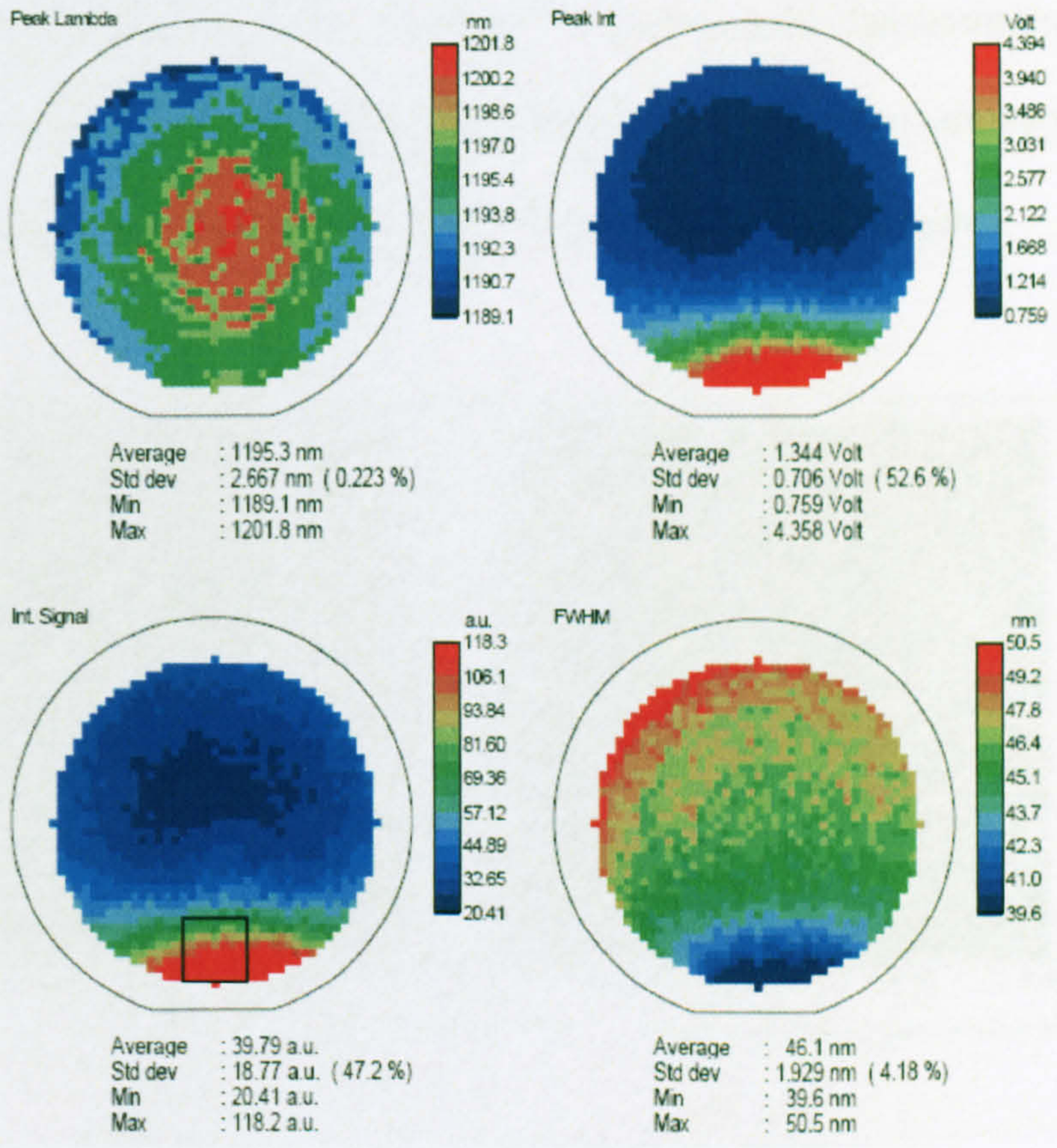

Fig.4.1.1. PL mapping of InAs on GaSb/GaAs wafer at room temperature, from top left to bottom right, the wavelength of the PL peak, Peak intensity in volts, signal intensity and FWHM. Square outline at bottom left indicates the area that was used

Prior to growth of the multi-layer QD structures an uncapped QD layer was grown in order to determine the QD density using atomic force microscopy (AFM). Fig.4.1.2 exhibits AFM images of (a) standard InAs/GaAs QDs and (b) the InAs QD sample grown with 1ML of Sb deposited at 500°C prior to the InAs deposition and nucleation. The QD density is found to be of a value of ~$6.0x10^{10}cm^{-2}$. This is nearly a two-fold increase compared to typical InAs/GaAs QD structures with dot densities of ~$2\text{-}3x10^{10}cm^{-2}$ [11].

The AFM image in Fig.4.1.2 (b) shows evidence of an inhomogeneous size distribution of QDs, but still no evidence of coalescence, demonstrating successful QD growth. Although the image is of lower resolution for the sample with InAs on GaSb/GaAs, it is still possible to accurately estimate the dot density.

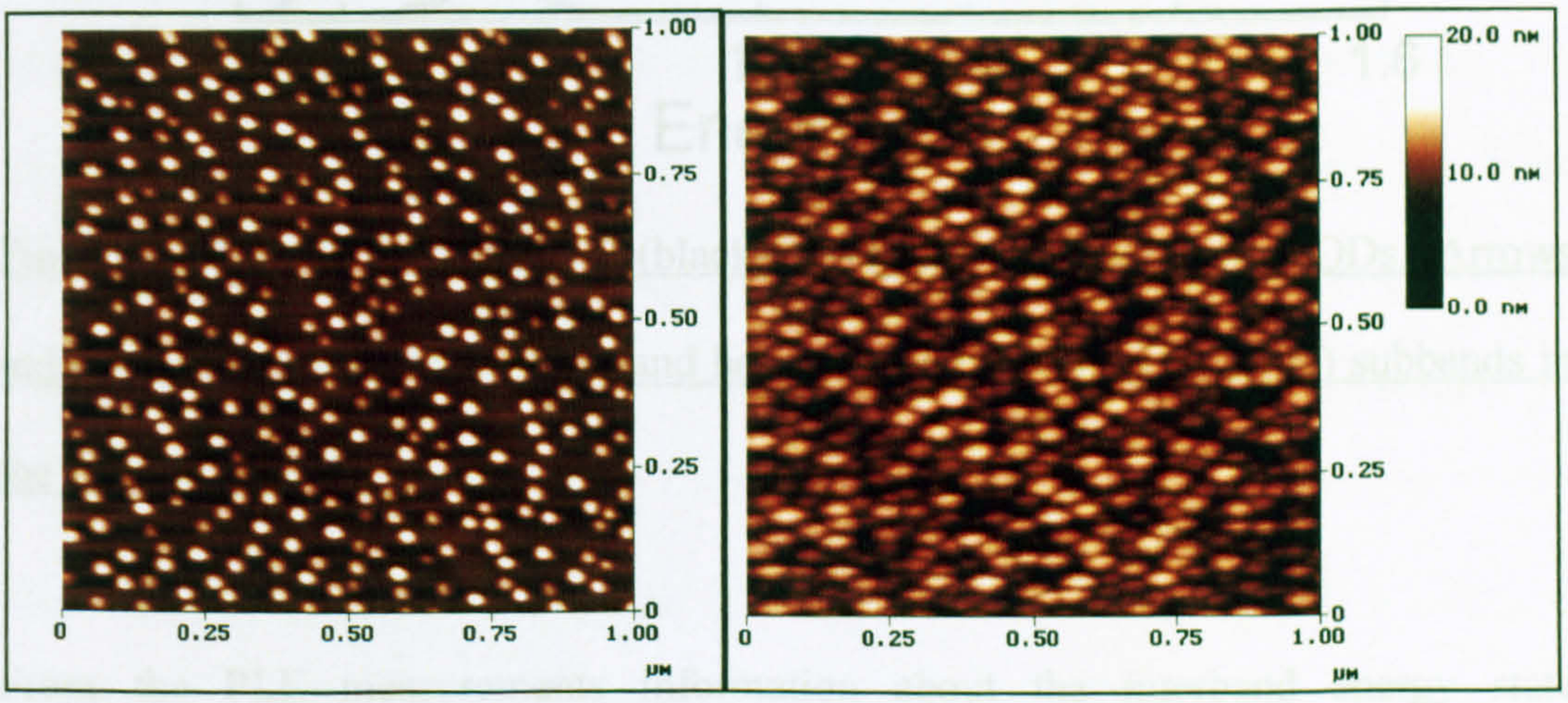

Fig.4.1.2: Atomic Force Microscopy (AFM) image of (a) standard InAs/GaAs QDs and (b) Sb-mediated grown InAs/GaAs dots with a dot density of ~$6x10^{10}cm^{-2}$ after deposition of 1ML of GaSb

The effect of this inhomogeneity is also observed in the PL spectra (taken at 77K and presented in Fig 4.1.3) as the high energy shoulder to the main PL peak, otherwise exhibiting narrow linewidth. In addition, PLE measurements were performed at 77K, which are also shown below in Fig 4.1.3.

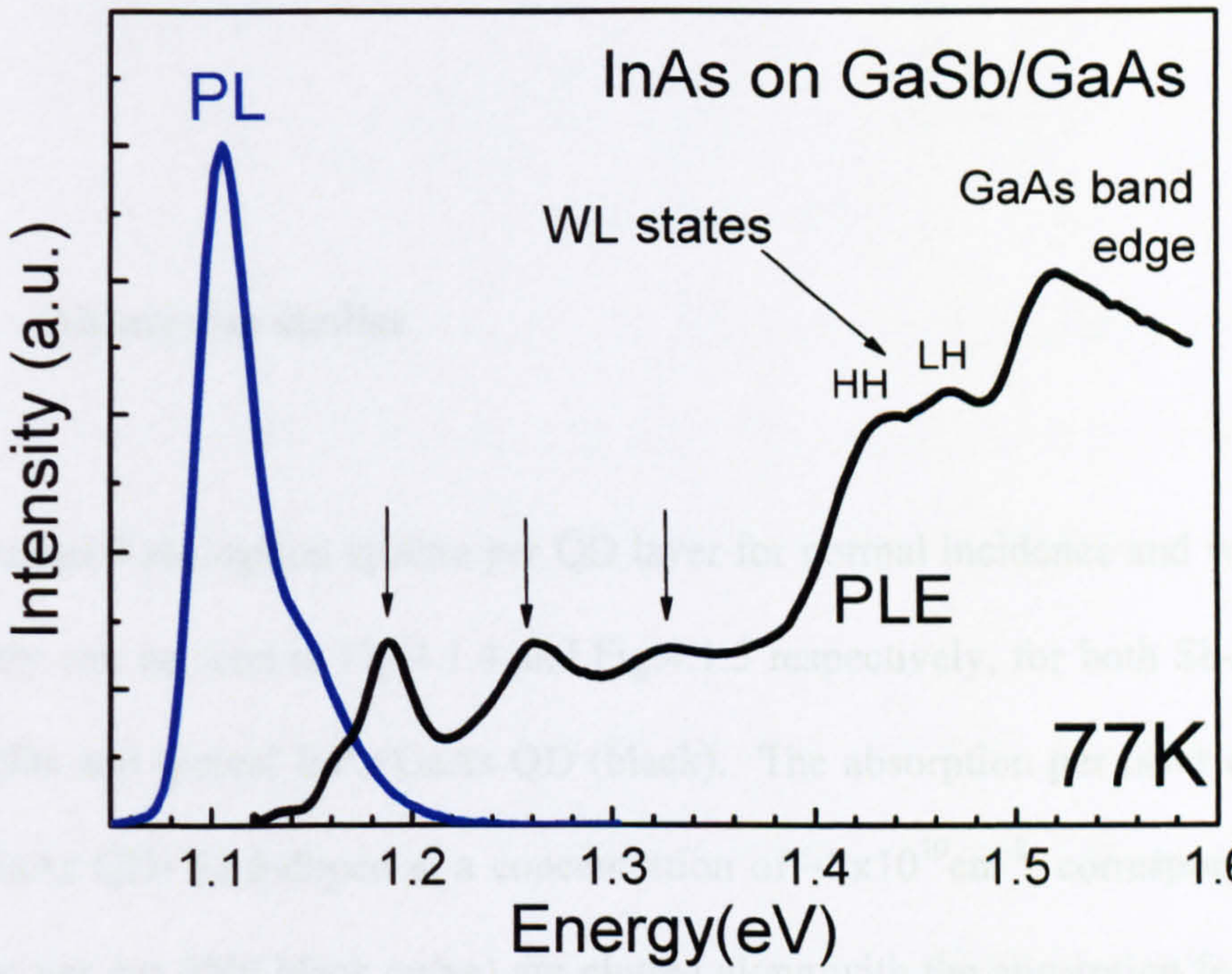

Fig.4.1.3. PL (blue line) and PLE (black line) for Sb-mediated grown QDs. Arrows indicate excited state transitions, and heavy hole(HH) - light hole(LH) subbands in the wetting layer (WL)

From the PLE measurements information about the interband energy state configuration is obtained. The energy spacing of the PLE peaks from the PL peak (ground state) attributed to states within the QD are approximately equivalent to conventional InAs/GaAs QDs [12], which verifies that the QD energy configuration is not altered with the incorporation of antimony. The first excited state (~1.187eV) is found to be at an energy ~82meV higher from the ground state (1.105eV)

followed by excited states in the QD at 1.26eV and 1.32eV (~155meV and ~225meV from the ground state respectively). The two peaks at 1.440eV and 1.468eV are attributed to wetting layer transitions from the electron ground state to heavy hole (HH) and light hole (LH) subbands respectively [12]. The feature at 1.52eV corresponds to the GaAs band edge.

4.1.3. Absorption studies

The intraband absorption spectra per QD layer for normal incidence and waveguide geometry can be seen in Fig.4.1.4 and Fig.4.1.5 respectively, for both Sb-mediated (red) QDs and typical InAs/GaAs QD (black). The absorption per layer of typical InAs/GaAs QDs Si δ-doped at a concentration of ~$2x10^{10}cm^{-2}$, corresponding to 1 electron per dot (thin black curve) are plotted along with the absorption for an InAs on GaSb/GaAs QD sample (thick red curve) doped at a concentration of ~$6x10^{10}cm^{-2}$ also corresponding to approximately 1 electron per dot for the increased density.

The normal incidence absorption in Fig.4.1.4 is associated with *s*-polarised transitions (electric field component of light parallel to the QD plane) from the QD ground state to non-degenerate *p*-like first excited states (*s*-*p*).

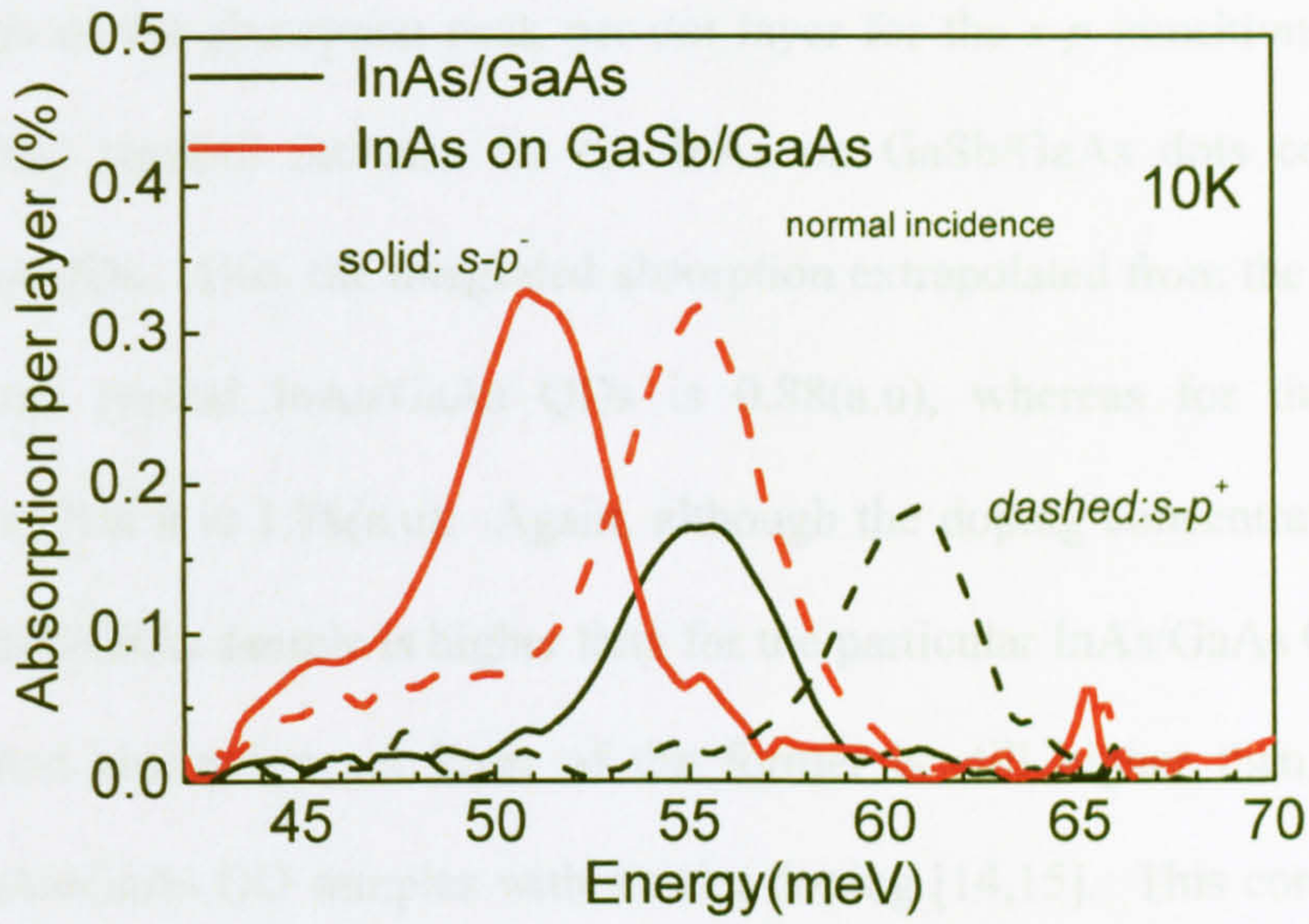

Fig.4.1.4: a) Intraband absorption per layer for InAs/GaAs QDs (thin black line) and InAs on GaSb/GaAs (thick red line) QDs for normal incidence. Solid lines represent s-p^- transitions whereas dashed lines represent s-p^+ transitions

The apparent red-shift between the InAs (55meV) and InAs on GaSb/GaAs dots (51meV) is within the range of 48-60meV, which is the typical range of variation for standard QD structures, depending on growth parameters. The normal incidence absorption peaks for s-p^- and s-p^+ transitions were measured for both samples along the [011] and [0-11] crystallographic directions respectively. A more detailed discussion of this splitting was discussed in chapter 3.1 and Ref [13]. The energy splitting for the InAs on GaSb/GaAs QDs is indeed smaller (4.4meV) than the value for the InAs QDs reported here (5.5meV), but is again within the range of values for typical InAs QDs [14]. Also, the splitting is typically ~10% of the transition energy so for lower transition energies the splitting also reduces. Using the same method as in chapter 3.1, the hole quantization energies can be determined by the comparison of interband and intraband results, and an energy of 31meV for the lowest excited valence band state transition was found.

The strength of the absorption peak per dot layer for the *s-p* transitions shows an approximately twofold increase for the InAs on GaSb/GaAs dots compared to typical InAs QDs. Also, the integrated absorption extrapolated from the spectra per layer for the typical InAs/GaAs QDs is 0.88(a.u), whereas for the InAs on GaSb/GaAs QDs it is 1.98(a.u). Again, although the doping concentration for the InAs on GaSb/GaAs sample is higher than for the particular InAs/GaAs QD sample, the integrated absorption per layer of the former is still higher than previously reported InAs/GaAs QD samples with similar doping [14,15]. This correlates well with AFM results in Fig.4.1.2. There is also evidence of a low energy shoulder on the intraband normal incidence absorption for the InAs on GaSb/GaAs sample, which could be attributed to the inhomogeneous distribution of QDs also observed in the AFM image and PL spectrum shown previously.

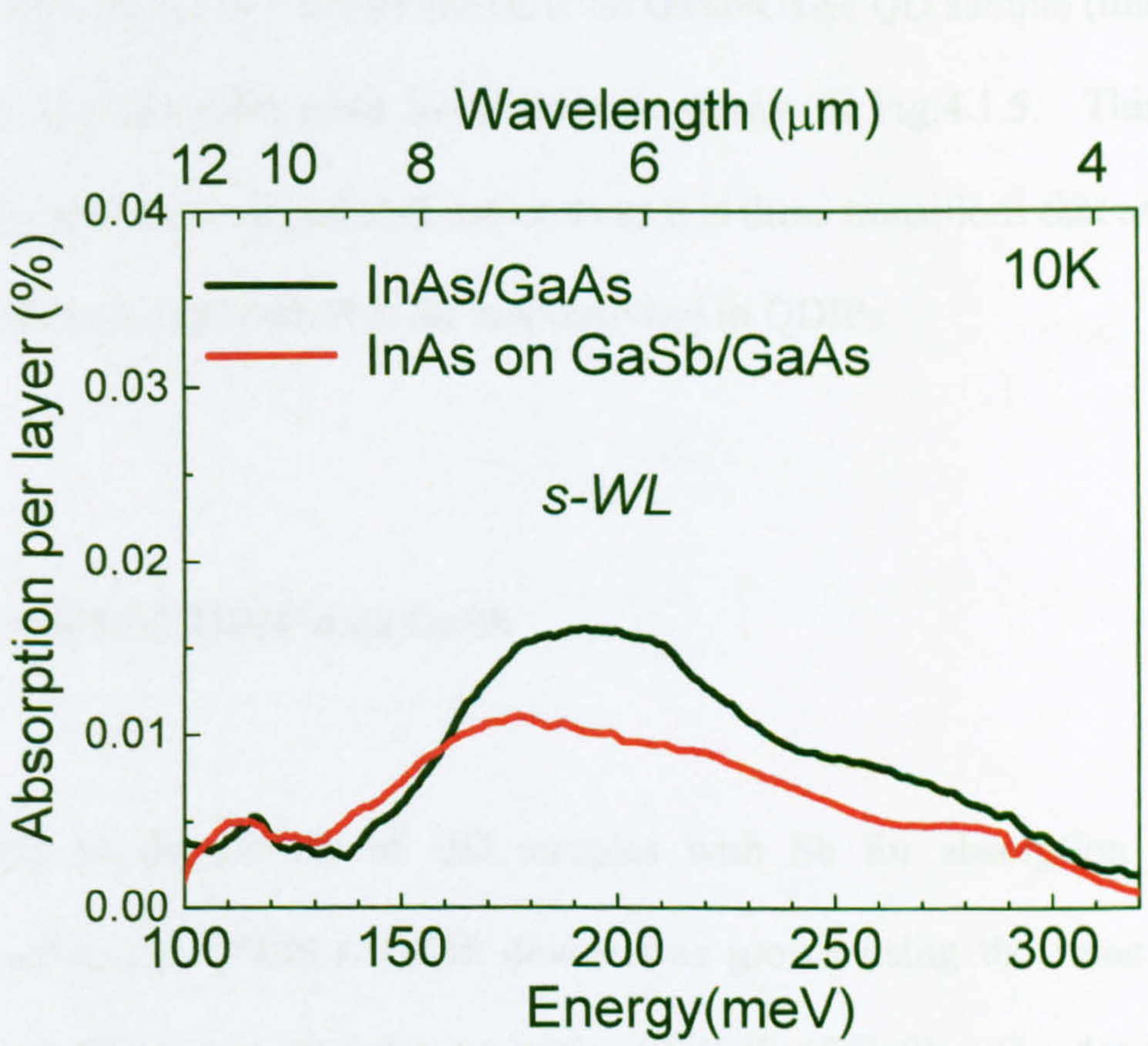

Fig.4.1.5 45° multipass waveguide p-polarised absorption per layer for, InAs/GaAs QDs (thin black line) and InAs on GaSb/GaAs (thick red line) at 10K

The higher energy absorption spectra measured at 10K is shown in Fig.4.1.5. It is evident that in this case the spectra are of a broader nature and are more complicated to interpret, since transitions from the dot ground state to both the wetting layer (WL) states as well as states within the dot (*d*-like, *f*-like states), and also to GaAs continuum states are contributing to the absorption [12]. Nevertheless, the combination of these mid-IR and far-IR spectroscopic results for normal incidence above, provide an effective method for probing the conduction band, and it is evident that there are no unwanted effects arising from the incorporation of antimony, since the transition strengths remain equivalent to those for typical InAs QDs.

Furthermore, an increase in the integral absorption for the mid-infrared transitions is observed by a factor of ~1.5 for the InAs on GaSb/GaAs QD sample (thick red line) compared to InAs QDs (thin black line) as shown in Fig.4.1.5. This is a very promising result for mid-infrared detectors as it is these transitions that are related to the photocurrent (and therefore the responsivity) in QDIPs.

4.1.4. DWELL QDIP with GaSb

In addition to the growth of QD samples with Sb for absorption studies, an InAs/$In_{0.15}Ga_{0.85}As$ DWELL QDIP device was grown using the same method of growing the QD layers after the deposition of 1ML of GaSb. The dot density was determined from AFM imaging to be of the value of ~$7x10^{10}cm^{-2}$. The device was grown containing 10 periods of InAs dots placed within an 80Å $In_{0.15}Ga_{0.85}As$

quantum well, with 20Å of the well below the dots and 60Å above, separated by 1000Å of undoped GaAs. The growth parameters and doping concentrations were as for the absorption sample, but with 3.0 monolayers of InAs deposited during QD growth. The overall device structure is otherwise the same as for the samples presented in chapter 3 (see, for example, section 3.5). The same problem of non-uniformity also occurred for the same reasons in this wafer. Again the area closer to the major flat was used to cleave process and fabricate detector devices.

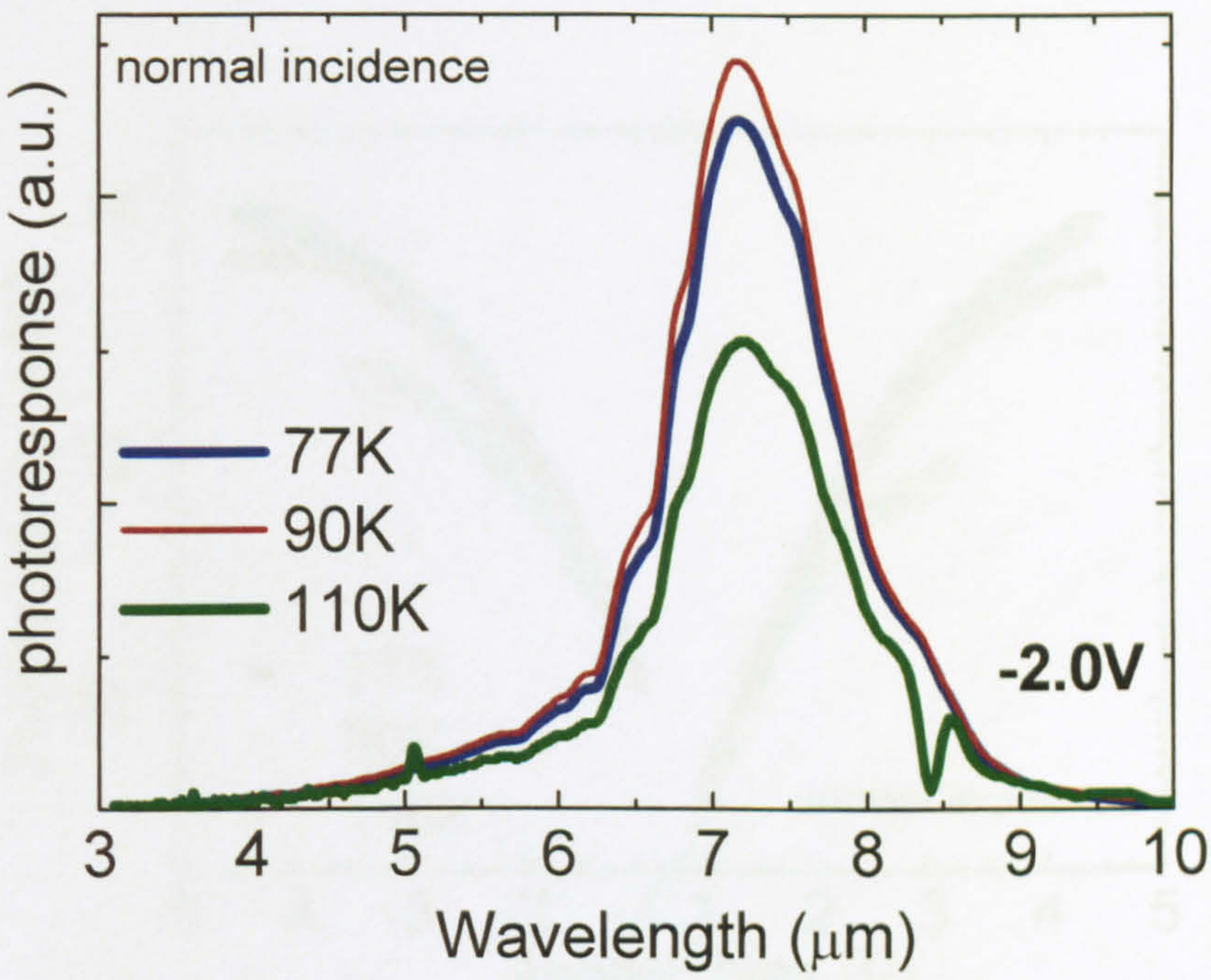

Fig.4.1.6. Spectral photoresponse for DWELL QDIP with GaSb at 77K (black), 90K (red) and 110K (blue) at normal incidence.

The photoresponse spectra measured at different temperatures (77, 90 and 110 K) exhibited a peak centred at a wavelength of ~7.5μm at -2.0V, shown in Fig.4.1.6. The spectra exhibit narrow linewidth ($\Delta\lambda/\lambda$~17%, FWHM=29meV) over a wide range of biases, and the bias dependence is similar to that previously reported for DWELL structures [16,17,18]. An increase of the photocurrent from 77K to 90K

was observed, due to thermally activated processes, typically observed for QWIPs and QDIPs [2, 19].

Furthermore a narrow photocurrent signal at the same operating bias was observable up to 110K. The peak responsivity R_p of the detector was measured using a black body source at 1005K at normal incidence. The bias dependence of the responsivity can be seen in Fig.4.1.7, and values of R_p ~1A/W were observed at around -4.0V at 77K.

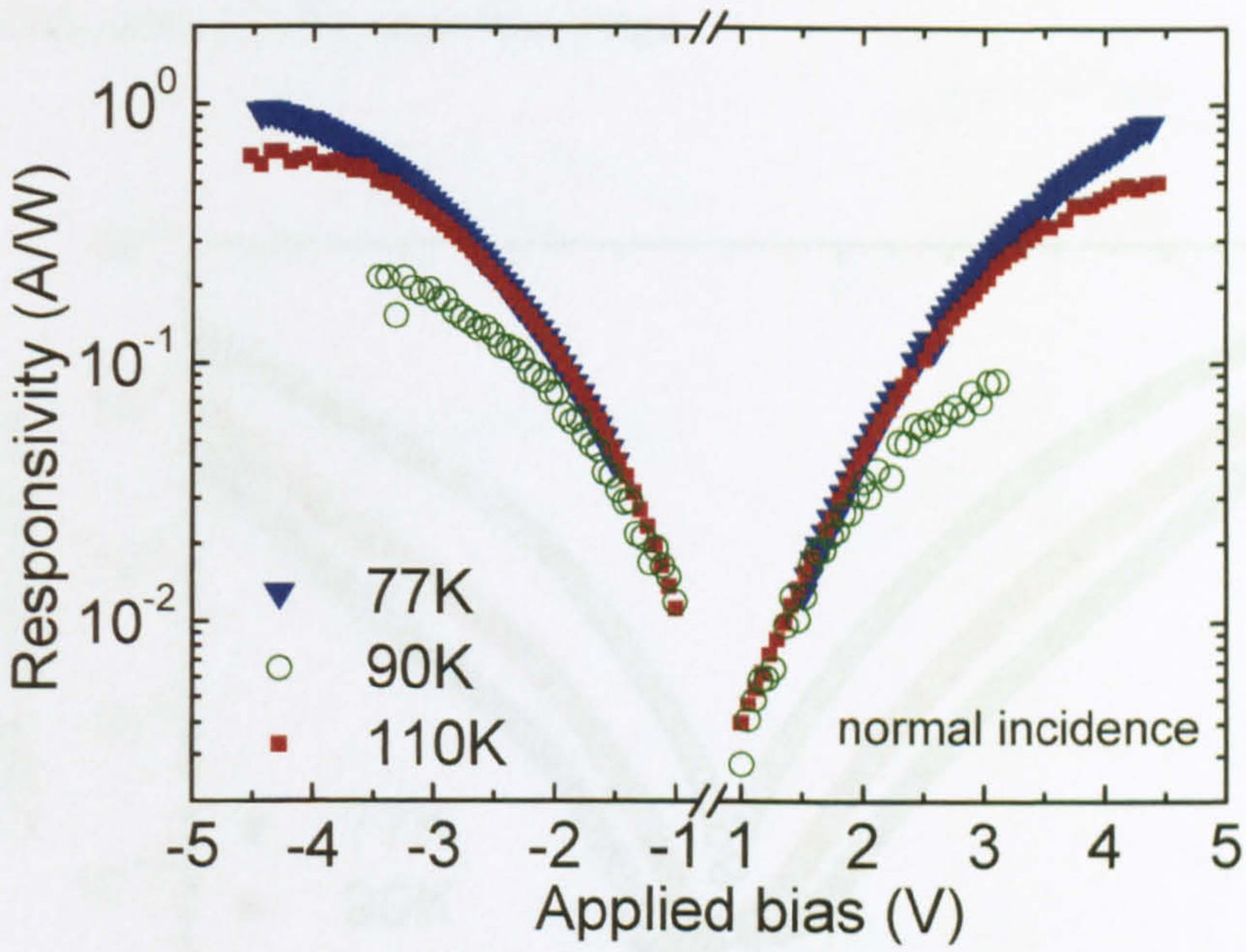

Fig.4.1.7. Responsivity for DWELL QDIP with GaSb at 77K (royal blue), 90K (wine red) and 110K (olive green) at normal incidence.

At this bias at 90K R_p only reduces to ~0.6A/W, whereas at 110K the photoresponse is overwhelmed by the dark current (I_d) at high biases, thus reducing the maximum operating voltage to -2.8V, where R_p is 0.16A/W (Fig.4.1.7).

The detector however, exhibited very good dark current behaviour with currents as low as 0.1μA at -3.0V at 77K (Fig.4.1.8) (10μA for previously grown detectors without Sb at similar conditions). As temperature increases thermal activation is enhanced and at 90K, I_d has increased by one order of magnitude (1μA at -3.0V). The detector was found to be background limited at 77K for a FOV 33° (f/3). The lower dark current for the DWELL QDIP with Sb could be explained by the fact that the effect of Sb also suppresses the formation of defects, as well as increasing the dot density [20]. However the larger barrier of 100nm compared to 50nm for the DWELL QDIP with the lowest dark current could also be the reason for the reduced dark current in the same bias range.

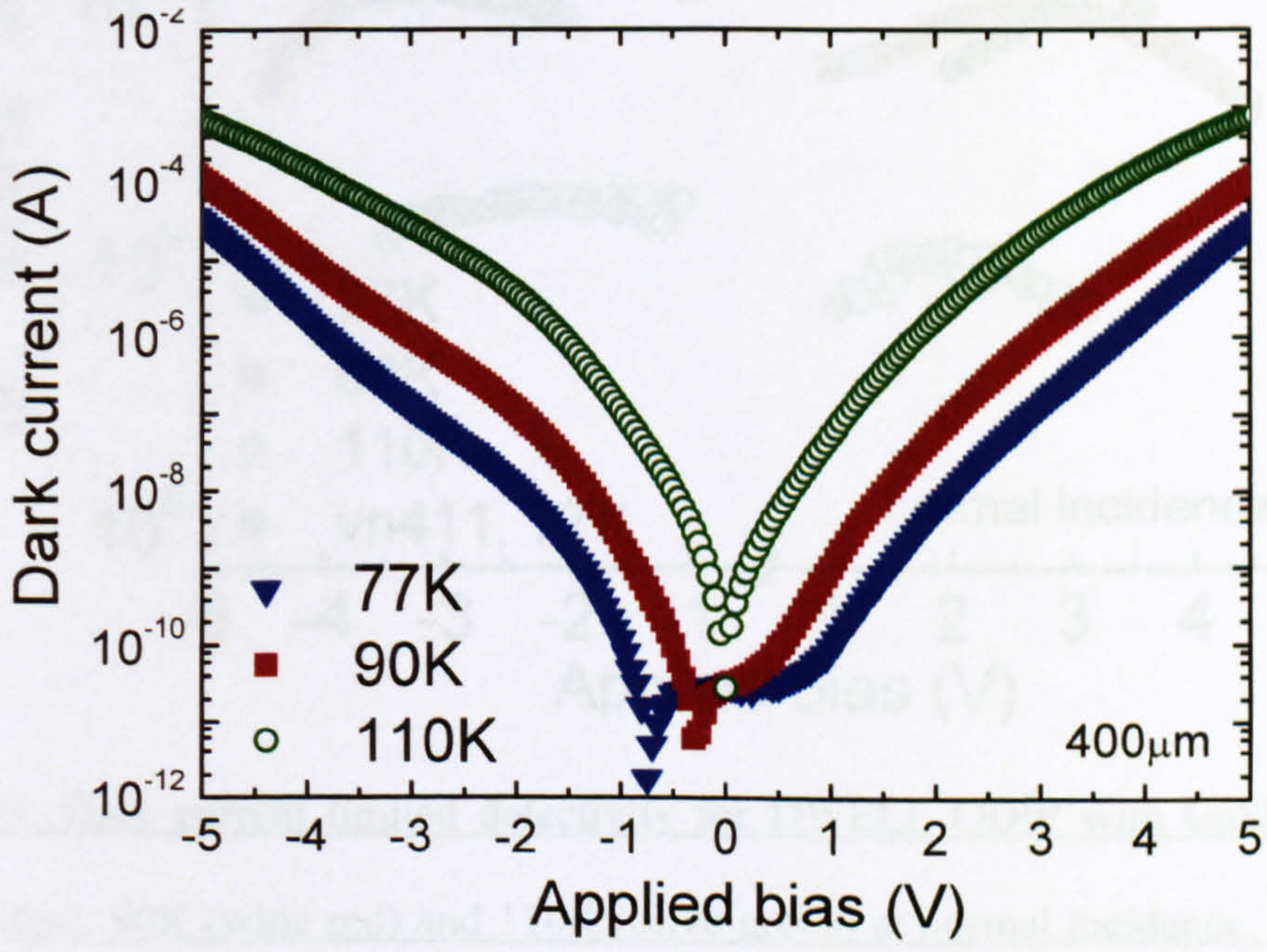

Fig.4.1.8. Dark current for DWELL QDIP with GaSb at 77K (royal blue), 90K (wine red) and 110K (olive green) for a 400μm diameter mesa device.

A high dark current limited detectivity (D^*_{DL}) was calculated at 77K of ~$5x10^{10}cmHz^{1/2}W^{-1}$ at -2.8V and 7.5μm (Fig.4.1.9), mainly due to the low dark

current ($1.5x10^{10}$cmHz$^{1/2}$W^{-1} for previously grown detectors without Sb at the same conditions). D^*_{DL} at 90K is reduced to $1.6x10^{10}$cmHz$^{1/2}$W^{-1} (for the same bias) since the increase of the dark current is faster than the increase in responsivity. D^*_{DL} was estimated to be ~ $1.5x10^{9}$cmHz$^{1/2}$W^{-1} at -2.8V and 110K, which is still one of the highest detectivities reported at this temperature for a DWELL QDIP grown by MBE in this wavelength range [2,12] pointing towards the realisation of high temperature QDIPs at this atmospheric window.

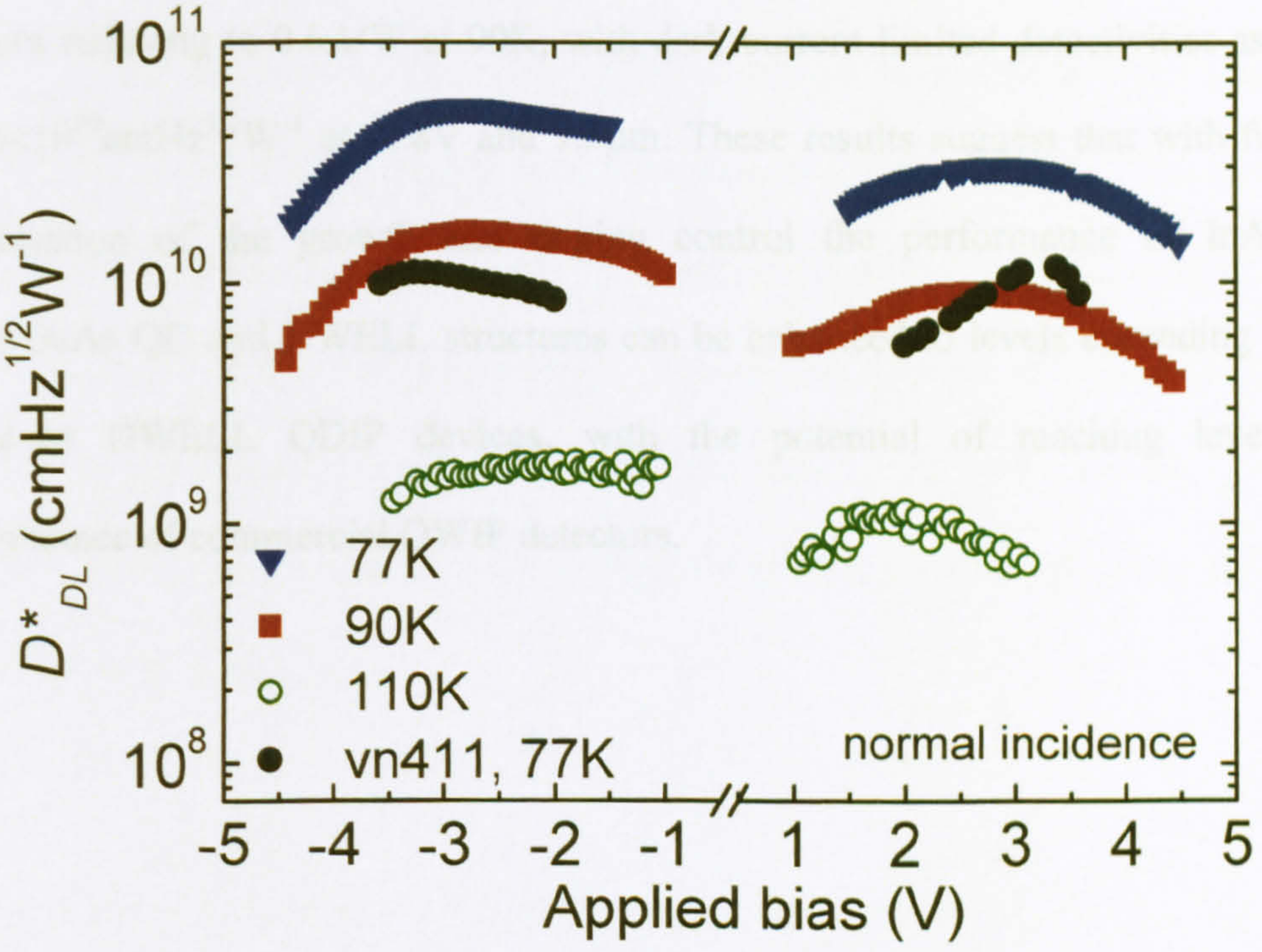

Fig.4.1.9. Dark current limited detectivity for DWELL QDIP with GaSb at: 77K (royal blue), 90K (wine red) and 110K (olive green) at normal incidence. Red dots represent the best 77K detectivity for a previous device (see Chapter, 3.5, Fig.3.4.4)

4.1.5. Summary

An increase in the quantum dot (QD) density from typically ~2-3x10^{10}cm^{-2} to ~6x10^{10}cm^{-2} via the deposition of 1ML of antimony prior to InAs QD growth, was reported. A ~2 times stronger intraband integrated absorption was observed, with no significant changes occurring to the energy band configuration of the QDs. Furthermore an implementation of this method to a quantum dot-in-a-well infrared photodetector was demonstrated, with responsivity values of ~1A/W at 77K and ~7.5μm reducing to 0.6A/W at 90K, with dark current limited detectivities as high as ~5x10^{10}cmHz$^{1/2}$W^{-1} at -2.8V and 7.5μm. These results suggest that with further optimisation of the growth and doping control the performance of InAs on GaSb/GaAs QD and DWELL structures can be enhanced to levels exceeding state-of-the-art DWELL QDIP devices, with the potential of reaching levels of performance of commercial QWIP detectors.

.

4.2. Incorporation of AlGaAs layers in InAs/InGaAs QD detectors

4.2.1. Introduction

As discussed in chapter 1, dark current is a major limiting factor in the performance of photoconductors (discussed in chapter 1.2), since it determines the maximum operating temperature of the device. QDIPs should, in principle, have low dark currents due to the 3D confinement of the electronic states [21,22]. This has been demonstrated experimentally for InAs QD based detectors [23,24]. Furthermore, it has been reported that by incorporating AlGaAs as barriers or current blocking layers [2], which have a wider bandgap than GaAs, one can suppress the dark currents even further, which could potentially lead to QDIPs operating at higher temperatures [25,26].

In this chapter, studies on the incorporation of AlGaAs layers in DWELL QDIPs, as barrier layers and current blocking layers, are presented. A significant suppression of thermal excitation has been achieved through this technique. However, the current blocking mechanism is also found to affect the photogenerated current, thus limiting responsivity. Nevertheless, evidence that this is a promising approach is presented, and the issues which need to be addressed for further application of this technique are identified.

4.2.2. Thick (50nm) AlGaAs barrier layers

A structure was grown to investigate the effect of having AlGaAs barrier layers instead of GaAs. The structure (vn359) consisted of a 5 period DWELL absorbing region, (1 electron per dot) with 2.55ML of InAs dots placed within an 80Å $In_{0.05}Ga_{0.95}As$ quantum well separated by 500 Å of $Al_{0.1}Ga_{0.9}As$ barrier layers. The indium composition in this structure was reduced to obtain approximately the same band-offset as the devices separated by GaAs barrier layers.

Of note is that these structures were grown on a double polished substrate since single polished substrates were not available at the time of growth. The double polished substrate is not a requirement for QDIP n-i-n device fabrication, and although it should make no difference, the growth at the time had not been optimised in terms of the temperature control during the growth. So although it is possible to draw conclusions on the use of AlGaAs barriers, it should be kept in mind that the growth was not of the usual standard.

The photoresponse for the first device is illustrated below in Fig.4.2.1. A DWELL like peak is observed for negative biases but not for positive. This could imply that the asymmetry of the dot within the well is higher, and that for positive biases the QW state is at a lower energy which is too confined with respect to the band edge. This could also indicate that the reduced indium composition significantly changes the strain in the structure, and hence the conduction band could be significantly different to the one presented in chapter 3, especially in terms of the in-build electric field (see chapter 3.3). This could affect the shape of the conduction band potential and cause the enhanced asymmetry in the photoresponse

It should be noted that the transition energy for negative bias is at higher energy than previous samples described in chapter 3. This could be attributed to the band gap for AlGaAs (even with a composition as low as y=0.1) being higher than GaAs, so that the combined y=0.1 and x=0.05 for the InGaAs QW does not correspond to the same offset for $In_{0.15}Ga_{0.85}As$ in GaAs (an estimated 10meV higher for the AlGaAs sample). Also the transition only appears in the spectrum for high values of applied bias (>-4.0V). This indicates that the state is deeply confined with respect to the band edge, limiting operation to a small bias range

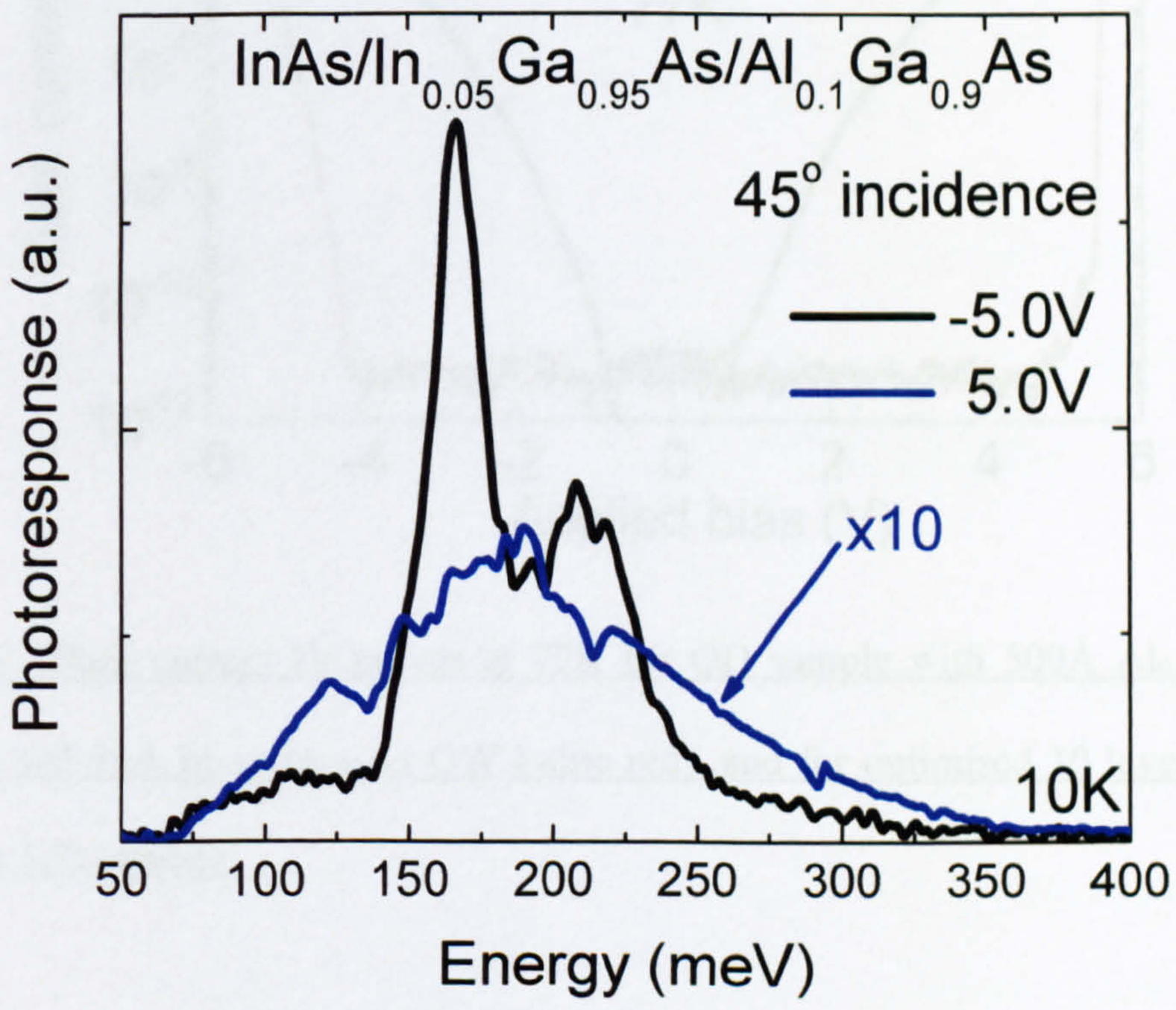

Fig.4.2.1. 10K spectral photoresponse of QD sample with 500Å $Al_{0.1}Ga_{0.9}As$ barriers and 80Å $In_{0.05}Ga_{0.95}As$ QW, measured at 45° polished geometry. The positive bias response does not exhibit DWELL like behaviour, and shows an increased asymmetry between negative and positive bias

Evidently from Fig.4.2.2, the dark current is drastically reduced in comparison with one of the lower dark currents previously measured for an InAs/InGaAs/GaAs device of the same diameter. The dark current is so low it is below the noise floor of the measurement unit up to ±4V. Once exceeding ±4V the dark current increases, with values which are still very low compared to the literature [2, 21-24] but again, only for a limited range of ~-4 up to ~-5V (Fig.4.2.1).

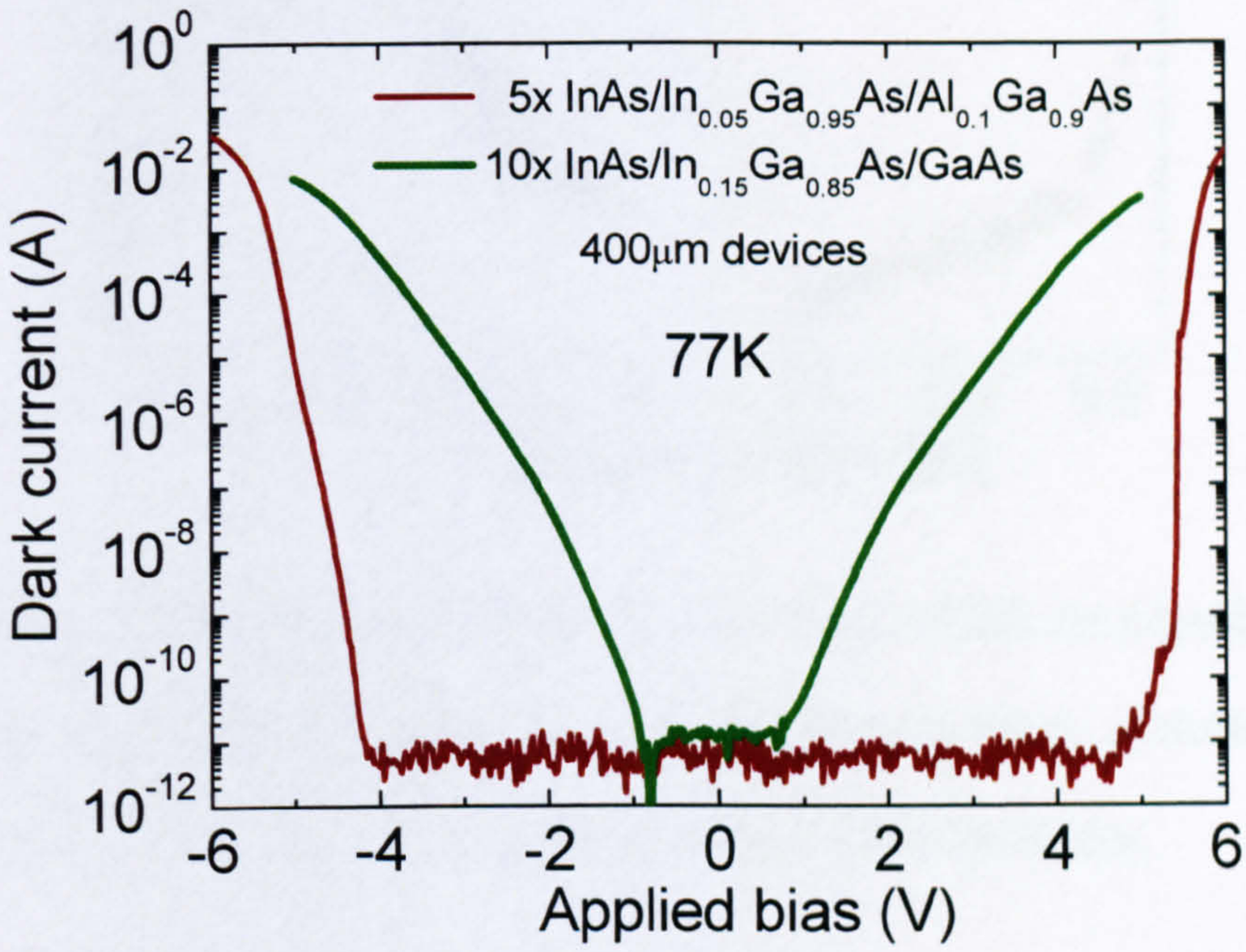

Fig.4.2.2. Dark current IV curves at 77K for QD sample with 500Å $Al_{0.1}G_{0.9}aAs$ barriers and 80Å $In_{0.05}Ga_{0.95}As$ QW (wine red), and for optimised 10 layer sample (chapter 3.5) (green).

The responsivity of the sample was measured and indeed found to be very low compared to previous GaAs barrier samples, which shows how the photocurrent is affected from the deep confinement of the QW state as well as the enhanced barrier height of the AlGaAs as shown in Fig.4.2.3. This effect has been observed by other reports on similar techniques [2]. This is undesired since for a good detector a good

optical signal is required, as well as a low dark current. However, this technique is not necessarily unrewarding, since there could be ways to optimise the performance of such a design.

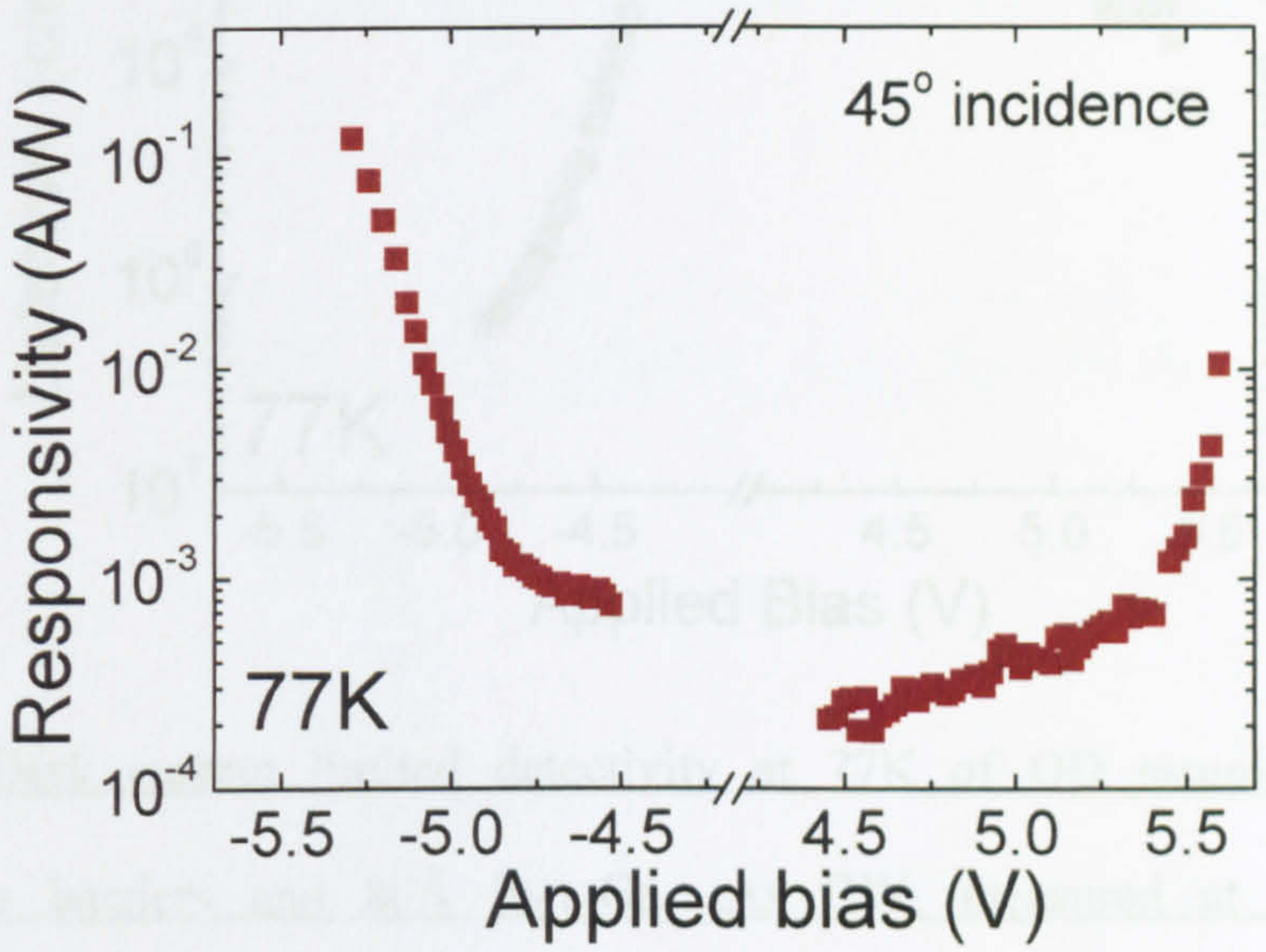

Fig.4.2.3. Peak responsivity at 77K of QD sample with 500Å $Al_{0.1}G_{0.9}aAs$ barriers and 80Å $In_{0.05}Ga_{0.95}As$ QW, measured at 45° polished geometry. The responsivity shows an increased asymmetry between negative and positive biases.

As discussed above the control over the temperature of growth of these particular device structures was not optimum compared to the growers' typical standards. Temperature control is of major importance in the growth of AlGaAs layers as to minimise non-radiative carrier traps/defect density, even for thin layers such as these [27-29] and this could significantly affect the performance.

A detectivity of ~$1x10^{10}cmHz^{1/2}W^{-1}$ at 77K and -4.2V was deduced, shown at Fig.4.2.4, which is a very good level of performance for a detector of such small responsivity and this number of layers, but again the detectivity only remains at this high level for a limited bias range.

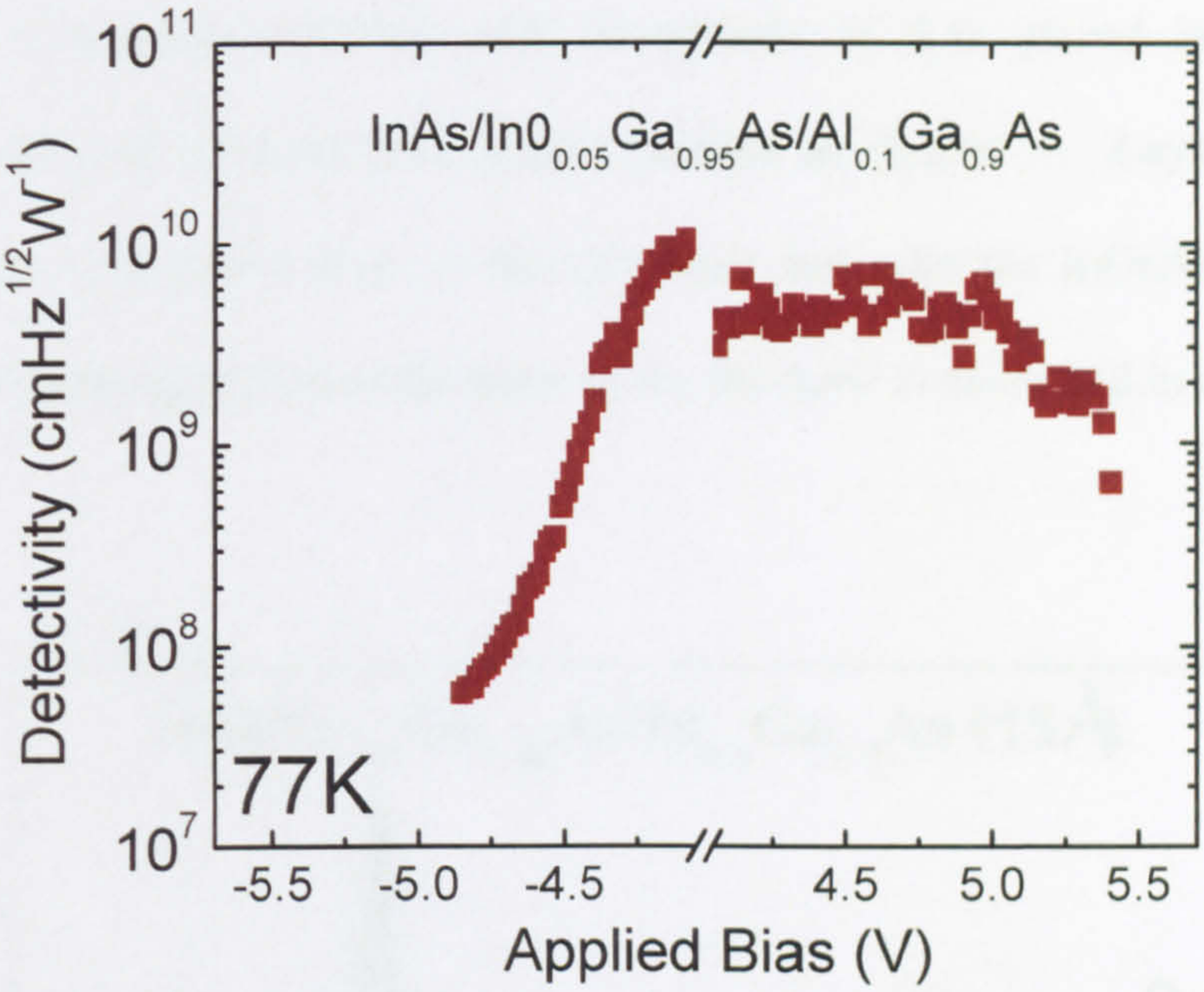

Fig.4.2.4. Dark current limited detectivity at 77K of QD sample with 500Å $Al_{0.1}G_{0.9}aAs$ barriers and 80Å $In_{0.05}Ga_{0.95}As$ QW, measured at 45° polished geometry.

4.2.3. Thin AlGaAs current blocking layers

Another technique of reducing the dark current with the incorporation of AlGaAs is by depositing thin current blocking layers which should in principle block the dark current while avoiding the introduction of traps in the AlGaAs, which is more probable for thicker layers. This technique is also easier to implement, and should in fact suppress the dark current while allowing the tunnelling of photogenerated carriers, and successful examples had been previously demonstrated in the literature using similar techniques [2].

A sample was grown (vn747) with 10 periods of dots placed inside an 80Å $In_{0.15}Ga_{0.85}As$ well as previously grown devices in chapter 3. Layers of 15Å of $Al_{0.2}Ga_{0.8}As$ were grown prior to the QD layer and after the InGaAs well. In all other respects the growth was the same as for the devices discussed in chapter 3.

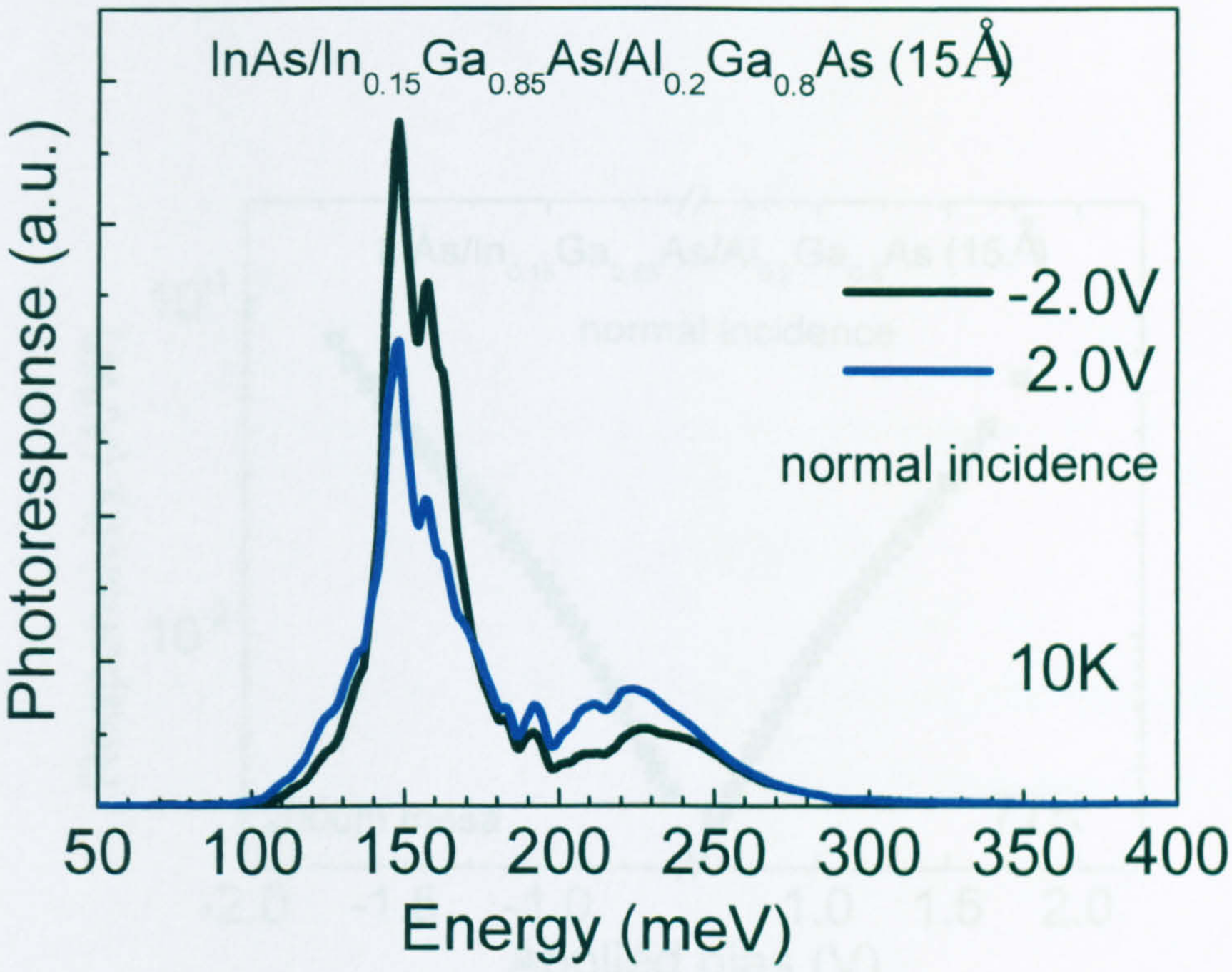

Fig.4.2.6. 10K spectral photoresponse at normal incidence of sample with $InAs/In_{0.15}Ga_{0.85}As/Al_{0.2}Ga_{0.8}As$ at -2.0 and 2.0V.

The device was found to have a relatively good photoresponse, exhibiting the expected features for a DWELL detector as shown in Fig.4.2.6. It is evident that the spectral behaviour is not affected by the AlGaAs current blocking layers as in the case of thicker barrier in the previous section.

What can also be extracted from Fig.4.2.6 is that the voltage required to see a transition from the QW, is much lower than previously, which is also beneficial in terms of technological issues in focal plane arrays. The hybridisation process (integrating detectors and read out-circuit) in FPAs is usually limited by the operational voltage of the read-out circuit, and typically detectors operating at voltages below 4.0V are preferable.

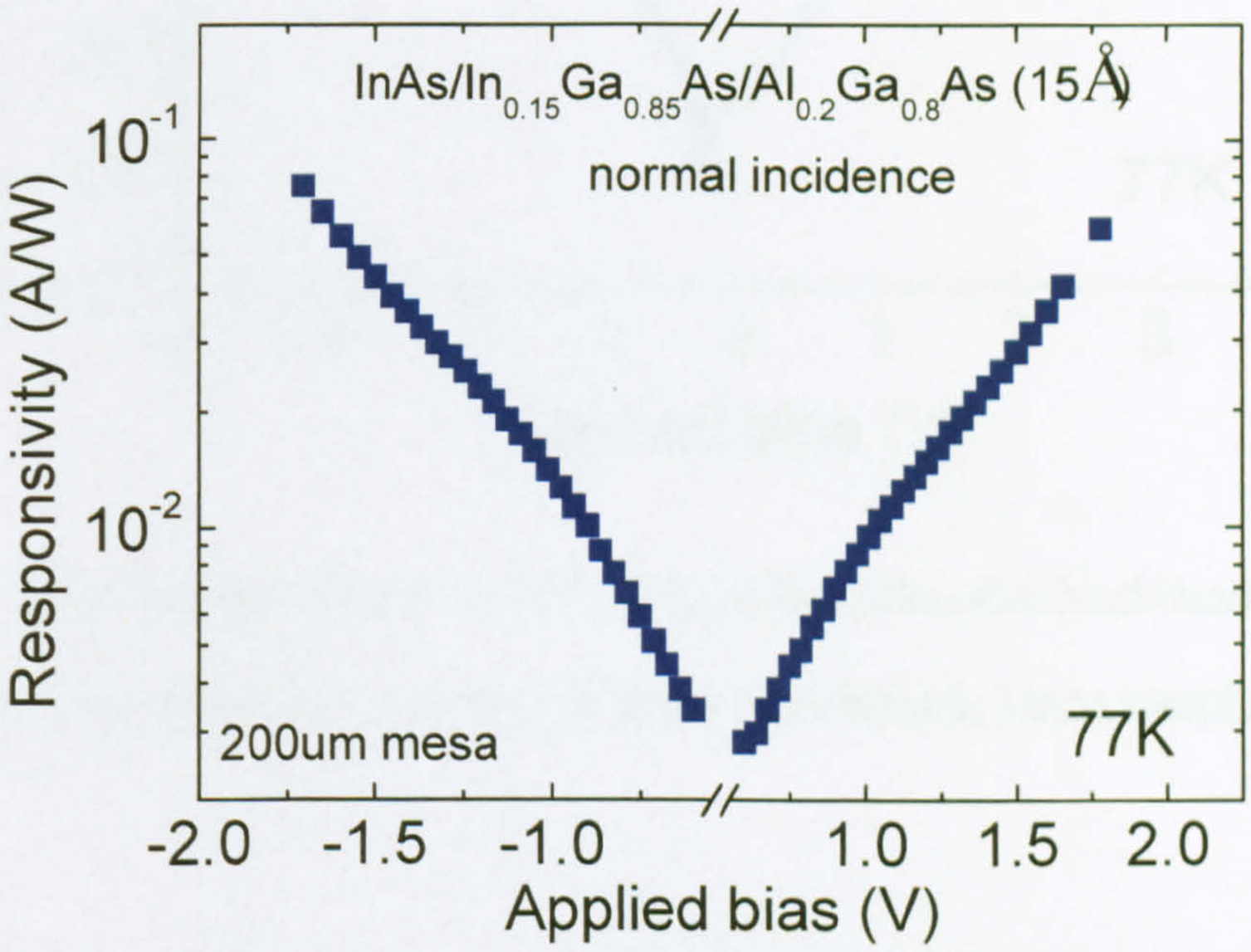

Fig.4.2.7. Peak normal incidence responsivity at 77K of $InAs/In_{0.15}Ga_{0.85}As/Al_{0.2}Ga_{0.8}As$ at 77K. The operating range is reduced from that at 10K, with maximum values going up to ±1.75V.

The peak responsivity of this device was found to have values of ~80mA/W at-1.7V and 77K for normal incidence. This is a lower value than previously observed for 5 layers of DWELL QDIPs with 1 electron per dot, without current blocking layers. It is reasonable that the responsivity decreases since, even with a thin barrier there will

be some suppression of the escape and tunnelling of photogenerated carriers as well as of thermally excited ones.

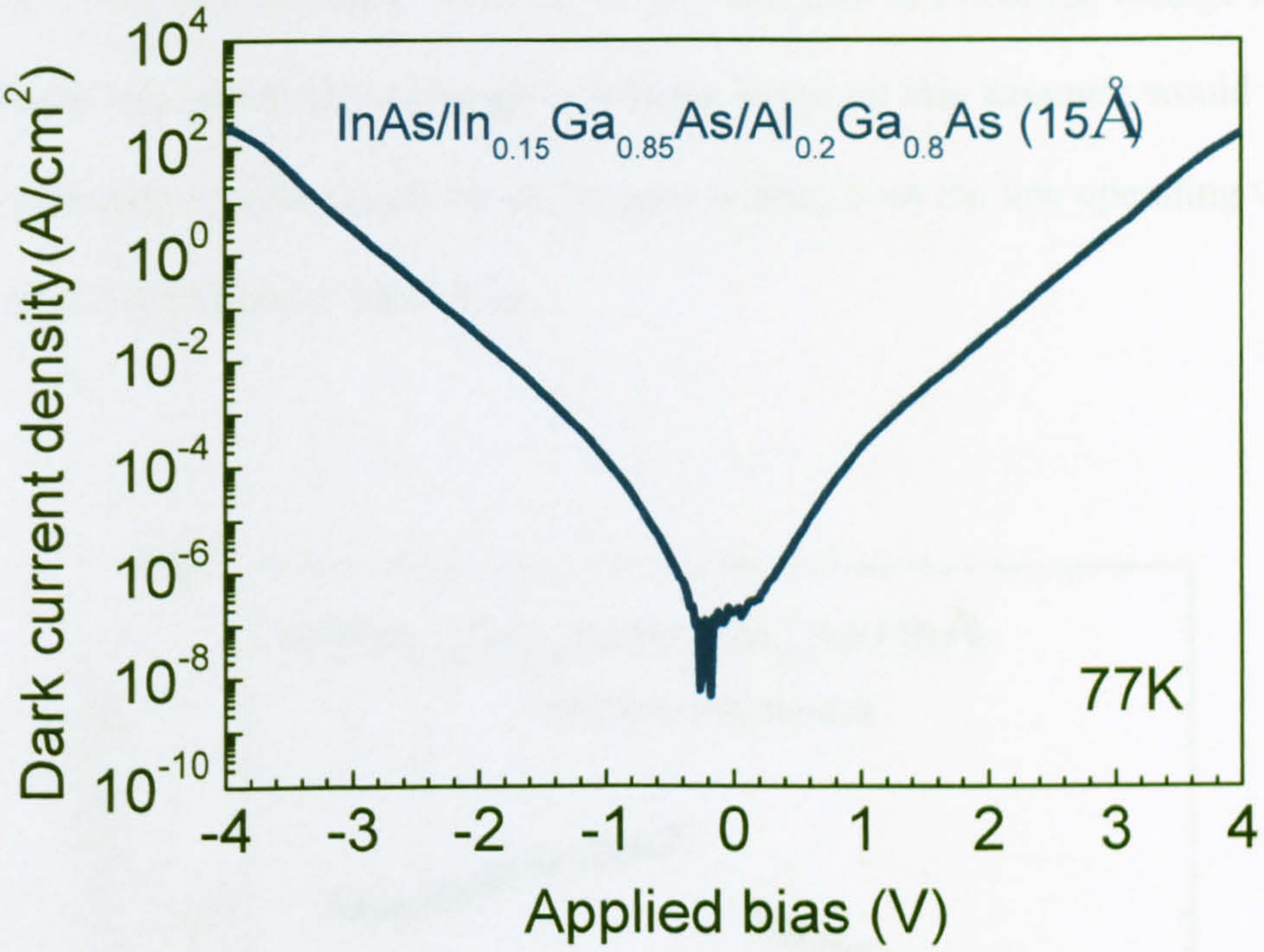

Fig.4.2.8. Dark current density at 77K of $InAs/In_{0.15}Ga_{0.85}As/Al_{0.2}Ga_{0.8}As$ at 77K, plotted along the curve for a 5 layer equivalent InAs/InGaAs/GaAs sample (vn190).

Nevertheless the dark current density for this sample was found to be low with values of $3x10^{-2}A/cm^2$ at ±2.0V. The dark current was not as low as for the thick AlGaAs barrier sample described in the previous section but at the same time this design had improved spectral characteristics while still suppressing the dark current compared to a design without AlGaAs current blocking layers. Fig.4.2.8. shows the dark current density IV curves of the sample with AlGaAs blocking layers.

The resulting calculated detectivity at 77K is illustrated below in Fig.4.2.9. It was found to exhibit a maximum value of $1.8x10^{9}cmHz^{1/2}W^{-1}$ at ~-0.6V. Although as an

absolute value this is inferior to the one measured for the sample with thick AlGaAs barriers (~$1x10^{10}$cm$Hz^{1/2}W^{-1}$), the latter exhibited such detectivity values at -4.2V and for a very limited range. This factor of 7 decrease of operating voltage is quite significant and means that although a detector based on this structure would have a smaller detectivity there could be advantages arising from the low operating voltage in terms of hybridisation into FPAs.

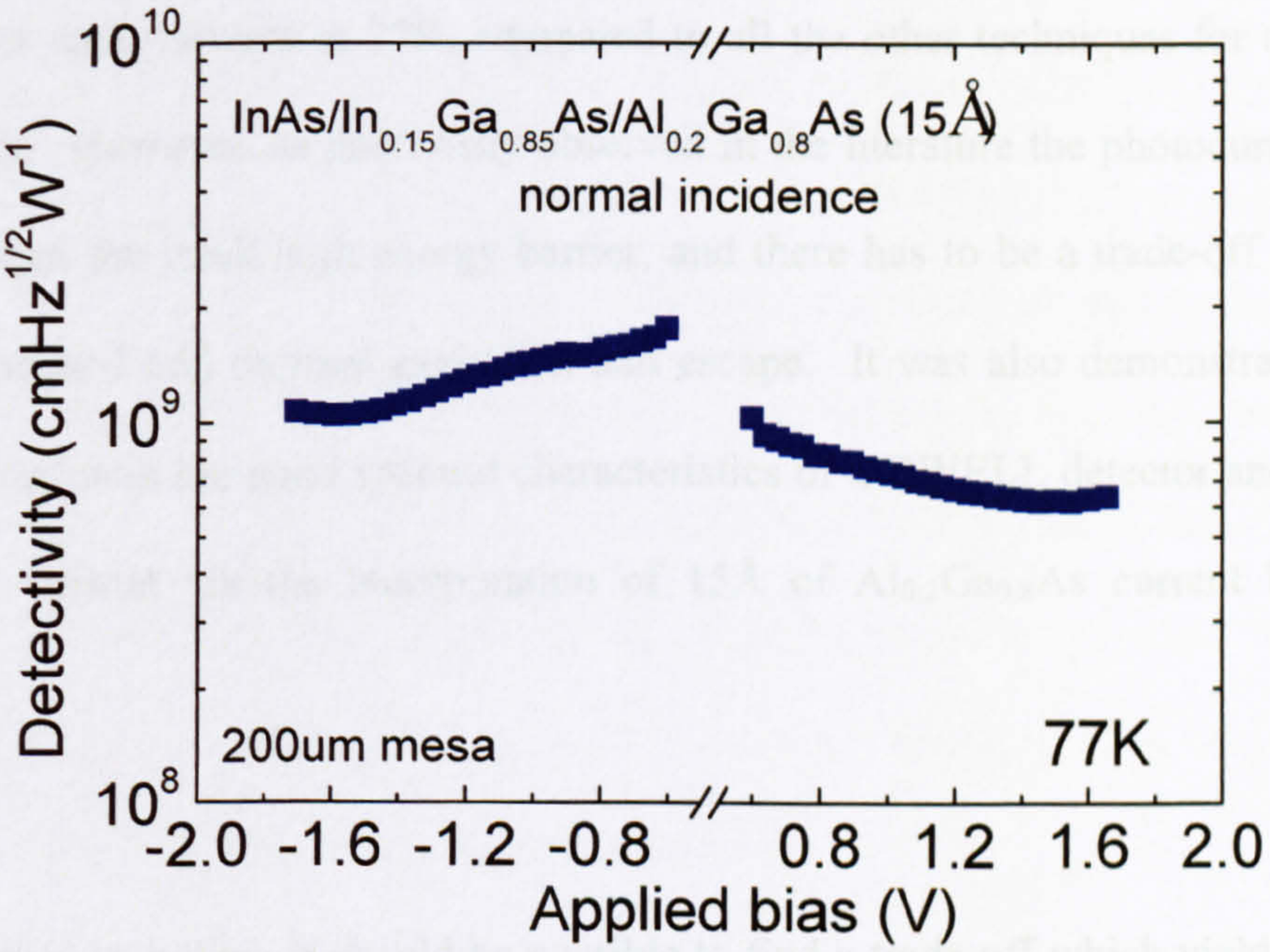

Fig.4.2.9. Dark current limited detectivity at 77K of $InAs/In_{0.15}Ga_{0.85}As/Al_{0.2}Ga_{0.8}As$ at 77K. The operating range is reduced from compared with the thick barrier sample ±1.75V, and maximum detectivity occurring at -0.6V.

Further more it is believed that the problems with the control of temperature of growth of Al have not yet been totally overcome, which could mean that this design is actually very promising for feature growths, and perhaps with a larger number of layers.

4.2.4. Summary

In the above section, 2 different design approaches to using AlGaAs layers were presented to reduce the dark currents in QDIPs, and thus improve the signal to noise ratio. It was shown how the dark current could be reduced with the use of these methods.

From all the above it would appear that using thick 500Å AlGaAs barriers results in the lowest dark currents at 77K, compared to all the other techniques for a similar bias range. However, as previously observed in the literature the photocurrent also suffers from the thick high energy barrier, and there has to be a trade-off between photogenerated and thermal excitation and escape. It was also demonstrated how one can maintain the good spectral characteristics of a DWELL detector and reduce the dark current via the incorporation of 15Å of $Al_{0.2}Ga_{0.8}As$ current blocking layers.

As a general technique it should be possible to find a trade-off which yields a good photocurrent/ dark current ratio using AlGaAs, and reports of successful structures have been presented in the literature mentioned above. It would also be a desirable system especially if the In content can be minimised as this would enable the growth of multilayer QDIP structures with >10 periods. However, there are issues such as the short wavelength of the final photocurrent state observed (<8μm), which would be unsuitable for operation in the LWIR. Also the introduction of non-radiative traps in thick AlGaAs layers, as well a intrinsic reduction of the photocurrent due to the high energy barrier present for AlGaAs.

4.3. Incorporation of GaP strain-balancing layers towards large absorbing regions in DWELL QDIPs

4.3.1. Introduction

As discussed in the above sections, one of the main issues concerning QD device performance is the lower mid-IR absorption for typical QD structures compared to equivalent QW devices. One way of addressing this issue by increasing the QD density, was the subject matter of section 4.1. Another way of increasing the overall absorption of a QD device, which is presented here (in this case a detector), is to grow multiple repeats of the active region. If 50 and more layers could be grown, this would lead to high gain and high absorption detectors [19], which could potentially lead to higher temperature operation.

So far structures with 5 and 10 QD layers have been discussed. The growth of many QD layers where each layer has QDs with similar size and density and is without defects for the InAs/InGaAs system becomes increasingly difficult once more than 10 repeats are exceeded [30,31]. Each layer is highly strained and, after several layers, dislocations will start to appear in the upper layers [32,33]. The strain introduced by the InGaAs which is compressively strained with respect to GaAs (see Fig.4.3.1), leads to strain relaxed dislocations affecting the optical and electrical performance severely. Even when thick GaAs spacer layers are used

between the layers, dislocations will occur when many layers are stacked. There are several techniques that are currently employed to deal with unwanted strain induced effects [34], including the growth of strain compensation (SC) layers. SC through the deposition of GaN_xAs_{1-x} layers had been reported [35] although it has be found to affect the QD growth, and also causes a red shift in the QD PL wavelength. Although this is beneficial for QD lasers aiming for operation near 1.55μm, in QDIPs operating in the LWIR this could be detrimental. There have also been a few reports of the use of GaP SC layers in the growth of QD test structures [3,36], as well as laser structures [37,38], and this technique is highly relevant to this section.

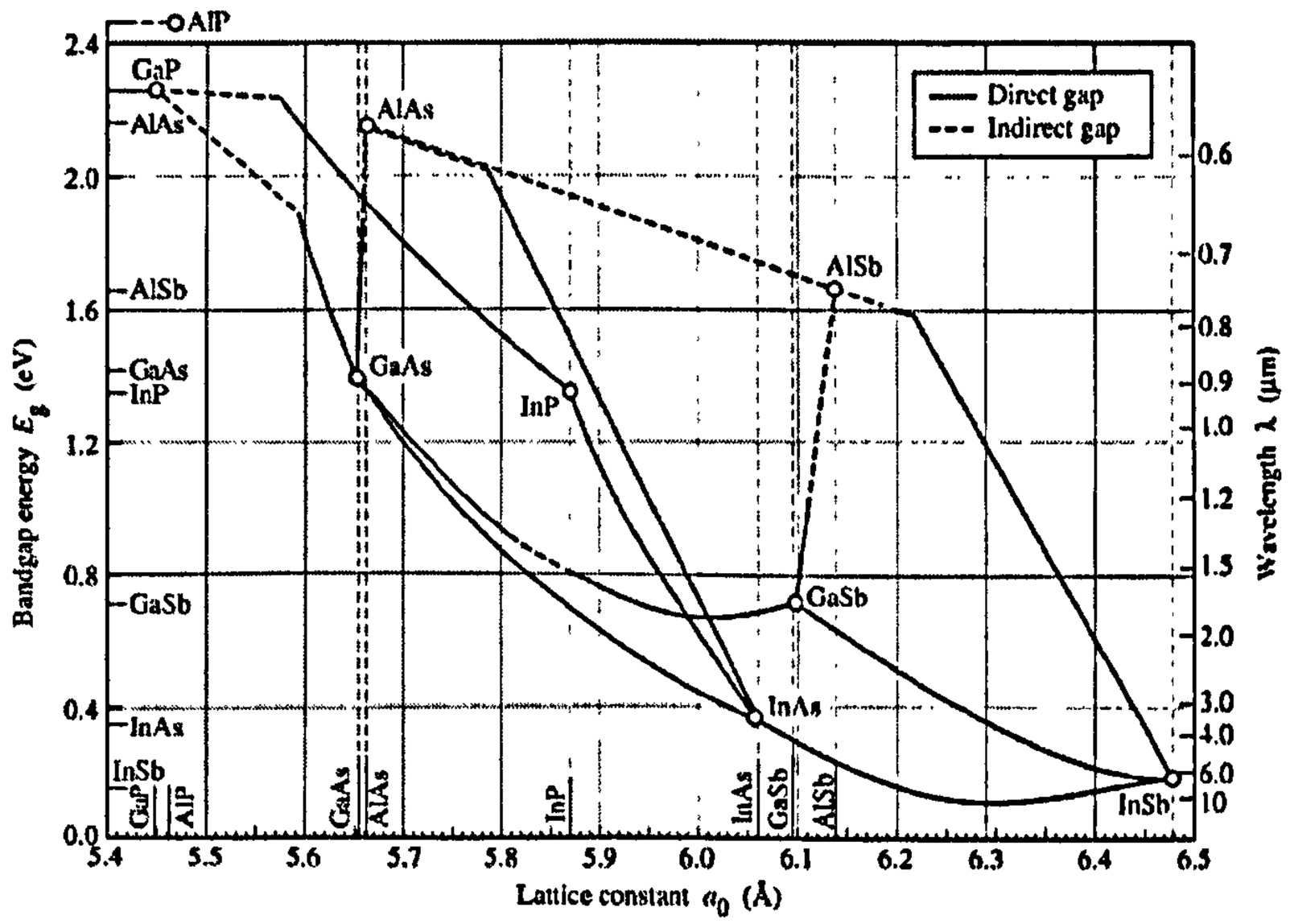

Fig.4.3.1. Bandgap energy and lattice constant of various II-V semiconductors at room temperature

This section deals with the incorporation of GaP strain compensating layers. GaP is tensile strained with respect to GaAs, with a lattice mismatch of 4%, and is therefore used to balance some of the compressive strain of the In (lattice mismatch ~7%

w.r.t. GaAs). Growing a thin layer of GaP before the deposition of the dots should enable the growth of 20+ layers of DWELL QDIPs, since the compensating layer would prevent the strain field from the previous layer affecting the nucleation of the dots in the upper layers of a stacked structure. This should in principle result in multi-layer structures where the bottom and top QD layers are similar in terms of dot density and size.

This technique has been previously demonstrated for InGaAs as well as InAs dots grown by metal organic chemical vapour deposition (MOCVD) [3,36]. An implementation of this technique in a laser structure was also demonstrated with beneficial effects [37]. So far, no demonstrations of MBE grown QDIPs with strain-compensating (SC) layers have been reported. Furthermore due to the larger conduction band offset of GaP relative to GaAs (~500meV-see Fig.4.3.4), the incorporation of GaP layers would introduce a current blocking layer, which could also help suppress the dark current.

4.3.2. Structural Information-Characterisation

In this investigation, three samples were grown to investigate the strain compensation properties of GaP and the effects on the electrical performance and optical characteristics of DWELL QDIPs. The overall MBE growth method was similar to that previously mentioned in chapter 3. In summary, 2.55ML of InAs deposited during growth, embedded in an 80Å $In_{0.15}Ga_{0.85}As$ QW, in a 500Å GaAs barrier matrix, with $1e^-$/dot. The three samples included a 5 layer sample, which

was grown to compare with previous non-compensated growths in term of the strain effects on the performance, a 20 layer sample to demonstrate the capability of growth of such a large structure without significant defects, and a further 5 layer sample with a smaller In composition (0.1) in the QW. All samples incorporated ~1ML of GaP roughly 40Å below the WL.

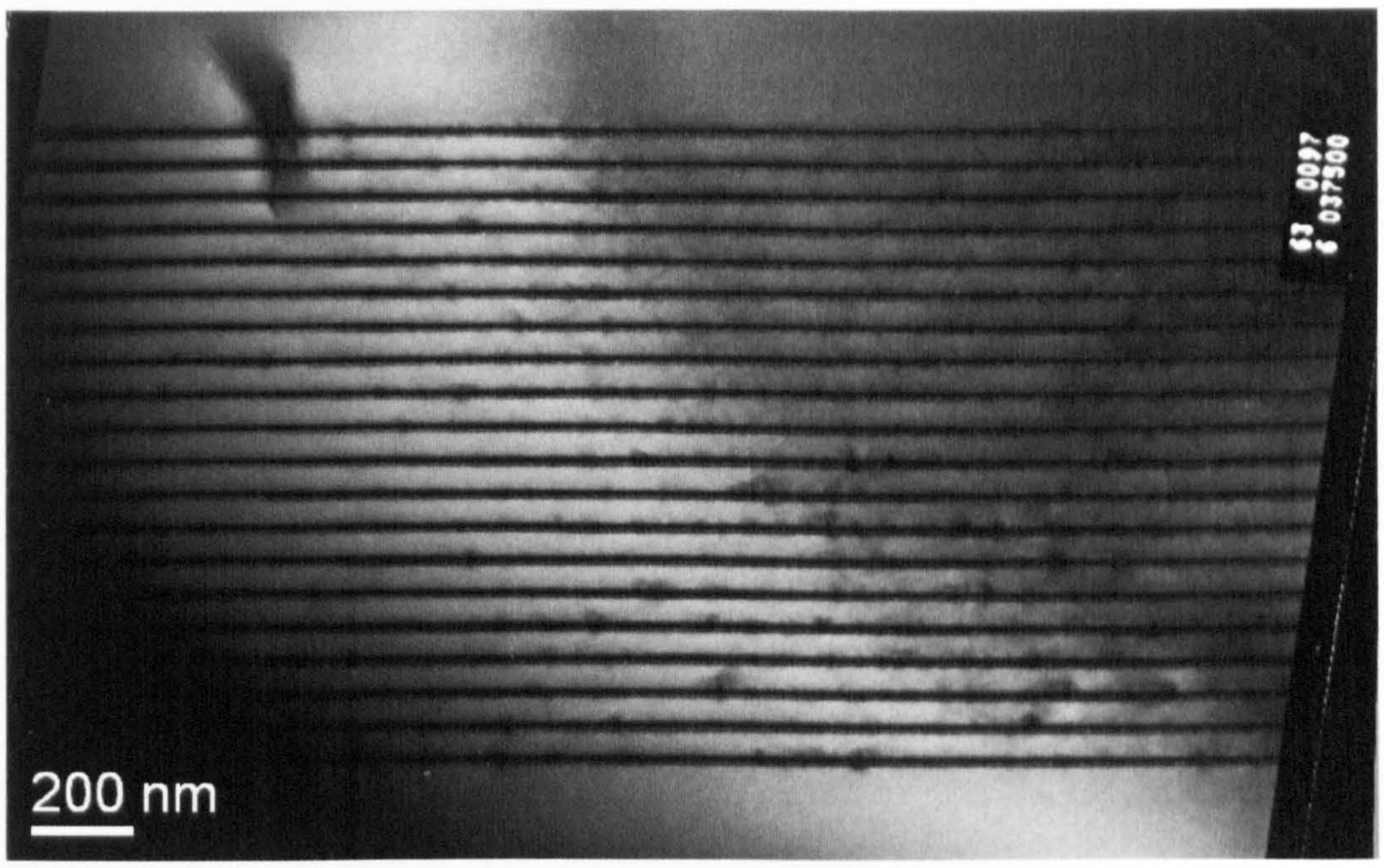

Fig.4.3.2. Cross-sectional TEM image of 20 layer InAs/InGaAs DWELL structure with 1ML of GaP deposited prior to growth

Cross-sectional transmission electron microscopy (TEM) was performed to observe the layer quality. The image shown in Fig.4.3.2 is the TEM of the 20 layer structure showing overall good quality, and with the exception of the relaxed dislocation on the left hand side of the image the structure seems relatively defect-free. It is evident that there are areas of localised defects, but these can also arise when the sample is cleaved for preparation of TEM imaging. If one zooms in the

image with the TEM, it can be observed whether the top and bottom layers are of similar dot size and density. Unfortunately high resolution TEM was not available, and as can be seen from the images in Fig.4.3.3, it is hard to distinguish accurately and furthermore quantify the variation of dot size and density. It is possible to distinguish from these pictures that the QDs seem to be 'flatter' than conventional DWELL QDs, particularly for the bottom and middle layers.

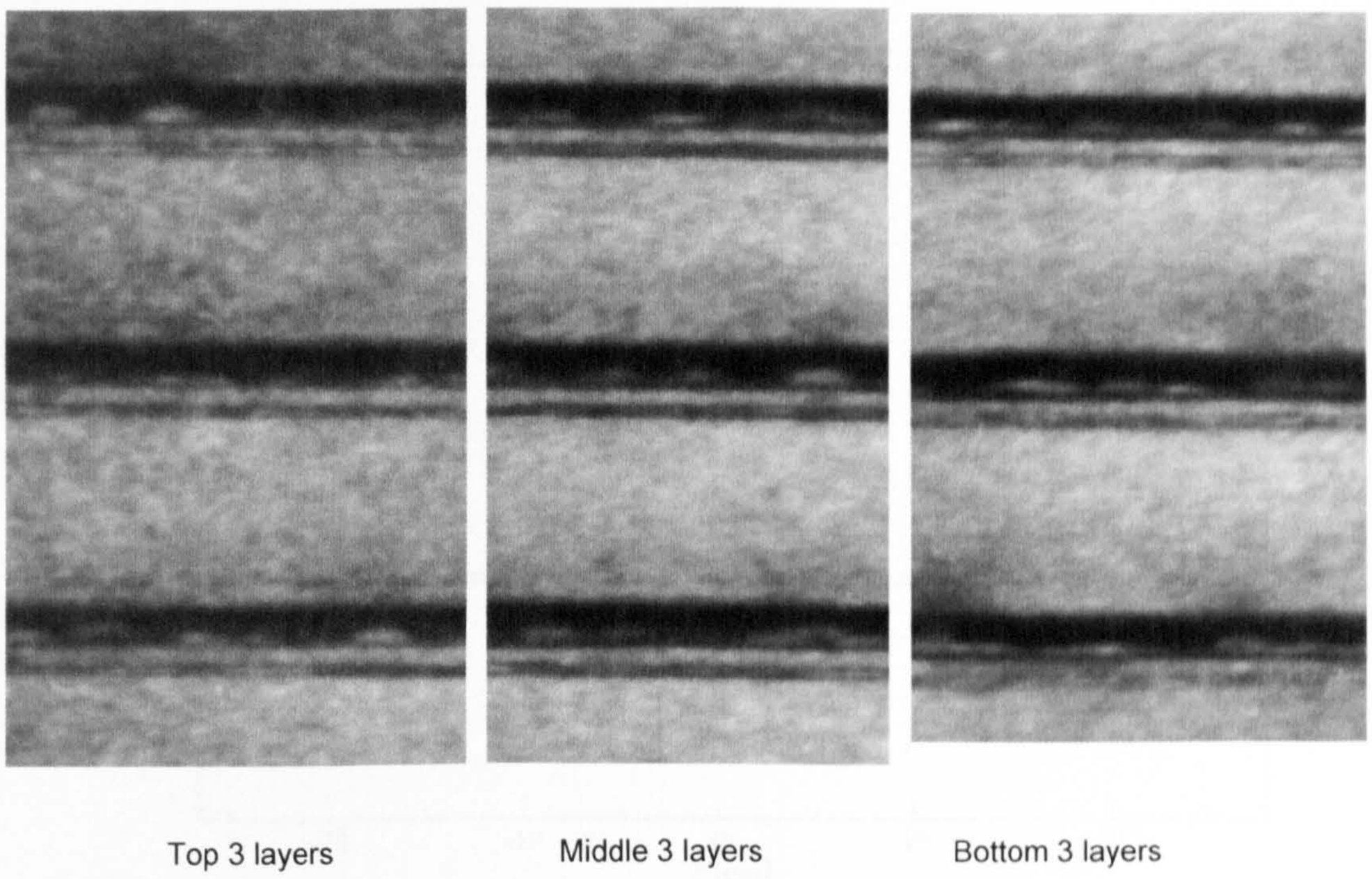

Fig.4.3.3. Magnification of the Cross-sectional TEM image of the 20 layer InAs/InGaAs DWELL structure with 1ML of GaP, 40Å below the WL, showing the top, middle and bottom 3 layers of the structure

Apart from balancing some of the strain, it has been shown [3] that if the GaP layer is close to the WL or in fact directly below it, the surface roughness is smoothed out causing changes to nucleation and therefore dot density, as well as a reduction of dot size for the upper layers. Lever et al [3] had shown that it was better to have the

GaP layer away from the dots at 200Å below the dot layer and 100Å above for a 300Å barrier, to avoid alterations in dot size and density. The distance should not necessarily be the same in the case of MBE grown QDs, but it is a good indication that the GaP layer should not be close enough to the QD layer to affect nucleation.

This distance was chosen to be 40Å, which now is believed to have been underestimated. For a 500A barrier like the one in our case, the GaP layer should have perhaps been 200Å above the dots and ~300Å below the consecutive layer.

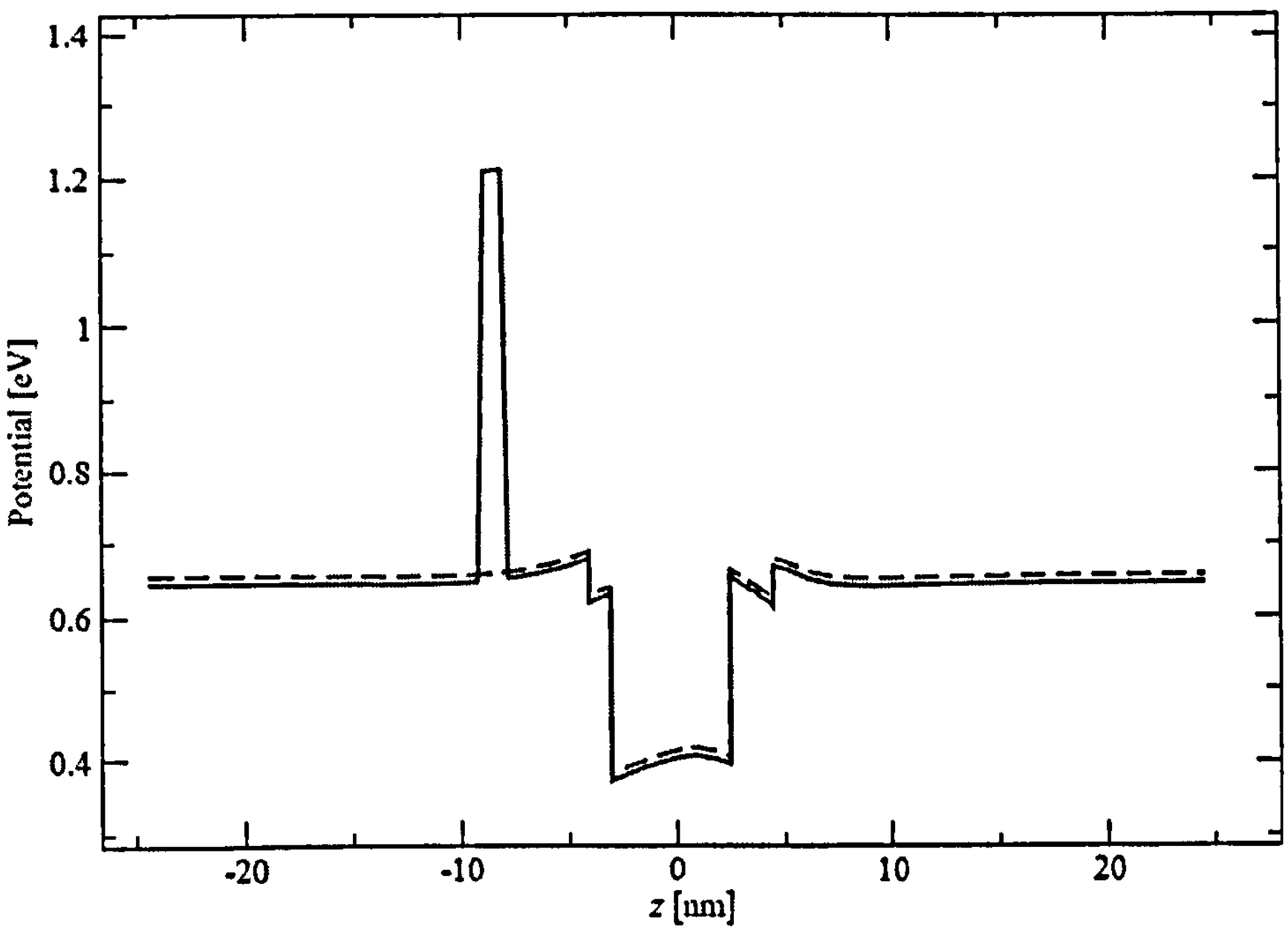

Fig.4.3.4. Calculated profile of DWELL QDIP with 10Å GaP layer 40Å below the InAs/InGaAs region.

A calculation of the conduction band is shown in Fig.4.3.4 and has been provided by Nenad Vukmirovic*. The calculated profile shows the strain-induced built-in electric field effect at the interface of the QW and the barrier. This is slightly reduced compared to the calculated profiles at chapter 3.3. As mentioned

*N. Vukmirovic, '*Physics of Intraband Optoelectronic devices*' PhD Thesis, Institute of Microwaves and Photonics (IMP), Leeds University, 2007

previously, the GaP also provides a current blocking layer which would potentially suppress the dark current (as well as the photogenerated signal, see previous section 4.2). It has been shown for laser structures with GaP SC layers that by increasing the thickness of the GaP layer the strain compensation can be increased [9]. After a 'critical thickness' the tensile strain will exceed the compressive strain it is meant to balance, leading to 'anti-dot' formation. Also, with the increase of GaP thickness even below the critical level, the barrier thickness would increase, and the escape of photoexcited carriers would become less probable. Nonetheless, the dark current would decrease as well, and an optimum could be reached.

Therefore in terms of optimising the design of the SC layers one needs to consider the position of the layer in terms of the effects of GaP on nucleation, as much as the optimum thickness of GaP in terms of strain compensation and tunnelling efficiency.

4.3.3. Detector performance

Although from structural characterisation, it seemed that the overall growth was successful, the GaP did not help to improve QD detector performance. The dark current was measured at 77K for the 5 layer and 20 layer samples. Compared to previous 5 layer DWELL detectors a decrease in dark current was observed, with increased asymmetry attributed to the conduction band barrier introduced by the

GaP incorporation as illustrated in Fig.4.3.5. It was also observed that for the 20 layer sample the dark current characteristics clearly deteriorated. This indicates that defects were indeed introduced even if the GaP did provide partial strain compensation. In order to achieve good quality multi layer DWELLs with GaP SC layers, there needs to be further optimisation with respect to the thickness and position in the barrier of the GaP layer. It should be noted that this design was a first attempt, and did not follow from an optimisation process.

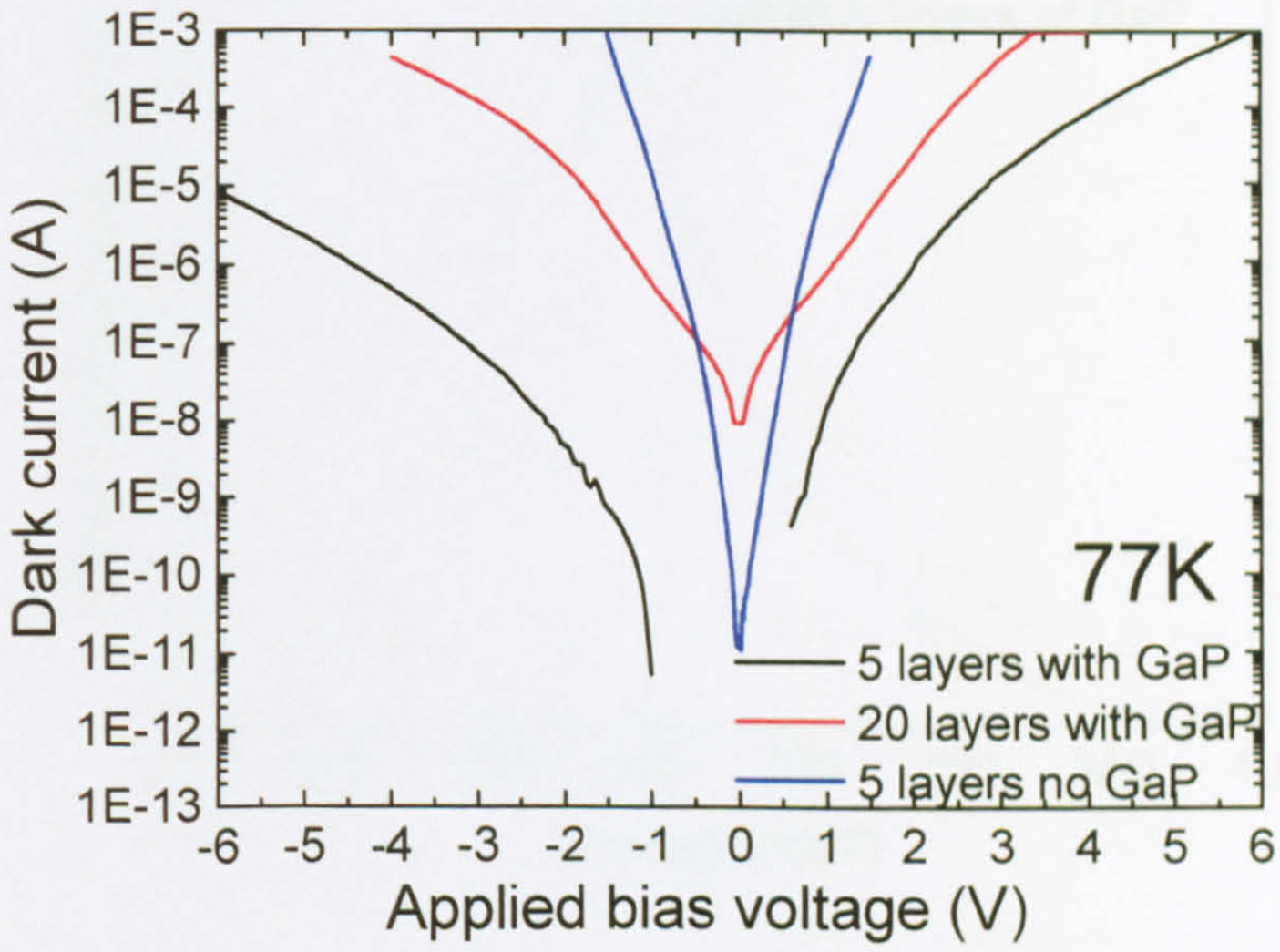

Fig.4.3.5. Dark current IV curves for samples with GaP and control sample at 77K.

Nevertheless the reduction of the dark current for the 5 layer sample is a combined effect of the barrier offset and a reduced defect density in the structure. Therefore the strain is partly balanced for 5 layers, although further attempts of growing such a structure would be required to achieve many period layers of low defect densities.

As mentioned previously, another parameter that was underestimated was the distance of the GaP layer from the dot layer to avoid the effects of GaP on QD

nucleation. As a result of this it is possible that the QD size has been affected thus altering the expected conduction band configuration. The spectra of these devices for either 5 and 20 layers, were observed to be of a broad nature centred around 220-200meV respectively (Fig.4.3.6), for the full range of their operating bias, indicating that the observed response is due to bound to continuum transitions. This could mean that somehow the tunnelling from the QW state is suppressed.

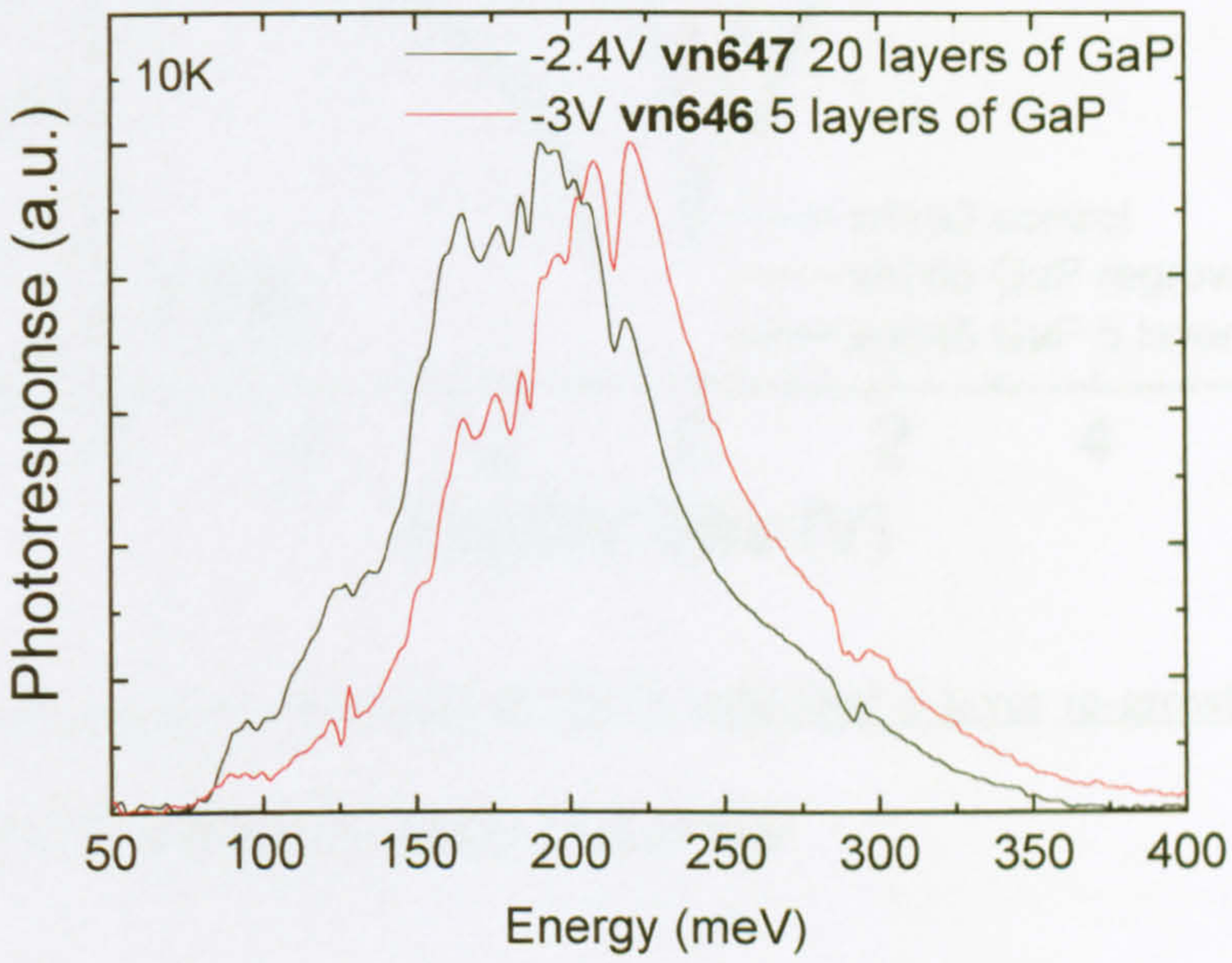

Fig.4.3.6. Spectra of samples with GaP SC layers; 5layers (red) and 20 layers (black)

This was initially assumed to be a combined effect of the QW state being deeply confined in an $In_{0.15}Ga_{0.85}As$ well with the GaP barrier further decreasing the tunnelling probability. A re-growth of the 5 layer sample was therefore attempted at a later stage with an $In_{0.1}Ga_{0.9}As$ well. This was expected to increase the dark current, but in fact the measured dark current performance of the device was much

inferior to that expected and more so compared to the previous GaP containing device. The dark current comparison with the previous 5 layer sample and the control sample is illustrated in Fig.4.3.7.

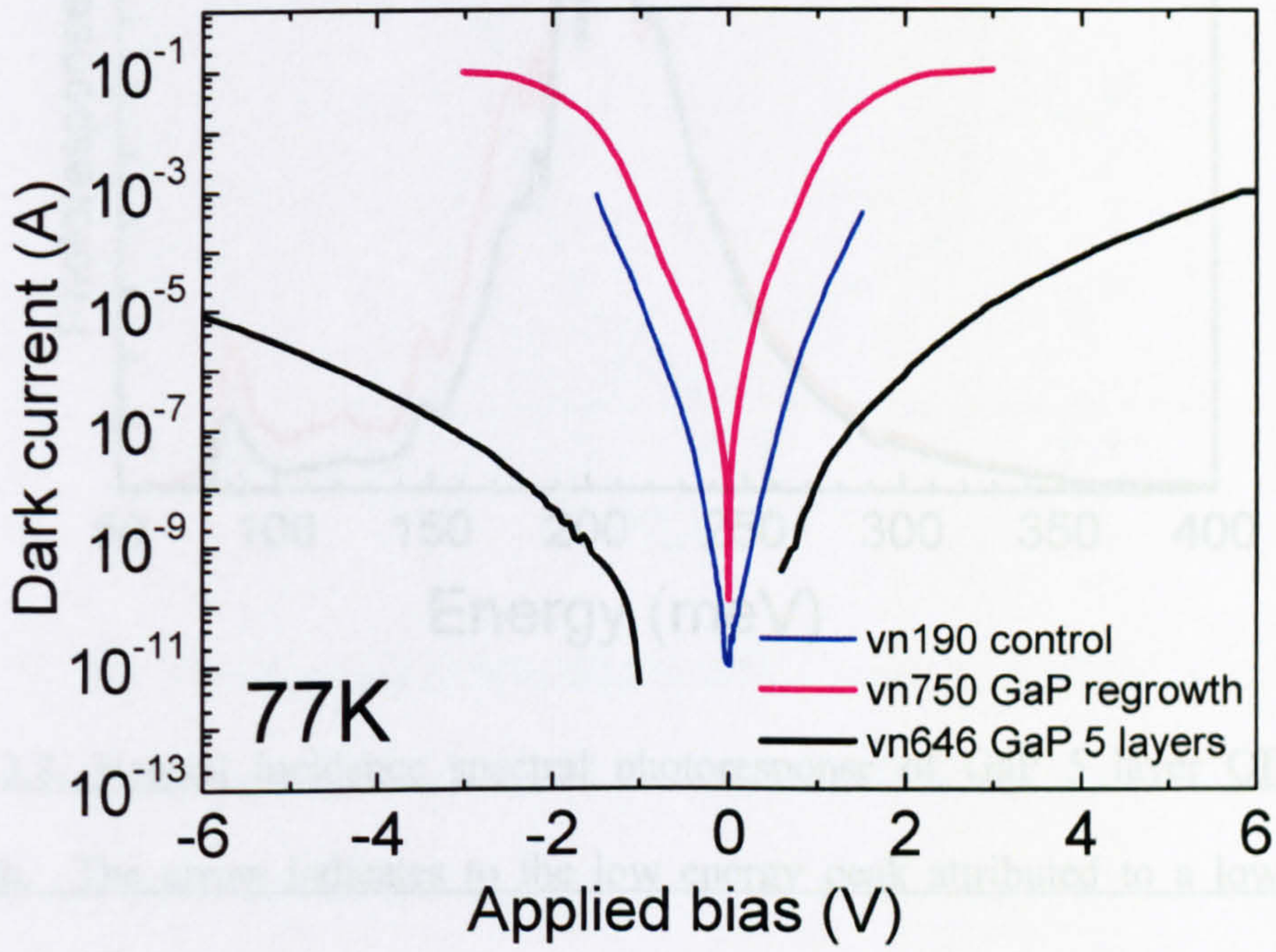

Fig.4.3.7. Dark current comparison of QDIP with GaP 5 layer re-growth compared with initial growth and control sample with no GaP

The spectral photoresponse of this sample was also observed to have broad features centred on ~220meV, similar to the previous attempt. However there was evidence of a second peak at ~85meV (~15μm) for a range of biases as it is shown on Fig.4.3.8. This is a low energy compared to previously observed bound-to-QW transitions (100-150meV). If it is assumed that the GaP is close enough to the QD layer to affect nucleation and cause the dots to be smaller in the growth direction, then the energy separation between the ground state and the state in the well will decrease (as the ground state goes to higher energy, and assuming that this has no effect on the QW state position.

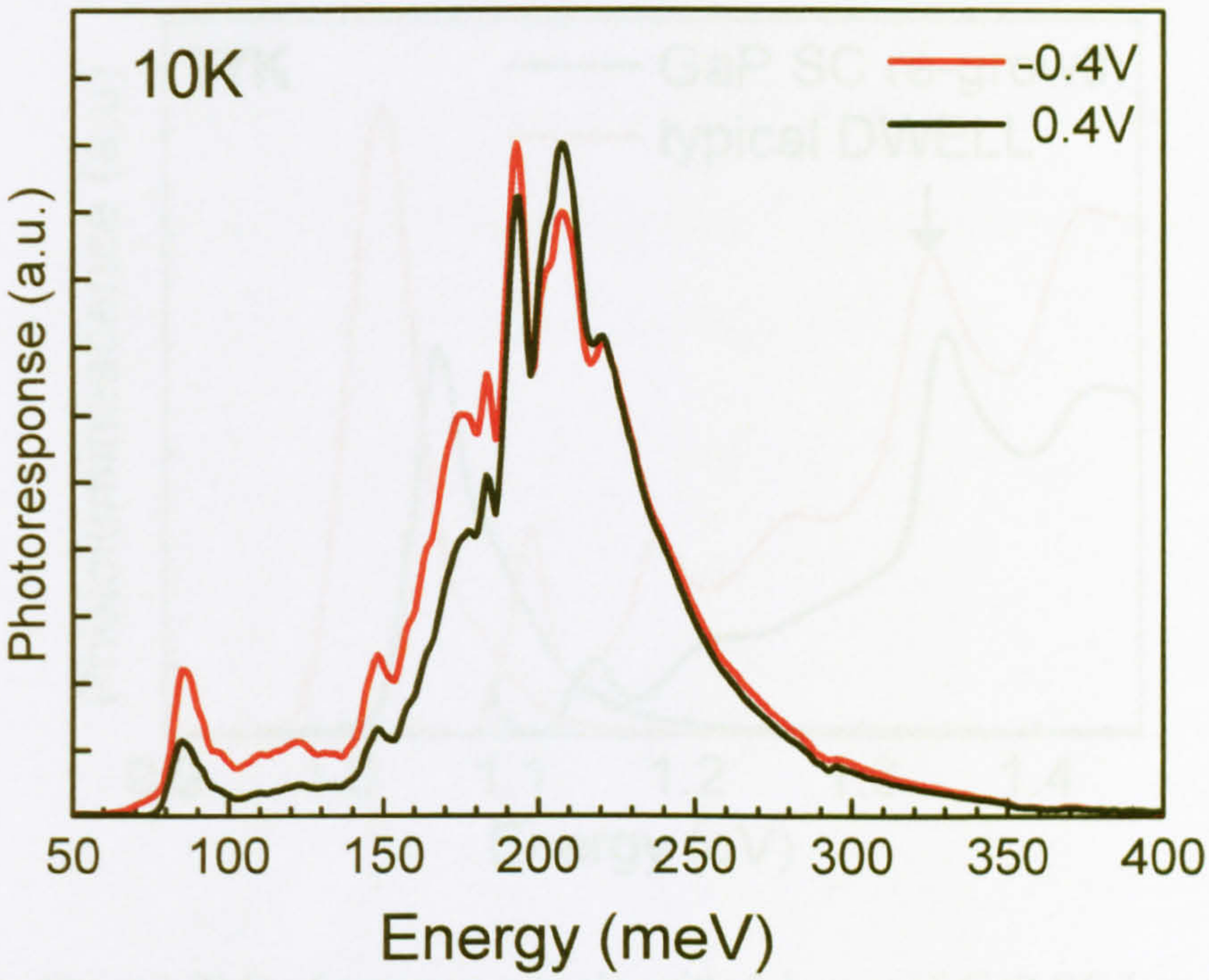

Fig.4.3.8. Normal incidence spectral photoresponse of GaP 5 layer QDIPs re-growth. The arrow indicates to the low energy peak attributed to a low energy bound-to-QW transition.

Fig.4.3.9 illustrates the QD PL of the sample with GaP SC layers and a typical DWELL detector (vn411, see chapter 3.4). The PL peak for the GaP SC sample is blue shifted from 1.02eV to 1.06eV. This 40meV shift is also observed in the PLE spectra (also plotted in Fig.4.3.9) for the peak attributed to the QD first excited state. However, the peak attributed to the QW state in the PLE curve, does not seem to be affected significantly. This is a clear indication of a lower QD height resulting in higher PL energy for the sample with GaP SC layers. The reduced energy separation between the ground state and the QW state, would lead to lower intraband photocurrent energy for the $E_1 \rightarrow E_{QW}$ transition, which agrees with the observed low energy feature in Fig.4.3.8.

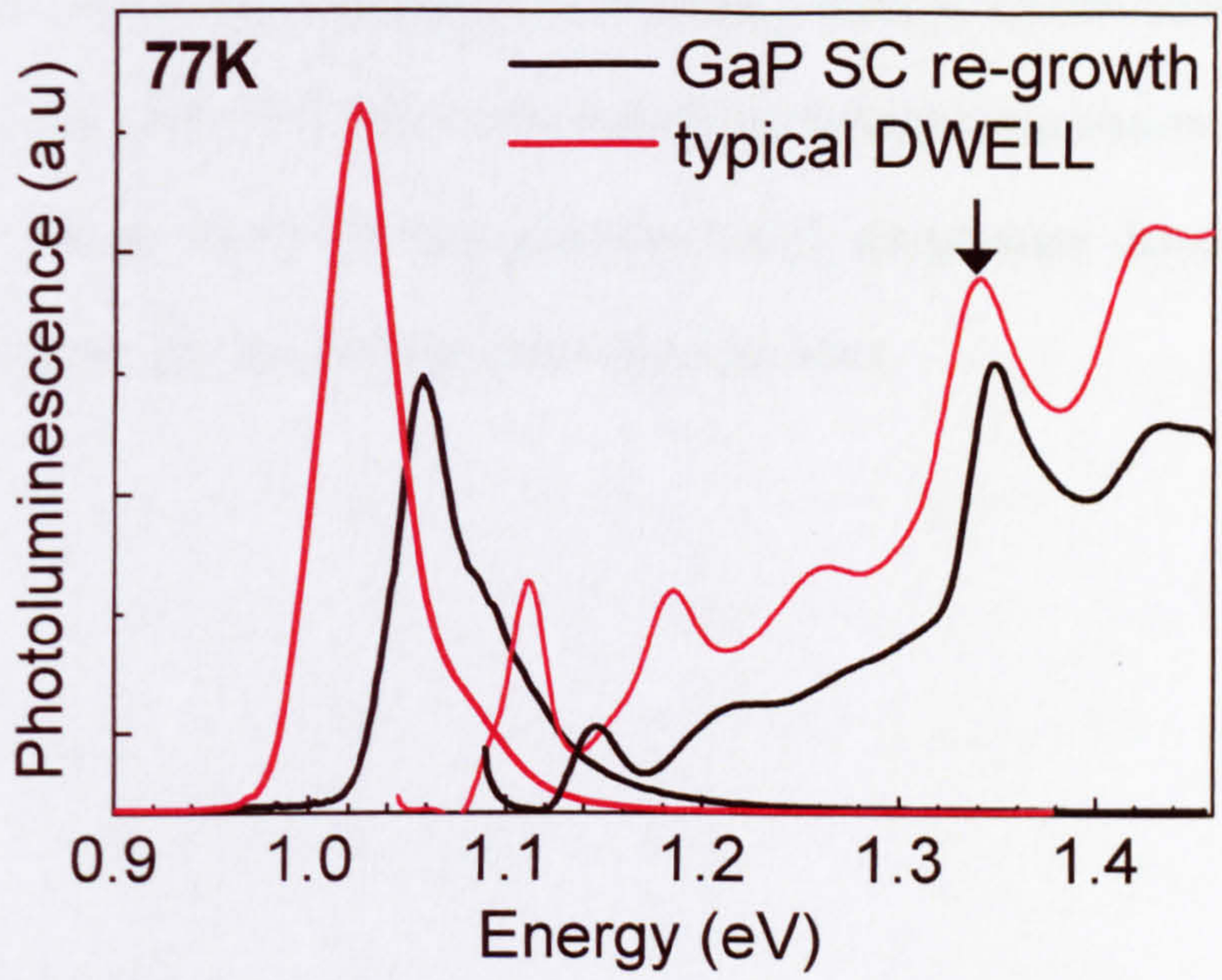

Fig.4.3.9. PL and PLE of regrown sample with 5 layers of GaP SC layers plotted against a typical InAs/InGaAs DWELL structure previously discussed in chapter 3.4. (Arrow indicates QW state)

4.3.4. Summary

As discussed in this section, it is possible to partially balance the compressive strain introduced by the indium in InAs/InGaAs/GaAs DWELL QDIPs with the insertion of GaP SC layers which are tensile strained relative to GaAs. TEM imaging was used to demonstrate the growth of a 20 layer structure with a low defect density. However, there needs to be further optimisation of the growth of such structures, and particularly with respect to the position of the GaP layers from the QD layer, since it has previously been shown that GaP affects the QD nucleation process. Furthermore, the number of GaP MLs should be optimised, bearing in mind the critical thickness in terms of the strain balance.

In conclusion, whilst this technique is a promising route to QDIPs containing many (>20) QD layers, there still needs to be significant further optimisation to enable the production of high absorption and potentially high temperature detectors, without compromising the spectral and electrical characteristics.

4.4. Discussion

In this chapter it was shown how different techniques can be applied to control and enhance the performance of DWELL QDIPs. It was demonstrated how the low QD density, which limits the number of absorbing electrons, can be increased, through the incorporation of a thin layer of antimony prior to QD growth. It was also shown that the incorporation of AlGaAs barriers can reduce the detector dark current but not without reducing the optical performance. Finally, by depositing GaP strain balancing layers, the growth of large numbers of periods of active QD regions can be achieved.

In my opinion, of the three techniques discussed in this chapter, the incorporation of antimony is the most promising. Not only did this yield the best results, but also addresses one of the most significant issues in self assembled QD devices generally, namely the QD density. In addition it was observed that the dark current also

reduces with this technique possibly due to suppressed defect formation influenced by the GaSb surfactant.

One would imagine that for high density ensembles (perhaps even ordered [see *Infrared Physics & Technology 50 (2007) 162–165*], the doping control would improve as well as the number of absorbing electrons, especially as uniformity of distribution would improve. This would therefore be a more successful way of reducing the dark current rather than using AlGaAs barriers, which as shown can deteriorate the optical performance of the detector.

Finally the growth of GaP strain balancing layers towards the production of multi-layer (>20) DWELL detectors was demonstrated and discussed. This is quite a promising technique, especially for detectors for high temperature operation. This technique also introduces a current blocking barrier in the conduction band, which decreases the dark current. However, there needs to be further growth and design attempts in order to optimise the position and composition of the SC layers. Nevertheless, it could provide a very interesting approach for strain compensation in QD based devices.

In conclusion, the incorporation of antimony in DWELLs as well as the principle of strain compensation with GaP, are both promising techniques towards the production of high performance DWELL QDIPs. With standardised QD growth, allowing the precise control of QD density and doping, these techniques will most certainly be capable of producing very high quality, competitive detectors in the LWIR atmospheric window.

References

1 Koichi Yamaguchi, Toru Kanto,, Journal of Crystal Growth 275 (2005) e2269–e2273

2 See, for example, D.T. Le, C.P. Morath, H.E. Norton, D.A. Cardimona, S. Raghavan, P. Rotella, S.A. Stintz, B. Fuchs, S. Krishna, Infrared Phys. Technol. **44**. 517-526 (2003); Z.H. Chen , O. Baklenov , E.T. Kim , I. Mukhametzhanov, J. Tie, A. Madhukar , Z. Ye, J.C. Campbell, J. Appl. Phys. **89**, 4558 (2001); S.Y. Wang, S.D. Lin, H.W. Wu, C.P. Lee, Appl. Phys. Lett. **78** (8) 1023 (2001)

3 P. Lever, H.H. Tan, C. Jagadish, J. Appl. Phys. 95 (10) 5710-5714 (2004)

4 D. Guimard, Masao Nishioka, Shiro Tsukamoto, Yasuhiko Arakawa, Journal of Crystal Growth 298 548–552 (2007)

5 Heedon Hwang et al, Appl. Phys. Lett. Vol 85, 6383, 2004

6 J. Massies, N. Grandjean, and V. H. Etgens, Appl. Phys. Lett. **61**, 99 (1992)

7 C. S. Peng, Q. Huang, W. Q. Cheng, J. M. Zhou, Y. H. Zhang, T. T. Shengd, and C. H. Tung, Appl. Phys. Lett. **72**, 2541 (1998)

8 D. Guimard, Masao Nishioka, Shiro Tsukamoto, Yasuhiko Arakawa, Appl. Phys. Lett. **89**, 183124 (2006)

9 Y. Sun, S. F. Cheng, G. Chen, R.L. Woo, R.F. Hicks, J. Applied Physics **97**, 053503, 2005

10 A. Portavoce, I. Berbezier, A. Ronda, Phys. Rev. B 69 (2004) 155416

11 E.A. Zibik, A.D. Andreev, L.R. Wilson, M.J. Steer, R.P. Green, W.H. Ng, J.W. Cockburn, M.S. Skolnick, M. Hopkinson, Physica E 26 (2005) 105-109

12 E. Zibik, A. Adawi, L. R. Wilson, A. Lemaitre, J. W. Cockburn, M. Hopkinson, G. Hill, J. Applied Physics **100**, 013106 (2006)

13 E.A. Zibik, W.H. Ng, L.R. Wilson, , M.S. Skolnick, J.W. Cockburn, M. Gutierrez, M.J. Steer, M. Hopkinson, Appl.Phys.Lett. **90**, 163107 (2007)

14 E.A. Zibik, L.R. Wilson, R.P. Green, G. Bastard, R. Ferreira, P.J. Phillips, D.A. Carder, J.P.R. Wells, J.W. Cockburn, M.S. Skolnick, M.J. Steer, M. Hopkinson, Phys. Rev. B **70**, 161305(R) (2004)

15 E.A. Zibik, L.R. Wilson, R.P. Green, G. Bastard, R. Ferreira, P.J. Phillips, D.A. Carder, J.P.R. Wells, M.S. Skolnick, J.W. Cockburn, M.J. Steer, M. Hopkinson, Physica E 26 (2005) 408-412

16 Z. Ye, J. C. Campbell, Z. Chen, E.T Kim, and A. Madhukar, J. Applied. Physics, **92** 7462 (2002)

17 S. Krishna, S. Raghavan, G. von Winckel, A.Stintz, G. Ariyawansa, S.G. Matsik, A.G.U Perera, Appl.Phys.Lett, **83**, (14) 2745 (2003)

18 P. Aivaliotis, N. Vukmirović, E. A. Zibik, D. Indjin, J. W. Cockburn, P. Harrison, C. Groves, J. P. R. David, M. Hopkinson, and L. R. Wilson, J. Phys. D: Appl. Phys. **40** 5537-5540, (2007)

19 H. Schneider, H. C. Liu, 'Quantum Well Infrared Photodetectors, Physics and Applications', Springer Series in Optical Sciences, Springer-Verlag Berlin Heidelberg 2007

20 R. Enzmann, S. Dachs, R. Meyer, J. Finley, and M-C Amann, Appl. Phys. Lett. **91**, 083111 (2007)

21 V. Ryzhii, Semicond. Sci. Technol. **11** 759 (1996)

22 V. Ryzhii, V. Pipa, I. Khmyrova, V. Mitin, M. Willander, Jpn. J. Appl. Phys. **39**, 1283 (2000)

23 E.T. Kim, A. Madhukar, Z.M. Ye, J.C. Campbell, App. Phys. Lett. **84**, 3277 (2004)

24 S. Raghavan, P. Rotella, A. Stintz, B. Fuchs, S. Krishna, C. Morath, D.A. Cardimona, S.W. Kennerly, Appl.Phys.Lett. **81** (8) 1369 (2002)

25 D. Pal and E. Towe, Appl. Phys. Lett. **88**, 153109 (2006)

26 S. Chakrabarti, A. D. Stiff-Roberts, P. Bhattacharya, S. Gunapala, S. Bandara, S. B. Rafol, S. W. Kennerly, IEEE Photonics Technology Letters, **16**, (5) 1361 (2004)

27 M. Kaniewska, O. Engstrom, A. Barcz, M. Pacholak-Cybulska, Materials Science in Semiconductor Processing **9** 36–40 (2006)

28 A. Cavallini, B. Fraboni, F. Capotondi, L., G. Biasiol, Microelectronic Engineering **73–74** 954–959 (2004)

29 J.M. Zanardi Ocampo, N. Kamata, K. Hoshino, M. Hirasawa, K. Yamada, M. Nishioka, Y. Arakawa, Journal of Crystal Growth **210** 238-241(2000)

30 J. Pangrac, J. Oswald, E. Hulicius, K. Melichar, V. Vorlicek, I. Drbohlav, T. Simecek, Thin Solid Films **380**, 101 (2000)

31 Q. Zhang, J. Zhu, X. Ren, H. Li, and T. Wang, Appl. Phys. Lett. **78**, 3830 (2001)

32 K. Stewart, M. Buda, J. Wong-Leung, L. Fu, C. Jagadish, A. Stiff-Roberts, P. Bhattacharya, J. Appl. Phys. **94**, 5283 (2003)

33 K. I. Shiramine, Y. Horisak, D. Suzuki, S. Itoh, Y. Ebiko, S. Muto, Y. Nakata, and N. Yokoyama, J. Cryst. Growth **205**, 461 (1999)

34 See, for example, H. Sasakura, S. Kayamori, S. Adachi, S. Muto, J.Appl.Phys. **102** 013515 (2007); J. P. McCaffrey , M. D. Robertson , S. Fafard , Z. R. Wasilewski, E. M. Griswold , L. D. Madsen, J.Appl.Phys **88** (2000) 2272

35 See for example, X.Q. Zhang, S. Ganapathy, H. Kumano, K. Uesugi, I. Suemune, J. Appl. Phys. **92** (2002) 6813; X.Q. Zhang, S. Ganapathy, I. Suemune, H. Kumano, K. Uesugi, Y. Nabetani, T. Matsumoto, Appl.Phys.Lett. **83** 4524 (2003), O. Schumann, S. Birner, M. Baudach, L. Geelhaar, H. Eisele, L. Ivanova, R. Timm, A. Lenz, S.K. Becker, M. Povolotskyi, M. Dahne, G. Abstreiter, H. Riechert, Phys. Rev. B **71**, 245316 (2005), R. Oshima, T. Hashimoto, H. Shigekawa, Y. Okada, J. Appl. Phys. **100**, 083110 (2006)

36 N. Nuntawong, S. Huang, Y.B. Jiang, C.P. Hains, D.L. Hufakker, Appl.Phys.Lett. **87** 113105 (2005)

37 N. Nuntawong, Y.C. Xin, S. Birudavolu, P.S. Wong, S. Huang, C.P. Hains, D.L. Hufakker, Appl.Phys.Lett **86**, 193115 (2005)

38 J. Tatebayashi, N. Nuntawong, Y.C. Xin, P.S. Wong S. Huang, C.P. Hains, L.F. Lester, D.L. Hufakker, Appl.Phys.Lett. **88** 221107 (2006)

5. Novel directions in quantum dot infrared photodetectors

The previous two chapters dealt with the optimisation of design parameters and methods of enhancing the performance of DWELL QDIPs. This final experimental chapter is dedicated to the study of novel concepts in the field of DWELL QDIP research.

In the first part of this chapter, the capability to tune the spectral photoresponse of DWELL QDIPs via rapid thermal annealing (RTA) is discussed in detail. RTA studies have been widely reported mainly for QWs and non-detector QD structures [1]. In this section however, the first demonstration of wide spectral tunability across the whole LWIR window is reported for DWELL QDIPs. In addition, it was observed that using this technique to tune the wavelength after a device growth did not diminish the detector performance beyond expected levels.

The second section deals with non-linear optical effects in DWELL QDIPs. Standard methods for the detection of mode-locked and pulsed quantum cascade lasers as well as other pulsed sources in the MIR and FIR typically use non-linear

crystals to generate second-harmonic light, which is measured by a slow linear detector. This section reports the first demonstration of two-photon operation of a DWELL QDIP. Two photon (2P) processes have been studied in QWIPs [2], with high sensitivity 2P detectors of mid-infrared sub-picosecond pulses demonstrated. The development of 2P QDIPs would be highly significant as they are capable of true normal incidence operation, have long intermediate state lifetimes resulting in high 2P absorption co-efficients and have an intrinsic energy level configuration which makes them particularly attractive for operation in the terahertz region.

In the final section of this chapter, the design and fabrication of photovoltaic QDIPs is discussed. Photovoltaic operation had been previously observed in photoconductive QDIPs, due to the in-built strain-induced electric field [3]. Nonetheless, optimised detector structures for photovoltaic operation had only been reported for QWIPs. This section includes results from two DWELL QDIPs designed to introduce a controlled in-built electric field and achieve high performance photovoltaic MIR detection.

5.1. Rapid thermal annealing for intermixing DWELL QD structures

5.1.1. Introduction

As mentioned in previous chapters, there have been demonstrations of QDIP performance levels that are beginning to approach those of the more mature QWIP technology. However, a serious drawback is the relative complexity to design QDIPs for a specific wavelength range, because the QD size control requires the variation of many different growth parameters. Rapid thermal annealing (RTA) is a common tool used to give post growth alteration to the transition energies inside semiconductor structures by inter-diffusion of constituent atoms (intermixing) [1]. There have been several reports showing that it is possible to retain the 3-dimensional confinement in QDs after high temperature annealing [4,5]. Intermixing affects both the height and shape of the QD confining potential, hence changing the transition energies and the intersublevel spacing [6]. Additionally, the photoluminescence linewidth for ground state transitions significantly decreases for increased intermixing, indicating a reduction of the QD size and strain inhomogeneities [7].

Previous studies in QWIPs have demonstrated the possibility to tune the spectral response of the detectors by quantum well intermixing (QWI) e.g. strained InGaAs QW systems, where shifts of 1.2μm have been achieved [4], and GaAs/AlGaAs QW systems, where shifts of 1.6 and 1.8μm have been achieved [5,6]. Typically for

QWI, RTA is used along with ion implantation, which provides a precise control of the amount and depth of the defects introduced upon intermixing [5], since using solely RTA usually results in significant spectral broadening and degradation of the dark current (>order of magnitude). There have recently been reports on the effect of intermixing in QDIPs, with small shifts compared to QWI, accompanied by a significant degradation in performance [7].

In this section the post-growth tailoring of the spectral photoresponse of DWELL QDIPs is discussed, whereby shifts as large as 4μm (46meV) have been achieved using post-growth RTA. The narrow photoluminescence and intraband photocurrent spectra for the as-grown devices display further narrowing upon annealing. The device performance remained in a competitive range for QDIPs for this wavelength range with the detectivity reducing from $1.1x10^{10}cmHz^{1/2}W^{-1}$ at 8μm, to $3x10^{9}cmHz^{1/2}W^{-1}$ at 10.9μm at 77K. This threefold reduction across this wavelength range was found to be comparable to that calculated for QWIPs, based on the reduction of detectivity with wavelength for a photoconductor [8]. This indicates that although the control of the amount of point defects is not as precise as with the aid of ion implantation, the introduction of undesirable amounts of defects is limited using this technique.

5.1.2. Absorption studies of annealed DWELL QDs

The DWELL sample studied here is the sample discussed in chapter 3.4 for absorption studies (vn758). The DWELL absorbing region consists of 30 periods of InAs dots placed within an 80Å $In_{0.15}Ga_{0.85}As$ quantum well, with 10Å of the well below the dots and 70Å above. The active region was Si δ-doped to a concentration corresponding to ~$1e^-$/dot. RTA was performed in a rapid thermal annealer (Mattson) at a temperature of 800°C for 2 and 4minutes. During the RTA process, the samples were sandwiched between 2 GaAs wafers to prevent As out-diffusion from the sample surface and were kept in a Nitrogen ambient environment.

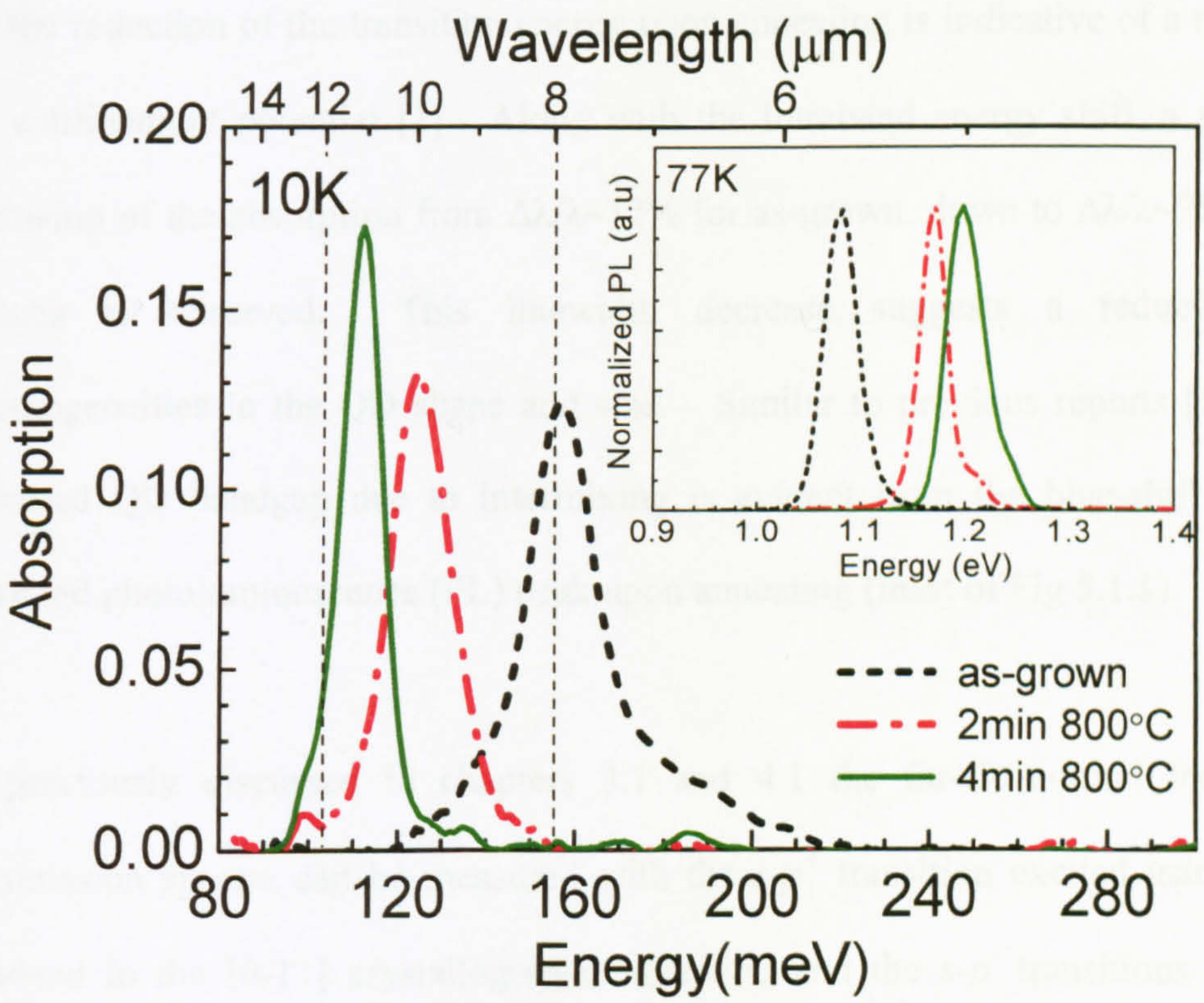

Fig.5.1.1 Mid-IR high energy intraband absorption of as-grown (black), 2 minutes (red) and 4minutes (green) annealed absorption samples at 800°C measured at 10K. The inset shows the corresponding photoluminescence at 77K for each sample.

Fig.5.1.1 shows the mid-IR absorption spectrum at 10K for the as-grown sample (black dotted line) attributed to the $E_1 \rightarrow E_{QW}$ transition, which was found to be stronger and narrower ($\Delta\lambda/\lambda$~12%@8μm, FWHM~18meV) compared to equivalent transitions from the QD to the wetting layer in InAs/GaAs QDs [9]. The sample was annealed for 2 and 4 minutes at 800°C. It was previously found that for 800°C, large shifts can be achieved for ground state to first excited state (*s-p*) transitions [1]. As illustrated in Fig.5.1.1, the absorption peak shifts from 157meV (~8μm) for the as-grown sample to 124meV (10μm) for 2min, and 112meV (11μm) for 4min of RTA.

Annealing is expected to change the composition, strain and anisotropy of the QDs and the reduction of the transition energy upon annealing is indicative of a reduced QD confinement potential [1]. Along with the intraband energy shift, a spectral narrowing of the absorption from $\Delta\lambda/\lambda$~12% for as-grown, down to $\Delta\lambda/\lambda$~9% for 4 minutes is observed. This linewidth decrease suggests a reduction of inhomogeneities in the QD shape and size. Similar to previous reports [10], the increased QD bandgap due to intermixing is evident from the blue-shift of the interband photoluminescence (PL) peak upon annealing (inset of Fig 5.1.1).

As previously discussed in chapters 3.1 and 4.1 the far-IR normal incidence transmission spectra can be measured with the $s\text{-}p^+$ transition excited using light polarised in the [0-11] crystallographic direction and the $s\text{-}p^-$ transitions excited using light polarised in the [011] direction. The green and blue lines in Fig.5.1.2 show the normal incidence absorption per layer, which were presented and

discussed in chapter 3.1. It should be noted that when the samples were annealed for 2 minutes, no intraband absorption was observed for the *s-p* transitions.

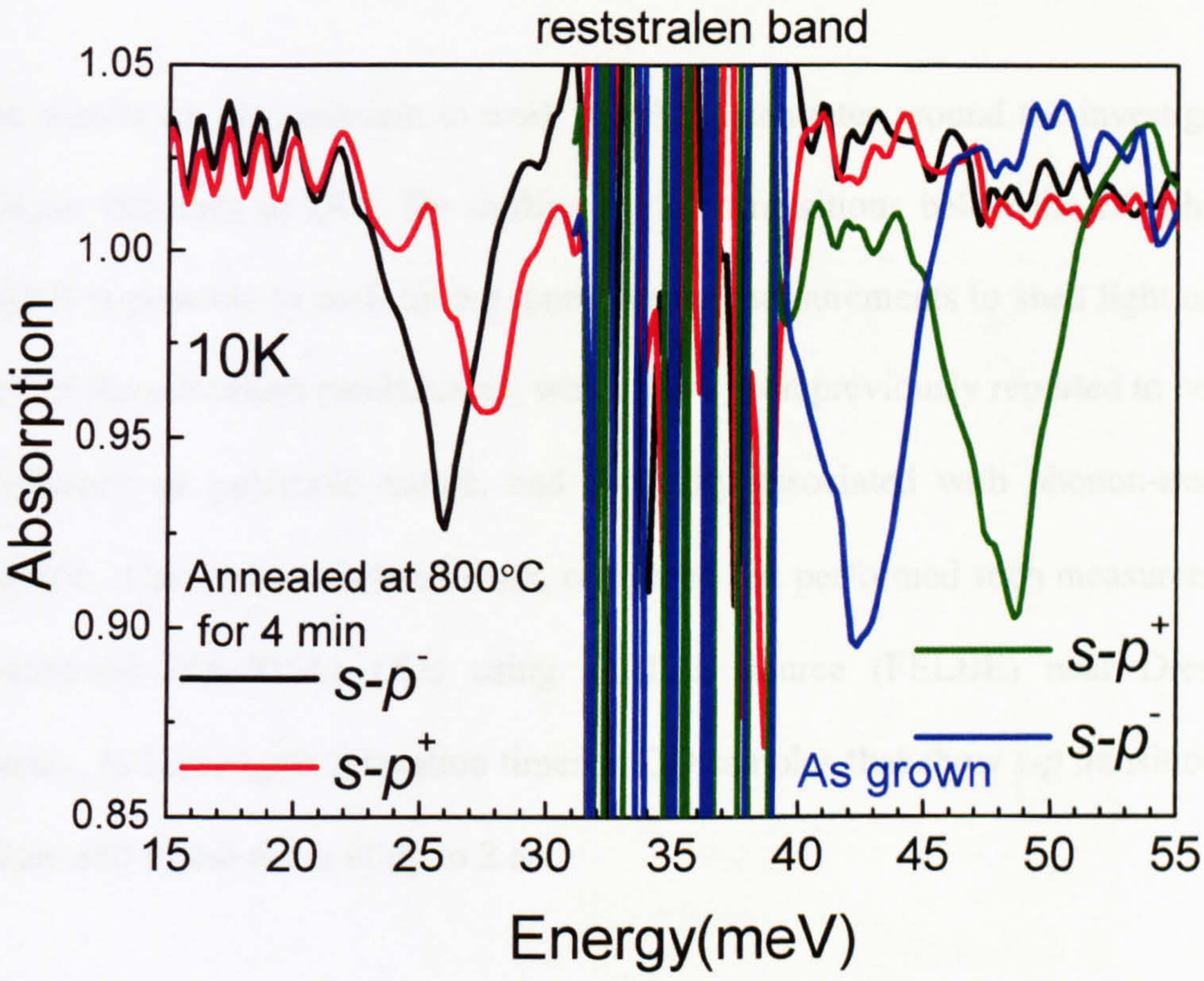

Fig.5.1.2. Normal incidence intraband absorption spectra in the far-IR for DWELL at 10K. For the as-grown sample, *s-p*$^-$ [011] and *s-p*$^+$ [0-11] transitions are shown in blue and green respectively at 42 and 48meV. The same transitions are shown in black and red respectively at 25 and 27meV. The 2 minute sample transitions are assumed to have shifted to energies within the reststrahlen band

It is assumed that when annealing the structure for 2 minutes the energy of the *s-p* transition is in the region of the reststrahlen band. This assumption is supported by the results for 4minutes RTA at 800°C which exhibit absorption peaks below the optical phonon energy at 25meV and 27meV for the s-*p*$^-$ and s-*p*$^+$ transitions, respectively. The anisotropy-associated splitting (discussed also in chapter 3.1) is

evidently reduced from 6 to 2meV, and this had been previously observed in InAs/GaAs dots by Zibik et al [1], demonstrating the reduction of the inhomogeneities in size and strain associated with the splitting [1].

These results are also relevant to work which concentrates around the investigation of carrier lifetimes in QDs. By shifting the QD transitions below the LO phonon energy it is possible to perform e.g. pump-probe measurements to shed light on the nature of the relaxation mechanisms, which have been previously reported to be of a multiphonon or polaronic nature, and generally associated with phonon-assisted relaxation. Currently, in related work, our group has performed such measurements on annealed InAs/GaAs QDs using an FEL source (FELBE) near Dresden, Germany, to investigate relaxation times in QD samples that show *s-p* transitions of ~100μm and found times of up to 2 ns.

5.1.3. Effects of intermixing on DWELL QDIP performance

The QDIP device structure which had been grown (vn411, see chapter 3.5), incorporated a bottom contact layer of 4000Å *n*+ Si doped GaAs, 10 periods of DWELL absorbing region, separated by 500Å of undoped GaAs and a final 4000Å *n*+ Si doped GaAs contact layer. The active region was doped to a concentration of corresponding to ~1e^-/dot. RTA was performed as in the previous section.

Fig.5.1.3 illustrates the intraband photocurrent spectra measured under normal incidence conditions at 10K and 3.0V. The photocurrent peak at +3.0V shifts from 8.1μm to 10.9μm for 2 min of RTA.

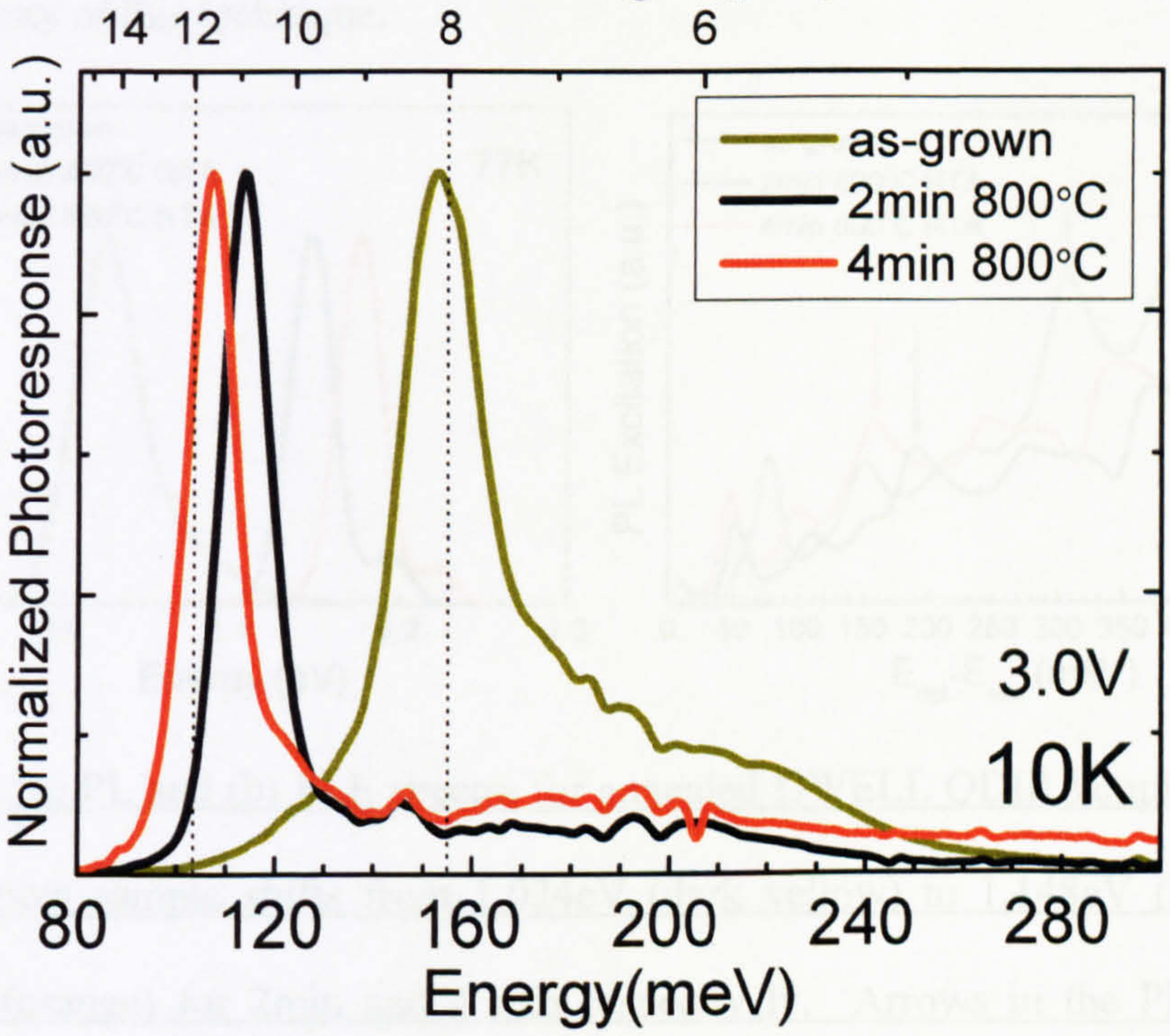

Fig.5.1.3 Intraband photocurrent spectra for as-grown (dark yellow), 2min (black) and 4min (orange) DWELL QDIP samples annealed at 800°C measured at 3.0V and 10K.

When annealing the device for 4min at 800°C a further shift of the peak wavelength up to 11.6μm is observed with a cut-off at ~13.5μm. A high energy tail is evident for the as-grown detector as well the absorption sample. This has been previously attributed to bound-to-continuum transitions [11]. The tail could additionally be influenced by inhomogeneous broadening of the QD distribution, which reduces upon annealing and causes a subsequent reduction of the high energy shoulder.

PL measurements of the as-grown DWELL QDIP exhibit a narrow linewidth of $\Delta\lambda/\lambda$~4.5% (FWHM~42meV) and PL peak energy of 1.024eV. The PL peak shifts to 1.148eV and 1.177eV for 2min and 4 min, respectively, with the linewidth reducing down to ~28meV after 4min of annealing as shown in Fig.5.1.4 (a). The rate of the PL peak shift is similar to the absorption sample, demonstrating the repeatability of this technique.

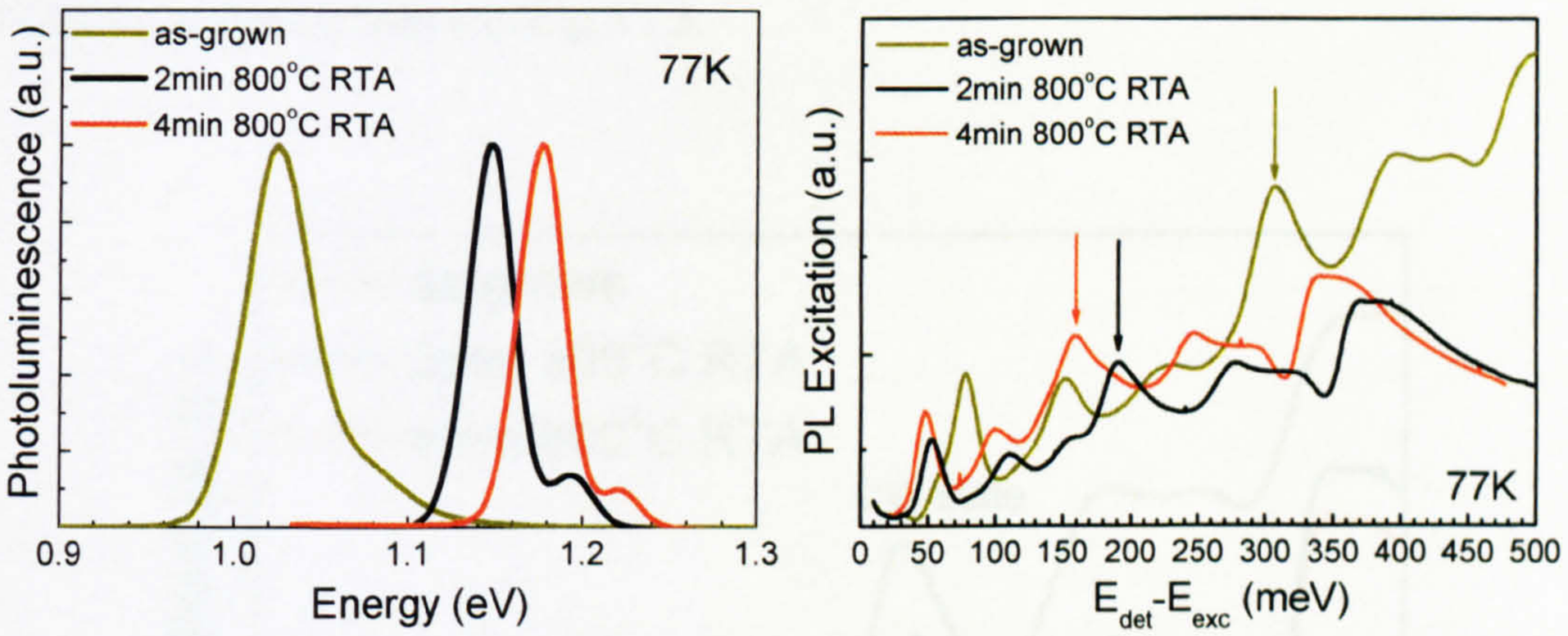

Fig.5.1.4. (a) PL and (b) PLE spectra for annealed DWELL QDIP samples. PL for the as-grown sample shifts from 1.024eV (dark yellow) to 1.148eV (black) and 1.177eV (orange) for 2min and 4 min respectively. Arrows in the PLE spectra indicate the position of the peak corresponding to the QW state. PLE spectra shown were subtracted from the PL detection energy.

The PLE spectra (Fig 5.1.4 (b)) allow the determination of the relative interband energies of the ground state and excited states in the QD and to measure how these change upon annealing. The peaks corresponding to the first excited state and QW state are indicated for the as-grown and annealed samples. This data can be used in conjunction with the intraband photocurrent data to estimate the relative change of the conduction band to valence band ratio, for different annealing times at least as far as the $E_1 \rightarrow E_{QW}$ transition is concerned. The energy of E_{QW} with respect to the

ground state shifts from 306meV (as-grown) to 183meV (2 minute RTA) and 158meV (4 minute RTA)

Prior to subtracting the PLE excitation energies from the PL detection energy, it is evident that the interband energy gap between the electron and hole states confined in the QW does not change as significantly as the ground state emission energy of the QD, as shown below in Fig.5.1.5.

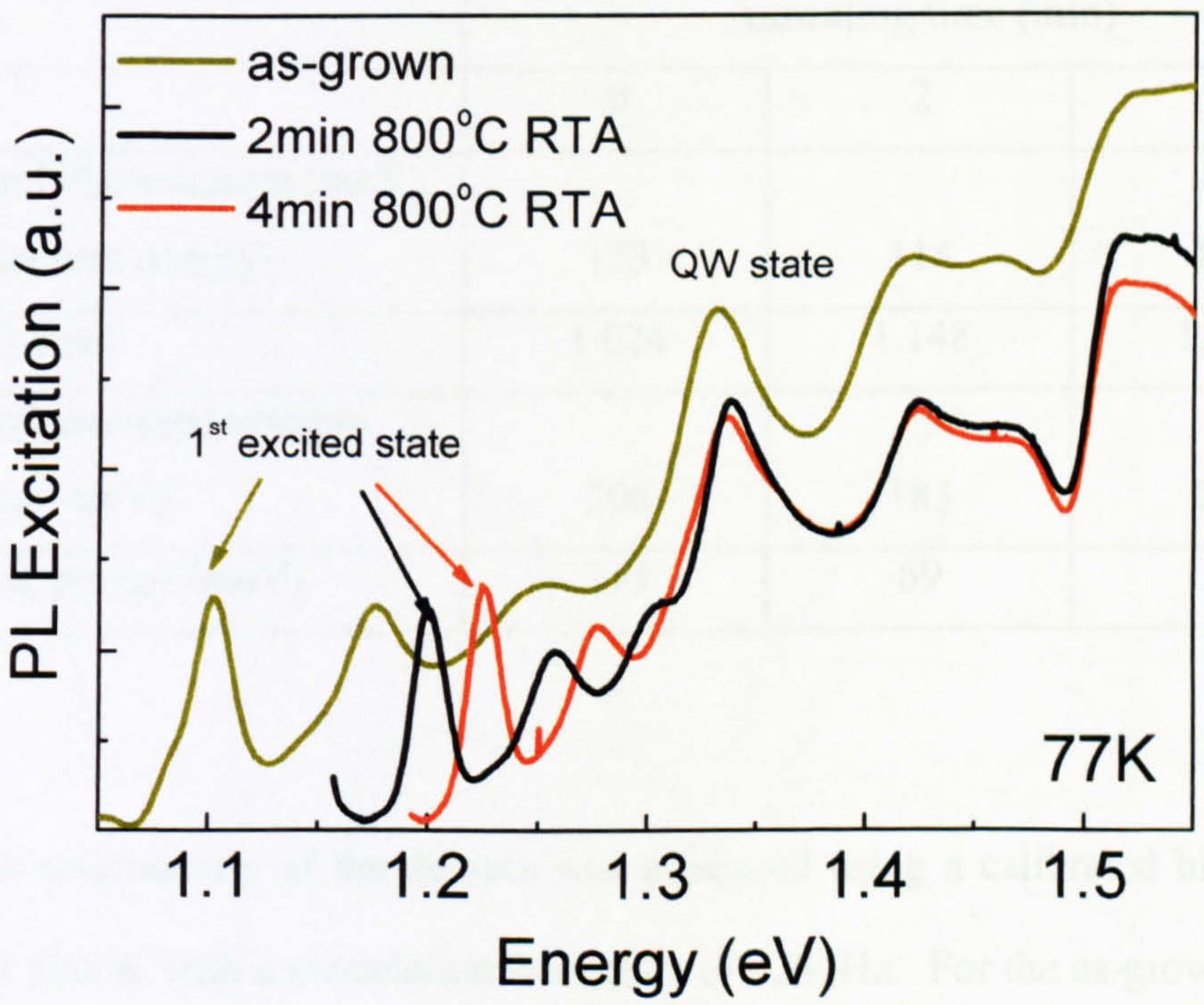

Fig, 5.1.5. PLE spectra for as-grown (dark yellow), 2min@800°C (black) and 4min@800°C (orange), showing how the quantization energy of the QW state is not as affected by intermixing as the energy of the states in QD.

It is thus possible to deduce that annealing mainly effects the QD, and to a lesser extent the QW. A comparison of the QW state energy in the PLE spectra with the intraband photocurrent peaks which correspond to the transitions in the CB, enables

the derivation of the shift of the hole energies upon annealing. The hole quantisation energies for E_{QW} shift from 153meV to 69meV, down to 51meV from as-grown to 2min and 4 min of RTA respectively. Accordingly, the CB contribution to the interband transitions increases with annealing time, from ~50% to ~62% up to ~68%. The table below summarises the above results:

Table 5.1. Effects of different annealing times on detector characteristics. The PLE peak values corresponding to the QW state are indicated in Fig.5.1.4(b)

	Annealing time (min)		
	0	2	4
Intraband Photocurrent (meV), (E_{QW} electron energy)	153	114	107
PL (eV) peak	1.024	1.148	1.177
PLE peak corresponding to QW state (meV)	306	183	158
E_{QW} hole energy (meV)	153	69	51

The peak responsivity of the devices was measured using a calibrated black body source at 1005K with a modulation frequency of ~230Hz. For the as-grown sample where the dark current density is low (4.7mA/cm^2@–2.7V and 77K) illustrated in Fig.5.1.6 (b), the responsivity can be measured up to +/-3.8V, with values of ~3A/W at 77K, as shown in Fig.5.1.6 (a).

However, once the detector is annealed for 2 minutes the dark current density increases by more than one order of magnitude (~40x higher) as shown if Fig.5.1.6 (b), to 0.2A/cm^2@-2.7V and 77K, limiting the detector operating voltage to a range of +/- 2.7V.

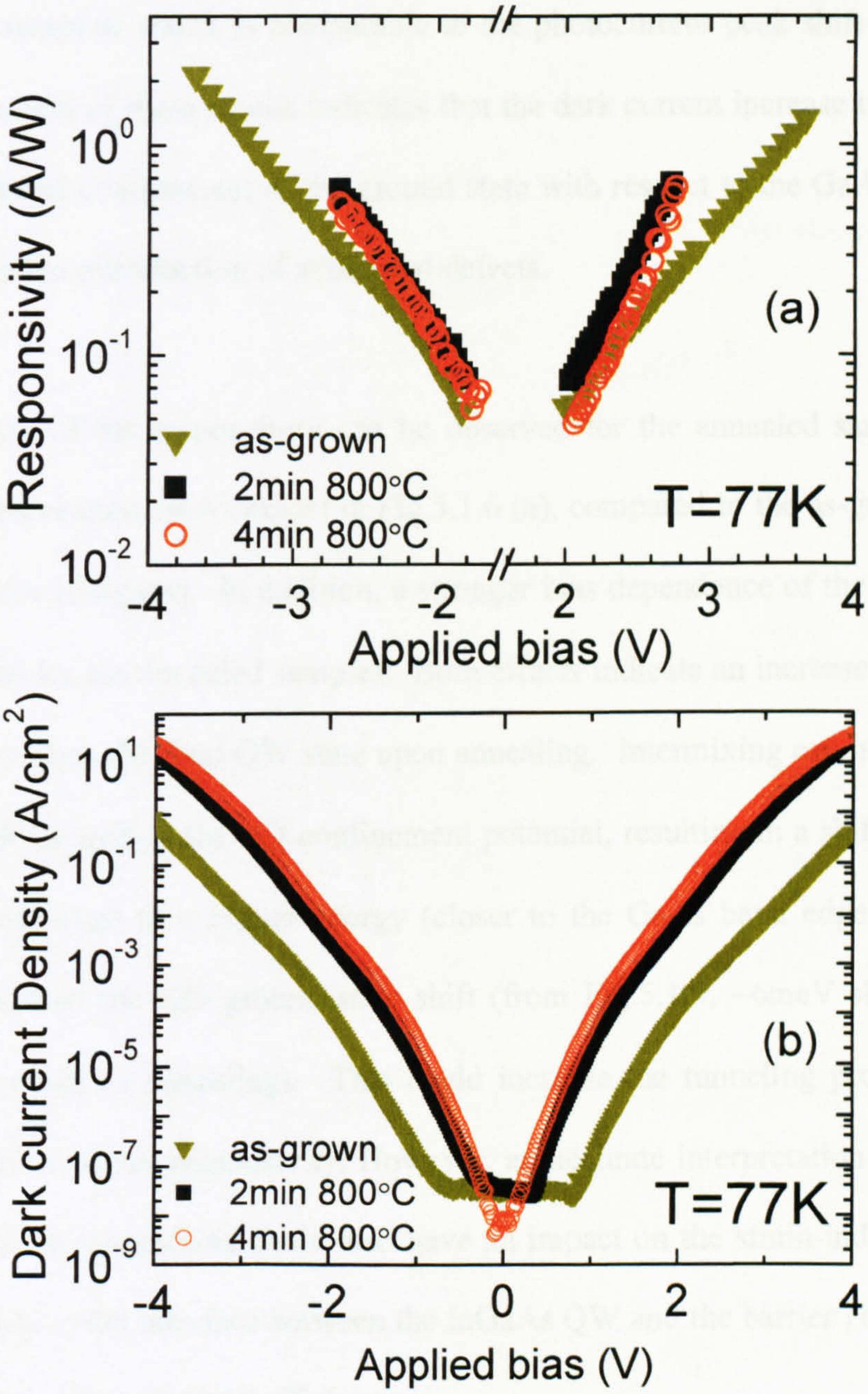

Fig.5.1.6. (a) Peak responsivity and (b) Dark current density at normal incidence measured at 77K for DWELL QDIPs: as-grown (dark yellow triangles), 2min@800°C (black squares) and 4min@800°C (orange open circles).

A further twofold increase of the dark current density occurs for 4 minutes of annealing (0.42A/cm^2@-2.7V and 77K). The activation energies for these devices were derived from temperature dependent dark current measurements [7]. We find

a reduction of ~50meV of the activation energy between the as-grown and 4 min annealed samples, which is comparable to the photocurrent peak shift of ~46meV. The agreement of these results indicates that the dark current increase is mainly due to the reduced confinement of the ground state with respect to the GaAs band edge rather than the introduction of additional defects.

An increase of the responsivity can be observed for the annealed samples (black squares and orange open circles) in Fig.5.1.6 (a), compared to the as-grown sample (dark yellow triangles). In addition, a stronger bias dependence of the responsivity is observed for the annealed samples. Both effects indicate an increase in tunneling probability from the final QW state upon annealing. Intermixing can have an effect on the QW as well as the QD confinement potential, resulting in a shift of the final photocurrent state to a higher energy (closer to the GaAs band edge), albeit at a lower rate than the QD ground state shift (from Fig.5.1.5, ~6meV shift from as-grown to 4min of annealing). This could increase the tunneling probability and hence yield a higher responsivity. However, an accurate interpretation of the effect is difficult, as intermixing could also have an impact on the strain-induced built-in electric field at the interface between the InGaAs QW and the barrier [12] that could also influence the tunneling efficiency.

The peak responsivity at -2.7V is increased from 0.35A/W for the as-grown sample to 0.6A/W for the 2min@800C sample. When annealing further to 4min, the responsivity decreases compared to the 2min sample, which is more evident for positive low biases.

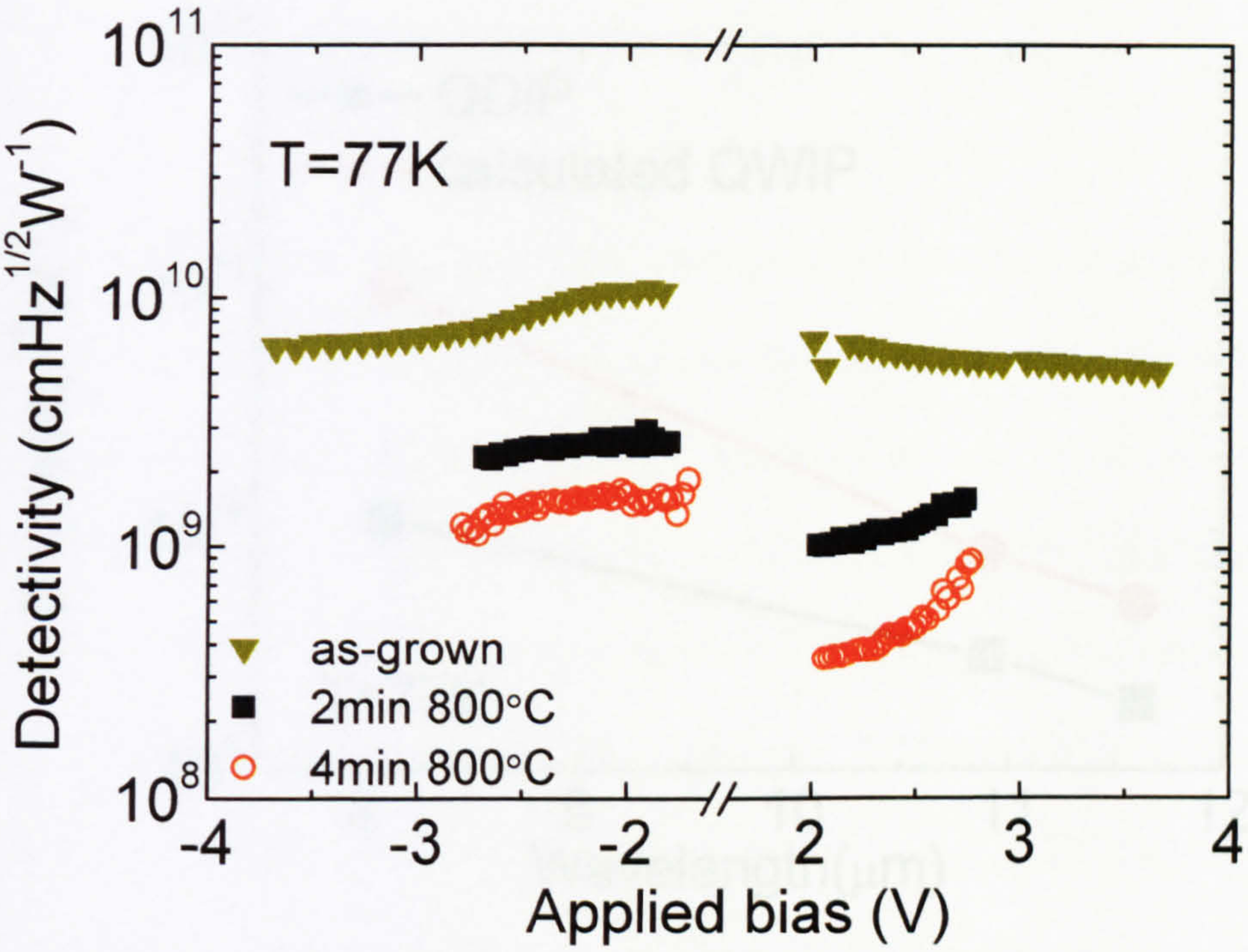

Fig.5.1.7. Dark current limited detectivity of DWELL QDIPs measured at 77K; as-grown (dark yellow triangles), 2min@800°C (black squares) and 4min@800°C (orange open circles).

In order to better quantify the effects of annealing on the detector performance, the dark current limited detectivity [8] can be estimated from the responsivity and dark current densities at 77K. Observed values of D^*=1.1x10^{10}cmHz$^{1/2}$W^{-1} for the as-grown sample were reduced down to 3x10^{9}cmHz$^{1/2}$W^{-1} and 2x10^{9}cmHz$^{1/2}$W^{-1} for 2 and 4 minutes of annealing at 800°C, respectively, as shown in Fig. 5.1.7. Similar magnitudes of reduction in detectivity have been calculated for LWIR QWIPs [8,13], as a function of detection wavelength from 8-12μm as illustrated in Fig.5.1.8. This indicates that upon annealing the performance is reduced to expected levels, due to the weaker confinement potential, and that the introduction of additional defects that would further deteriorate the performance does not play a significant role.

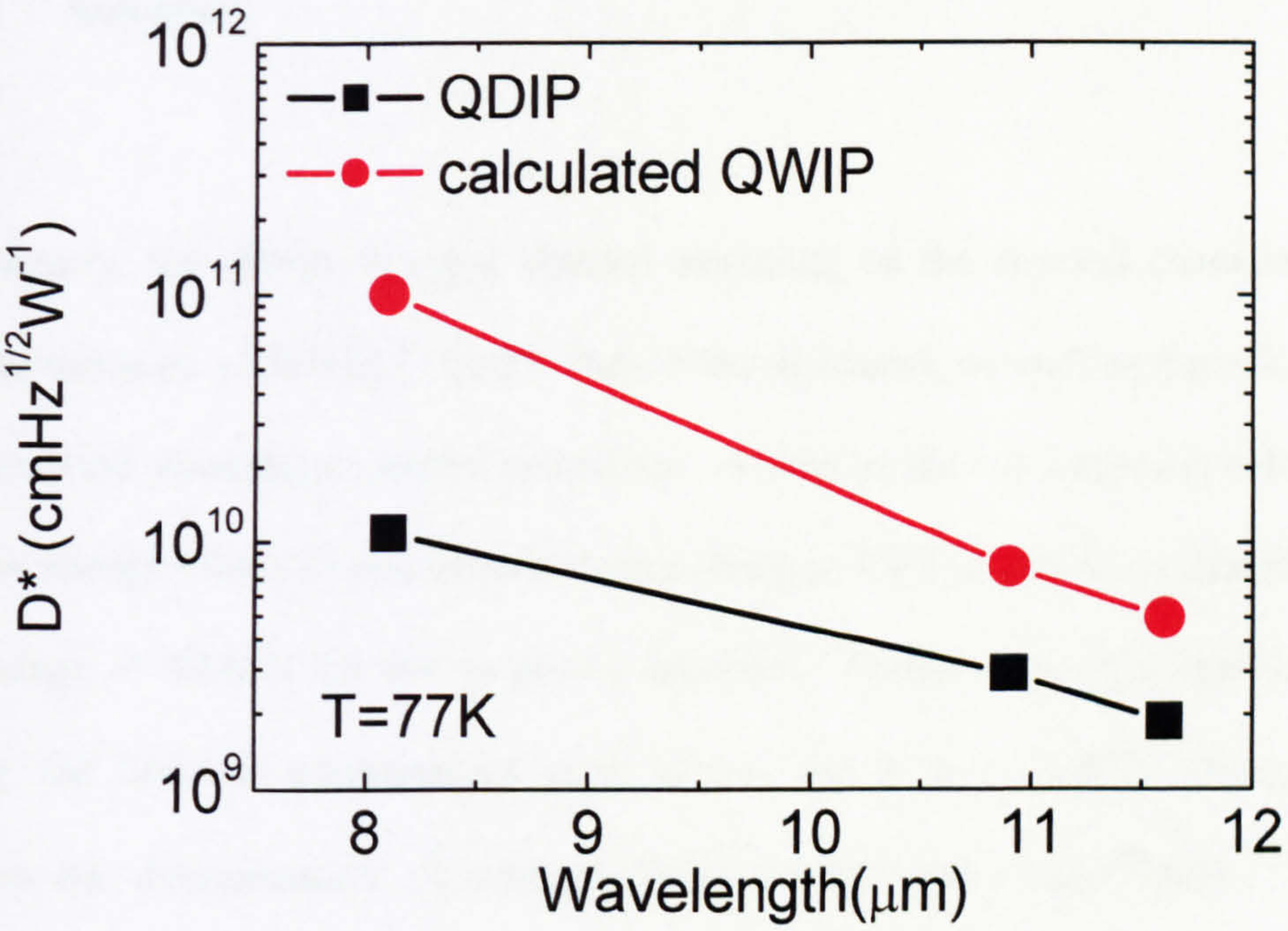

Fig.5.1.8. D^* reduction of annealed DWELL QDIPs with wavelength (for -2.0V) compared to that of calculated QWIPs[14]

These results are very promising as they reveal the suitability of these devices for dual band focal plane array (FPA) applications in the LWIR, whereby two different narrow bands with minimum spectral cross talk [14] can be fabricated on the same wafer. Also, using a technique whereby depositing a sputtered SiO_2 cap upon the wafer surface, it is possible to shift the emission of a wide range of material systems by ~100meV [15]. This is a useful technique as it results in lower required temperatures than usually employed by rapid thermal annealing while achieving significant intermixing. The potential benefits of such a technique also include the ability to select the areas that will be intermixed by photolithographically patterning the areas that will be sputtered with SiO_2 [15], which could facilitate further the fabrication of large dual-band FPAs [14].

5.1.4. Summary

In summary, the effects of rapid thermal annealing on the spectral characteristics and performance of DWELL QDIPs have been discussed, as well as the effects on the intraband absorption spectral behaviour. A shift of the *s-p* transition below the phonon energy (26meV) was observed upon 4min of RTA at 800°C compared to an *s-p* energy of 42meV for the as-grown structure. Furthermore, the capability of tuning the detector photocurrent peak across the 8-14μm LWIR atmospheric window was demonstrated. A reduction in detectivity from $1.1x10^{10}cmHz^{1/2}W^{-1}$ to $3x10^{9}cmHz^{1/2}W^{-1}$ has been found to be comparable to the expected reduction of detectivity for similar QWIPs. The combined result of the achieved ~4μm spectral shift and the very narrow spectral linewidths, makes this an appealing technique for fabricating dual-band QDIPs for FPA applications.

5.2. Two-photon absorption in DWELL QDIPs

5.2.1. Introduction

The development of emitters in the mid-infrared (MIR) and far infrared (FIR), such as quantum cascade lasers, that are capable of pulsed and mode-locked operation with pulse widths in the order of ~ps, have created the necessity for the development of fast and sensitive detectors for monitoring and characterising short optical pulses in these regions [16,17]. Standard methods where the second-harmonic generated light in a non-linear crystal is measured by a slow linear detector, can be potentially substituted by non-linear infared photodetectors [18].

Non-resonant two photon (2P) processes have been studied in QWIPs [19], and more recently optimised structures for 2P absorption were investigated, where energetically equidistant subbands resulted in resonantly enhanced 2^{nd}-order intrinsic non-linearities [16]. As a result, high sensitivity 2P detectors of mid-infrared sub-picosecond pulses have been demonstrated [17,18,20].

The development of 2P QDIPs would be highly significant as they are capable of true normal incidence operation, have long intermediate state lifetimes resulting in high 2P absorption co-efficients and have an intrinsic energy level configuration which makes them particularly attractive for operation in the terahertz region. Non-linear studies in non-detector QD structures have demonstrated second harmonic generation with very high nonlinear susceptibilities [21]. However no studies of non-linear optical processes have yet been reported for QDIPs.

Two photon normal incidence detection of FIR picosecond pulses using DWELL QDIPs are presented in this section along with a quadratic increase of the photocurrent with the incident power for bias range of 0.2V-0.8V. For higher applied bias (1.2V) this behaviour changes to linear, as the escape probability increases and the one photon (1P) photocurrent overcomes the 2P process. Finally, second-order autocorrelation measurements of short FIR pulses of ~3ps at λ~26.5μm were performed. The DWELL sample is structure vn189, the growth of which is described in detail in chapter 3.1.

Measurements were performed using the Dutch free electron laser FELIX in Nieuwegein. The output of FELIX consists of a train of macropulses of ~4μs in length running at a repetition rate of 5 or 10 Hz. In our case each macropulse is made up of 100 micropulses with a pulse-width of 3-4ps, a repetition rate of 25MHz and a pulse separation of 40 ns. FELIX was continuously tuned from 18 to 35μm, and detected by our QDIP, cooled to 5K

5.2.2. 2P Photocurrent spectral and power dependence

Fig.5.2.1 shows the photocurrent at +1V measured using FTIR spectroscopy, where 1P transitions dominate and the possible DWELL conduction band transitions are indicated in the inset of Fig.5.2.1. The observed photocurrent arises due to $E_1 \rightarrow E_{QW}$ (peaked at ~10μm) or to $E_1 \rightarrow E_{cont}$ (peaked at ~6μm) as discussed in chapter 3.

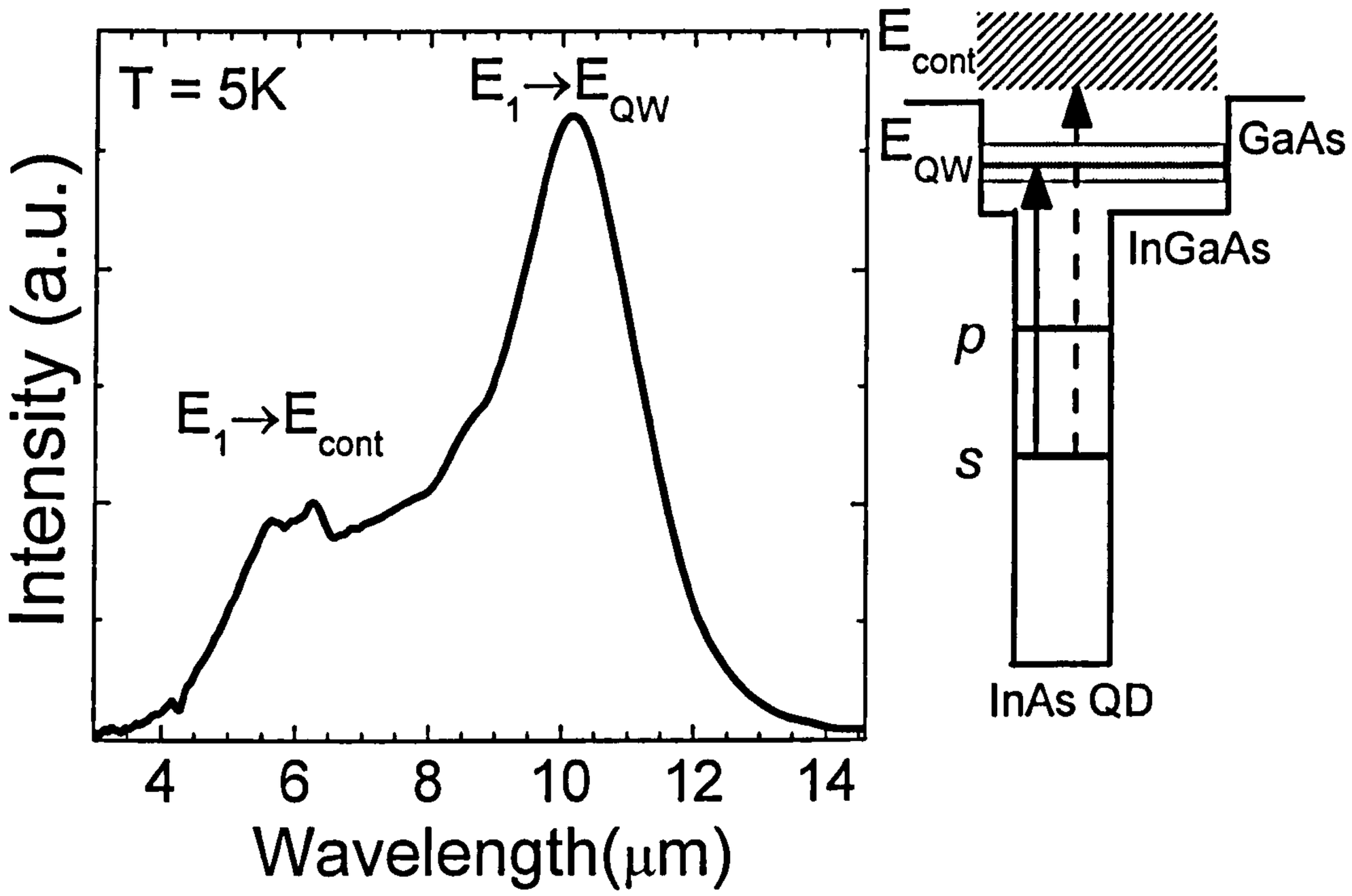

Fig.5.2.1. One photon photocurrent measured by FTIR spectroscopy at 0.8V and 5K. Inset shows a conduction band diagram with the relevant transitions in DWELL QDIPs; the $E_1 \rightarrow E_{QW}$ transition is indicated by the solid arrow, peaked at ~10μm, and the $E_1 \rightarrow E_{cont}$ transition is indicated by the dashed arrow, peaked at ~6μm

To investigate the spectral dependence of 2P transitions, the output of FELIX was used. Fig.5.2.2 displays the photocurrent spectra at 5K measured by tuning the FELIX wavelength from 18-35μm, showing a photocurrent peak at λ~26.5μm (47 meV). This energy corresponds closely to the dot ground state E_1 (*s*) to first excited (*p*) state transition energy (*s-p*) observed in previous absorption studies [22,23] and 1P photocurrent studies of DWELL QDIPs [11] (also in chapter 3.1), thus strongly indicating the photocurrent is associated with the *s-p* transition within the dots.

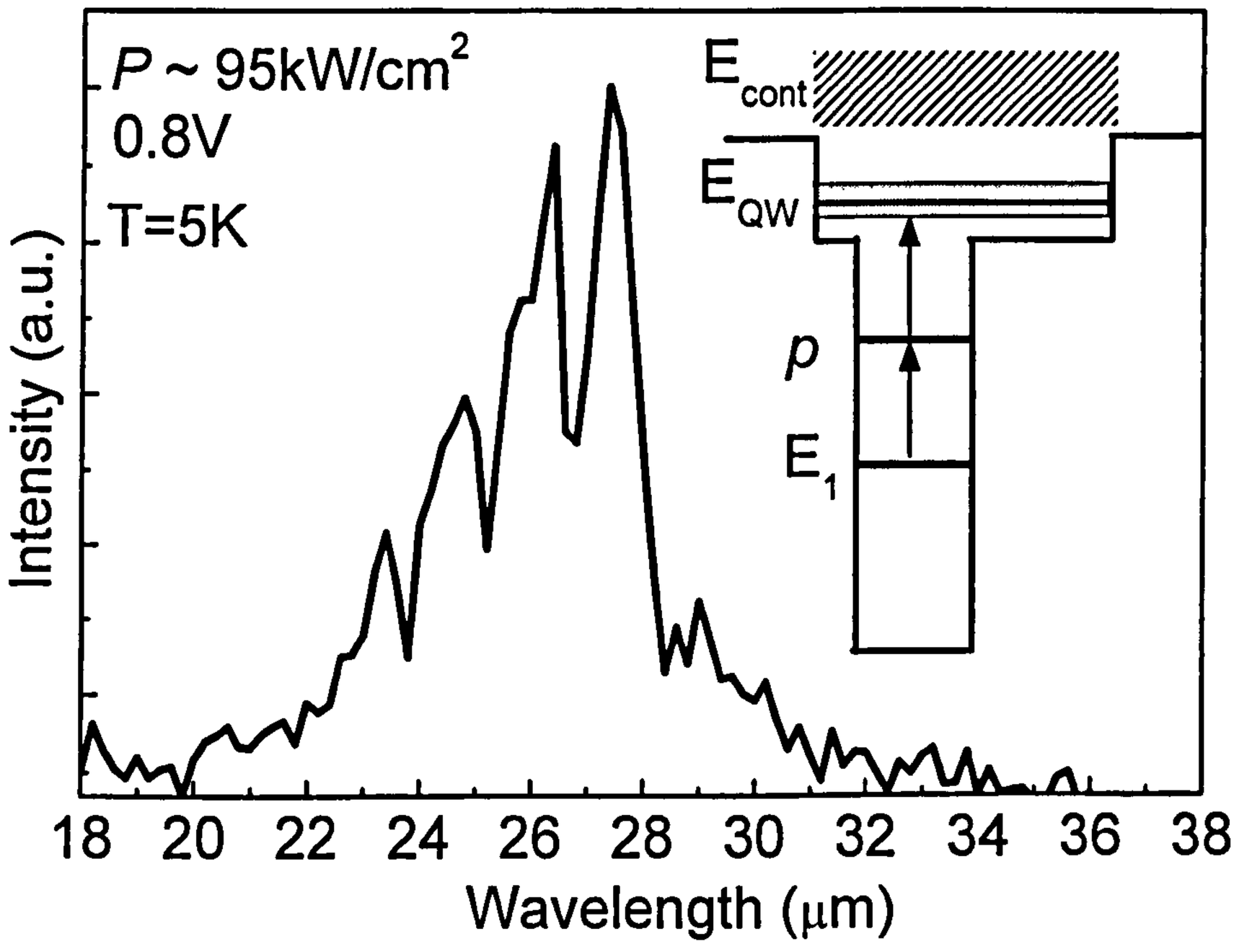

Fig.5.2.2. Two photon (2P) photocurrent spectra at 5K for DWELL QDIP illuminated with ~95kW/cm^2 peak power at normal incidence. The dips in the spectrum are due to atmospheric absoprtion in this spectral region. Inset shows the possible 2P process involving intermediate *p*-states.

As described below, power dependent measurements show that under these conditions a 2P electron transition can be excited involving the *s*-state of the QD, the intermediate *p*- state in the QD and states in the QW (shown schematically in the inset of Fig.5.2.2).

By investigating the dependence of the photocurrent on incident power for different bias conditions, exciting with the FELIX output at $\lambda = 26.5\mu m$ (resonant with the *s*-*p* transition) it is possible to determine whether a 1P or 2P process is involved. For these measurements the QDIP was connected to a current preamplifier and the output signal was measured using an oscilloscope.

Fig.5.2.3 shows the photocurrent dependence on peak power density P for 0.2V, 0.5V, 0.8V and 1.2V, at T = 5K. For 0.2V up to 0.8V, a quadratic dependence of P was observed in the range of 10kW/cm^2 to 400kW/cm^2, showing that 2P processes dominate.

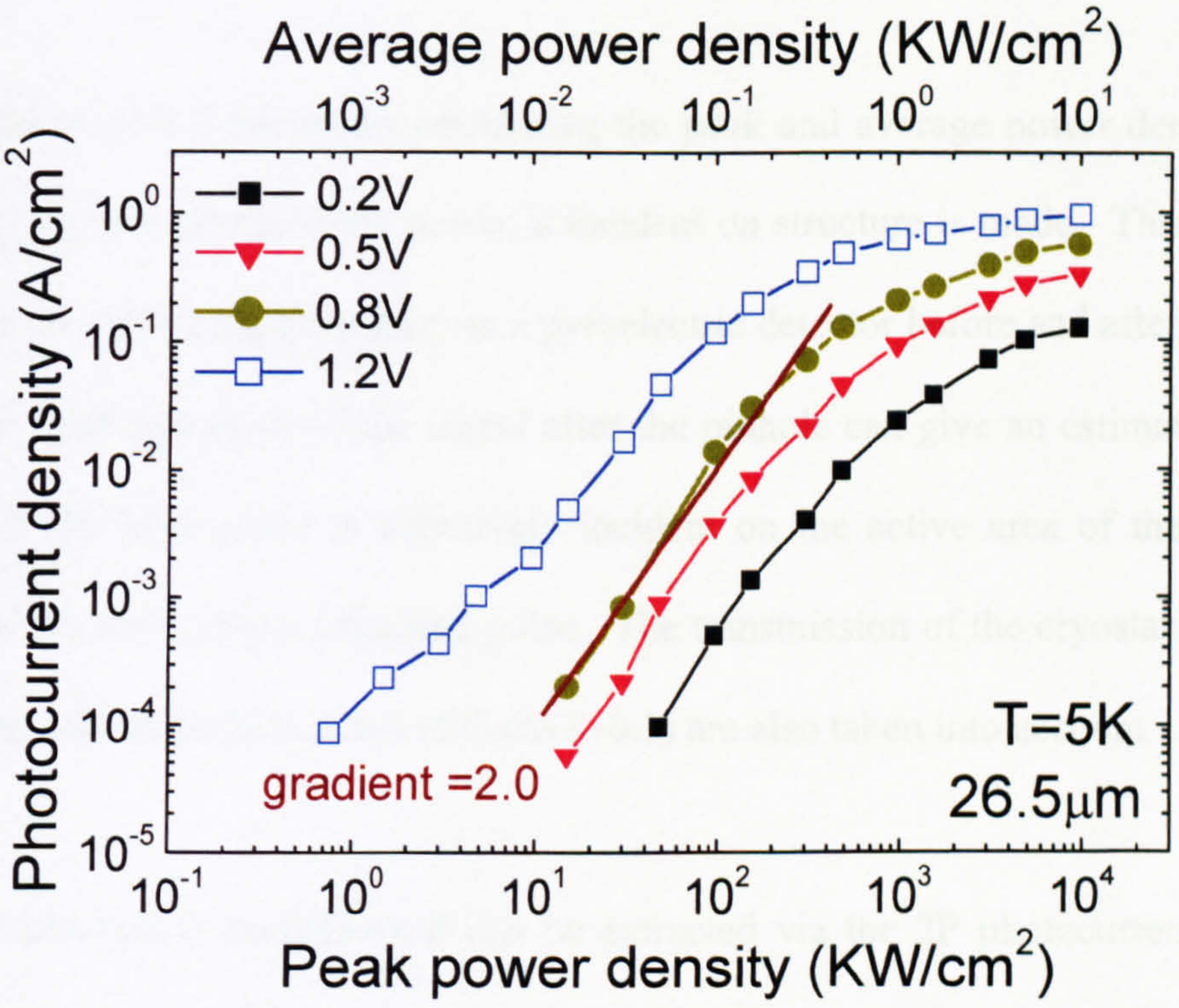

Fig.5.2.3. Photocurrent power dependence at 5K for 0.2V (black closed squares), 0.5V (red triangles), 0.8V (dark yellow circles) and 1.2V (blue open squares). The dependence is quadratic from ~10kW/cm^2 up to ~400kW/cm^2, after which it saturates

An overall increase of the photocurrent magnitude is observed when increasing the bias due to the increased escape probability from the final photocurrent state. When the applied bias is increased to 1.2V, the dependence becomes more linear (over the range from 10kW/cm^2 to 400kW/cm^2); indicating that tunnelling directly from the *p*-state becomes significant and therefore 1P processes give rise to the photocurrent.

From Fig.5.2.3 it can also be seen that a gradual decrease of the quadratic behaviour occurs with increasing peak power density. A further increase in P leads to saturation of the photocurrent at approximately 4MW/cm^2, which could be attributed to space charge saturation [20], absorption saturation [24], or contact effects [25].

It should be noted that when calculating the peak and average power densities, an estimate of how much of the power is incident on structure is made. This estimate is based on measuring the signal on a pyroelectric detector before and after a 600μm pinhole. The reduction of the signal after the pinhole can give an estimate of how much of the laser pulse is effectively incident on the active area of the detector (400μm diameter), for a Gaussian pulse. The transmission of the cryostat windows (0.49) and the refractive index of GaAs (~0.3) are also taken into account.

The 2P absorption coefficient β can be extracted via the 2P photocurrent density (Fig.5.2.3), j_{2P}, by [17]:

$$j_{2P} = \frac{e\beta L f_\theta g}{h\nu} P_{ave}^2 \qquad (5.1)$$

Where L is the thickness of the active region, which for a 5 layer structure is L = 40nm and P_{ave} is the average power density. The factor f_θ is related to the angle of incidence and is equal to unity for normal incidence. Under the assumption that the gain is near unity [26], from (5.1), β is estimated to be ~1x10^7 cm/GW, close to the values reported for resonant 2P QWIPs [17,20], and is 6 orders of magnitude higher than for bulk materials such as GaAs or Si.

It is therefore clear that even for unoptimised DWELL QDIP structures such as those studied here large values of β are possible. Growth of DWELL QDIP samples in which the *s-p* and $E_1 \rightarrow E_{QW}$ transitions are resonant would result in approximately one order of magnitude larger values of β. It was shown in previous chapters how the energy level configuration in DWELL can be controlled by varying either the well width or number of InAs monolayers deposited during QD growth. In addition, as discussed in the previous section, intermixing studies show that transition energies can be fine-tuned using post-growth rapid thermal annealing.

Also, as demonstrated in previous studies and shown in chapter 3.3, the $E_1 \rightarrow E_{QW}$ energy can be varied in DWELL structures via the Stark effect [27], whilst the *s-p* energy should be far less sensitive to applied bias, providing a further method for tuning the relative energy level separations and hence the 2P absorption co-efficient.

A power dependence of the photocurrent was also carried out at 80K to study the effect of temperature on the two photon process. Fig.5.2.4 shows the behaviour at higher temperatures at 0.8V plotted along with the 0.8V photocurrent at 10K (from Fig.5.2.3). At 80K the bias dependence becomes linear with power, with the linear regime attributed to thermal population of the intermediate state [18] and subsequent enhanced escape probability via a 1P channel.

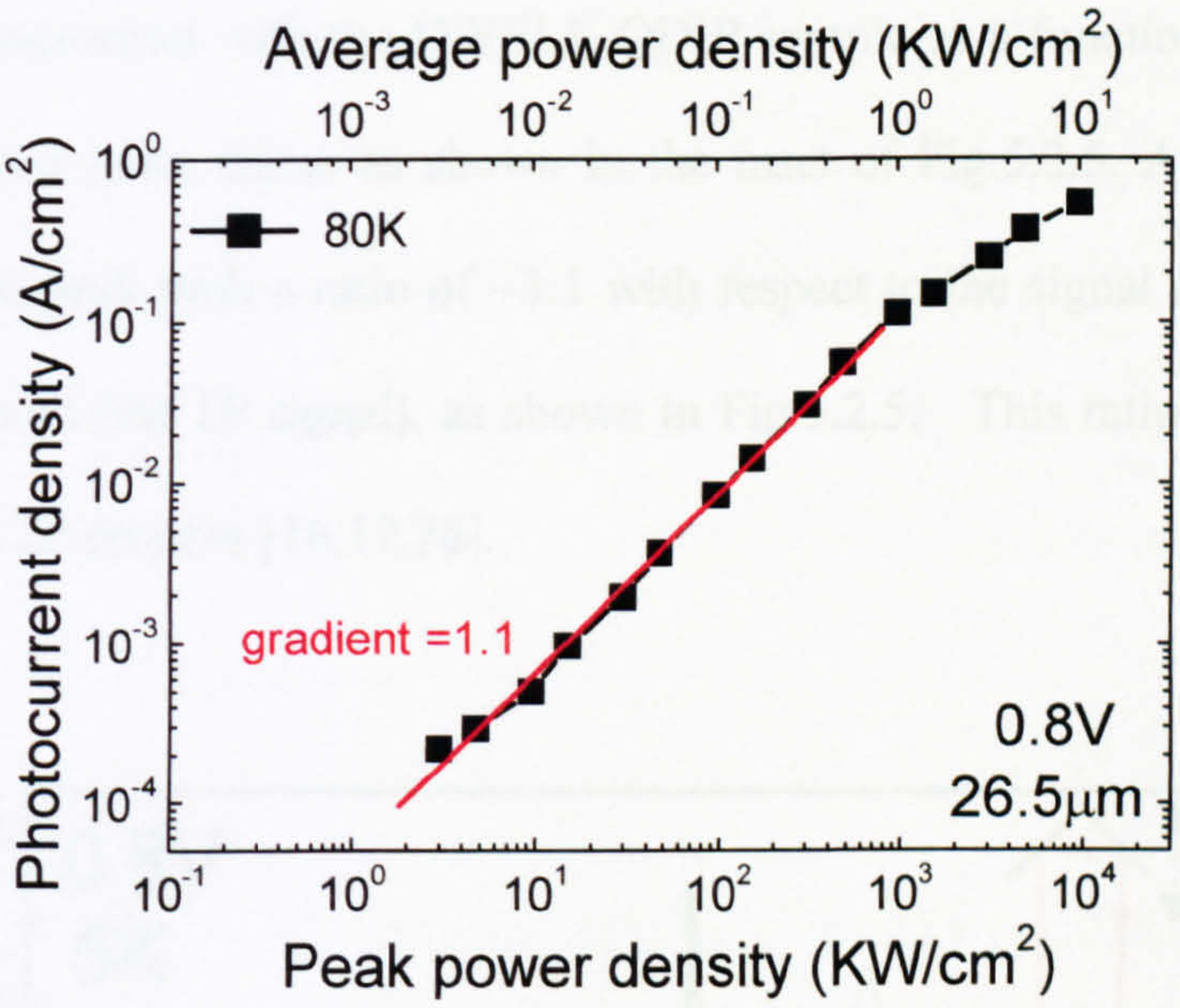

Fig.5.2.4. Photocurrent power dependence at 10K (dark yellow circles) and 80K (black closed squares) for 0.8V. At high temperatures the dependence is linear for all of the bias range.

As part of these studies I also investigated additional samples with a 1P photocurrent peak (i.e. energy of final state) of 160meV. For these samples the final state energy is far from twice the *s-p* transition energy (~50 meV), and no quadratic photocurrent behaviour was observed.

5.2.3. Autocorrelation measurements

The time evolution of the 2P photocurrent signal was analysed using second-order autocorrelation measurements. As discussed in chapter 2.5, autocorrelation measurements can provide information on the relaxation times of the intermediate state. The FELIX output was split into two identical pulse trains and the 2P

photocurrent measured with the DWELL QDIP sample as a function of delay time between the two pulse trains as shown in the inset of Fig.5.2.5. At zero delay an autocorrelation peak with a ratio of ~3:1 with respect to the signal away from zero delay is observed (the 1P signal), as shown in Fig.5.2.5. This ratio is close to that expected for a 2P process [16,17,28].

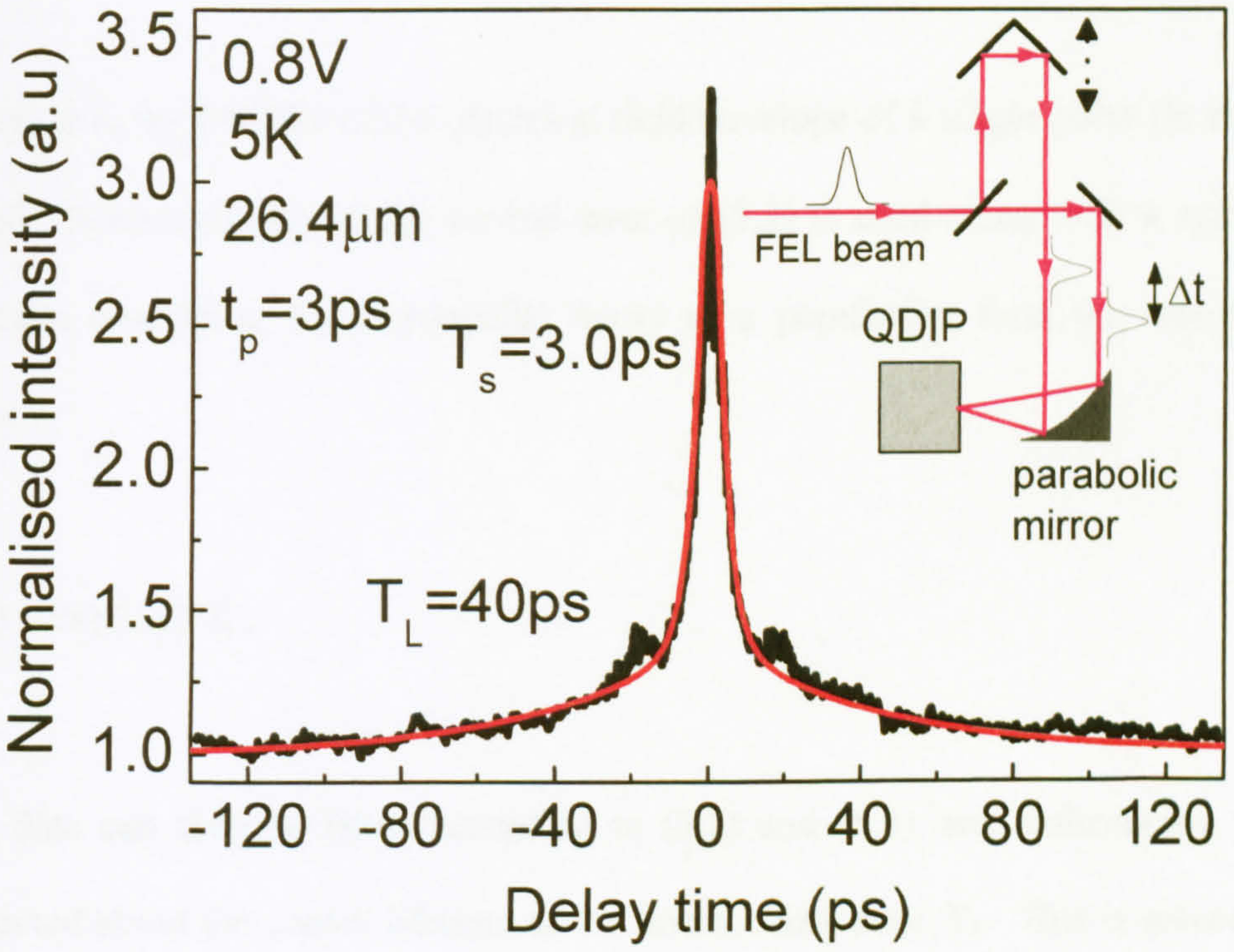

Fig.5.2.5. Autocorrelation trace of DWELL QDIP at ~95kW/cm^2 and 0.8V at the peak of the spectrum (~26.5μm) measured at normal incidence (red line). A bi-exponential fit (black line), yields a T_s = 3ps and T_L = 40ps. Inset shows a schematic of the experimental set-up.

There is some evidence of interference symmetrically away from zero delay at ~18ps. This could be a result of reflections from the back of the sample (as it is a normal incidence measurement).

Following the approach of Nessler et al [29], the autocorrelation measurements are numerically fitted and information is extracted about the carrier lifetime of the intermediate state. This is done via the following expression for an ideal autocorrelation trace ($S_{ideal}(\tau)$):

$$S_{ideal}(\tau) = 1 + 2 \cdot \exp(-4 \cdot \ln 2 \cdot (\tau / \sigma)^2) \quad (5.2)$$

where, σ is the FWHM of the electrical field envelope of a single pulse (in this case ~3ps). A convolution of the second term of (5.2) is used along with a symmetric function describing the exponential decay of a population from the intermediate state:

$$f(t) = \exp(-|t| / T_1) \quad (5.3)$$

The data can then be fitted according to (5.2) and (5.3), and information can be extracted about the carrier lifetime of the intermediate state T_1. This is solved again for another longer time constant T_{long} and the two numerical calculations fit the bi-exponential decay of the trace. A bi-exponential decay fit of the autocorrelation trace yields a short time (T_s) and a longer time constant (T_L) with times of T_s~3ps and a T_L ~40ps. T_L is associated with the lifetime of the *p*-like intermediate state, which has been extensively studied [21,22] using pump-probe spectroscopy yielding typical times between ~30 and 60ps, depending on the energy of the *s-p* transition.

The origin of T_s is not well understood, but can be explained, considering recent observations of the effects of acoustic phonon sidebands (APSs) in the QD

absorption spectrum [30,31]. The single QD absorption spectrum typically consists of a zero phonon line (ZPL) which is significantly broadened by APSs, a schematic of which is shown Fig.5.2.6. This was originally observed for QD excitons [30] and also in *s-p* absorption spectra using four-wave mixing spectroscopy [31]. The presence of acoustic phonon sidebands in an inhomogeneously broadened QD ensemble can result in resonant 2P absorption involving ZPL, as well as APS. The characteristic time in autocorrelation measurements in the latter case is determined by a very short (~ps) decoherence time due to emission of coherent acoustic phonons.

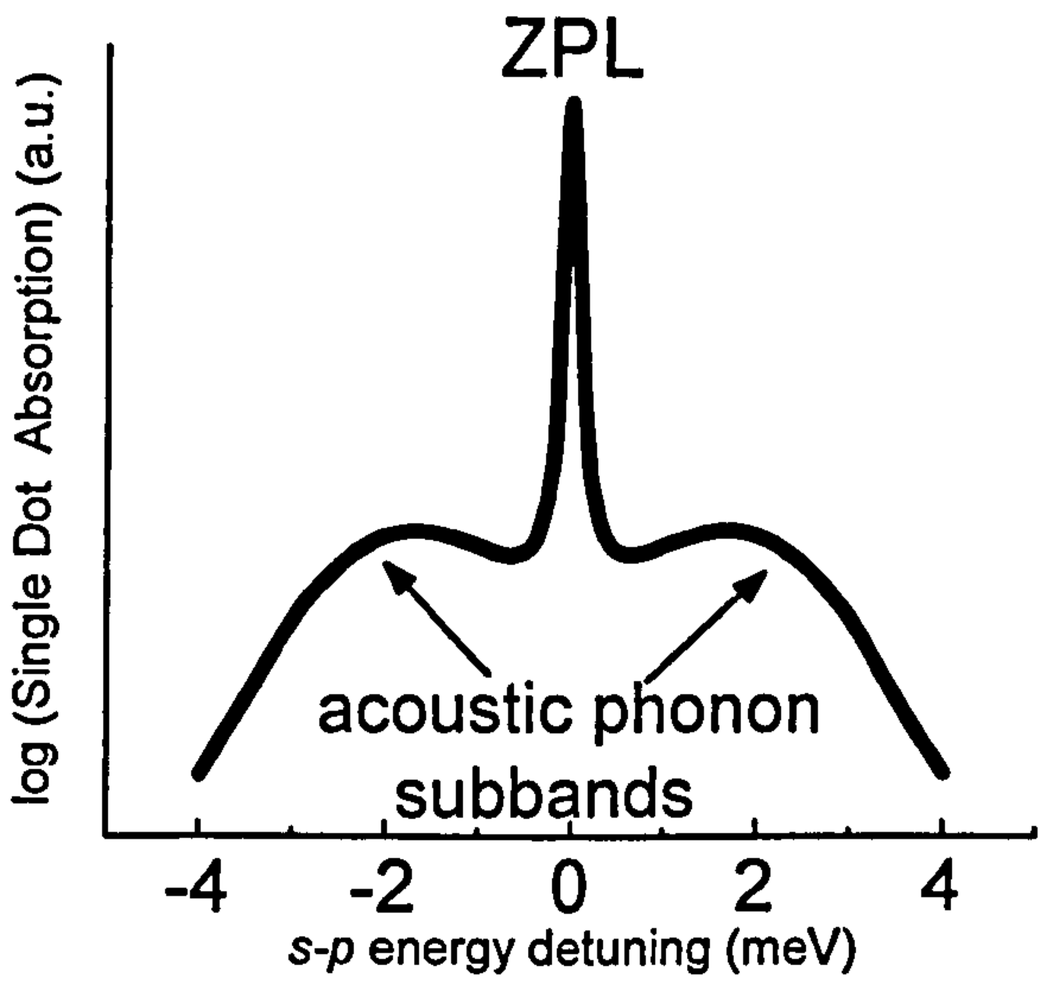

Fig.5.2.6. Schematic of the single dot intraband absorption line composed of the zero phonon line (ZPL) and acoustic phonon sidebands

Although the absorption of APSs is much smaller compared to ZPL, the number of dots for which the resonant 2P absorption via APSs is possible will be significantly larger than the number of QDs with 2P absorption via ZPL due to the relatively large ~2meV broadening of the absorption line. However, in order to explain the origin of T_s more explicitly, further detailed studies will have to be performed.

5.2.4. Summary

In summary, the two–photon normal incidence detection of FIR ultrashort optical pulses using DWELL QDIPs was presented. A quadratic increase of the photocurrent was observed with incident power tuned into resonance with the ground-first excited state transition in the quantum dots. This dependence changed to linear with either high applied bias or elevated temperature, the former being attributed to a field assisted increase of the electron escape probability from the intermediate state, and the latter due to a thermally assisted escape from the intermediate state. Second order autocorrelation measurements were used to determine the dynamics of the photodetector. The results in this section demonstrated the potential of normal incident non-linear DWELL QDIPs for the characterisation of few picosecond far-infrared laser pulses and provide insight into the relaxation dynamics in these devices.

5.3. Photovoltaic quantum dot infrared photodetectors

5.3.1. Introduction

Another class of infrared detectors, briefly mentioned in the introduction chapter 1, are photovoltaic (PV) detectors. The advantage of PV over photoconductive detectors (PC) is the elimination of the dark current, which removes generation-recombination noise at zero applied fields [8]. This results in a better theoretical upper limit for detector signal to noise ratio, as well as simplification in biasing, and providing a more accurate prediction of the responsivity [32]. In principle, all the materials used to make PC detectors can be used to make PV detectors and there are many examples of Si, HgCdTe and InSb PV detectors, and more recently PV QWIPs and QDIPs [8,33-37], which are the subject matter of this section.

PV intraband detectors are based on an in-built inversion asymmetry to provide an effective electric field, thus eradicating the need for an external applied voltage. Although the dark current is reduced to zero, the PV approach also results in a much smaller gain, affecting the photocurrent of the device compared to equivalent PC detectors. This leads to PV detectors having comparable achievable detectivities to PC detectors. It has been demonstrated for QWIPs that optimised PV structures can achieve similar detectivity values as previously optimised PC QWIPs [8]. Therefore, although PC detectors are better for applications requiring high responsivities, PV detectors can be used when the integration time of an FPA is limited by the storage capacity of the read out circuit (ROIC) [8], which is often the case in large 2D arrays where the ROIC size is limited by the FPA pitch.

Previous reports on PV QWIPs have demonstrated the photovoltaic effect using a variety of designs. Kastalsky et al, observed PV detection in an n-type GaAs/AlGaAs superlattice with a built-in graded AlGaAs barrier [3], and Goosen et al showed how it is possible to achieve PV detection by introducing a two-dimensional electron gas produced by modulation doping in the AlGaAs spacer [34]. Schneider et al also reported a PV QWIP based on asymmetrically doped double-barrier QW [35]. There have also been reports on PV operation in QDIPs, as a result of the intrinsic inversion asymmetry of the band structure of the self-assembled dots [36]. More recently, Hwang et al reported PV QDIP operation which was due to the segregation of Si atoms in the QDs and to the shape of the dots, but also enhanced by an AlGaAs single sided barrier [37]. Also QWIP detectors based on a quantum cascade configuration have shown promising results for PV operation [38,39], but have certain shortcomings, such as current leakage from resonant miniband states. The absence of the dark current could also lead to high temperature uncooled detectors and reports of PV QWIPs have recently shown near RT operation for the near-IR [40] as well as the LWIR [41].

Probably the most interesting design that has been recently demonstrated for QWIPs, was based on a 'four-zone scheme' by Schneider et al [41,42]. This design provides an enhancement of the asymmetry as well as considering very thoroughly the tunnelling and capture probability, with respect to the thickness of the barriers and their position. One important parameter in designing an intraband PV detector is ensuring the direction of the current flow, or in other words the direction of the in-built electric field. This design is believed to achieve this efficiently and for that reason the designs proposed herein follow from the same principles, although they

have significant differences. The proposed design in this chapter has the advantage of the sensitivity to normal incidence, a high RoA (the product of differential resistance and detector area) and narrow linewidth photoresponse, which make it a very promising technique towards the fabrication of PV DWELL QDIPs.

In this section the design and operation of two PV QDIP designs are presented with responsivities in the range of 0.2mA/W at 77K, and RoA products of ~$10^6\Omega cm^2$, yielding detectivities of $10^{10}cmHz^{1/2}W^{-1}$ at 77K and 7μm. Prior to the growth of these structures, significant simulation work was carried out, by a model solving the transfer matrix Schroedinger equation for the wavefunctions of the energy states involved. Although this has been shown not be precise for the 3D QD system it is quite accurate for the 2D QW case and hence was mainly used to optimise the superlattice (SL) design discussed below.

The principle of operation of these two devices is based on an inversion asymmetry introduced by a combination of (a) an asymmetric GaAs/$Al_yGa_{1-y}As$ superlattice, (b) an $In_xGa_{1-x}As$ QW (for the first design) and (c) and an InAs/InGaAs DWELL region separated from (b) by a thin AlAs barrier. The in-built strain induced electric field which was discussed previously is not considered in the simulations, but could well be contributing to the effect. A discussion of the dynamics of the predicted, and experimentally observed detector operation are discussed in the individual sections for each of the designs that follow.

5.3.2. Design approach 1 - using a superlattice and adjacent InGaAs quantum well

Table. 5.3.1 Growth details of PV QDIP including GaAs/AlGaAs superlattice and InGaAs capture zone.

Repeats	Thickness (A)	material	x	dopant	type	Nonc(cm-3)
1	4000	GaAs		Si	n	2X10+18
1	400	GaAs				
7	50	InxGa(1-x)As	0.1			
7	5	GaAs				
7	18	AlAs	1			
7	70	InxGa(1-x)As	0.05			
7	7	InAs (2.55 ML)				
7	10	InxGa(1-x)As	0.05			
7	5	GaAs				
7	3	Si-delta doping 1x the dot density		Si	n	1 to 2 e/dot
7	5	GaAs				
7	20	AlGaAs	0.2			
7	100	GaAs				
7	20	AlGaAs	0.2			
7	130	GaAs				
7	20	AlGaAs	0.2			
7	200	GaAs				
1	4000	GaAs		Si	n	2X10+18
1	SI-GaAs Substrate					

The above table shows the layer structure for the first design. The QDIP device structure incorporated a bottom contact layer of 4000Å *n*+ Si doped GaAs, an undoped layer containing 7 periods of active region, and a final 4000Å *n*+ Si doped GaAs contact layer. The active region is Si δ-doped in the GaAs barrier layers, to a concentration of $6x10^{10}cm^{-2}$ corresponding to approximately 1 electron per dot.

Using in-house software previously described in chapter 3 and used frequently for simulation of QW structures (e.g. QCLs), the conduction band of the above structure was calculated. The first simulation is illustrated in Fig. 5.3.2. Fig.5.3.1 on the other hand shows a simple schematic illustrating the processes that occur in the conduction band. Arrows indicate the direction of the electron flow.

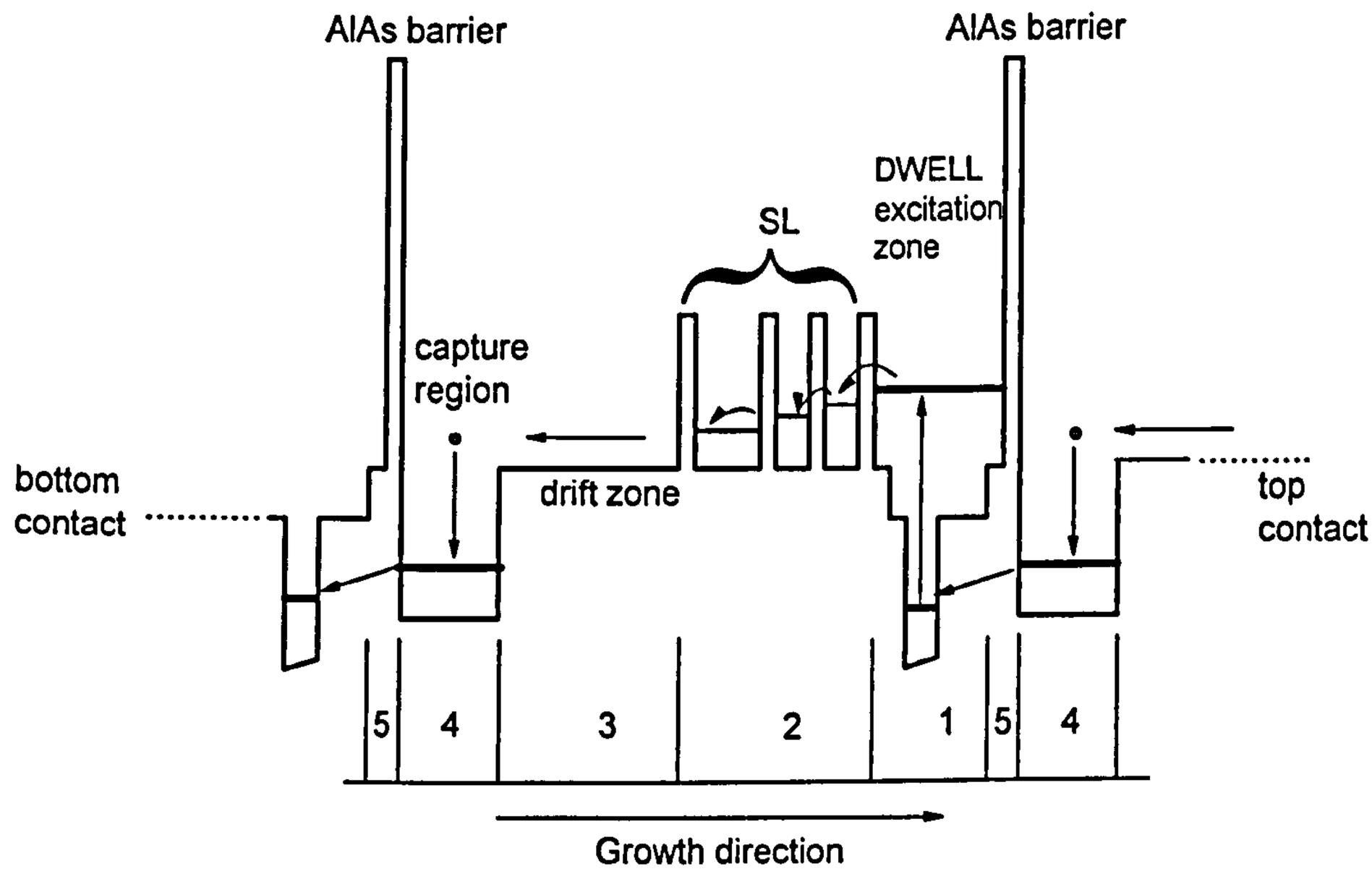

Fig.5.3.1. Schematic of the five-zone scheme for PV QDIP detector (not-in-scale), (1) excitation zone, (2) GaAs/AlGaAs superlattice, (3) drift zone, (4) capture zone, (5) tunnelling zone

With radiation incident on the detector, electrons will be photoexcited from the ground state of the QD to the state which is quasi-confined by the AlAs and first AlGaAs barriers (hereby referred to as DWELL state). The electrons should then tunnel through the first AlGaAs barrier of the SL in zone 2. Tunnelling in this direction is favourable because the state in the first QW of the SL is close to the

final photocurrent DWELL state and also because the electron flow is impeded along the growth direction by the AlAs thin layer which make it more probable for electrons to flow in the direction opposite to the growth direction. The tunnelling of electrons from the DWELL state through the AlGaAs barrier should in principle be faster (~1ps) [43] than the time it takes for them to relax back to the ground state (~5ps - see chapter 3.1).

The consecutive AlGaAs barriers are designed to have equal composition and width, but are designed with an increasing spacing (opposite the growth direction) as to introduce a built-in potential to assist the tunnelling in the required direction. This is considered to be a better approach than introducing a compositionally graded AlGaAs barrier, as the tunnelling should be more efficient, and a digital grading generally involves less complicated growth conditions. The electron then passes through a drift zone of thickness of about 20nm of GaAs, before relaxing into the InGaAs QW capture zone. If the state to which the electron relaxes in the well is slightly above resonance with the QD ground state, then the electron should tunnel efficiently through the AlAs barrier to the next layer of dots. For this to occur the thickness of the AlAs barrier has to be calculated relating to the desired tunnelling efficiency and this can be done by estimating the tunnelling times for AlAs barriers [43]. However in this case the situation is slightly more complicated as the carriers will have to tunnel through a thin GaAs layer and the InGaAs capping layer.

The QW was designed such that it had only one 'ground' state to avoid transitions within the well which could result in loss of oscillator strength. The design of the

well however was based on a trade off between having a high indium composition, to tailor an energy level near the adjacent QD ground state, and not introducing more than one confined state in the well for the reasons mentioned above. Also the increased indium composition would increase the strain in the structure and may lead to defect formation. However as reported [42], the energy of the QW state needs to be close to the energy of the adjacent QD state, and although for the current structure presented below this was somewhat understated, future attempts could in principle attempt a higher In composition in the adjacent well to lower the energy of QW state closer to the QD state, and investigate the effects this would have on performance.

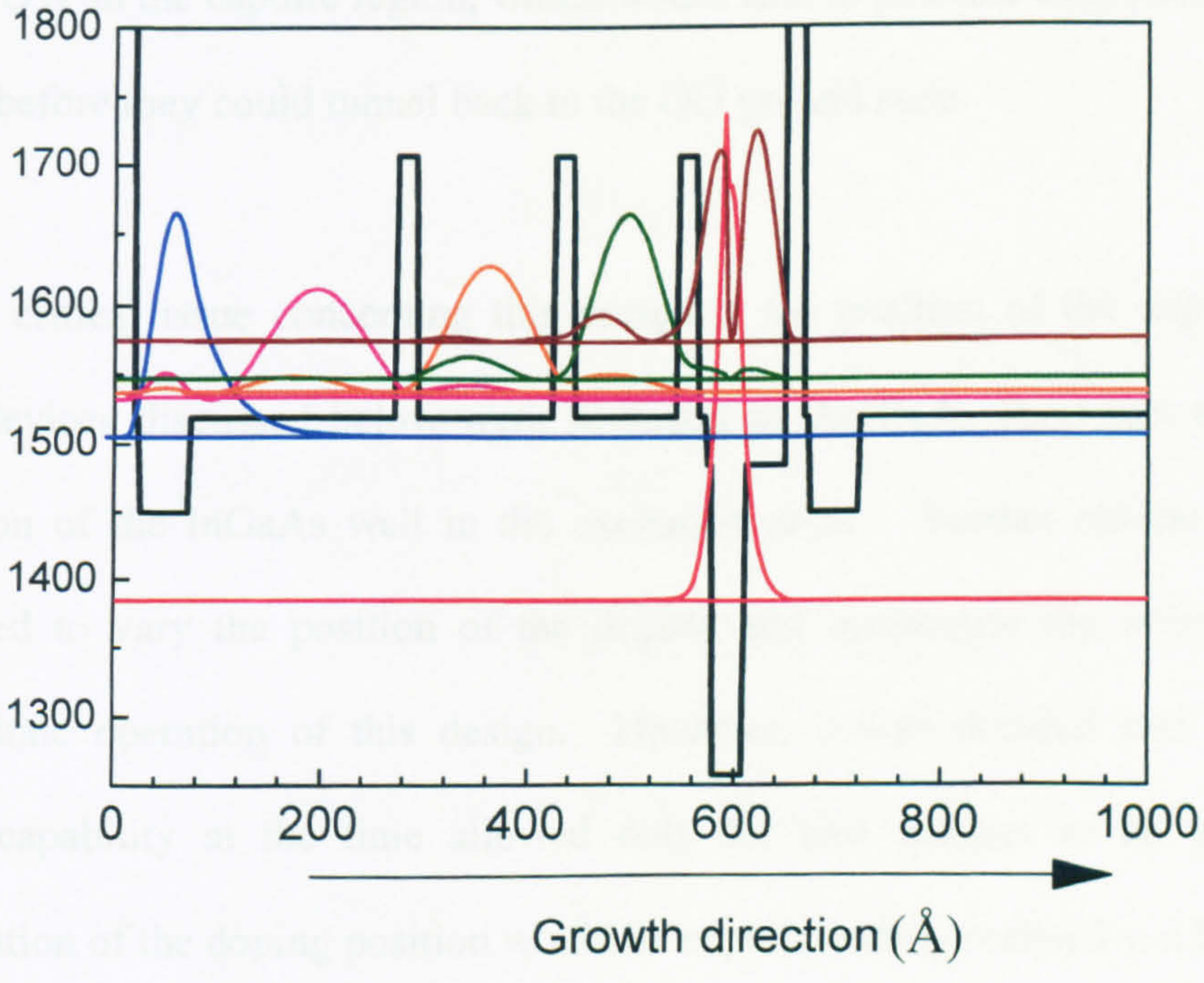

Fig.5.3.2. Simulation of the design described in table.5.3.1. The calculated squared wavefunctions of the energy levels involved are shown.

The calculation for the first design is illustrated above in Fig.5.3.2. The model uses an effective mass approximation to solve the Schroedinger equation and is the same that was used for preliminary calculations in chapter 3.3. The InAs QDs are simulated using a narrow InGaAs well. Although this is not very precise for modelling the QD wavefunction, the model is mainly used to estimate the appropriate distance between the AlGaAs barriers and the barrier height and width for effective tunnelling through the SL. Also it helps in investigating the maximum indium composition for the capture zone QW before introducing undesired bound states that the electron relaxing into the well could be re-excited to. The InGaAs QW in the DWELL excitation zone has been grown with a smaller indium composition (x=0.05) to ensure that there are no states resonant with the adjacent InGaAs QW in the capture region, which would lead to possible direct tunnelling of carriers before they could tunnel back to the QD ground state.

Another critical issue concerning this design is the position of the doping. The grown devices discussed below were Si-doped in the GaAs layer just before the deposition of the InGaAs well in the excitation zone. Further studies could be performed to vary the position of the doping and investigate the effects on the photovoltaic operation of this design. However, it was decided that since the growth capability at the time allowed only for two designs to be grown, an investigation of the doping position would be experimentally realised at a later date.

It is clear from the above discussion that this design is of high complexity. However preliminary simulations showed that other variations of the design (e.g.

with InAs/GaAs in the excitation zone, or more and less AlGaAs barriers), would be less effective overall, so the presented design was used.

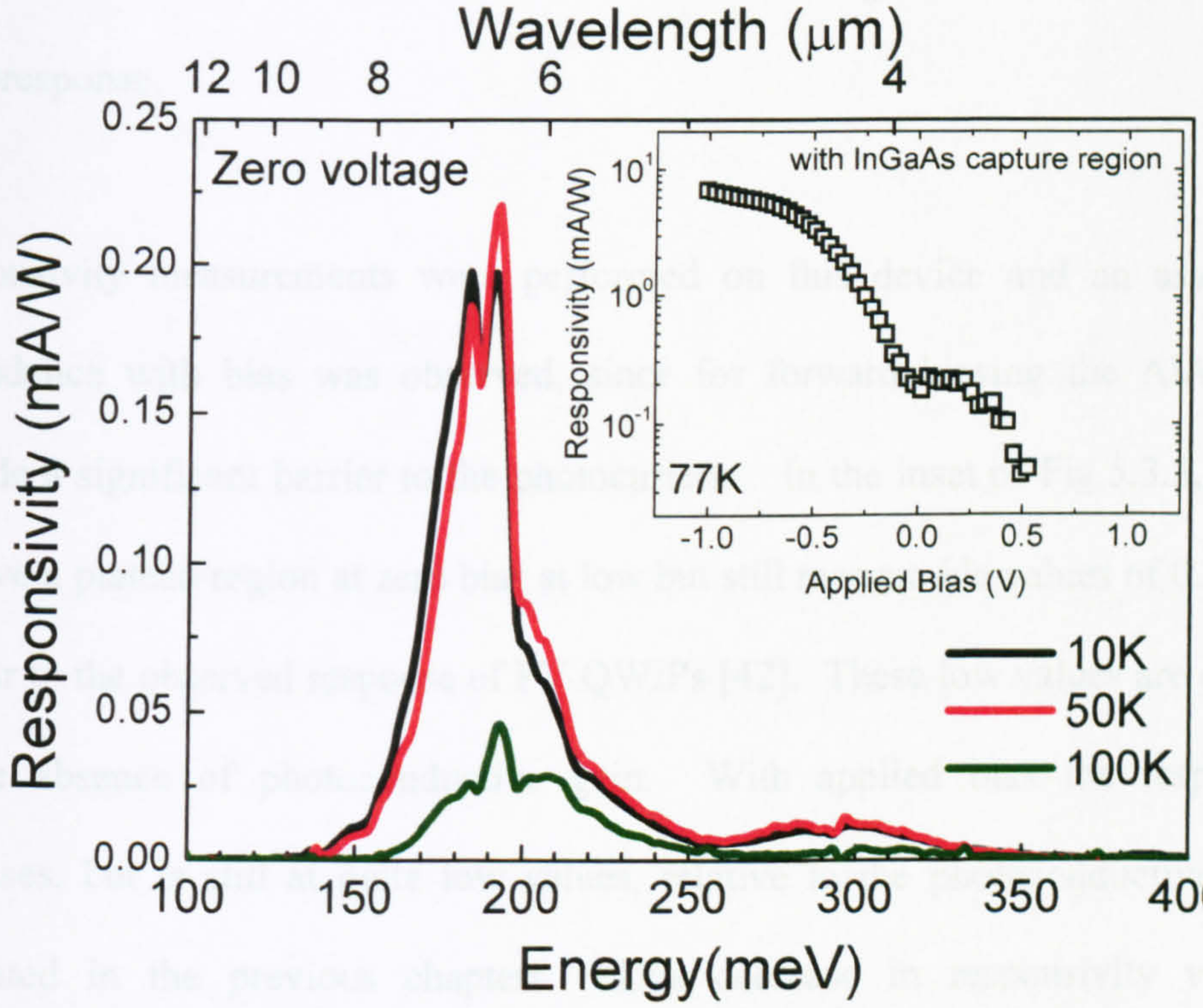

Fig.5.3.3. Measured Normal incidence photoresponse of PV SL QDIP at 10K (black), 50K (red) and 100K (green). Inset shows the peak responsivity of the device at 77K.

Fig.5.3.3 shows the normal incidence spectral results of the first design at three different temperatures. Although it has been mentioned that these devices have a stronger *p*-polarised photoresponse, as discussed in chapter 3, the normal incidence response is still quite clear. A peak feature attributed to the $E_1 \rightarrow E_{QW}$ transition is observed up to 100K without the application of an external electric field. A high energy shoulder is observed, attributed to transitions to the continuum of states,

similar to that observed for photoconductive QDIPs presented in this thesis. This indicates that the confinement of higher energy continuum states does not become enhanced with the incorporation of the AlAs and AlGaAs barriers, and hence transitions from these states do not contribute significantly to the spectral photoresponse.

Responsivity measurements were performed on this device and an asymmetric dependence with bias was observed, since for forward biasing the AlAs layers provide a significant barrier to the photocurrent. In the inset of Fig.5.3.3, one can observe a plateau region at zero bias at low but still measurable values of 0.2mA/W, similar to the observed response of PV QWIPs [42]. These low values are expected in the absence of photoconductive gain. With applied bias the responsivity increases, but is still at quite low values, relative to the photoconductive QDIPs presented in the previous chapters. This decrease in responsivity values is associated with the AlGaAs and AlAs barriers suppressing the photogenerated carriers, indicating that the design requires further optimising.

Also it is believed that the doping concentration was low for the PV design. Usually in the photoconductor case the structures are lightly doped, to limit the dark current and avoid occupation of higher energy states in the QD. However in this case the absence of the dark current should allow increased doping concentrations, to optimise the signal response of the detector.

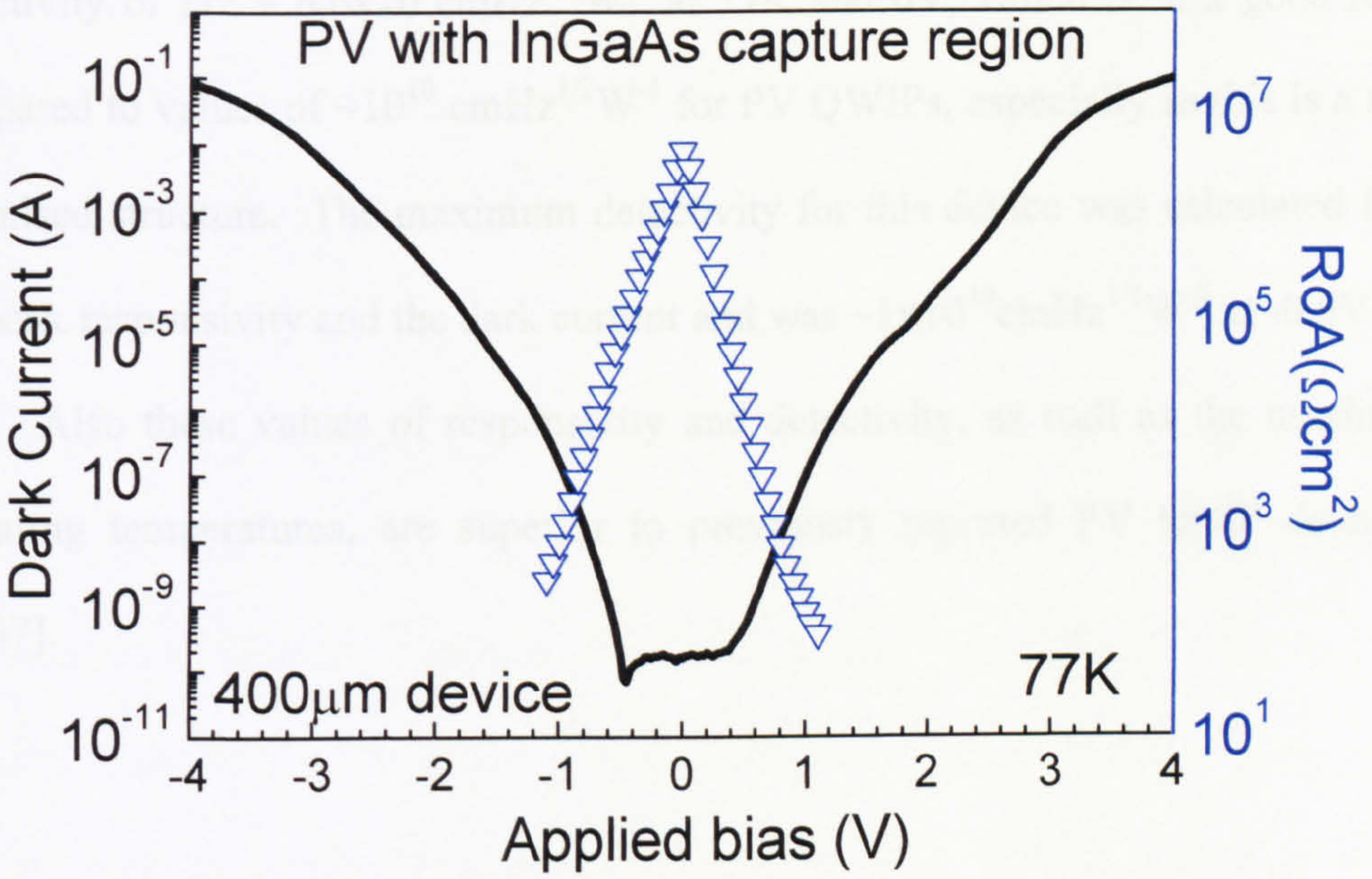

Fig.5.3.4. Dark current IV curve (black line) and RoA product at 77K of the PV QDIP with a InGaAs capture zone, Ro being the differential resistance of the device and A its area.

The dark current under bias was measured for this device, as well as the differential resistance of the detector, shown in Fig.5.3.4. The differential resistance was calculated by measuring an IV of the device under black body illumination. The RoA product was then deduced by multiplying the differential resistance with the area of the device (diameter: 400μm).

From the values for responsivity (Fig.5.3.3. inset) and RoA (Fig.5.3.4) one can estimate the detectivity of the PV detector using the equation [38,39].

$$D^* = R(\lambda)\sqrt{\frac{R_o A}{4k_B T}} \tag{5.3}$$

Where, RoA = $4.63 \times 10^6 \Omega cm^2$ at 0V (Fig.5.3.7), R(λ) ~0.2mA/W at 77K, and k_B is the Boltzmann constant = $1.3806503 \times 10^{-23}$ m^2 kg s^{-2} K^{-1}. This results in a

detectivity of $D^* = 6.6x10^9 cmHz^{1/2}W^{-1}$ at 77K and 0V, which is in a good range compared to values of $\sim 10^{10}$ $cmHz^{1/2}W^{-1}$ for PV QWIPs, especially as this is a non-optimised structure. The maximum detectivity for this device was calculated from the peak responsivity and the dark current and was $\sim 1x10^{10} cmHz^{1/2}W^{-1}$ at -0.5V and 77K. Also these values of responsivity and detectivity, as well as the maximum operating temperatures, are superior to previously reported PV QDIP detectors [36,37].

5.3.3. Design approach 2 – without adjacent quantum well

Table 5.3.2 Growth details of PV SL QDIP without InGaAs capture zone.

Repeats	Thickness (A)	material	x	dopant	type	N concentration (cm-3)
1	4000	GaAs		Si	n	2X10+18
1	400	GaAs				
7	18	AlAs	1			
7	70	InxGa(1-x)As	0.05			
7	7	InAs (2.55 ML)				
7	10	InxGa(1-x)As	0.05			
7	5	GaAs				
7	3	Si-delta doping 1x the dot density		Si	n	1 to 2 e /dot
7	5	GaAs				
7	20	AlGaAs	0.2			
7	100	GaAs				
7	20	AlGaAs	0.2			
7	130	GaAs				
7	20	AlGaAs	0.2			
7	200	GaAs				
1	4000	GaAs		Si	n	2x10+18
1	SI-GaAs Substrate					

A second design was considered, very similar to the previous one, but with the absence of an InGaAs QW in the capture zone. Therefore in this design the drift

zone and the capture zone are combined. This device was grown to see the extent of the effect of the capture zone on the device operation. The structure was grown as shown above in Table 5.3.2.

As the purpose of this structure was to elucidate the effects of the absence of the capture zone and its role in the overall design, independent simulation work to optimise this design separately was not carried out. Fig.5.3.8 shows the photoresponse of the PV QDIP without an InGaAs capture zone. A signal of similar intensity is observed at zero applied field at 10K at a slightly longer wavelength of 7.5μm. The responsivity of the device was similar to the previous design for negative biases, but showed a less asymmetric dependence on bias.

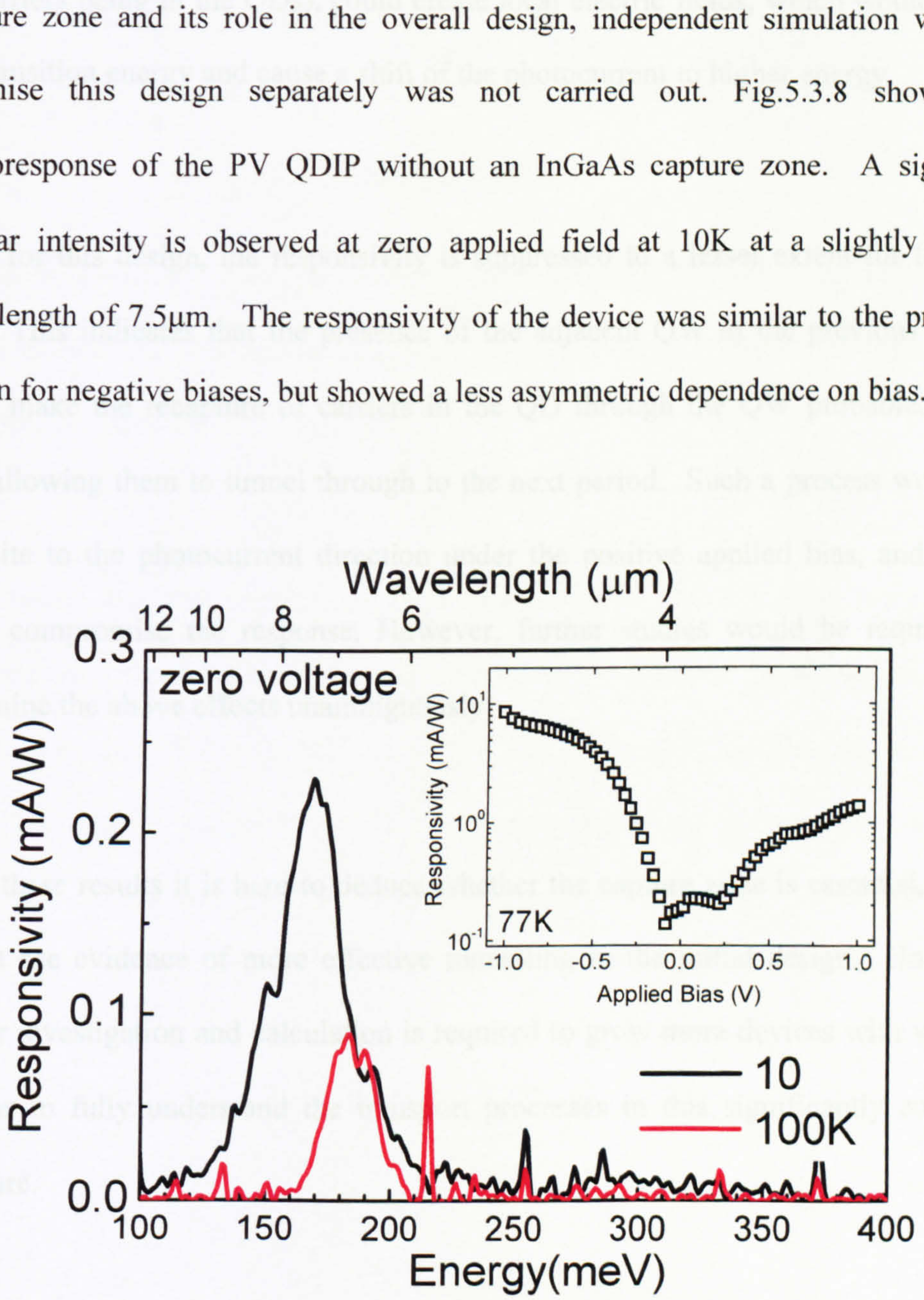

Fig.5.3.5. Spectral response of PV QDIP without InGaAs capture zone at 10K(black) and 100K (red). Inset shows the 77K peak responsivity of the device.

Of note is the spectral shift of the photoresponse when the temperature is increased at 100K. This could be due to thermal ionisation from small to large dots with increasing temperature. Such a process would result to a reduction in linewidth as is observed here (26 meV to 19meV for 10K and 100K respectively). Also the possible redistribution of carriers at higher temperatures within the structure (i.e. not all carriers being in the QDs), could create local electric fields, which would affect the transition energy and cause a shift of the photocurrent to higher energy.

Also, for this design, the responsivity is suppressed to a lesser extent for forward bias. This indicates that the presence of the adjacent QW in the previous design could make the recapture of carriers in the QD through the QW probable, rather than allowing them to tunnel through to the next period. Such a process would be opposite to the photocurrent direction under the positive applied bias, and hence could compromise the response. However, further studies would be required to determine the above effects unambiguously.

From these results it is hard to deduce whether the capture zone is essential, as we do not see evidence of more effective tunnelling in the initial design. However, further investigation and calculation is required to grow more devices with varying designs to fully understand the transport processes in this significantly complex structure.

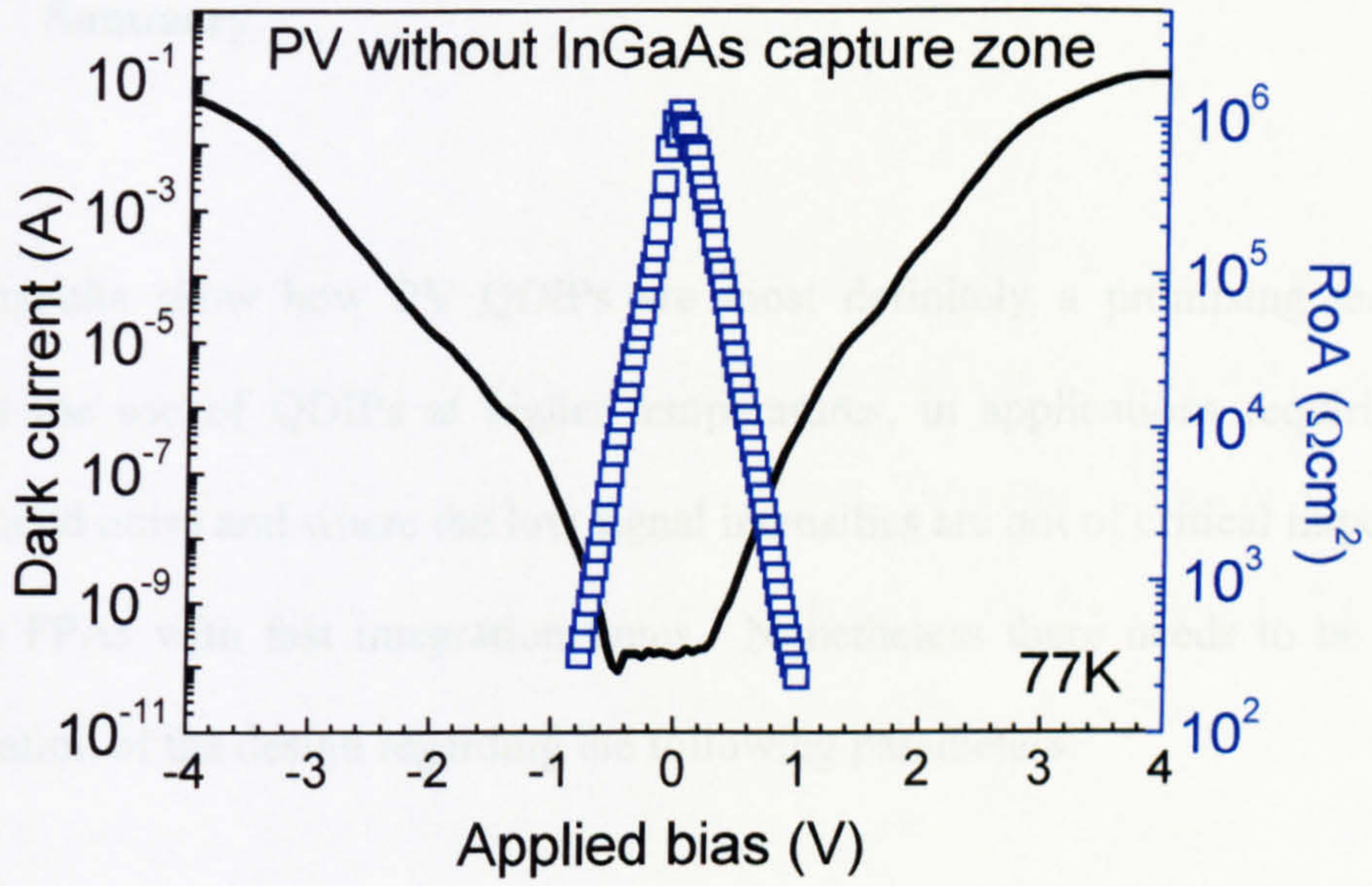

Fig.5.3.6. Dark current IV curve (black line) and RoA product at 77K of the PV QDIP without an InGaAs capture zone, Ro being the differential resistance of the device and A its area.

Nonetheless, the dark current and RoA product for this design were measured at 77K and from these (as above) the detectivity of the detector can be deduced from eq.5.3. A value of $D^* = 3.9\text{x}10^9\text{cmHz}^{1/2}\text{W}^{-1}$ at 77K and 7.5μm and 0V, showing a twofold decrease compared to the previous sample are observed, whereas the maximum detectivity for this sample is observed at -0.55V with values of $8\text{x}10^9\text{cmHz}^{1/2}\text{W}^{-1}$ at 77K.

5.3.4. Summary

These results show how PV QDIPs are most definitely a promising technique towards the use of QDIPs at higher temperatures, in applications requiring low background noise and where the low signal intensities are not of critical importance, such as FPAs with fast integration times. Nonetheless there needs to be further optimisation of the design regarding the following parameters:

- Tailoring of the capture region QW state to be closer to resonance with the QD ground state for efficient tunnelling to occur
- Thickness of the AlAs barrier for same reason as above
- Doping position
- Doping concentration
- Excitation region design variation to achieve longer wavelengths (also achievable by rapid thermal annealing)

5.4. Discussion

In this chapter, new directions in QDIP research at Sheffield were presented. It was shown how QDIPs can be designed or manipulated to suit various new, as well as existing applications. The capability to tune the spectral photoresponse of DWELL QDIPs across the 8-12μm LWIR atmospheric window by rapid thermal annealing was demonstrated, as well as the potential of shifting the far infrared *s-p* transitions below the phonon energy (<35meV). This could enable the operation of detectors in the terahertz region were there is a limited availability of imaging detectors. This would expand the applications for QDIPs, especially as there is a growing interest in the use of terahertz emitters for a range of applications including medical imaging (providing good contrast for different types of tissue-useful for types of skin cancer and other diseases) as well detection of explosives, prohibited substances and concealed objects.

Another way of producing a fast, sensitive detector operating in the FIR was presented in this chapter. This involved utilising the *p*-like QD states as intermediate states between the QD ground state and the final photocurrent state in DWELLs, in order to induce two-photon detection. It was shown how the photocurrent of such a detector had a quadratic dependence on incident power when the incident wavelength matched that of the s-*p* state separation. Using two-photon detection, the device was successfully used to perform autocorrelation measurements using a free electron laser. This detector was not designed *a priori* for resonant two-photon absorption (i.e. the *p*-state energy was not half way between the the QD ground state and the QW final state). Nonetheless the results indicated a very high absorption

coefficient compared to bulk GaAs materials, and also was found comparable to other two-photon QWIPs in the literature. Upon further optimisation, two-photon DWELL QDIPs can prove a very useful technology for the characterisation of ultrafast laser pulses in the FIR, from free electron laser sources or mode-locked QCLs.

Finally, the potential of DWELL QDIPs specifically designed for photovoltaic operation was presented, whereby two designs attempted to provide an enhanced in-build electric field to maximise the current flow in the absence of external bias. Photovoltaic mid-IR detectors are highly relevant as they are less prone to one of the main limitations of photoconductors in the same region which is the dark current. As photovoltaic detectors have no dark current they have a higher theoretical limit for the signal-to-noise ratio (or detectivity). It was shown how it is possible to design a photovoltaic detector to introduce a significantly enhanced in-built electric field that would favour the current flow in one direction towards the collector (in an n-*i*-n device). Although the design is still at the first stages of optimisation, the basic principles were demonstrated, and upon optimisation of the doping concentration, as well as several minor alterations to the design, this could prove a very promising approach to low-noise QDIPs.

References

1 See, for example, E.A. Zibik, W.H. Ng, L.R. Wilson, M.S. Skolnick, J.W. Cockburn, M. Gutierrez, M.J. Steer, M. Hopkinson, Appl. Phys. Lett. **90**, 163107 (2007); J. H. Marsh, Semicond. Sci. Technol **8** 1136 (1993); R. Leon, Y. Kim, C. Jagadish, M. Gal, J. Zou, and D. J. H. Cockayne, Appl. Phys. Lett. **69**, 1888 (1996)

2 H. Schneider, T. Maier, H. C. Liu, M. Walther, P. Koidl, Optics Letters, **30** 287 (2005)

3 D. Pan, E. Towe, S. Kennerly, Appl.Phys.Lett. 76 (22) 3301 (2000)

4 A. S. W. Lee, E. Herbert Li, G. Karunasiri, J. Appl. Phys. **86** (6) 3402, 1999

5 L. Fu, H. H. Tan, C. Jagadish, Na Li, N. Li, X. Liu, W. Lu and S. C. Shen, Infrared Phys. Technol. **42**, 171-175 (2001)

6 Na Li, Ning Li, W. Lu, X. Q. Liu, X. Z. Yuan, Z. F. Li, H. F. Dou, S. C. Shen, Y. Fu, M. Willander, L. Fu, H. H. Tan, C. Jagadish, M. B. Johnston, M. Gal, Superlattices and Microstructures **26** (5) 317, 1999

7 L. Fu, H.H. Tan, I. McKerracher, J. Wong-Leung, C. Jagadish, N. Vukmirovic, P. Harrison, J.App.Phys. **99** 114517 (2006)

8 H. Schneider and H. C. Liu, *Quantum Well Infrared Photodetectors: Physics and Applications*, Springer Series in Optical Sciences, Springer, Berlin, Heidelberg, 2006, Vol. 126, p. 68-69, 142

9 E.A. Zibik, L.R. Wilson, R.P. Green, G. Bastard, R. Ferreira, P.J. Phillips, D.A. Carder, J.P.R. Wells, M.S. Skolnick, J.W. Cockburn, M.J. Steer, M. Hopkinson, Physica E 26 (2005) 408-412

10 S. Fafard, Z. R. Wasilewski, C. Ni. Allen, D. Picard, M. Spanner, J. P. McCaffrey, and P. G. Piva, Phys. Rev. B **59**, 15368 (1999); S. Fafard and C. Ni. Allen, Appl. Phys. Lett. **75**, 2374 (1999).

11 S. Krishna, S. Raghavan, G. von Winckel, A. Stintz, G. Ariyawansa, S.G. Matsik, A.G.U. Perera, App. Phys. Lett. **83**, 2745 (2003)

12 A. S. W. Lee, E. H. Li, Appl. Phys. Lett. **69**, 3581 (1996), N. Hatefi-Kargan, D.P. Steenson, P. Harrison, E.H. Linfield, S. Khanna, S. Chakraborty, P. Dean, P.C. Upadhya, I. Farrer, D.A. Ritchie, B. Sherliker, M. Halsall, Infrared Phys. Technol. **50** 106-112, 2007

13 A. Rogalski, '*Quantum well infrared photoconductor in Infrared Detectors Technology*', Intersubband Infrared Photodetectors, Selected Topics in Electronics and systems 2003, Vol.27, p.4

14 A. Nedelcu, X. Marcadet, O. Huet, P. Bois, App. Phys. Lett. **88** 191113 (2006)

15 O. P. Kowalski, C. J. Hamilton, S. D. McDougall, J. H. Marsh, A. C. Bryce, R. M. De La Rue, B. Vogele, C. R. Stanley, C. C. Button and J. S. Roberts, App. Phys. Lett. **72** (5) 581 (1998)

16 T. Maier, H. Schneider, M. Walther, P. Koidl, H. C. Liu, Appl.Phys.Lett. **84** 5162 (2004)

17 H. Schneider, T. Maier, H. C. Liu, M. Walther, P. Koidl, Optics Letters, **30** 287 (2005)

18 H. Schneider, O. Drachenko, S. Winnerl, M. Helm, T. Maier, M. Walther, Infrared Phys. Technol. **50** 95 (2007)

19 See, for example, E. Dupont, P. Corkum, H. C. Liu, P. H. Wilson, M. Buchanan, Z.R. Wasilewski, Appl.Phys.Lett. **65** 1560 (1994); J. Jiang, Y. Fu, Ning. Li, X. S. Chen, H. L. Zhen, W. Lu, M. K. Wang, X. P. Yang, G. Wu, Y. H. Fan, Y. G. Li, Appl.Phys.Lett. **85** 3614 (2004)

20 H. Schneider, O. Drachenko, S. Winnerl, M. Helm, M. Walther, Appl.Phys.Lett. **89** 133508 (2006)

21 S. Sauvage, P. Boucaud, T. Brunhes, F. Glotin, R. Prazeres, J.-M. Ortega, J.-M. Gerard, Phys.Rev.B **63** (2001) 113312

22 E. A. Zibik, L. R. Wilson, R. P. Green, G. Bastard, R. Ferreira, P. J. Phillips, D. A. Carder, J-P. R. Wells, J. W. Cockburn, M. S. Skolnick, M. J. Steer and M. Hopkinson, Phys. Rev. B **70**, 161305 (2004).

23 P. Aivaliotis, S. Menzel, E. A. Zibik, J.W. Cockburn, L.R. Wilson, M.Hopkinson, Appl.Phys.Lett. 91 (under review)

24 J.Y. Duboz, E. Costard, J. Nagle, J.M. Berset, J. M. Ortega, J.Appl.Phys. **78** 1224 (1995)

25 M. Ershov, H. C. Liu, M. Buchanan, Z. R. Wasilewski, V. Ryzhii, Appl.Phys.Lett. **70** (1997) 414

26 H. Lim, B. Movaghar, S. Tsao, M. Taguchi, W. Zhang, A. A. Quivy, and M. Razeghi, Phys. Rev. B **74** (2006) 205321;

27 P. Aivaliotis, N. Vukmirovic, E. A. Zibik, J. W. Cockburn, D. Indjin, P. Harrison, C. Groves, J. P. R. David, M. Hopkinson and L. R Wilson, J. Phys. D: Appl. Phys. **40** 5537-5540, (2007)

28 T. Maier, H. Schneider, H. C. Liu, M. Walther, P. Koidl, Infrared Phys. Technol. **47** 182 (2005)

29 W. Nessler, S. Ogawa, H. Nagano, H. Petek, J. Shimoyama, Y. Nakayama, K. Kishio, J. Electron. Spectrosc. Relat. Phenom. 88 495 (1998).

30 See, for example, P. Borri, W. Langbein, S. Schneider, and U. Woggon, R. L. Sellin, D. Ouyang, and D. Bimberg, Phys. Rev. Lett. 87 (2001) 157401; I. Favero, G. Cassabois *, R. Ferreira, D. Darson, C. Voisin, J. Tignon, C. Delalande, G. Bastard, and Ph. Roussignol, J. M. Gérard, Phys. Rev. B 68, 233301 (2003)

31 E. A. Zibik, T. Grange, B. A. Carpenter, R. Ferreira, G. Bastard, N. Q. Vinh, P. J. Phillips, M. J. Steer, M. Hopkinson, J. W. Cockburn, M. S. Skolnick, L. R. Wilson,arXiv:0710.5095v1 [cond-mat.mes-hall]

32 J.D. Vincent, *Fundamentals of Infrared Detector Operation and Testing*, *Wiley series in pure and applied optics*, ISSN 0277-2493, 1990

33 A. Kastalsky, T. Duffield, S.J.Allen, J. Harbison, Appl.Phys.Lett. **52** 1320 (1988)

34 K.W. Goosen, S.A. Lyon, K. Alavi, Appl.Phys.Lett. **52** 1701 (1988)

35 C. Schönbein, H. Schneider, G. Bihlmann, K. Schwarz, P. Koidl, Appl.Phys.Lett. **68** 973 (1996)

36 D. Pan, E. Towe, S. Kennerly, Appl.Phys.Lett. **76** 3301 (2000)

37 S.H. Hwang, J.C. Shin, J.D. Song, W.J. Choi, J.I Lee, H. Han, S-W. Lee, Microelectronic Engineering, **78**, 229, Mar 2005

38 L. Gendron, M. Carras, A. Huynh, V. Ortiz, C. Koeniguer, and V. Berger, Appl. Phys. Lett. **85**, 2824 (2004)

39 See for example: M. Graf, N. Hoyler, M. Giovannini, J. Faist, D. Hofstetter, Appl. Phys. Lett. **88**, 241118 (2006); F. R. Giorgetta, E. Baumann, M. Graf,

L. Ajili, N. Hoyler, M. Giovannini, J. Faist, D. Hofstetter, P. Krötz, G. Sonnabend, Appl. Phys. Lett. 90, 231111 (2007)

40 K.T. Lai, S.K. Haywood, A.H. Mohamed, M. Missous, R. Gupta, Appl.Phys.Lett.87, 192113 (2005)

41 H. Schneider, C. Schönbein, G. Bihlmann, P. van Son, H. Sigg, Appl.Phys.Lett. 70 (12) 1602 (1997)

42 H. Schneider, C. Schönbein, M. Walther, K. Schwarz, J. Fleissner, P. Koidl, Appl.Phys.Lett. 71 (2) 246 (1997)

43 J.J. Finley, R.J. Teissier, M.S. Skolnick, J.W. Cockburn, G.A. Roberts, R.Grey, G. Hill, M.A. Pate, R. Planel, Phys.Rev.B, 58, (16)10619 (1998)

6. Future directions

In this final chapter of this thesis, the issues that could be addressed to improve DWELL QDIP performance, and the ways with which the already discussed approaches can be improved are summarised, and future approaches and techniques that could be implemented to investigate the properties of QDs and their relevance to the optical and electrical performance of QDIPs are discussed.

As discussed in chapter 3.1, DWELL structures benefit from narrow linewidth strong high energy absorption, with longer relaxation times from high energy states to the ground state of ~5ps compared to ~1ps for the equivalent relaxations in QWIPs. This lifetime is highly relevant to QD detectors as it is pertinent to the responsivity. It would be interesting to investigate DWELL structures with different dot sizes, and with different well widths, in terms of this lifetime, to see if it could be maximised. The investigation of relaxation times under applied bias would elucidate the long decay time which was observed. This is a non-trivial task as processed devices which can be biased are difficult to measure with ultrafast spectroscopy due to scattering from the contacts and other practical limitations. However there are techniques for applying electric fields on unprocessed semiconductor wafers, such as cryogenic probe stations, which could be used to do pump-probe measurements while applying lateral or vertical applied fields.

It has to be said that although various design alterations can improve QDIP performance, the successful growth of the QDs is the most important factor for the device's operation. In order to monitor this and investigate the effects of variations in the growth, structural information using techniques such as planar and cross sectional transmission electron microscopy (TEM) and scanning tunnelling microscopy (X-STM), would elucidate the relation of the physical aspects of the QD with the observed optical and electrical properties. A good example was discussed in chapter 3.3, where the observed bias dependent Stark shift increased with the number of InAs monolayers (N_{ML}) deposited during growth. Although the 8 band k•p method model used to simulate this behaviour provided a good understanding of the effect, the use of X-STM on samples with different N_{ML} could verify the interpretation, as well as supply more information on the strain build-up with increasing In, and the compositional distribution within the dot as well as the vicinity of the dot within the InGaAs QW. A clear understanding of the strain mechanisms in DWELLs is very important since it affects the offset of the DWELL conduction band and therefore the electron tunnelling and escape.

Additionally, as discussed in chapter 4, different techniques can be applied to control and enhance the performance of DWELL QDIPs. It was demonstrated how the low QD density, which limits the number of absorbing electrons, can be increased, through the incorporation of a thin layer of antimony prior to QD growth. In addition a reduction of the dark current was observed with this technique possibly due to suppressed defect formation influenced by the GaSb surfactant.

However, the further optimisation of this technique, primarily in terms of the growth of such structures with uniform size distribution, and the highest attainable dot

density, is yet to be undertaken. Also in the case of DWELLs where the In composition in the InGaAs QW affects the dot density and size distribution, this technique becomes more complicated. It could be possible that for this technique the optimum In composition in the QW is not the same as it is in conventional InAs/InGaAs DWELLs. This is one of the most promising techniques presented in this thesis.

The optimisation of GaSb containing DWELL QDIPs will definitely be one of the main areas of research in the near future, especially as it is also highly relevant to QD lasers, whose performance is also affected by the low QD density in present devices. A further addition to this technique would be the attempt to grow ordered high dot density ensembles [see *Infrared Physics & Technology 50 (2007) 162–165*], which could improve the doping distribution and perhaps even allow the doping to be positioned in the dot layer.

In terms of the incorporation of AlGaAs barriers for the development of InAs/GaAs/AlGaAs DWELLs to reduce the detector dark current, it has been demonstrated to be an efficient enough technique, since it also helps reduce the strain in the structure allowing the growth of multilayer (>20) structures (since less or no indium is required). This technique can probably produce good detectors and some have already been used in FPAs. Nonetheless, using this technique there is not much room for improvement, and if QDIPs are to be a competitive technology to QWIPs in any of the applications that they are aimed for, the need to have orotund advantages rather than just being equivalent. The use of surfactants such as antimony or the other techniques discussed below are certainly more promising and capable to produce competitive QDIPs.

Another method towards the production of multi-layer (>20) DWELL detectors, whilst maintaining the advantages of an InAs/InGaAs structure, is via the growth of GaP strain balancing layers. This was shown to be a promising technique, especially for detectors for high temperature operation. This technique also introduces a current blocking barrier in the conduction band, which decreases the dark current. As discussed in chapter 4.3, further growth and design optimisation is required to adjust the composition of the SC layers as well as their position in the structure. This could provide a very interesting approach for strain compensation in QD based devices in general. Again, X-STM and further TEM images could provide information on the effects that GaP has on the nucleation of the InAs dots, as well as the changes in the strain.

The use of rapid thermal annealing capability to tune the spectral photoresponse of DWELL QDIPs across the 8-14μm LWIR atmospheric window was demonstrated, as well as the potential of shifting the far infrared *s-p* transitions below the phonon energy (<35meV). This could enable the operation of detectors in the terahertz region were there is a limited availability of detectors. This would expand the applications for QDIPs, especially as there is a growing interest in the use of terahertz emitters for a range of applications including medical imaging or detection of concealed objects and explosives. Detectors in this region could also prove an interesting alternative to bolometers for certain applications requiring narrower band detection.

As discussed in chapter 5.2, another way of producing a sensitive detectors operating in the FIR makes use of a *p*-like QD state as an intermediate state between

the QD ground state and the final photocurrent state in a DWELL QDIP, in order to induce two-photon detection. It was shown how the photocurrent of such a detector had a quadratic dependence on incident power when the incident wavelength matched that of the *p*- state. Using two-photon detection, detectors can be used to characterise ultrafast pulses in the FIR from free electron laser sources or mode-locked QCLs. The two-photon QDIP presented in this thesis was not designed to have equidistant states that would induce resonant two-photon absorption.

Nonetheless, a very high absorption coefficient was derived even for this unoptimised structure. Future studies could involve the design of optimised structures with equidistant states. Furthermore, the p^--p^+ splitting of the intermediate state could be taken advantage of, since it would enable the tuning of the 2P process on and off resonance. In addition a polarisation dependence of the two photon absorption could be performed via 45° waveguide geometry to investigate the polarisation sensitivity of the 2P process, since it involves an intermediate state that is strongly *s*-polarised and a final state which is strongly *p*-polarised.

Other future approaches could include the optimisation of the presented photovoltaic QDIPs, with higher doping concentrations, and different widths of barriers in the superlattice.

Overall, I believe that the approaches discussed in this thesis adequately demonstrate the potential of DWELL QDIPs not only to reach the maturity level of QWIPs, but also to lead the way into new applications for infrared detectors.